# Measurements of Underwater Radiated Noise from Non-cavitating Propellers in Atmospheric Towing Tank

by

@ Md Saiful Islam

A thesis submitted to the School of Graduate Studies in partial fulfillment of the requirements for the degree of Master of Engineering.

Faculty of Engineering and Applied Science

Memorial University of Newfoundland

May 2022

St. John's, Newfoundland and Labrador, Canada

**Abstract**

Propeller-induced underwater radiated noise (URN) has been an increasing threat to marine ecosystems. The design of silent ships requires a set of regulations and standards that allow naval architects to assess the URN from new ships in the early design stages. Tests in towing tanks are established experimental procedures to assess the hydrodynamic performances of new ships. Recently researchers have started to focus on developing model testing to assess URN from propellers, which are major sources of the URN.

In this work, the acoustic parameters of a towing tank have been analyzed both experimentally and numerically. The outcomes allow us to measure URN in the towing tank without the influence of reverberation and free surface interference. Additionally, I present a procedure to assess URN from non-cavitating propellers in atmospheric towing tanks at different hydrodynamic conditions. A MATLAB program is developed to analyze the results both in narrow and 1/3 octave bands.

## General Summary

Ships are major sources of underwater noise emission, and their impact on the marine environment is a major concern. Developing mitigation guidelines and shipping regulations is necessary to understand and reduce the adverse effects of commercial shipping noises. Usually, propeller noise in the non-cavitating condition is measured in a towing tank at different hydrodynamic conditions. The confined environment of the tank heavily affects the measured sound level, and necessary acoustic characterization of the facility is needed.

I have developed an experimental procedure to study the reverberation characteristics of a towing tank. It provides valuable information about the experimental setup and measurement procedure for model testing. I have also developed a numerical method to predict the acoustic characteristics of any tank.

Using the acoustic information about the test facility, I have conducted model testing experiments to measure the noise in different propeller loading conditions. I have found that the background noise generated from the carriage influences the propeller-induced noise measurement. However, the noise measurements in bollard conditions, i.e., when the ship is at rest provide good results. My experimental results will be helpful to validate the CFD model and help the international community to develop a noise mitigation policy framework.

**Acknowledgement**

Foremost, I would like to express my deep gratefulness to God, the Almighty, for his blessing, grace, and mercy throughout my research and for the successful completion of my M. Eng. thesis work.

I would like to express my sincere gratitude to my supervisor, Dr. Lorenzo Moro, for his continuous scientific and technical support, patience, advice, and motivation. I could not imagine having a better advisor and mentor for completing my research and education. I would also like to thank Dr. Mohammed (Shameem) Islam of Ocean Coastal and River Engineering Research Centre of National Research Council Canada (the NRC-OCRE) for sharing his experience during the model testing, insightful comments, and critical reviews.

My sincere thank goes to my teammates: Jacopo Fragasso, Khaled Helal, Alireza Jahanbakhsh, Alessandro Zambon, Kareem Wael Altaiby, Alice Affatati, for their continuous support, motivation, and sharing valuable technical knowledge.

I also want to acknowledge my research funding from Transport Canada, NRC and InnovateNL through the "Propeller Induced Noise and Vibration (PINOV)" project. My thanks also extended to the PINOV team members at the NRC-OCRE for the support during model testing.

Last but not least, I would like to acknowledge with gratitude my family: my parents Md Abdus Salam and Umme Habiba Begum, my lovely sister Sanjida Afrin for their love, prayers, and sacrifices for educating me. You have always been there for my need, and I am thankful for everything. Finally, I would like to dedicate my thesis book to my late sister Sadia Afrin. I miss you a lot and may my Almighty rest your soul in peace.

## Table of Contents

## List of Tables

## List of Figures

## List of Symbols

| | |
|---|---|
| $D$ | Decay rate (dB/s) |
| $f$ | Modal frequency (Hz) |
| $k$ | Wave constant |
| $N$ | Number of eigenvalues |
| $n$ | Speed of the model (RPS) |
| $p$ | Acoustic pressure (Pa) |
| $R$ | Reflection coefficient |
| $Q$ | Propeller Torque (Nm) |
| $S$ | Surface area of the towing tank ($m^2$) |
| $S$ | Wetted surface area ($m^2$) |
| $t$ | Thrust deduction factor |
| $T$ | Propeller thrust (N) |
| $V$ | Volume of the towing tank |
| $V_a$ | Advanced speed (m/s) |
| $C_A$ | Ship correlation |
| $CF_{LM}$ | Correction factor for Llyod's mirror effect (dB) |
| $C_T$ | Total resistance coefficient |
| $C_R$ | Residual resistance coefficient |
| $CF_D$ | Distance normalization correction factor (dB) |
| $F_P$ | Bollard pull of the model (N) |
| $F_D$ | Skin-friction correction force (N) |
| $f_c$ | Schroeder frequency (Hz) |
| $H(\omega)$ | Impulse response function |
| $L_E$ | Sum of edge length (m) |
| $L_p$ | Sound pressure level (dB) |
| $L_M$ | Length of the model (m) |
| $L_S$ | Length of the ship (m) |
| $N_{rays}$ | Number of rays |
| $R_T$ | Total resistance force (N) |

| | |
|---|---|
| $r_c$ | Critical radius (m) |
| $I_0$ | Acoustic Intensity (W/m$^2$) |
| $T_{60}$ | Reverberation time (s) |
| $T_S$ | Thrust force generated by ship (N) |
| $T_M$ | Thrust force generated by the model (N) |
| $P_{ref}$ | Reference pressure (1 µPa) |
| $\Delta C_F$ | Roughness allowance |
| $V_R$ | Volume of the receiver (m$^3$) |
| $V_M$ | Velocity of the model (m/s) |
| $V_S$ | Velocity of the ship (m/s) |
| $C_F$ | Frictional resistance coefficient |
| $Z_0$ | Characteristics impedance of the medium |
| $\rho$ | Density of fluid (kg/m$^3$) |
| $\lambda$ | Scale factor |
| $\alpha$ | Sound absorption coefficient |
| $\omega$ | Angular frequency (rad/s) |
| $\sigma$ | RMS roughness of the surface |

## List of Abbreviations

| | |
|---|---|
| UNCTAD | United Nations Conference on Trade and Development |
| ICS | International Chamber of Shipping |
| URN | Underwater Radiated Noise |
| IMO | International Maritime Organization |
| ABS | American Bureau of Shipping |
| EU | European Union |
| DPWB | Depressurized Wave Basin |
| NRC | National Research Council |
| OCRE | Ocean, Coastal and River Engineering Center |
| RTM | Ray Tracing Model |
| ITTC | International Towing Tank Conference |
| BEM | Boundary Element Method |
| FVM | Finite Volume Method |
| FWH | Ffowcs-Williams and Hawkings |
| RANS | Reynolds Averaged Navier–Stokes |
| ANSI | American National Standards Institute |
| SILENV | Ships Oriented Innovative Solutions to Reduce Noise and Vibrations |
| AQUO | Achieve QUieter Oceans |
| SONIC | Suppression of Underwater Noise Induced by Cavitation |

# Chapter 1

# Introduction and Overview

## 1.1 Background

Sound is the primary way of underwater communication since electromagnetic waves can not propagate through the water. Perception of sound is essential for marine mammals and other organisms to recognize information and understand their marine environment [1]. Aquatic animals use sound to locate habitat, find prey, avoid predators, guide their navigation, find mates, and communicate with each other [2]. In addition to these marine mammals, fish and other species use sound to communicate through inner ear hearing receptors. Ocean noise refers to sounds produced from natural sources or by human activities, which can interfere and reduce the communication ability of marine animals in the ocean [3]. Ocean noise is deadly and causes physical damage, internal injuries and stranding to marine mammals. Indirectly, underwater noises mask and overlap the communication frequency of marine animals, reducing their ability to hear vital environmental clues for survival and navigating to preferred habitats [4]. Moreover, they disturb many complex ecosystems by unbalancing predator-prey interaction, which endangers marine life [5].

Furthermore, ocean noise pollution has a disturbing impact on mating and nursing young, which reduces their reproduction and grave consequences in the total population [6]. Sea noise levels have increased remarkably over the last century and are identified as a major threat to marine organisms [7]. Even in some areas, the ambient noise levels

have doubled every decade for the last 60 years. It is reported that low-frequency noise levels have increased approximately 15 dB from 1950 to 2000 [8]. The ocean is filled with different types of noise. Both natural and anthropogenic activities can lead to underwater noise emission [9]–[11]. The sources can be divided as follows:

i. **Natural Sources**
    a. Ocean surface
    b. Atmospheric sources
    c. Wind, waves, and ice
    d. Geologic sources
    e. Biological sources (marine animals)

ii. **Anthropogenic (Human-induced) sources**
    a. Maritime traffic
    b. Oil and gas exploration
    c. Seismic profile
    d. Military sonar
    e. Offshore structures
    f. Explosives

Some noises are always present in the ocean, which can be identified by their unique frequencies. In the low-frequency range (20-500 Hz), ambient noise is primarily generated by shipping traffic. The noise level is also greater in busy shipping traffic regions. However, surface noise generated by spray and bubbles associated with breaking waves causes noise pollution in the mid to high-frequency range (500-100,000 Hz). The surface noise highly depends on the wind speed and increases with increasing wind speed. Above 100,000 Hz, the noise is generated by the random motion of water

molecules, called thermal noise. The natural noises are uncontrollable and beyond research capabilities. Therefore, anthropogenic noise sources and their levels are essential to understanding the characteristics of underwater noise pollution.

Over the last century, humans have progressively altered the marine environment by commercial shipping, energy exploration, coastal constructions, sea-bed mining, sonar navigation, etc. Moreover, these activities are not limited to the coast and offshore areas but also the deep ocean [12]. Noise from these activities increases overall underwater noise levels in many coastal and offshore ecosystems [13]. Among them, commercial shipping is considered as the primary contributor to aquatic noise pollution, especially at low frequencies (20-500 Hz). Increased shipping traffic in the Arctic ocean doubled the underwater noise in the last six years [14]. Similarly, underwater noise in the eastern North Pacific has doubled since the 1950s, with a 3 dB increase every ten years. However, this increase in noise level is not only for commercial shipping but also due to vessel traffic and other anthropogenic activities.

Noise pollution from commercial shipping is a growing concern due to the increasing global trade, transportation, ship size, service speed, and operating hours [15]. International trade depends on maritime shipping, and 80% of all goods are carried by sea because of their reliability and low transportation costs. According to UNCTAD [16], the world commercial fleet consisted of 93,161 vessels in January 2017, with a combined deadweight tonnage of 1.86 billion. International Chamber of Shipping (ICS) estimated that about 11 billion tons of goods are transported by ship each year. Over the last four decades, this massive shipping volume and ships have increased deep-ocean noise levels [17]. The low-frequency noise levels in the ocean increase by 3.3 dB approximately per decade. The trend is related to commercial shipping activity and

global economic growth [8]. The underwater radiated noise (URN) from commercial shipping is continuous and at a lower frequency range. The ship radiated noise peaks at 50-150 Hz during regular operation but can extend to 10,000 Hz. The ocean background noise level increased by 20-30 dB, particularly in the 10 to 300 Hz frequency range [18]. Additionally, the mapping of shipping noise from 2013 to 2019 in the Arctic Ocean shows an increase of 5-15 dB noise, particularly at 25 Hz and 63 Hz. The low-frequency noise can propagate over immense distances in all directions due to longer wavelength (peaks have lower pressure), negligible transmission loss, and lower attenuation level.

Noise emissions from ships depend on local traffic, size, operation, speed, bathymetry, and sound propagation characteristics. It is necessary to understand the generation and propagation of ship radiated noise to assess the impact on the marine environment. The sources of ship radiated noise can be categorized according to Urick [19] into three major classes:

i. Propeller noise due to the displacement of the blades, friction between suction and pressure surface, fluctuating wakes, and sudden collapsing of the cavitation bubbles
ii. Hydrodynamic noise due to the flow over the ship hull, its appendages and the propeller
iii. Machinery noise due to the vibrations of propulsion machinery, auxiliary engines, drive train, shafting system, etc. [20]

Propeller is the dominant noise source compared to the others. Marine propellers can generate noise in both cavitating and non-cavitating conditions. Cavitation of the underwater propeller is the most prevalent source of noise, which is responsible for 80-

85% of total maritime noise. However, below cavitation speed, the propeller noise mainly comes from propeller, machinery and hull pressure [21]. Additionally, A fixed pitch propeller at low ship speeds operates in a non-cavitating condition.

Understanding various noise generation mechanisms is still an ongoing area of research. Organizations like International Maritime Organization (IMO), European Union (EU) and American Bureau of Shipping (ABS) are already making efforts to improvise guidelines and regulations for shipping noise to save marine life and habitats. The need to conform to regulatory requirements increases the necessity to measure and report ship-radiated underwater noise in the ocean. Therefore, developing different methods to predict and quantify ship-generated noise during the design process becomes more important and imminent. Although many complex physical aspects are involved in propeller noise, researchers have developed methods or tools to characterize propeller-induced noise. The highly accepted methods or tools to predict and measure propeller induced noise are listed as follow:

i. Semi-Empirical method
ii. Hybrid CFD method
iii. Model testing
iv. Full-scale measurement

The semi-empirical methods are analytical and high-speed tools to give the first estimate. However, they are limited only to simple propeller systems. In contrast, the CFD method is a computational tool to predict flow physics, but it needs quality input and a longer time to acquire statistical data. Moreover, numerical noise modelling is limited by the reliability, precisions, computational expense, and the inability to model

background noise and other experimental factors. Full-scale measurements in the open sea are challenging due to the uncontrolled underwater environment, complex instrumentation, and cost of the experiments. Although model testing is expensive and time-consuming, researchers prefer model testing for reliable noise measurement. The model scale yields good results similar to full-scale measurement with an acceptable level of accuracy [22].

Model testing for non-cavitating noise measurement is performed in an atmospheric towing tank maintaining Froude's similarity. The model scale results show good agreement with full-scale measurements for similar flow conditions. The Special Committee On Hydrodynamic Noise developed the scaling procedure at 28$^{th}$ ITTC (Volume II) meeting [23]. However, the measurement systems require an expensive test setup and careful model installation to reduce background noise. In addition, the confined environment due to the restricted boundaries of the tank influences the model scale noise measurement. Moreover, the sidewalls and free surface of water reflect the incident sound waves and cause echo. The reflected sound from the boundary dominates the actual sound, and the sound does not appear to come from a single source. Acoustic reverberation of the tank highly influences the noise measurement in the towing tank because it modifies the sound pressure field and results in a biased estimate of the acoustic source strength. The effect is related to the length of the noise wave of interest due to the restricted tank dimension. Therefore, the hydrophones need to be correctly positioned with respect to the propeller for precise and actual noise measurement.

The other significant effect comes from the free surface of the tank, especially for low-frequency noise measurement. The free surface acts as a mirror for a submerged sound source. It reflects the incident sound wave, which causes an interference pattern

between the direct sound and reflected sound from the free surface. This inference phenomenon is also known as Lloyd mirror effect. This effect highly depends on the relative position between the source and receiver. A correction in the dB level is needed to estimate the noise source level emitted by the propeller.

The most critical part of model scale noise measurement is the background noise. Background noise in the tank is present at different frequency ranges starting from 100 Hz to 100,000 Hz. The towing carriage is the most noticeable source of background noise [24]. The other sources are electric appliances (compressors, heaters, transformer), measuring systems, activities outside the tank, etc. Vibrations of the carriage wheels and the rails generate loud carriage noise, which is transferred through the concrete walls to the water. It is challenging to distinguish propeller noise from carriage noise at high carriage speed.

A proper and universally adopted standard to measure the ship radiated noise and understand the radiation characteristics is essential to control and alleviate the ship noise. ITTC developed procedures for measuring ship noise on a model scale. Unfortunately, there is no widely adopted procedure for URN measurements at model scale despite similar installation methods, test conditions, data acquisition/analysis and scaling techniques to full scale. Therefore, the research communities adopted noise measurement procedures based on their facility size, type, and available range of operating conditions. In this scenario, the accuracy and reliability of URN measurement is a crucial challenge that necessities the development and validation of reliable noise assessment and prediction tools.

## 1.2 Objectives

As discussed in this chapter, model tests have been demonstrated as effective tools to study ship hydrodynamic in early design phases. Now they are used to measure underwater radiated noise from propellers. An accurate procedure allows the researchers to solve potential issues before the ship is constructed. Model tests will reduce the propeller design cost, given that potential hazardous URN could be dentified before the actual propeller is manufactured. In order to have accurate model tests, there is a need for accurate characterization of the atmospheric tank and identifying the sources affecting the noise measurements. The thesis work considers all the possible factors that influence the measurement of non-cavitating propeller induced noise in the towing tank and encompasses the following objectives:

i. An experimental procedure to measure underwater radiated noise from a non-cavitating propeller in an atmospheric tank;
ii. Acoustic characterization of a towing tank;
iii. Model testing of a ship model to measure propeller URN and check the quality of the measurements.

This thesis is a part of a large research project, ‘Propeller Induced near- and far-field Noise and ship hull Vibration (**PINOV**)” funded by Transport Canada (TC), National Research Council (NRC) and Department of Industry, Energy and Technology of the government of Newfoundland and Labrador. The primary objectives of this project are the development of design tools to predict underwater radiated noise and propeller-induced hull vibration from non-cavitating propellers. The work presented in this thesis is fundamental to provide guidelines for experimental tests of URN measurements in

towing tank. The outcomes of these experimental tests will be used to validate numerical models and help the development of the design tool.

## 1.3 Thesis Organization

The content in this thesis book is arranged according to a paper-based format suggested by Memorial University and subdivided into four chapters. The outcomes of this Master of Engineering thesis have led to two journal articles under preparation at the time of this submission. **Chapter 1** gives a detailed overview of propeller-induced noise, the importance of noise measurements, and the challenges of accurate noise estimation. **Chapter 2** describes the reverberation characteristics of the towing tank and acoustic numerical simulations to model the absorption characteristics inside the tank. The experimental procedure to validate the ray-tracing model is also presented in this chapter. **Chapter 3** describes efficient, accurate and well-validated research tools to estimate propeller-induced near- and far-field noise. It includes test setup, experiment matrix, data recording system, noise measurement and analysis procedures. Finally, **Chapter 4** provides a summary and recommendations for future research.

## 1.4 Co-authorship Statement

I am the primary author for the two articles listed above in **Section 1.3**. As the primary author, I completed the literature review, participated in the model testing experiments, recorded and stored the experimental data, developed data analysis procedures, performed all the analyses, and prepared the manuscript. The contributions from the co-author, **Dr. Lorenzo Moro** and **Dr. Mohammed (Shameem) Islam**, included reviewing the results and reviewing and revising the manuscript.

# Chapter 2

## Acoustic Characterization of the Towing Tank

### 2.1 Abstract

Propeller-induced underwater radiated noise (URN) has been an increasing threat to marine ecosystems. Proper predictions and assessments of propeller-induced noise are necessary to develop policy frameworks and guidelines to regulate noise in the ocean. The propeller-induced underwater noise measurements are usually conducted in a towing tank facility. The acoustic characterization of the tank is necessary to observe the effect of wall reflection and free surface interference on the measured noise. In this study, the reverberation characteristics of a towing tank are analyzed both experimentally and numerically for the frequency range 630 Hz to 12.5 kHz. A numerical ray-tracing model is developed to predict the reverberation time of the same tank. Additionally, the fundamental acoustic characteristics like sound absorption coefficient, critical frequency, and reverberation radius are measured using modal acoustic theories. A procedure to correct the free surface effect is also developed based on Llyod's mirror theory. The numerical results showed excellent agreement with the experimental results.

## 2.2 Introduction

Commercial shipping has increased rapidly over the past few decades due to increasing global trade, ship size, service speed, and operating hours [11]. Although both natural and anthropogenic activities generate underwater radiated noise (URN), propeller-induced noise is the primary contributor, especially at low frequencies (10-500 Hz) [25], [26]. This low-frequency noise could mask and overlap the communication frequency of marine mammals, preventing them from identifying prey or predators and resulting in compromised marine ecosystems and biodiversity [27], [28]. Regulations to protect the marine environment from URN necessitate developing appropriate methods to precisely measure URN and experimental and simulation methods to assist ship designers in the project of silent ships. Self-propulsion tests in towing tanks are established tests to measure hydrodynamic performances of ship models. More recently, researchers have used these tests to measure URN from model-scale propellers [29]. However, tow tanks have highly sound reflective boundaries that lead to an acoustic field significantly different from an open water (acoustic free-field) environment [30] and make noise measurements challenging.

The accuracy of URN measurements strongly depends on the acoustic response of the towing tank. A typical towing tank consists of four vertical concrete walls parallel to the sound source and a water column depth limited to a few meters. The acoustic behaviour of a towing tank lies between a tunnel and a room [31] . Therefore, the free-field acoustic condition could be achieved only in the axial dimension (longitudinal) of the tank [29]. Due to this long rectangular cross-section, the transversal eigenmodes could be excited with enough external excitation. The modal behaviour and wall

reflections from the tank significantly modify the acoustic field compared to free field conditions (open sea).

The acoustic propagation at low frequencies in the tank could be described by modal propagation theory. However, the total number of propagating modes increases at higher frequencies, and sound propagation can be simulated by using energy methods [32]. At low frequencies, the acoustics at different locations in the tank is dominated by discrete, spatial, and frequency-wise irregular distribution of tank resonances. Additionally, resonances create dramatic fluctuations of sound pressure distribution throughout the tank. Moreover, modes are apparent as standing waves with localized regions of high and low sound pressure [33]. As a result, the sound amplitude varies when the frequency or the position of the source changes. High and low-pressure regions create inaccurate pressure signals for the hydrophones if not positioned correctly.

In contrast, these resonances become so tightly packed in space that the room behaves relatively uniform at high frequencies. A diffuse sound field is fully developed when the eigenmodes are densely packed, and sound pressure is uniform irrespective of the position [34]. The reflected sound from the boundary dominates the sound, and the sound does not appear to come from a single source [35].

In addition to these acoustic modes, high reverberations and strong Lloyd interference at the free surface (air-water interaction) affected the acoustic measurements. Acoustic reverberations highly influence the noise measurement in towing tank because it modifies the sound pressure field and results in a biased estimate of the acoustic source strength. Primarily for noise measurement above 1 kHz, the sound pressure is highly affected by the sidewalls, and generally, no facility corrections are required since the

noise field is uniform [36]. However, facility corrections should apply for any measurements below 1 kHz. Reverberation radius is the acoustic parameter of the facility that identifies the transition from the direct field to the diffuse field. It is also known as the critical distance from the source, where the sound pressure from the direct field and reverberant field is equal. It largely depends on the geometry and absorption coefficient of the sidewalls, dimensions and shape of the sound source [37]. There is no influence of reflections within the reverberation radius. However, the sound pressure varies with the relative position inside the direct field.

On the other hand, the reverberant field is dominant over the direct field outside the critical radius (diffuse field). Therefore, the hydrophone measures the same sound pressure irrespective of the position in the diffuse field. A detailed understanding of the acoustic characteristics of the tank is needed before experimentation to correct the effect of reverberation in the measurement facility and achieve an equivalent free field condition. Many studies have investigated the acoustic properties of the towing tank, both experimentally and numerically, by taking measurements inside and outside the reverberation radius. Kooij and Bruijn [36] experimentally characterize the reflection properties of a depressurized wave basin (DPWB) using the impulse response method and two different amplitude sweep-tones (10 to 1000 Hz and 1000 to 10,000 Hz) to analyze the reflection pattern. The source was fixed at the middle of the tank, and the hydrophone was placed at variable distances above and underneath the source. The direct field was dominant at low frequency (100 to 1,000 Hz) for the underneath hydrophone. However, reverberation was still negligible even at high frequency (1,000 to 10,000 Hz) for the abeam hydrophone. The authors suggest locating the hydrophone close to the propeller to avoid pronounced standing waves. Cochard *et al.* [38]

developed an experimental procedure for acoustic measurement in a test tank using aerial acoustic and electromagnetism theory. The spectral pressure was measured in some randomly distributed positions in the reverberated field. Their technique measures the calibrated source with a high precision of ±1.5 dB. Trinh *et al.* [39] developed a method to accurately measure the source level in a water tank based on acoustic energy balance and critical radius. The source levels were measured in the reverberate field and compared with the known level. The method has a high level of accuracy, and the error between the calculated and known source output is 0.5 to 1.5dB only, which shows excellent agreement between the reverberant-field based calculation and the known source. Lafeber *et al.* [40] investigated the acoustic characterization of the DPWB for frequencies below 1.5 kHz and analyzed the effect of wall reflection and free surface on the measured noise. Two different techniques: impulse response and direct response, were used to measure the reverberation radius. They suggest ignoring the influence of wall reflections up to a distance of 2 m (within reverberation radius) from the source. Moreover, they proposed to neglect free surface reflection if the source is directly above the hydrophone. However, with the increasing horizontal distance, the influence of the image source increases, and correction for this effect should be applied for low-frequency measurements. Eastland and Buck [41] characterize the reverberation time inside an anechoic chamber using the interrupted noise and impulse response method. The model and methods are 95% accurate if the reverberant field is homogeneous and isotropic. Tani *et al.* [42] developed a technique to measure the transfer functions of the cavitation tunnel facility to account for the effect of tank characteristics on the noise tests and apply necessary correction to measured noise spectra.

Similarly, Boucheron *et al.* [32] used modal propagation theory to characterize the test section of a cavitation tunnel. Schroeder equation was derived for the test section, and experiments have been carried out in the tunnel to validate equation and critical frequency. In addition, statistical features of the acoustic field were analyzed experimentally by several data sets of the transfer function. Duncan *et al.* [43] numerically studied the pressure and particle velocity of a small tank at different frequencies using the finite difference method. The pressure and particle velocity vary smoothly in space below the lowest resonant frequency, although the velocity to pressure ratio differs from the free-field condition. However, above the lowest resonant frequency, the particle velocity and pressure fields vary rapidly both spatially and with changes in frequency. Way et al. [31] developed an analytic image model to predict the acoustic response of towing tanks. The image source model predicted the best hydrophone position for pressure measurements without the influence of lateral wave field and reverberation. The effect of the tank on acoustic measurement can also be predicted and determine acoustic energy loss around the source.

It is evident from the literature that experimental noise measurement in a laboratory-scale atmospheric tank is very challenging due to modal propagation, sound reflections from the sidewalls and the free surface of the water. The homogenous reverberation and diffuse acoustic fields are very complex phenomena and challenging to achieve in actual practice. The source itself introduces some errors in the near field, and the hydrophone position influences the accurate noise measurement. Therefore, it is essential to understand these effects before performing any experiments.

This paper intends to understand the acoustic properties (absorption coefficient and reverberation time) and modal frequencies inside the towing tank. The reverberation

measurement was made near and far from the source to analyze both the direct field and diffuse field in a closed space. The modal frequencies and reverberation characteristics of the tank have been studied using modal acoustic theory and the ray-tracing method. Experiment testing was performed in a small deep tank (3.65m × 3.65m × 3.65m) to estimate the sound absorption coefficient. A sound projector is driven with white noise in the frequency band (500 Hz-16 kHz), and the response was recorded by a hydrophone in different positions inside the tank. The recorded signal was filtered in 1/3 octave frequencies and post-processed using an integrated impulse response procedure to estimate the reverberation time and absorption properties. The acoustic properties are then plugged into the ray-tracing model to study the deep tank numerically. The reverberation time predicted from the ray-tracing model is compared with experimental results at different 1/3 octave frequencies to validate the model. Upon validation, the ray-tracing model is used to characterize a large tank (200m × 12m × 7m) having similar boundary conditions. Later, a complete procedure is developed to account for the free surface effect on the measured sound using Lloyd image theory.

## 2.3 Acoustic Characterization of the Towing Tank

Propeller-induced non-cavitating noise measurements were performed in the NRC-OCRE towing tank located in St. John's, NL, Canada. The tank is 200 m long, 12 m wide, and 7 m in depth. The sidewalls of the tank are made of concrete and painted with a thickness of 6mm. The sidewalls and the bottom of the tank are flat while the water surface is open to the atmosphere.

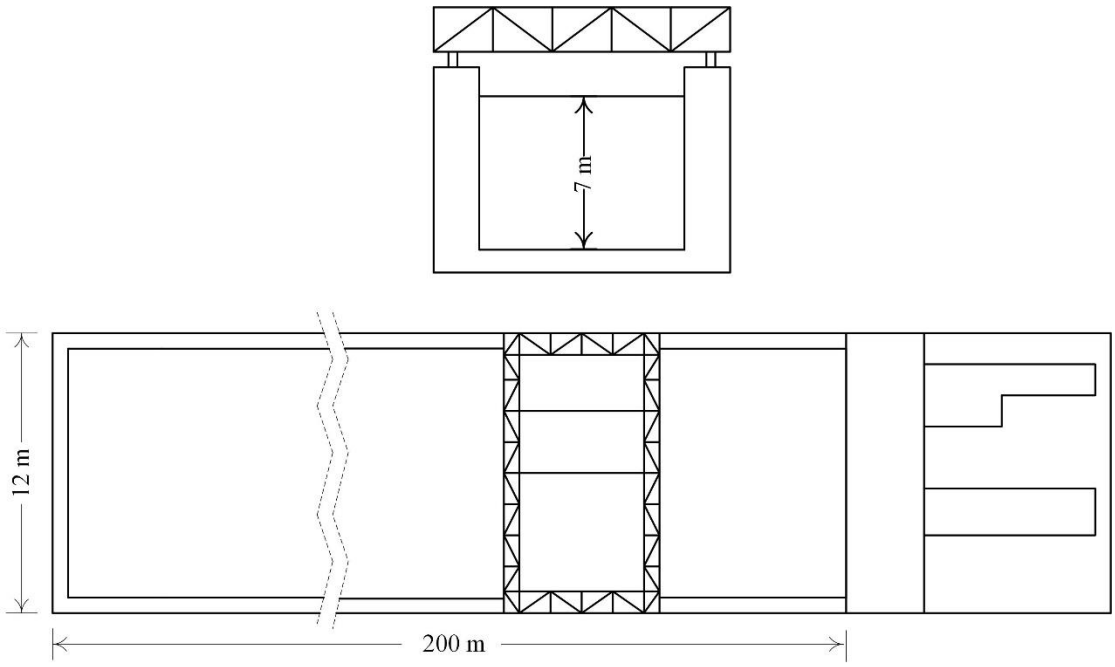


**Fig. 2.1:** Complete layout of the NRC towing tank

For propeller-induced noise measurement, the ideal condition should be a semi-infinite space under the water surface so that sound radiated from the propeller can freely propagate without disturbing reflections from walls and the bottom. However, the towing tank is a confined space enclosed by five solid walls and a free water surface with a water-air interface. Acoustically the behaviour of a towing tank lies between a tunnel and a room (a long rectangle). This rectangular shape allows generating axial, tangential, and oblique modes inside the tank due to the reflecting sound wave. The free

field conditions can be achieved only in the axial dimension of the tank. Due to the high impedance of the tank walls (water-concrete-air) and the free surface open to the atmosphere (water-air), this tank could be considered as a highly reverberant acoustic space with water as the acoustic medium. The acoustic energy is either transmitted through the tank wall or converted into heat energy by the volumetric absorption of the water. The impedance difference at the fluid-solid interface usually reflected the acoustic waves, although some waves could be transmitted into the wall. The free surface of the basin acts as a mirror for a sound source, and the reflected wave undergoes total internal reflection with phase change and causes interference and is known as Lloyd mirror effect [44].

### 2.3.1 Modal Frequencies of the Tank

Due to the geometrical shape, the tank could be considered an acoustic channel with a free surface opened at its extremes and rectangular cross-section. The acoustic propagation is similar to propagation in a room except for the free surface. Before experimenting, it is necessary to analyze the dynamic characteristics of the test tank. Modal analysis is the simplest way to determine the natural frequencies of the towing tank, which gives a valuable idea about the constructive and destructive interferences of sound. Modes measure resonances in the tank when the tank is excited by an acoustic source, i.e., propeller in this case. The resonances profoundly affect the low and mid-frequency response of sound and create difficulties for accurate measurement [45]. Modal frequencies are directly related to the tank dimension since they are generated by reflecting sound from various wall surfaces. Novak et al. [46] considered the room acoustics theory to study the acoustic response of a small fishing tank. Rayleigh wave Eq. (2.1) could characterize the resonance behaviour of the tank at low frequencies.

$$\frac{\delta^2 p}{\delta x^2} + \frac{\delta^2 p}{\delta y^2} + \frac{\delta^2 p}{\delta z^2} + k^2 p = 0 \quad (2.1)$$

$$k = \frac{\omega}{c}$$

Where $p$ stands for pressure, $k$ for wave constant, $c$ for sound speed at the water (1481m/s), and $\omega$ for angular frequency.

Using separation of variables, the general solution of Eq. (2.1) can be written as:

$$p(x, y, z) = p_1(x)p_2(y)p_3(z) \quad (2.2)$$

Putting the general solution in Eq. (2.1) splits it into three ordinary differential equations and $p_1$must satisfy:

$$\frac{\delta^2 p_1}{\delta x^2} + k_x^2 p = 0 \quad (2.3)$$

for the boundary conditions, $\frac{\delta p_1}{\delta x} = 0$ when $x = 0$ and $x = L$

Similar equations hold for $p_2(y)$ and $p_3(z)$ and the newly introduced constants $k_x$, $k_y$ and $k_z$ are related to-

$$k^2 = k_x^2 + k_y^2 + k_z^2 \quad (2.4)$$

The solution of Eq. (2.3) for the given boundary conditions leads to

$$p_1(x) = A_1 cos(k_x x) + B_1 sin(k_x x)$$

$k_x = \frac{u\pi}{L}$ for $u = 0, 1, 2, \dots, n$

Where $A_1$and $B_1$are the constants and n represent a integer number. Similarly,

$$k_y = \frac{v\pi}{W}$$

$$k_z = \frac{w\pi}{H}$$

Putting these values in Eq. (2.4) yields the eigenvalues of the Helmholtz wave equation as follow:

$$k = \pi \left[ \left(\frac{u}{L}\right)^2 + \left(\frac{v}{W}\right)^2 + \left(\frac{w}{H}\right)^2 \right]^{\frac{1}{2}} \quad (2.5)$$

The eigenfrequencies of Eq. (2.5) can be calculated from $k = \frac{\omega}{c}$ for each resonance mode.

$$f = \left(\frac{c}{2}\right)\sqrt{\left(\frac{u}{L}\right)^2 + \left(\frac{v}{W}\right)^2 + \left(\frac{w}{H}\right)^2} \tag{2.6}$$

Where f is the modal frequency, L, W, H represents the length, width, and depth of the tank, respectively and u, v, and w represent the wave number for three axial modes. The three-dimensional standing wave except the time dependence sound pressure can be described by Eq. (2.7).

$$p(x, y, z) = Ccos\left(\frac{\pi u}{L}x\right)cos\left(\frac{\pi v}{W}y\right)cos\left(\frac{\pi w}{H}z\right) \tag{2.7}$$

Where C is a constant and depends on the boundary conditions.

### 2.3.2 Modal Density and Frequency Spacing

The tank will drive into resonance at frequencies where many wavelengths fit between the tank walls. The frequency response then contains a sharp peak at this modal frequency. But if there are many modes in the measured frequency band, such effects can be averaged out to give the desired uniformity. The mode density for a rectangular tank can be easily calculated using the k-space discussed in **Section 2.3.1.** $k_x, k_y$ and $k_z$ represents three orthogonal planes in k-space. The intersection of the planes corresponds to a specific eigenvalue. Since Eq. (2.5) is insensitive to the sign of subscripts, let consider a rectangular point lattice only in the first octant, as shown in **Figure 2.2.**

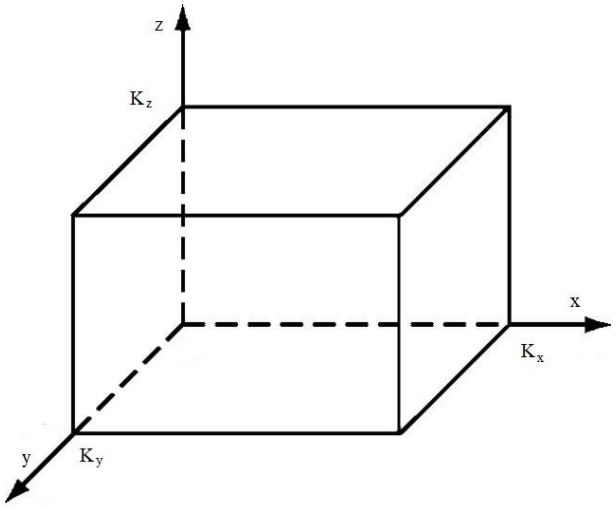


**Fig. 2.2:** Eigenvalue lattice in the k-space for a rectangular room

Eq. (2.4) represents a sphere, and the total volume for radius k is given by, $V = \frac{4}{3}\pi k^3$. The volume in the first octant is $v = \frac{V}{8} = \frac{1}{6}\pi k^3$. Since the distance between two successive lattice points in three coordinate directions are $\frac{\pi}{L}$, $\frac{\pi}{W}$, $\frac{\pi}{H}$ respectively, the k-volume for each lattice point is therefore $\frac{\pi^3}{LWH} = \frac{\pi^3}{V}$. The number of eigenfrequencies inside the first octant up to radius k for frequency limit 0 to $f = \frac{kc}{2\pi}$ is given by Eq. (2.8)

$$N = \frac{\frac{\pi k^3}{6}}{\frac{\pi^3}{V}} = \frac{Vk^3}{6\pi^2} = \frac{4\pi}{3} V \left(\frac{f}{c}\right)^3 \qquad (2.8)$$

The average density or number of eigenfrequencies per Hz at frequency $f$ and mean frequency separation between successive modes can be given by the following equations.

$$\frac{dN}{df} = \frac{4\pi}{3} V \frac{f^2}{c^3}$$

$$\Delta f_{mean} = \frac{c^3}{4\pi V f^2}$$

Modal density increases with the square of frequency, so many modes are expected at high frequencies compared to a few modes at low frequencies. Therefore, spatial variations are observed in sound pressure levels at low frequencies, but the fluctuations become small at high frequencies, and the field becomes more diffuse [47]. However, Eq. (2.8) is not accurate as the consideration is restricted to the first octant only. Since the points are in the coordinate plane and the axes represent total eigenvalues, correction is needed that yields Eq. (2.9) [48].

$$N = \frac{4\pi}{3} V \left(\frac{f}{c}\right)^3 + \frac{\pi}{4} S \left(\frac{f}{c}\right)^2 + \frac{E}{8} \frac{f}{c} \tag{2.9}$$

Where S is the total surface area of the tank, i.e., $S = 2(LW + LH + HW)$ and E is the sum of the edge length, i.e., $L_E = 4(L + W + H)$. The modified mode density in a narrow frequency band can be calculated as follow:

$$\frac{dN}{df} = \frac{4\pi}{3} V \frac{f^2}{c^3} + \frac{\pi}{2} S \frac{f}{c^2} + \frac{L_E}{8c}$$

### 2.3.3 Reverberation Time and Critical Radius

Reverberation time is one of the most significant acoustic properties of the tank since it defines how a tank responds to acoustic sound [49]. In the reverberate sound field, noise level depends on the acoustic power, tank size, and acoustic absorption properties of the boundaries. However, in a free field condition where the reflection is lower, the only significant sound is the direct sound. The reverberation phenomenon has little effect in the area near the source, where the direct sound dominates [50]. However, far from the source, and unless the boundary walls are highly absorbing, the noise level is significantly influenced by the reflected or indirect sound. The analytical formula to calculate reverberation can derive from classical acoustic theory. The rate of acoustic

energy ($W_t = EV$) stored in the reverberate field is the difference between the direct source energy supply ($W_d$) and acoustic energy dissipated in the wall ($W_a$) [38].

$$\frac{dW_t}{dt} = W_d - W_a$$

$$V\frac{dE}{dt} = W_d - \frac{cESa}{4}$$

Where $V$ is the volume of water in the tank, $S$ stands for surface area, and $a$ is the absorption coefficient of the wall. Substituting $\sum Sa = A$ and considering the initial condition of energy density $E = 0$ at time $t = 0$ yields,

$$E = \frac{4W_t}{cA}\left[1 - e^{-\left(\frac{cA}{4V}\right)/t}\right]$$

When $t \to \infty$, the sound field reached steady-state condition, $E_0 = \frac{4W_t}{cA}$. The energy reduction in the room follows exponential decay.

$$E = E_0 e^{-\left(\frac{cA}{4V}\right)/t}$$

The decay rate $D = 10log\left(e^{\frac{cA}{4V}}\right)$ in dB scale per second. The reverberation time, $T_{60}$ of a room is the time for the sound pressure levels to decrease by 60 dB. Reverberation time can be expressed as Eq. (2.10) and known as Sabine's reverberation formula [51].

$$T_{60} = \frac{60}{D} = \frac{60}{10log\left(e^{\frac{cA}{4V}}\right)} = \frac{6}{\log(e)} \times \frac{4V}{cA} = \frac{24In10}{c} \times \frac{V}{\sum Sa} \qquad (2.10)$$

Where V is the tank volume, S is the reflecting surfaces, c is the sound speed (1482.1 m/s), and $a$ is the absorption coefficient.

Any acoustic field with an omnidirectional source contains both the direct field and reverberated field. The acoustic energy in the direct field is identical to the source,

whereas, in the reverberate field, acoustic energy is significantly different due to the multiple reflections in the walls. The reverberation radius of the tank is the distance from a sound source at which the level of direct sound equals the reflected sound level and is known as the critical radius. The acoustic energy density in the direct field at a distance $r$ from the source is $E_d = \frac{P_s}{4\pi c r^2}$ and the reverberate energy density is $E_r = \frac{P_s T_{60}}{V \times log_e 10^6}$. At critical radius, both the quantity are the same [45].

$$E_d = E_r$$

$$\frac{P_s}{4\pi c r_c^2} = \frac{P_s T_{60}}{V \times log_e 10^6}$$

$$r_c = \sqrt{\frac{55.26 \times V}{c \times 16\pi \times T_{60}}} \quad (2.11)$$

Where, $P_s$ is the power emitted by the source. If the hydrophone is installed inside the critical radius ($r < r_c$), there will be no effect of the reverberation field. However, inside the critical radius, proper positioning of the hydrophone is crucial since sound propagates with varying amplitude.

### 2.3.4 Separation of Acoustic Field

At low frequencies, the density of Eigen frequencies is so low that the resonances are well separated. However, at higher frequencies, the resonances closely overlap, and the statistical method needs for the acoustic estimation. The transition between the normal-mode and statistical models is marked by the Schroeder frequency [32] and easily derived from modal theory. By modal theory, the high-frequency region will have a high degree of modal overlap where half-power bandwidths of the modes are large compared to the average spacing of modes. Half-power bandwith B depends only on the reverberation time.

$$B_{3dB} = \frac{log_e 10^6}{2\pi T_{60}} = \frac{6\ln(10)}{2\pi T_{60}}$$

Schroeder [52] suggested a 3-fold mode overlap as a low limit for the high-frequency region, i.e., the isotropic and homogeneous reverberated should have at least three modes in the half-power bandwidth of one mode.

$$3\Delta f_{mean} \leq \frac{6\ln(10)}{2\pi T_{60}}$$

$$3\frac{c^3}{4\pi V f^2} \leq \frac{6\ln(10)}{2\pi T_{60}}$$

$$f_c = \sqrt{\frac{C^3}{4\ln(10)} \times \frac{T_{60}}{V}} \quad (2.12)$$

Below critical frequency, the acoustics of different locations in the tank is dominated by discrete resonances. The acoustically most problematic frequency range is below the critical range because of the spatially and frequency-wise irregular distribution of room resonances. In addition, modes are manifest as standing waves having localized regions of high and low pressure [53]. As a result, the sound pressure amplitude varies when the source frequency or the hydrophone positioned has changed. The irregular pressure variation results from numerous eigenmodes according to their phase relations [54]. Above critical frequency, these resonances become so tightly packed in frequency and space that the room behaves relatively uniform.

## 2.4 Methodology

This study considers both the ray-tracing model (RTM) and experimental testing to study the sound propagation and reverberation characteristics of the tank. The experimental results were conducted to find the acoustic absorption properties of the towing tank, which is then fed into the numerical model. The towing tank acoustical

characterization was done by applying the similar boundary properties and background noise levels between the towing tank and deep tank.

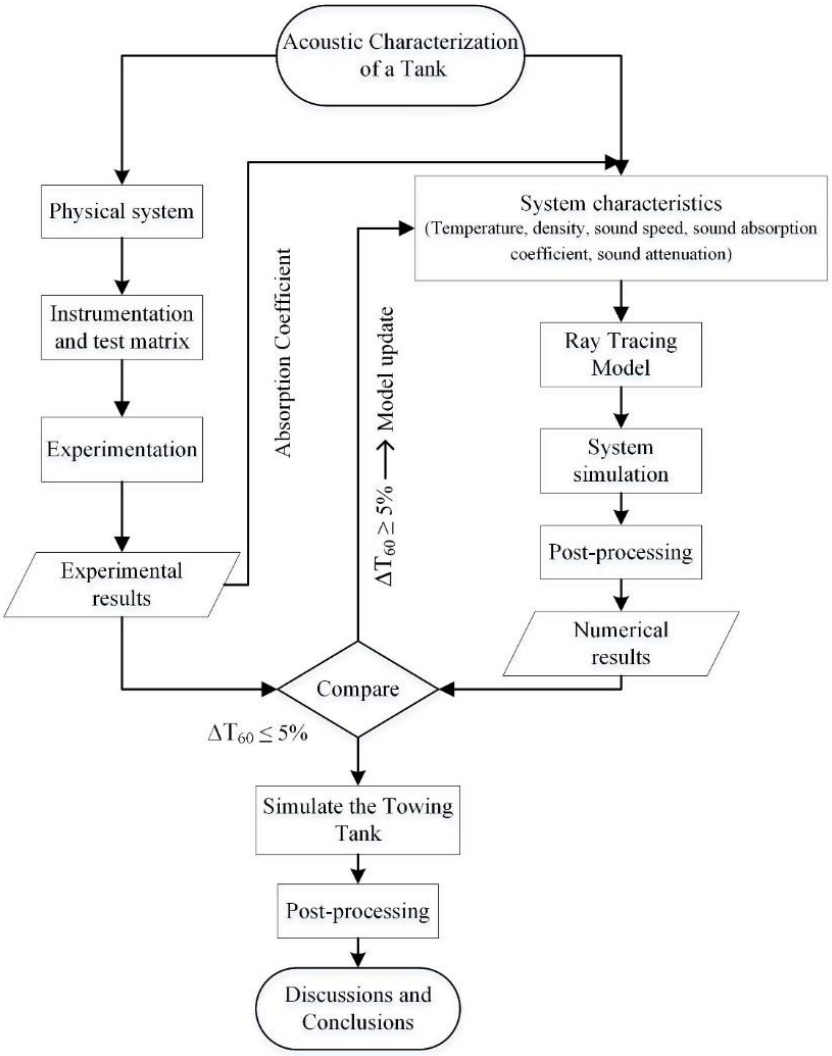


**Fig. 2.3:** Flowchart for the research outlined in this chapter

Experiment testing was performed in the small tank to find its acoustical characteristics and then validated with the numerical results. Based on the validation results, the absorptions coefficients are used to study the towing tank using RTM. The detailed methodology is demonstrated in **Figure 2.3**. The numerical results are then checked and compared to the experimental results to validate the RTM for a large tank

.

### 2.4.1 Experimental Approach

The deep tank, located at Memorial University, Ocean research laboratory, was used to conduct the experiment following previous studies, e.g., Cochard et al. [38] and Lafeber et al. [40]. The dimension of the small tank was 3.65 m × 3.65 m × 3.65 m to facilitate the instrumentation and setup. Additionally, the boundary conditions of the small tank were the same as the towing tank, with smooth painted concrete walls. As shown in **Figure 2.4**, the test setup was simple and consisted of a sound source and a hydrophone.

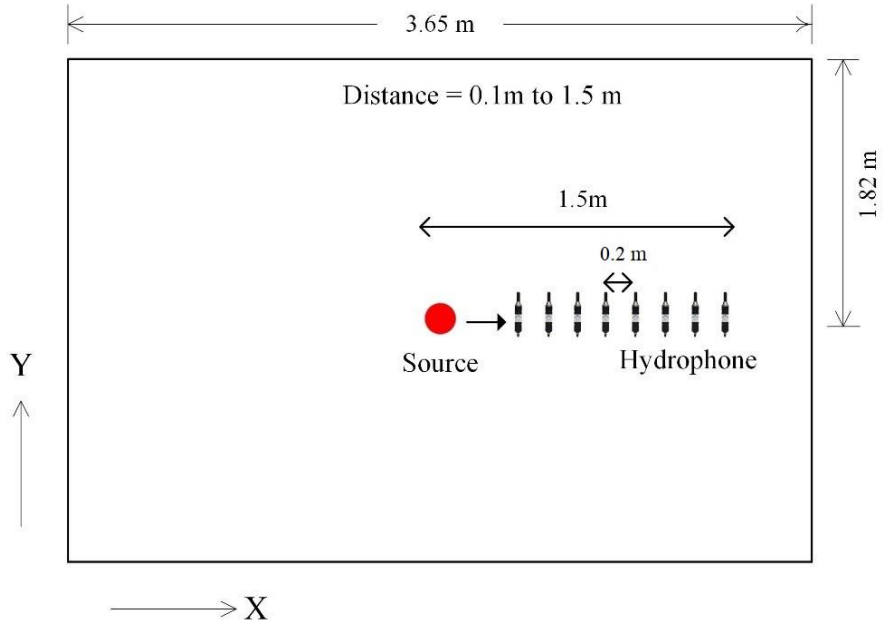


**Fig. 2.4:** Layout of the experimental setup in the deep tank

The sound projector (Benthowave **BII-7530, Canada)** was positioned at the volume centre of the deep tank. An icListen RB9 hydrophone (Ocean sonic, Canada) was placed 20 cm away from the projector at the same water depth. Then the source-receiver distance was changed from 20 to 130 cm while the projector was stationary. The input signal for the sound source was broadband excitation. The projector response was non-linear and frequency dependant at frequencies below 3000 Hz. **Figure 2.5** shows the

sound pressure level of the projector at 1/3 octave frequencies. The projector noise was measured by placing a hydrophone close to the source (20 cm).

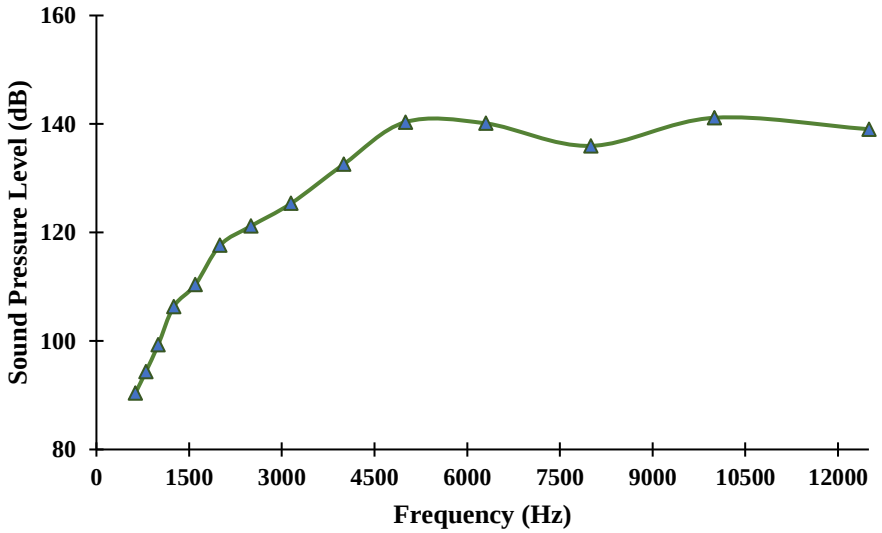


**Fig. 2.5**: Sound pressure level generated by the projector at different frequencies

The time ($T_{60}$) in which the sound pressure levels decreased by 60 dB was estimated experimentally for the deep tank. Impulse response and direct methods are the two ways to determine the $T_{60}$ using a projector and hydrophone [40], [31]. The methods were developed for room acoustics, but it was extended to be also used for underwater acoustics. The impulse response was selected to estimate the decay time because it shows precise information about the distribution and density of the reflected sound in a condition of high signal-to-noise (SNR) ratio [36], [38].

The $T_{60}$ estimation procedures are illustrated in sequential order as follows:

Firstly, the projector generated a white noise signal as an impulse signal based on Kooij and Bruijn [36] requirements. The hydrophone recorded the response with a sampling rate of 32 kHz for every position (20 cm, 40 cm, 60 cm, 100 cm, 130 cm). **Figure 2.4** also shows the hydrophone configurations at each measurement. The deep tank experiences some low-frequency noise as a background noise generated inside the

facility. Therefore, a high-pass filter with a passband of 100 Hz was applied to the recorded signal to increase the SNR. Since the results are estimated in one-third octave bands, the signal was filtered using a one-third octave filter at centre frequencies from 630 Hz to 12500 Hz for different hydrophone positions in the deep tank. The impulse response function $H(\omega)$ of the deep tank in a location is computed from the spectrum measured from the receiver signal $R(\omega)$, due to a source signal $S(\omega)$ (Lafaber et el. [37]).

$$H(\omega) = \frac{S_i^*(\omega)R_i(\omega)}{S_i^*(\omega)S_i(\omega)} \tag{2.13}$$

where the star in Eq. (2.13) denotes the complex conjugate. The impulse response function $h(t)$ is computed by the inverse Fast-Fourier Transform (FFT) of $H(\omega)$ and taking the Hilbert transform. Schroeder's integrated impulse response at time $t$ is given by Eq. (2.14).

$$IIR(t) = 10log_{10}\left[\int_t^T |h(t)|^2 dt\right] - 10log_{10}\left[\int_0^T |h(t)|^2 dt\right] \tag{2.14}$$

The sound energy is calculated using Schroeder's integration formula to show the decay of the sound level by time. Finally, the slope of decay was calculated to estimate the $T_{60}$. Based on room acoustics theory, the absorption coefficient by the boundaries can be estimated using Sabine's equation in the presents of the $T_{60}$ in seconds as given in Eq. (2.10).

### 2.4.2 Numerical Approach

#### 2.4.2.1 Theory of Ray Acoustic

A ray-tracing method from the commercial software package COMSOL 5.6a was used to model and simulate the acoustic characteristics in a closed tank. In ray tracing, rays are emitted from a source, reflected, and registered valid paths [55], [56]. The rays hit the wall, bounce back and continue in a new direction, and each of the rays is traced. The rays are energy carriers, travelling around the space at the speed of sound and losing energy after each reflection according to surface absorption properties. The RTM depends on source position, surface absorption, and degree of scattering.

An acoustic wave in a stationary fluid can express as a plane wave in the following form:

$$\phi = ae^{i\psi} \tag{2.15}$$

Where $\phi$ is the velocity potential, $\psi$ is the phase, and $a$ is the amplitude of the velocity potential. When the distance from any source is larger than the wavelength of an acoustic wave, the wave is considered as a plane wave for time $t$ and speed of sound $c$.

$$\psi = \vec{k}.\vec{q} - \vec{k}ct$$

The angular frequency of the wave is defined by $\omega$ for homogenous fluid velocity $u$.

$$\omega = c\left|\vec{k}\right| + \vec{u}.\vec{k}$$

In COMSOL, the ray-tracing method numerically solves a couple of first-order ordinary differential equations for instantaneous ray position q and wave vector k.

$$\begin{cases} \frac{dq}{dt} = \frac{\partial \omega}{\partial k} \\ \frac{dk}{dt} = -\frac{\partial \omega}{\partial q} \end{cases} \tag{2.16}$$

The equations above are known as Hamiltonian equations, and frequency-dependent boundary conditions can be used to solve them. The initial direction of the rays can be spherical, hemispherical, conical, or Lambertian. $N_{rays}$ number of rays are released from the point sources with an intensity $I_0$. The sampling distribution can be random or deterministic. The ray direction is a function of $\theta \in [0, \pi]$ and released from a user-defined grid point as follow:

$$f(\theta) = \frac{1}{4\pi} sin\theta$$

In RTM, each ray is treated as a propagating wavefront subtending a small solid angle, and this algorithm is only valid for a homogeneous medium. The value of ray intensity is stored in an auxiliary variable $I_0$ at the time of releasing the ray. The two principal radii of curvature, $r_1$ (maximum) and $r_2$ (minimum) is defined for the propagating wavefront at the intersection of the arbitrary plane. When the rays are reflected or refracted at boundaries, the principal radius change at a constant rate as follow:

$$\frac{dr_1}{ds} = -1$$

$$\frac{dr_2}{ds} = -1$$

The negative radii indicate an expanding wavefront as the ray propagates. The values of the curvature are stored as $r_{1,i}$ and $r_{2,i}$ whenever the ray reaches a boundary. The intensity at any point in the ray trajectory is equal to:

$$I = \frac{r_{1,0} r_{2,0}}{r_1 r_2} I_0 \tag{2.17}$$

The rays are terminated at the exact time when their intensity or power reaches the specified threshold, $I_{th}$.

$$I < I_{th}$$

The acoustic simulations in fluid media (air or water) usually do not consider any internal damping over the number of wavelengths. However, it is essential for underwater acoustics and noise propagation. The attenuation of sound in a fluid depends on both the frequency and physics of damping. The attenuation in the linear elastic model could be specified with an attenuation coefficient, $\alpha_m$ (dB/m). The complex sound speed $c_c$ is defined through complex-valued angular frequency $\omega$. Using Eq. (2.18), the user-defined attenuation coefficient dB/m (decibel per meter) adds damping losses in the linear elastic model.

$$c_c = \frac{c}{1 - i\frac{c}{\omega}\alpha'}$$

$$\alpha_m = \frac{\alpha'}{20log_{10}(e)}$$

The rays can gradually lose energy in absorbing media. If the medium has an attenuation coefficient $\alpha_m$, the intensity of the plane wave will decrease exponentially.

$$\frac{dI_0}{ds} = -2\alpha_m I_0 \qquad (2.18)$$

Sound absorption in water is crucial for long-distance propagation, specifically at a higher frequency regime (>1000 Hz). The frequency dependant sound attenuation (dB/m) in freshwater is shown in **Figure 2.6**. The sound attenuation is taken from a published article by Hovem [57]. The absorption increases with frequencies and exhibits a linear response with an increase in frequency.

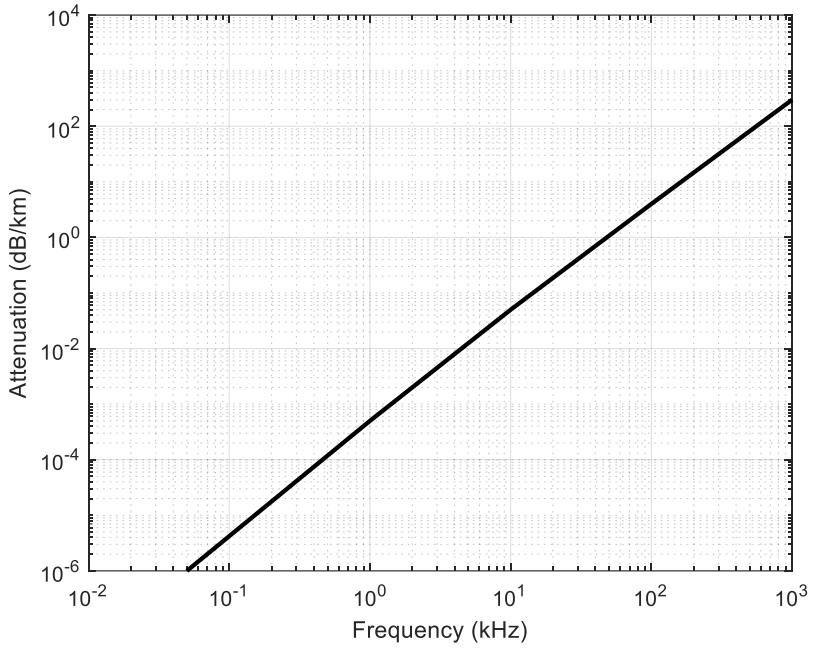


**Fig. 2.6:** Acoustic absorption (dB/km) for freshwater as a function of frequency (kHz) at 10°C and atmospheric pressure (Adapted from [57])

#### 2.4.2.2 Numerical Analysis and Model

In ray tracing, the emitted sound power from an omnidirectional source is defined by a finite number of rays. Each of the rays is considered as the energy or intensity carrier. These rays travel through the medium at a sound speed and bounce back after every impact with the room boundaries. The ray energy is absorbed in the medium and walls during the propagation, decreasing their power. The reflected rays cross the receivers where an energy calculation process is performed, and those data are stored. The solver tracks the incident rays, and when no active rays remain or the intensity of the rays is below a specific criterion, the solver stops. Finally, the impulse response at every receiver is obtained, and all desirable acoustic parameters are estimated. The acoustic simulation with ray tracing is a fast and efficient method because modelling ray propagation within domains and interaction with flat surfaces does not need very fine

mesh. For a flat surface, the shape of the surface mesh is the same as the geometric entities. Therefore, rays interact with the mesh instead of the geometry without any discretization error.

Consequently, it is feasible to compute ray trajectories precisely even with extremely coarse mesh. However, for complex geometry with curvature, fine mesh is recommended. However, a good practical approach is to use the mesh convergence technique to check the robustness of a solution. The geometry was built in COMSOL with proper full-scale dimensions to adjust and identify the domain needed for the acoustic modelling. The geometry with the receiver surface is meshed and presented in **Figure 2.7**. The general properties of the ray-tracing model are shown in **Table 2.1**.

**Table**: General properties of the ray-tracing model

| **Properties** | **Quantity** |
|---|---|
| Mesh vertices | 18347 |
| Triangles | 36640 |
| Edge elements | 700 |
| Vertex elements | 12 |
| **Domain element statistics** | |
| Number of elements | 36640 |
| Average element quality | 0.9743 |
| Element area ratio | 0.3535 |
| Mesh face area | 83.61 $m^2$ |

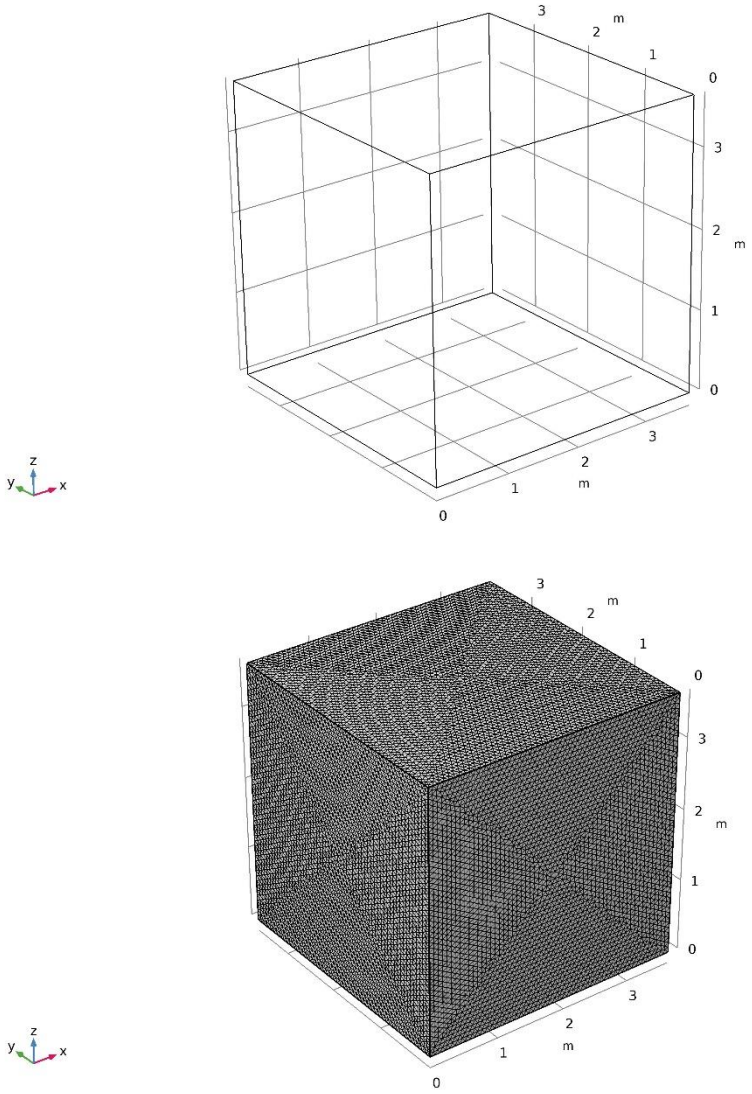


**Fig. 2.7**: Geometry of the deep tank (top) and meshed acoustic domain (bottom)

The number of emitted rays is very crucial in ray-tracing modelling. The limited number of rays to describe the sound field may introduce uncertainties in the results. Since all the rays are emitted from a point source, the representation is less accurate with increasing ray length. To achieve convergence criteria, a large number of rays are needed. A large number of rays decreases the solid angle that an individual ray will cover. However, it will affect the computation time, but limited rays can cause an insufficient number of detected reflections. The number of required rays depends on the

geometry and absorption coefficient, and it is difficult to know the exact number of rays needed before performing a simulation. Ondet and Barbry [58] studied the effect of the number of rays on solution accuracy and recommended an optimum number of the rays based on the following Eq. (2.19).

$$N_{rays} = \frac{10 \times V_{space}}{V_R} \tag{2.19}$$

Where $N$ is the number of rays, $V_{space}$ is the space volume, and $V_R$ is the volume of the receiver. The model needs secondary rays when an existing ray is subjected to certain boundary conditions. If the number of secondary rays is insufficient, a reflected ray may not be released when any existing ray is refracted.

#### 2.4.2.3 Noise Source and Receiver

Many acoustic rays are emitted from the sound source uniformly in all directions, either by a pre-defined distribution or in random directions like the Monte Carlo method. In this study, a spherical radiation pattern is used because of its excellent omnidirectional properties. The source is modelled as a point that emits many rays with uniform energy in all directions. A frequency dependant sound level is applied to model the point source, as shown in **Figure 2.5**. The source generates a sound power based on the following Eq. (2.20).

$$L_p = 20\ log_{10}\left(\frac{P_{rms}}{P_{ref}}\right)$$

$$P_{rms} = P_{ref} \times 10^{\left(\frac{L_p}{20}\right)}$$

$$I_0 = \frac{P_{rms}^2}{\rho c}$$

$$P_0 = I_0 \times 4\pi r^2 \tag{2.20}$$

Where $L_p$ represents sound pressure level (dB), $I_0$ is the initial intensity, $P_0$ is the emitted sound power, and $r$ is the distance from the source. The source was placed in the middle of the tank as in the experimental setup.

The impulse response (IR) of the tank is estimated by collecting the ray information using a receiver. Usually, the receiver is placed far from the source in the reverberate field. The probability of a ray being detected is a function of the size of the receiver. Therefore, plane or point receivers are inadequate to detect an infinitesimally thin ray. However, a spherical omnidirectional receiver can capture all directions of incidence. The size of the receiver affects the accuracy of ray tracing. A large receiver can cause additional errors as they can detect rays far from the point of interest. In COMSOL, the following Eq. (2.21) built-in expression determines the size of the receiver.

$$R = log_{10}(V_{space})d_{SR}\sqrt{\frac{4}{N_{rays}}} \tag{2.21}$$

Where $N_{rays}$ is the number of rays, $d_{SR}$ is the distance between the source and receiver, and $V_{space}$ represents the volume of the tank. The accurate results can be obtained by considering the length of the path a ray travels inside the receiver.

#### 2.4.2.4 Boundary Conditions

The lateral walls and bottom surface of the tank are made of concrete. These boundaries could be defined as absorption boundaries with a proper attenuation coefficient. Although the free surface is open to atmospheric air and acts as a soft boundary ($p_t = 0$), it is assumed here as an absorbing boundary similar to walls since the experimental study gave us an overall absorption coefficient. A similar assumption was previously used by Lafaber et al. [40]. Acoustically, the concrete wall of the tank responds between a sound-hard and sound-soft boundary. In ray modelling, this boundary is defined by a

reflection coefficient model with known absorption coefficients, which determines what happens to the rays when in contact with a boundary. The wall condition is considered a specular surface. In COMSOL, the wall boundary conditions can be defined explicitly or by absorption coefficient $\alpha$ or characteristics impedance of absorber $Z_1$. The principal square root is used when using $\alpha$ for the purpose of phase reinitialization.

$$R = \sqrt{1-\alpha} \tag{2.22}$$

When the characteristic impedance of the absorber $Z_1$ is used, the reflection coefficient $R$ can be defined using the following equation, where $Z_0$ is the characteristics impedance of the medium.

$$R = \frac{Z_1 cos\theta - Z_0}{Z_1 cos\theta + Z_0}$$

$$Z_0 = \rho c_c$$

The intensity and power of the reflected way from the flat boundary wall are calculated from the following equations:

$$I_r = I_i |R|^2$$

$$P_r = P_i |R|^2$$

However, if the surface is rough, the reflected intensity is multiplied by an additional factor to account for the surface roughness based on the Rayleigh roughness model.

$$I_r = I_i |R exp(0.5\Gamma^2)|^2$$

$$\Gamma = 2k\sigma cos\theta_i$$

Where $k$ is the wave vector and $\sigma$ represents RMS roughness of the surface. The average absorption coefficient $\alpha$ of all tank surfaces, including the free surface, is estimated from the experiment described in **Section 3.1**.

#### 2.4.2.5 Procedure and Implementation

The fluid domain properties were collected from the COMSOL library, where the temperature of the domain was 18$^{o}$C. A frequency-dependent point source was placed in the middle of the tank and at a constant water column depth. The main acoustic parameters, such as absorption boundary and damping, are correctly modelled using absorption coefficient and sound attenuation in water. A total of 20,000 rays were released from the source in a spherical pattern with the deterministic distribution. In addition, a maximum number of 500 secondary rays was used to avoid any discontinuity at the boundaries between different media. A time-dependent generalized-α solver was used to solve the ray tracing problems with tolerance factor 0.1. The number of degrees of freedom was 340,000. The solver solves the acoustic space for a 1/3 octave frequency sweep ranging from 630 Hz to 12.5 kHz. The output time step for the simulation was 1.8 seconds. A ray termination constraint was defined based on threshold intensity $I < I_{th}$ (6.75e$^{-21}$ W/m$^2$) to remove rays of sufficiently low intensity. All the reflections and intersections of the rays are computed to track the reflection paths they follow to reach the receiver from the sound source. The impulse response (IR) of the tank is post-processed by collecting the ray information at a receiver. The receiver was placed in the reverberate field (1.3m from source) at the same source plane. The total energy in all the rays is a function of time, and integrated response estimates the energy decay. The reverberation time could be accurately estimated from the decay. In classical statistical acoustics, the reverberation time $T_{60}$ is calculated using Sabine's formula as in Eq.

(2.10). However, for a large tank, Sabine's formula is corrected by adding absorption of the medium $\alpha_m$ as Eq. (2.23).

$$T_{60} = \frac{55.3\,V}{cA+4\,\alpha_m V} \tag{2.23}$$

Another commonly used method to calculate the reverberation time $T_{60}$ is Eyring-Norris formula as Eq. (2.24).

$$T_{60} = \frac{55.3\,V}{-cSln(1-\bar{\alpha})} \tag{2.24}$$

The formula described above to estimate reverberation time is valid only for the diffuse sound field. The sound pressure level $L_{p,i}$ is computed from wall intensity $I_w$. Based on the following equation. The sum is taken over all rays that hit the $i$th boundary element.

$$I_{w,i} = \frac{1}{A_i}\sum_j Q_j(|R|^2 + 2|R|\cos(\arg(R)) + 1)$$

The sound pressure level $L_{p,i}$ in the $i$th element for reference pressure $P_{ref}$ (1 µPa for the water) is estimated from Eq. (2.25).

$$L_{p,i} = 10log\left(\frac{\rho c I_{w,i}}{P_{ref}^2}\right) \tag{2.25}$$

## 2.5 Results and Discussions

### 2.5.1 Experimental Results

The input signal for the sound source was white noise in the frequency band (500 Hz to 16000 Hz). The acoustic response of the tank was measured with a hydrophone at different points. The procedure discussed in **Section 2.4.1** is followed to calculate the reverberation properties of the tank.

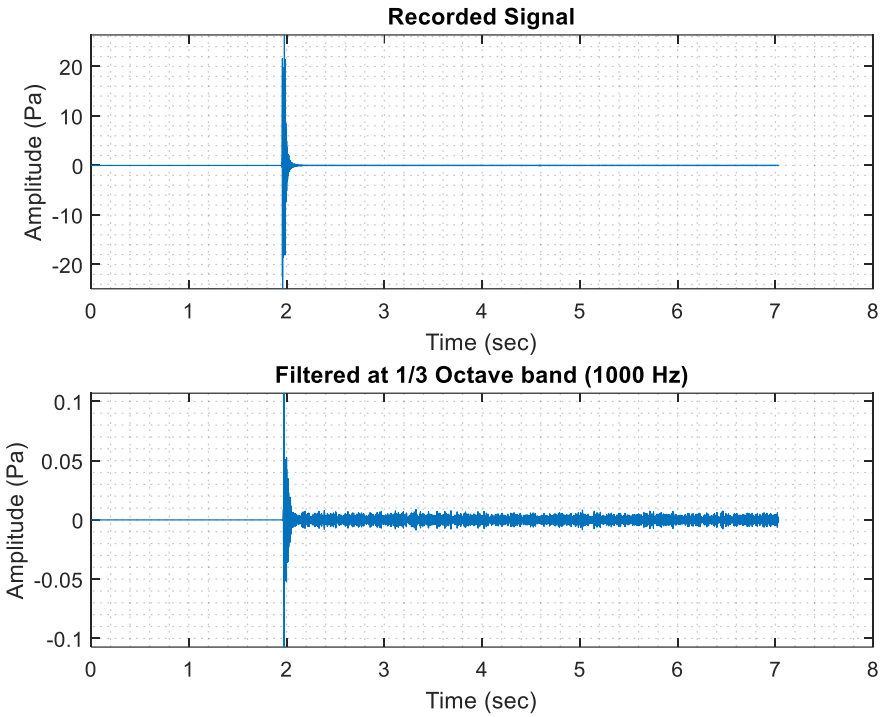


**Fig. 2.8:** Recorded white noise impulse (top) and the signal after filtered at 1/3 octave frequency (bottom)

The recorded signal was filtered using a high pass filter (> 200 Hz) to discard the low-frequency background noises and increase the SNR. The signal is then post-processed for at 1/3 octave frequencies starting from 630 Hz up to 12500 Hz. **Figure 2.8** shows the recorded signal and filtered (1/3 octave centred at 1kHz) signal in the time domain.

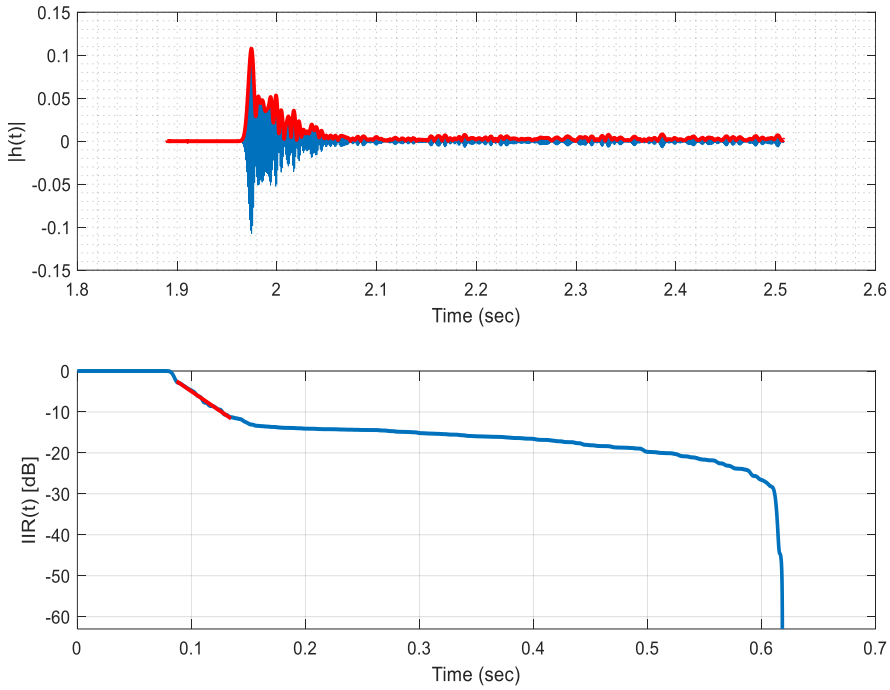


**Fig. 2.9**: The impulse response function $|h(t)|$ (top) and the Schroeder integrated impulse response function $IIR(t)$ (bottom)

The Hilbert transform was applied to the filtered signal to extract the impulse response function $|h(t)|$. The impulse response presents the direct and the reflected sound waves and how the sound energy is decayed by time after switching off the sound source. The direct signal and the free surface reflected signal are seen within a few milliseconds, followed by reflections from the walls. As the amount of reflections builds up, the sound field becomes more diffusive. The reverberation time is then determined from the slope of the integrated impulse response, as shown in **Figure 2.9**. The same procedure is repeated for other 1/3 octave frequencies and different hydrophone positions. The measured $T_{60}$ for different configurations is presented in **Table 2.2.** The absorption coefficient of the tank can be calculated from Eq. (2.15) for different values $T_{60}$. **Table**

**2.3** summarizes the absorption coefficient calculated for different conditions. The average absorption coefficient overall measurement is 0.10.

**Table 2.2:** Measured $T_{60}$ at different 1/3 octave frequencies and receiver position

| Frequency | Receiver distance from the source | | | |
|---|---|---|---|---|
| | 0.4 m | 0.6 m | 1 m | 1.3 m |
| 630 | 1.18 | 1.09 | 0.92 | 1.09 |
| 800 | 0.74 | 0.80 | 1.03 | 0.80 |
| 1000 | 0.26 | 0.32 | 0.27 | 0.32 |
| 1250 | 0.21 | 0.32 | 0.30 | 0.32 |
| 1600 | 0.16 | 0.20 | 0.17 | 0.20 |
| 2000 | 0.16 | 0.18 | 0.15 | 0.18 |
| 2500 | 0.24 | 0.27 | 0.25 | 0.27 |
| 3150 | 0.23 | 0.33 | 0.28 | 0.33 |
| 4000 | 0.19 | 0.21 | 0.22 | 0.21 |
| 5000 | 0.24 | 0.2 | 0.20 | 0.20 |
| 6300 | 0.13 | 0.13 | 0.15 | 0.13 |
| 8000 | 0.14 | 0.13 | 0.14 | 0.13 |
| 10000 | 0.20 | 0.25 | 0.20 | 0.25 |
| 12500 | 0.135 | 0.13 | 0.12 | 0.13 |
| Average | 0.31 | 0.33 | 0.32 | 0.33 |
| STD | 0.29 | 0.27 | 0.28 | 0.27 |

**Table 2.3:** Absorption coefficient of the deep tank at different 1/3 octave frequencies

| Frequency | Receiver distance from the source | | | | | Average |
|---|---|---|---|---|---|---|
| | 20 cm | 40 cm | 60 cm | 100 cm | 130 cm | |
| 630 | 0.03 | 0.01 | 0.02 | 0.02 | 0.03 | 0.02 |
| 800 | 0.06 | 0.03 | 0.02 | 0.02 | 0.03 | 0.02 |
| 1000 | 0.07 | 0.08 | 0.07 | 0.08 | 0.06 | 0.07 |
| 1250 | 0.09 | 0.10 | 0.07 | 0.07 | 0.10 | 0.08 |
| 1600 | 0.11 | 0.16 | 0.11 | 0.13 | 0.15 | 0.13 |
| 2000 | 0.14 | 0.14 | 0.12 | 0.14 | 0.13 | 0.13 |
| 2500 | 0.10 | 0.09 | 0.08 | 0.08 | 0.15 | 0.10 |
| 3150 | 0.07 | 0.09 | 0.06 | 0.08 | 0.11 | 0.09 |
| 4000 | 0.10 | 0.11 | 0.10 | 0.10 | 0.11 | 0.10 |
| 5000 | 0.11 | 0.09 | 0.11 | 0.10 | 0.13 | 0.11 |
| 6300 | 0.17 | 0.16 | 0.16 | 0.14 | 0.20 | 0.17 |
| 8000 | 0.15 | 0.15 | 0.16 | 0.15 | 0.16 | 0.16 |
| 10000 | 0.09 | 0.10 | 0.09 | 0.10 | 0.10 | 0.10 |
| 12500 | 0.17 | 0.168 | 0.17 | 0.18 | 0.20 | 0.18 |

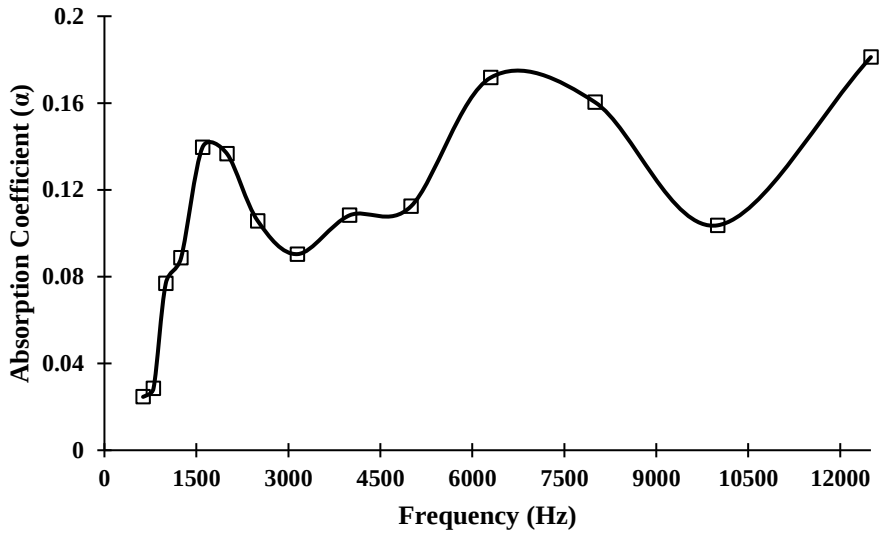


**Fig 2.10:** Absorption coefficient $\alpha$ measured in the deep tank

**Figure 2.10** shows the average absorption coefficient of the deep tank at different 1/3 octave frequencies. The absorption is low at frequencies below 1kHz. It starts increasing with the increasing frequency and is a maximum of 0.17 at 6.3 kHz. The absorption properties were plugged into the ray-tracing model to define the boundary.

Using the reverberation time $T_{60} = 0.32\ s$, the average reverberation radius of the towing tank is calculated from Eq. (2.11) as 0.32 m. The critical frequency of the tank is determined from Eq. (2.12) as $f_c = 1530\ Hz$. So the mode mixing condition will be fulfilled for any measurements above 1530 Hz.

### 2.5.2 Numerical Results

The ray-tracing method model the acoustics of a deep tank. The total listening volume was 48.93 $m^3$ with a total absorption surface area of 80.26 $m^2$. The wall and medium of the tank are fitted with reflecting surfaces. An omnidirectional source generates a pulse with an SPL previously shown in **Figure 2.5** at 1 m from the source. The receiver

(hydrophone) is positioned at 0.4 m, 0.6 m, 1 m, and 1.3 m, far from the source, respectively.

The sound pressure level (SPL) of the local wavefront after 10 ms at 1000 Hz is shown in **Figure 2.11**. **Figure 2.12** shows the wavefront propagation after 20 ms for 12.5 kHz frequency. The volume attenuation is highest at this frequency. The figures also visualize the wavefront curvature, intensity, and SPL along each ray.

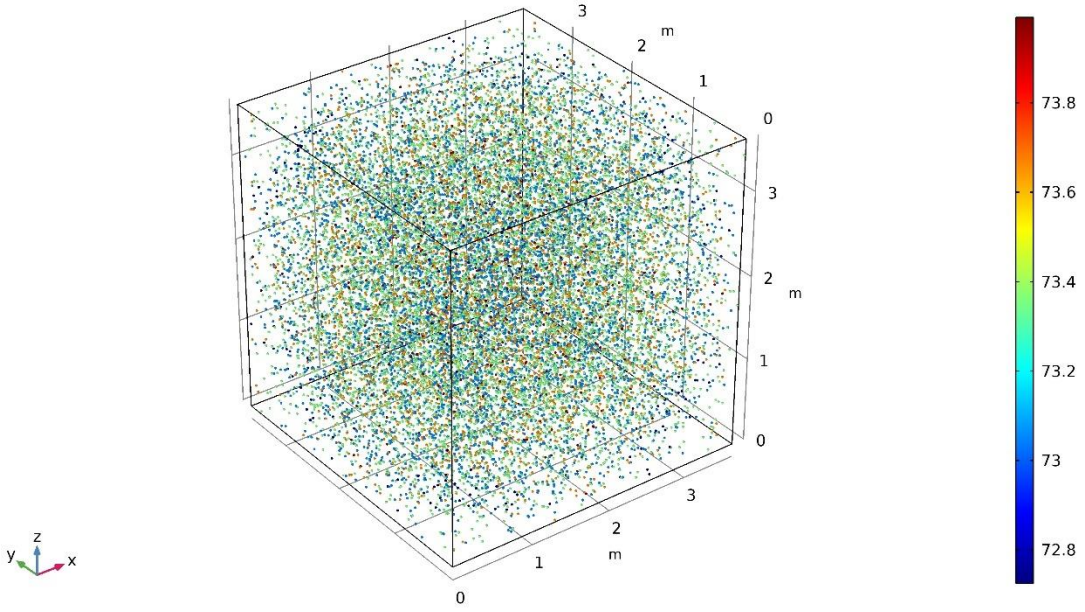


**Fig. 2.11:** Ray location and SPL of the ray after 10 ms at 1000 Hz

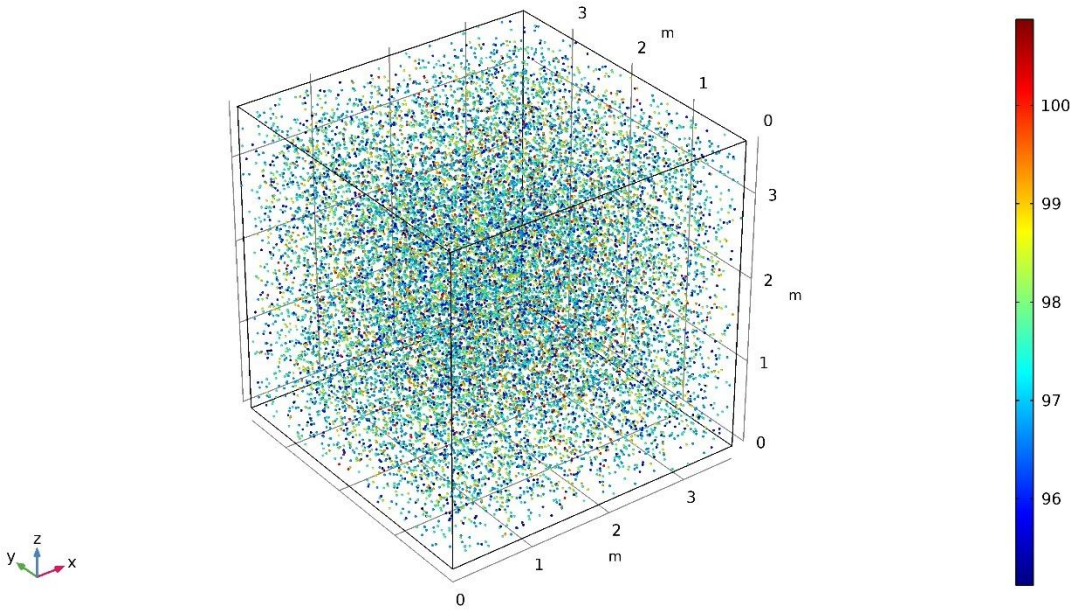


**Fig. 2.12:** Ray location and SPL of the ray after 20 ms at 12,500 Hz

The acoustic power transported by each ray is tracked while passing through the receiver. The direct sound arrives first and is expected to have maximum energy. Reflected sounds lose energy due to surface absorption and reach late with lower levels. The temporal impulse response (IR) for the source and receiver (1.3 m far from the source) is presented in **Figure 2.13**. The quality of the recorded IR increases with the number of rays $(N_{rays})$ and frequency resolution of model input (absorption coefficient). The impulse response (IR) shows an estimation of a sound field in space. The highest peak is the direct sound from the projector, followed by a very short propagation delay (a few milliseconds). The higher-order reflections (tail part) are identical and indicate the reverberant field. The sound wave loses energy with increasing reflections and eventually decays. The reverberant field is statistical, and decay is often linear. The IR contains information about arrival times and frequency content of direct sound and discrete reflections, reverberant characteristics, and signal-

to-noise ratio. **Figure 2.14** shows the corresponding frequency domain (FFT) of the recorded IR without smoothing and windowing.

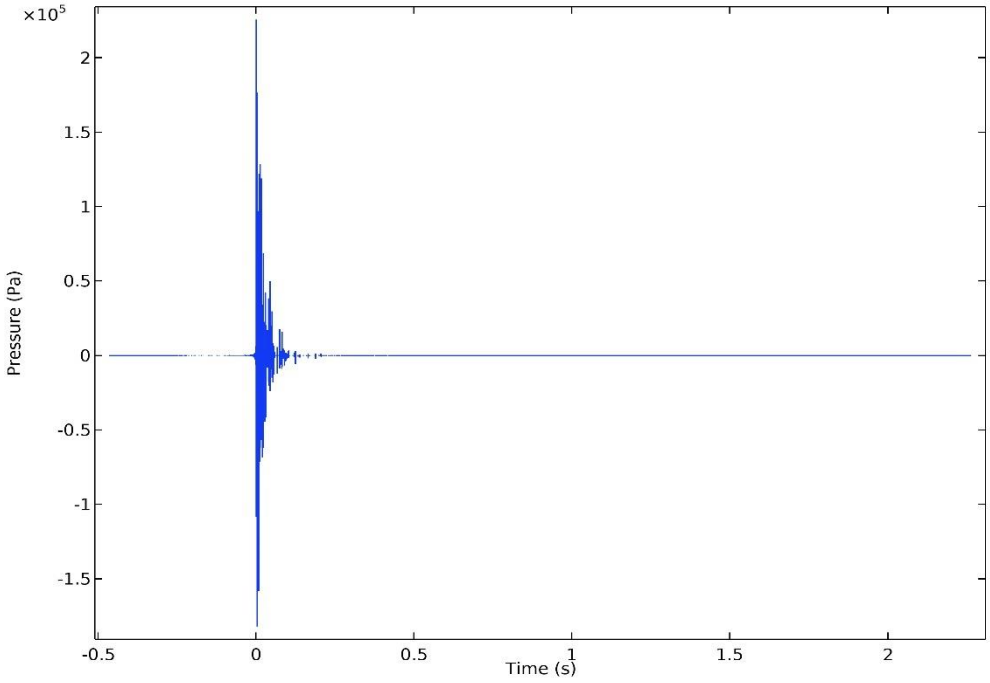


**Fig. 2.13:** Temporal impulse response computed at the 1.3 m from the source

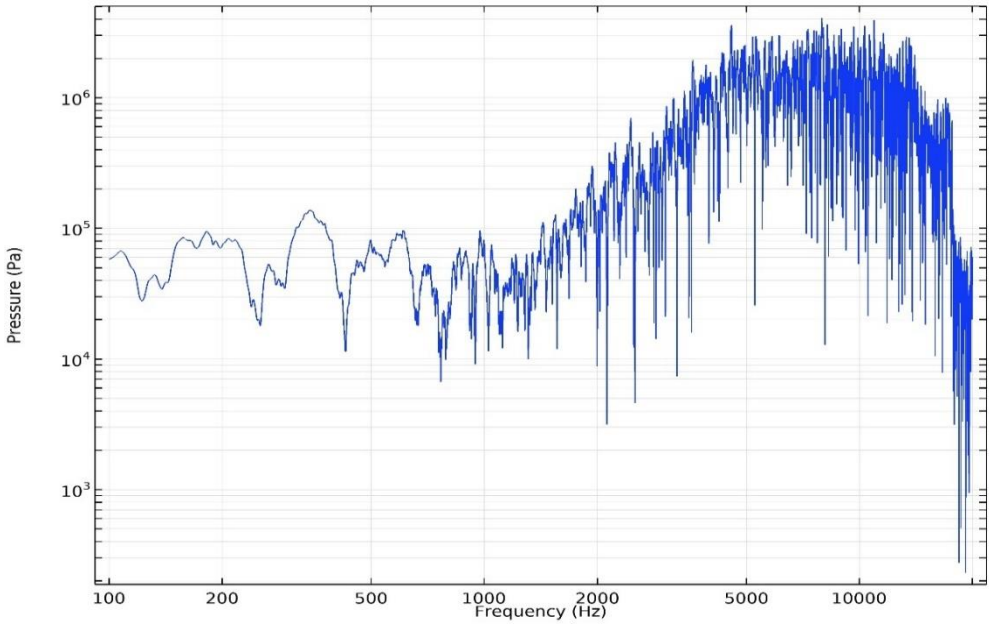


**Fig. 2.14:** FFT of the impulse response (no windowing/no overlapping)

The IR is post-processed to estimate the decay in the time domain. The sound power information in the receiver is put back into the time signal using the temporal filter kernels. Here, a Brick-wall filter with a Kaiser window is used with $\delta = 1e - 6$ Hz and sampling frequency 44,050 Hz for high resolution.

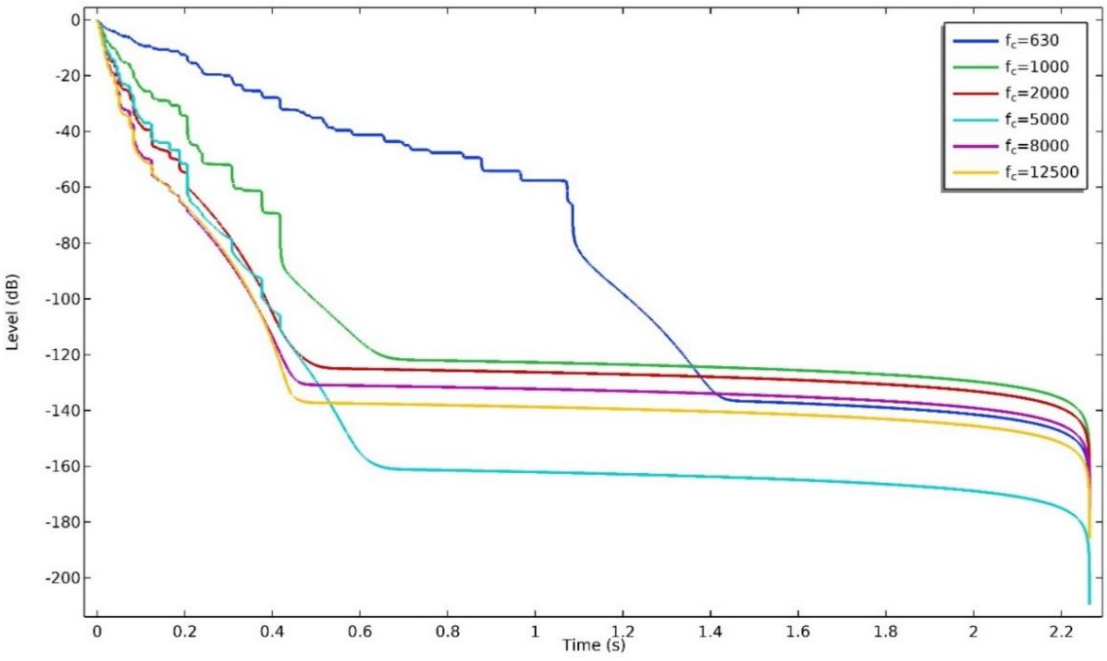


**Fig. 2.15:** Level decay curves for the different 1/3 octave bands (receiver at 1.3 m)

**Figure 2.15** shows the level decay curves for the different 1/3 octave bands used in the model. The reverberation time, $T_{60}$ is estimated from the slope of the decay. The decay slope is steeper at high frequency (12.5 kHz) than low frequency (630 Hz) due to the high absorption coefficient.

The reverberation time $T_{60}$ can be calculated from the reflectogram, which is the energy impulse response yields from the ray arrival time. **Figure 2.16** shows the reflectogram for 630 Hz and 12.5 kHz bands. The slope of the curves (point data) gives a visual indication of the reverberation time. In this case, about 1.06 s for 630 Hz and 0.2 s for the 12.5 kHz band.

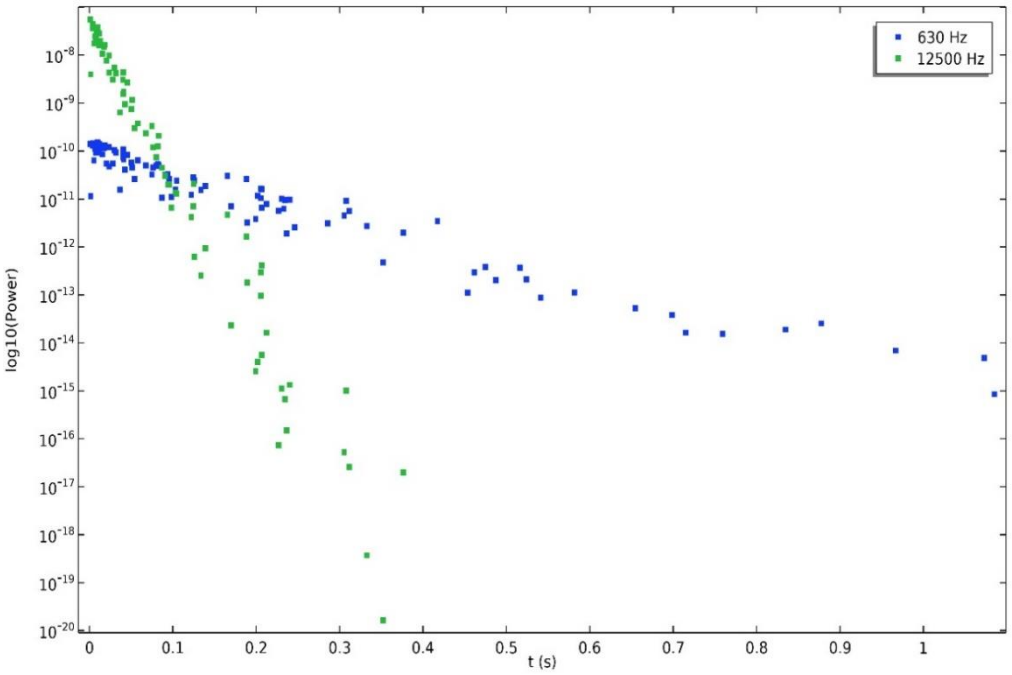


**Fig. 2.16:** Energy impulse response at 630 Hz and 12500 Hz (Receiver at 1.3 m)

The slope of the energy decay curve estimates the reverberation time $T_{60}$ at different 1/3 octave frequencies for a particular receiver position. The complete procedure was repeated for different hydrophone positions at 0.4 m, 0.6 m and 1 m, respectively.

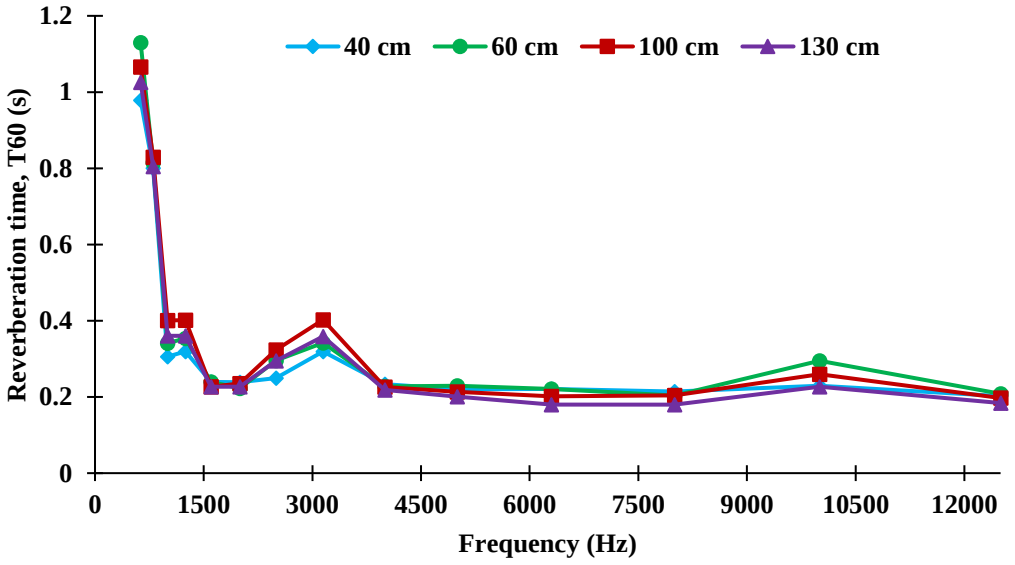


**Fig 2.17:** $T_{60}$ estimated from the ray-tracing method at different receiver locations

**Figure 2.17** shows the decay time $T_{60}$ for different receiver positions at 1/3 octave frequency. The decay time is high (1.1 s) for low frequency (<1000 Hz) compared to high frequencies because of low sound attenuation below 1000 Hz. However, no strong dependency has been found at a frequency above 1000 Hz. Moreover, increasing the distance between the source and receiver does not significantly affect the reverberation time. Far from the source, the sound field is fully diffused and dominated by reverberant sound.

## 2.6 Model Validation

The ray-tracing model is validated against experimental results based on reverberation time $T_{60}$. The model estimated $T_{60}$ values for different receiver positions as shown in **Figure 2.18** are compared with the experimental results presented in **Table 2.2** to validate the accuracy of the model. **Figures 2.19** to **2.20** compare the ray-tracing model and experimental results for receiver distances of 1 m and 1.3 m, respectively. The results show excellent agreement with the numerical results. A statistical technique student T-test is performed to validate the model.

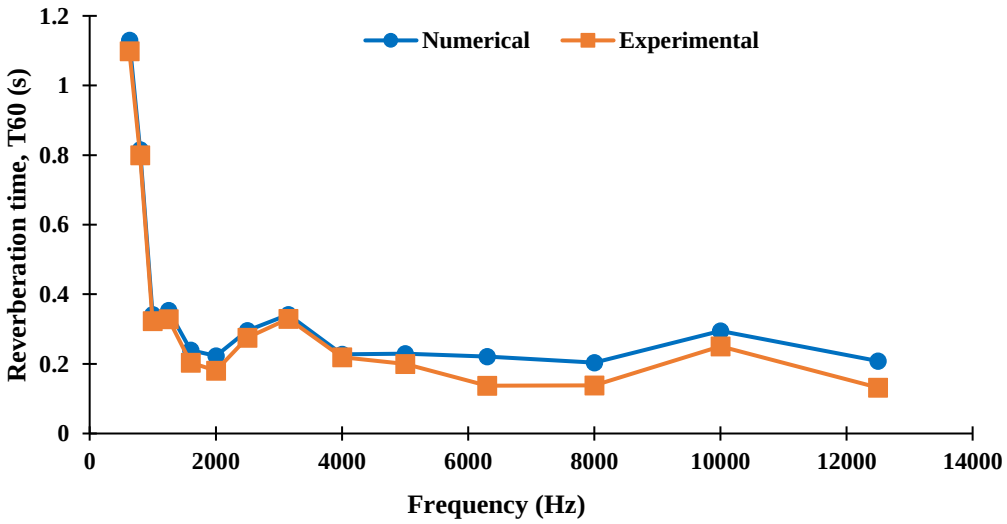


**Fig. 2.18:** Comparison of reverberation time for receiver distance 0.6m

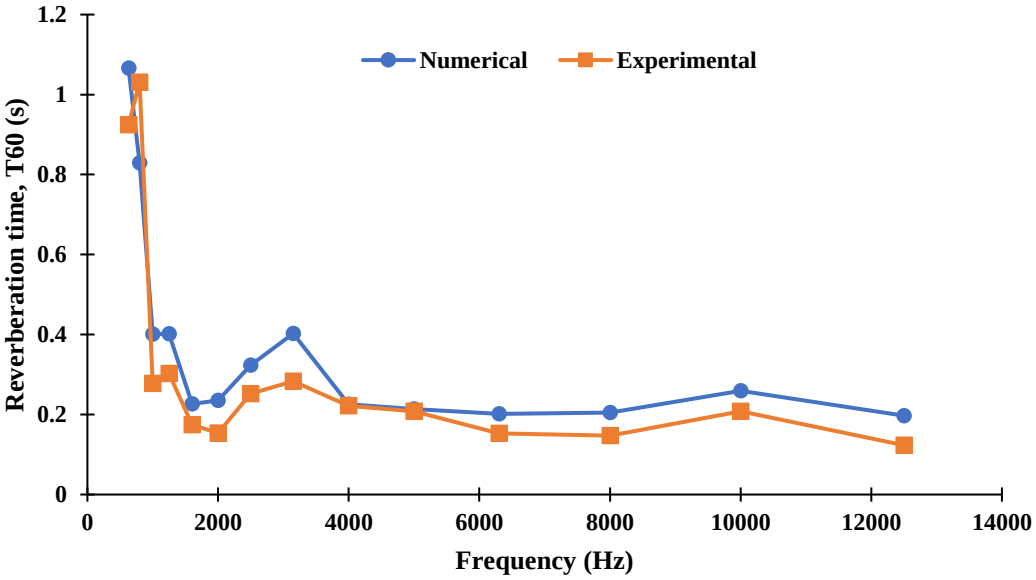


**Fig 2.19:** Comparison of reverberation time for receiver distance 1 m

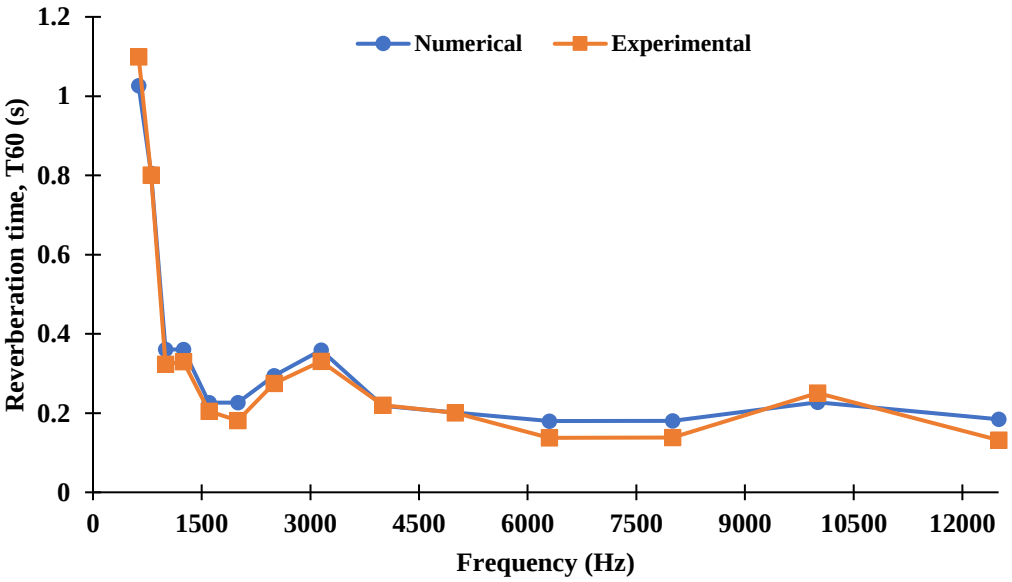


**Fig 2.20:** Comparison of reverberation time for receiver distance 1.3 m

**Table 2.4:** Comparison of experimental and numerical reverberation time, $T_{60}$

| Receiver distance (m) | Experimental (A) $T_{60}$ (s) | Numerical (B) $T_{60}$ (s) |
|---|---|---|
| 0.4 | 0.31 | 0.34 |
| 0.6 | 0.33 | 0.36 |
| 1 | 0.32 | 0.36 |
| 1.3 | 0.33 | 0.34 |
| Average | 0.32 | 0.35 |
| Std. Dev. | 0.009 | 0.015 |

Student t-test is an inferential statistical study to check the difference between two groups [59]. The validation of experimental and numerical reverberation time, $T_{60}$ (s), can be considered as a standard t-test problem where the following hypothesis can be tested.

Null hypothesis, $H_0: \mu_A = \mu_B$

Alternative hypothesis, $H_1: \mu_A \neq \mu_B$

$$\overline{X}_A = \frac{\sum x_A}{n} = 0.3225$$

$$\overline{X}_B = \frac{\sum x_B}{n} = 0.3525$$

$$S_A = \sqrt{\frac{\sum (x - \bar{X}_A)^2}{n-1}} = 0.009$$

$$S_B = \sqrt{\frac{\sum (x - \bar{X}_B)^2}{n-1}} = 0.015$$

$$t = \frac{\bar{X}_A - \bar{X}_B}{\sqrt{\frac{{S_A}^2}{n} + \frac{{S_B}^2}{n}}} = 0.0087$$

From standard t-table for the degree of freedom, $n - 1 = 3$ and confidence level 95%,

$$t_\alpha = \pm 3.18$$

The test statistic value (0.0087) is much smaller than the *t* value (3.18). Therefore, the null hypothesis is failed to reject, and the mean reverberation times are not significantly different for the 5% significance level, thus validating the numerical results.

A further validation method is used, which compares the computed value of $T_{60,}$ and simple statistical estimates as shown in **Figure 2.21**. The estimated values were calculated from Eq. (2.23) and Eq. (2.24), known as Sabine and Eyring equations, respectively. The result shows excellent agreement with the ray-tracing method. It is obvious that Sabine and Eyring's predictions do not match exactly with the ray-tracing model since the estimates are based on analytical models of direct energy, early energy, and late energy.

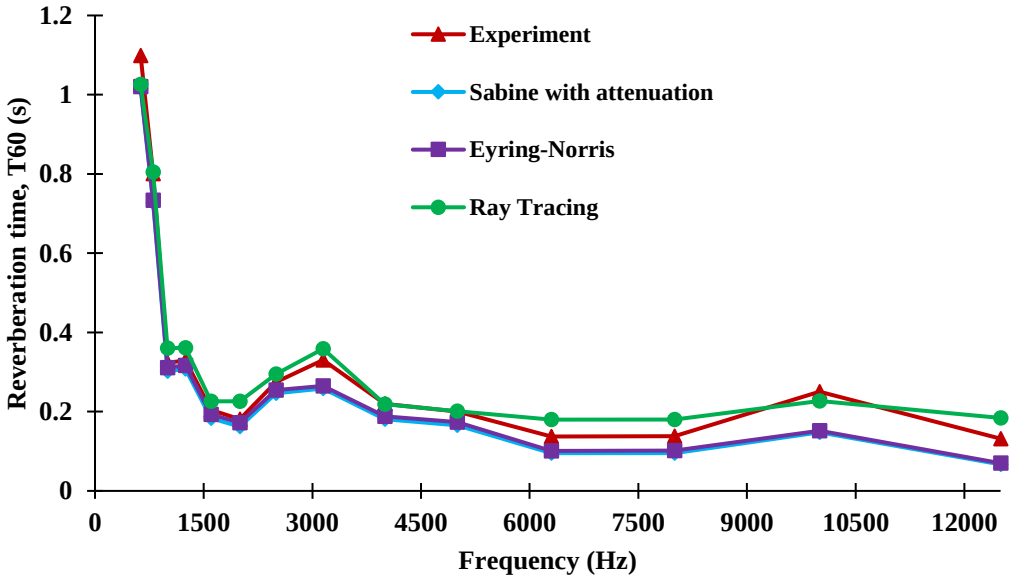


**Fig 2.21:** Comparison of the estimated reverberation time with experimental results and Sabine and Eyring estimation (receiver was 1.3 m from the source)

## 2.7 Acoustic Characteristics of NRC tank

Upon validation of the ray-tracing model, the same model was used to characterize the NRC-OCRE's tank. The walls and floor condition of the NRC-OCRE tank are made of the same materials as the deep tank. Therefore, the boundary of the NRC tank is considered to have the same absorption coefficient as the deep tank. The same projector source level was considered during the simulation while the receiver was 10 m far from the source in the reverberate field. **Figure 2.22** shows the estimated reverberation time $T_{60}$ for the NRC-OCRE tank. The average reverberation time for the large NRC-OCRE tank is calculated as 1.27 sec from the ray-tracing model.

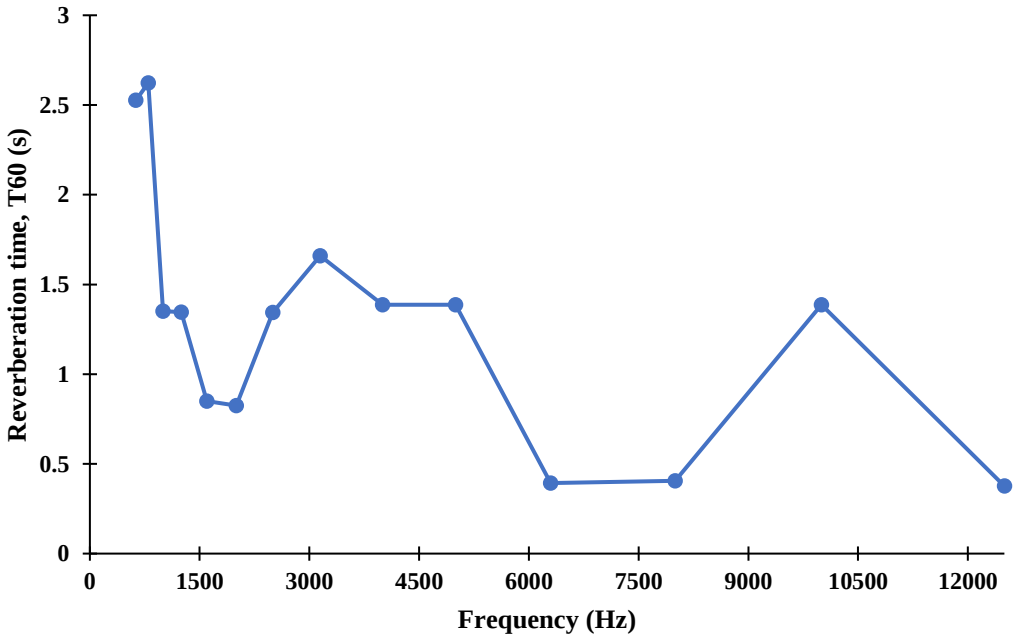


**Fig. 2.22:** Reverberation time of the NRC tank using the ray-tracing model

The NRC tank (200m × 12m × 7m) is acoustically characterized by reverberation time. The volume $V$ (16,800 $m^3$) and the total absorbing surface area $S$ (7,768 $m^2$) yield an average sound absorption coefficient of $\alpha = 0.065$ for reverberation time $T_{60}$ of 1.25s.

Using the reverberation time $T_{60} = 1.25\ s$, the average reverberation radius of the towing tank is 3.13 m. The critical frequency of the tank is $f_c = 162\ Hz$. So the mode mixing condition will be fulfilled for any measurements above 162 Hz.

## 2.8 Lloyd mirror effects

The free surface of water affects the overall noise measurements due to the interference between the direct sound from the source and reflected sound from the free surface, widely known as Lloyd mirror effect. The free surface is assumed to be perfectly flat, reflecting all the incident waves with a reflection coefficient of the amplitude of one $(R = -1)$ and a 180° phase shift.

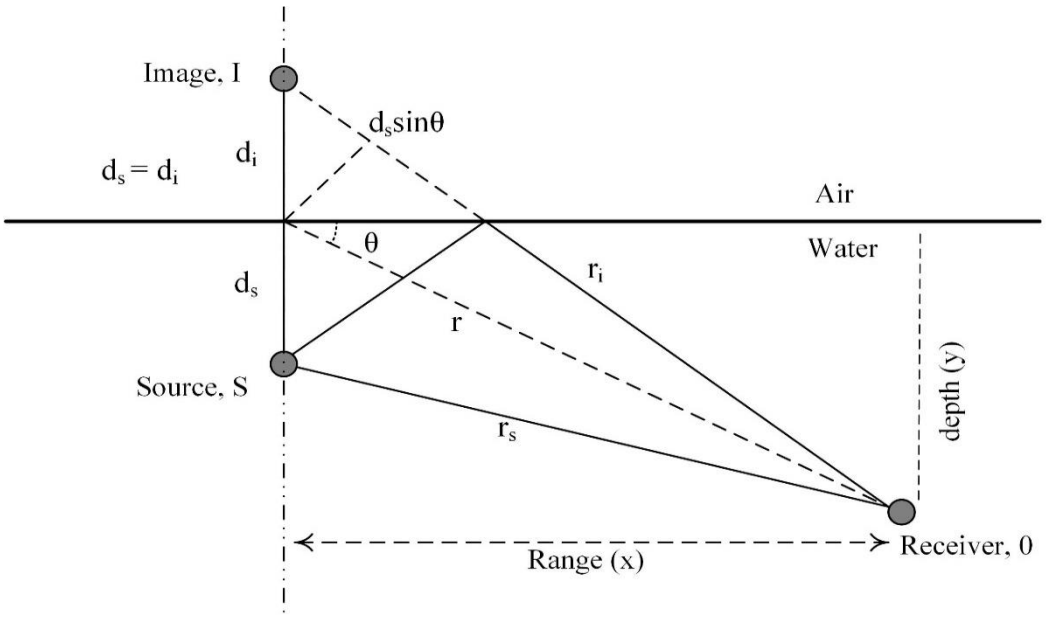


**Fig. 2.23:** Lloyd mirror effect in relation with monopole source

The travel distances of the direct path, $r_s$ and the surface-reflected path, $r_i$, were calculated using the following equations:

$$r_s = \sqrt{x^2 + (y - d_s)^2}$$

$$r_i = \sqrt{x^2 + (y + d_i)^2}$$

The total signal amplitude received at O is the sum of radiated pressure from the source and its image.

$$P(r,t) = P_s(r_s,t) + P_i(r_i,t) \tag{2.26}$$

For a monochromatic wave, this amplitude is given by:

$$P = \frac{A}{r} exp[i(kr - \omega t)]$$

Where $A$ is the source factor in $[\mu Pa.m]$, $r$ is the distance between source and hydrophone in $[m]$, $\omega$ is the angular frequency $[rad/s]$, and $k$ is the wavenumber $[rad/m]$.

$$P(r,t) = \frac{A}{r_s} exp[i(kr_s - \omega t)] + R\frac{A}{r_i} exp[i(kr_i - \omega t)] \tag{2.27}$$

If the water surface is smooth reflection coefficient is $R = -1$. However, if the surface is rough, it will scatter the sound and reflect less energy. If $\lambda$ is the acoustic wavelength, $h$ is the surface wave height (RMS), and $\theta$ is the grazing angle, the reflection coefficient for the rough surface can be approximated by the following equation [57]:

$$R = exp\left[-2\left(\frac{2\pi}{\lambda} hsin\theta\right)\right]$$

Expanding the source and image radial distances $r_s$ and $r_i$ with a Taylor series and neglecting the second-order terms, the sound intensity at O for a perfectly smooth interface $(R = -1)$ is calculated by:

$$I = \frac{1}{2\rho c} real(PP^*) = \left(\frac{A^2}{2\rho c}\right)\left(\frac{1}{r^2}\right)\left[1 + R^2 + 2Rcos(\frac{2kxy}{r})\right] = I_0\left(\frac{1}{r^2}\right)2\left[1 - cos(\frac{2kxy}{r})\right]$$

The correction factor considering the Lloyd mirror effect can be calculated by:

$$CF_{LM} = 10log_{10}\left|\frac{I}{I_0}\right| = 10log_{10}\left\{\left(\frac{1}{r^2}\right)2\left[1 - cos(\frac{2kxy}{r})\right]\right\} \tag{2.28}$$

The maximum and minimum correction factor depends on the cosine in the above equation. However, ITTC suggests following Lafeber et al. [40] to assess the influence of free surface on reverberation and noise measurements. Lafeber *et al.* [40] described an analytical procedure to calculate the correction for the Lloyd mirror effect in URN measurements for the various position of the source and hydrophones. The free-field pressure produced by a monopole point source is given by:

$$P_F = \frac{A}{r} exp[i(\omega t - kr)]$$

If the reflection coefficient is $R$, the ratio between the amplitude of total pressure from source and image and pressure from source only in a free field is given by Eq. (2.29).

$$CF_{LM} = 10log_{10}\left|\frac{P^2}{P_F^2}\right| = 10log_{10}\left\{1 + \left(R\frac{r_s}{r_i}\right)^2 + 2R\frac{r_s}{r_i}cos[k(r_i - r_s)]\right\} \qquad (2.29)$$

Lloyd effect reduces the measured noise level at low frequencies and increases the measured noise level at high frequency. **Figure 2.24** shows the corrections needed for Llyod's mirror interference at different receiver positions presented in **Table 2.5**. The effect is negligible when the receiver is below the projector (**R-4**); however, increasing the horizontal distance between the source and receiver increases the image source distance. Therefore, the influence of the free surface should be considered, and the corresponding correction should be applied to any acoustic measurements.

**Table 2.5:** Position of the receiver

| Receiver No | Origin (0,0) at Source center | | |
|---|---|---|---|
| | X-coordinate | Y-coordinate | Radial distance from the origin |
| R-1 | 1.3 | 0 | 1.3 m |
| R-2 | 1.3 | +0.50 | 1.39 m |
| R-3 | 1.3 | -1.0 | 1.64 m |
| R-4 | 0 | -0.5 | 0.5 m |

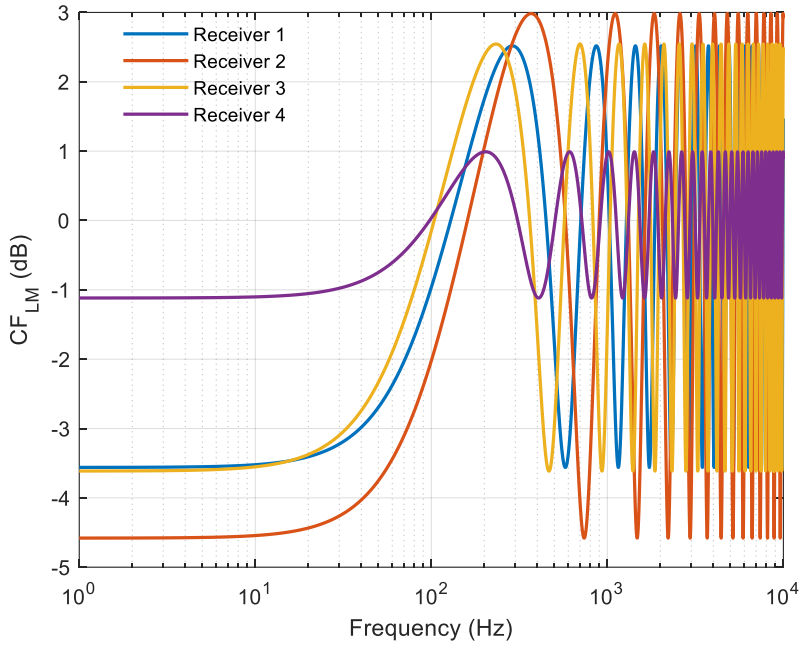


**Fig. 2.24:** Computed Lloyd mirror corrections for different receiver positions

## 2.9 Conclusions

The walls and free surface influence the underwater noise measurement in any acoustic facility due to reverberation phenomena. Therefore, proper acoustic characterization of a facility is a basic need before performing any sound-related experiment. In this study, a thorough procedure is developed to understand the dynamics and acoustic responses of a towing tank based on both numerical and experimental results. The experiments were conducted in a deep tank (48 $m^3$) with an impulse of white noise driven by a projector at a frequency range of 500 Hz to 16000 Hz. The response of the tank was recorded in different points inside the tank with properly calibrated hydrophones. The hydrophone signal was post-processed using Hilbert transform and Schroeder's integral method to estimate the reverberation time in 1/3 octave frequencies for different hydrophone positions. The fundamental acoustic characteristics like sound absorption coefficient, critical frequency, and reverberation radius are evaluated.

A numerical ray-tracing model is developed in the COMSOL software to predict the reverberation time of the deep tank. The numerical and experimental results were compared using a student t-test, and the results show excellent agreement for a 5% significance level. The validated ray-tracing model is then used to characterize the large NRC tank (16,800 $m^3$) by assuming the same boundary wall conditions. Results revealed that the influence of wall reflection could be ignored if the measurements are made inside the reverberation radius 3.13 m from the source.

However, the impulse response function shows the reflection from the free surface immediately after the impulse is generated, and the influence of the free surface should consider during acoustic measurements. A procedure to account for the free surface influence is also developed based on Lloyd mirror effect considering a point source and a perfectly reflecting surface. The effect is negligible when the receiver is below the projector; however, increasing the horizontal distance between the source and receiver increases the image source distance. Therefore, the influence of the free surface should be considered, and the corresponding correction should be applied to any acoustic measurements.

The acoustic reverberation characteristics of a towing tank have been investigated for the frequency range 630 Hz to 12500 Hz. Both the numerical and experimental approaches can determine the acoustic properties of a towing tank. However, it is necessary to extend the experimental study further to characterize the low-frequency (< 200 Hz) response of the towing tank. A good sound projector with a linear response at low frequency will be helpful to perform the analysis. A finite element model can be developed for a low-frequency acoustic response

# Chapter 3

## Propeller Induced Noise Measurements

### 3.1 Abstract

Propeller-induced underwater-radiated noise (URN) has been a major concern for commercial shipping for many years due to the harmful consequences in marine ecology and human health. This study develops an appropriate technique to measure non-cavitating propeller noise at a model scale in an atmospheric towing tank. The detailed experimental set-up, instrumentation and noise measurement procedure from the propeller in non-cavitating conditions is described. The hydrophones are placed in both direct and reverberation fields to measure the near and far-field noise based on the modal propagation theory. Simultaneous experiments at different hydrodynamic conditions with and without the propeller were performed to evaluate the contribution of the hull, propeller, and background noise on the overall noise at a range of frequencies (10 Hz to 3000 Hz). The towing carriage and operating conditions added considerable background noise. The study also identifies the background noise sources and estimates their corresponding noise level to distinguish propeller-induced noise.

## 3.2 Introduction

Ocean noise pollution is a recently concerning environmental issue that negatively impacts both marine ecology and sustainable shipping. Due to human activities like commercial shipping, oil and gas exploration, sonar, drilling, pile drivers, offshore wind turbines, etc., noise has increased significantly in the last century [60], [61]. Commercial shipping is considered the primary contributor to low-frequency noise propagation. Although shipping contributes 80% of global trade by volume at the lowest carbon footprint [62], underwater radiated noise (URN) from commercial shipping has gained much attention in the last two decades [15]. Additionally, the global shipping volume has been significantly increased due to the increasing international trade, transportation, ship size, service speed, and numbers of the operating hour [63]. The continuous low-frequency noise emission from the ships causes severe threats to marine mammals and other species. Ship radiated noise can interfere and overlap the communication signal of marine animals in the ocean [64]. It threatens the marine animal by reducing the ability to communicate, navigate, identify prey and avoid predators [65]. Moreover, the URN can cause physical injuries and even death to marine species. This noise pollutions impact and disturb many complex ecosystems by unbalancing predator-prey interaction, which endangers marine life [66].

Shipping noise is generated from several different sources and mechanisms. Before taking any regulatory actions to create awareness and mitigation measures among the ship owners and other stakeholders, it is necessary to identify and understand the possible noise sources that contribute to underwater noise pollution [67]. Propulsion machinery, propeller and hydrodynamic flow over the hull are the three primary sources of ship radiated noise. Propeller-induced noise is the dominant source of URN at a low-

frequency regime, specifically below 300 Hz [68]. The machinery and hydrodynamic noise could be distinguished by their generation and propagation characteristics. Machinery noise originates from the vibrations of propulsion machinery, auxiliary engines, drive train, shafting system, etc. [69], [70]. Machinery vibration excites the ship hull that radiates noise to the water [71]. At low speed without cavitation, machinery noise contributes to the propagated noise below 100 Hz [72]. The hull is the primary source of hydrodynamic noise. It is related to the flow over the ship hull, its appendages and the propeller. The flow over the hull creates broadband noise at much lower frequencies and increases with the ship speed.

Analysis of ship radiated noise by several research works identified their propulsion systems as a dominant source of underwater noise at frequencies below 200 Hz. The low-frequency noise can propagate over immense distances in all directions due to longer wavelength (peaks have lower pressure), negligible transmission loss, and lower attenuation level. Noise propagation from the propeller is caused by the displacement of the blades, friction between suction and pressure surface, fluctuating wakes, and sudden collapsing of the cavitation bubbles [73], [74]. Propeller noise has both discrete (tonal) and continuous (broadband) characteristics. Tonals are generally the blade frequency in the spectrum, while broadband noise corresponds to the flow fluctuation around the propeller blade. The propeller creates noise both in cavitating and non-cavitating conditions. Propeller cavitated noises from commercial ships show peaks between 50-150 Hz but can extend up to 100 kHz. However, the predominant radiated noise is caused by propeller cavitation below 100 Hz at a higher propeller load. Hildebrand *et al.* [75] identified that broadband and blade rate tonal produced by propeller cavitation is responsible for 80-85% of total noise made by maritime traffic.

As such, cavitation phenomena are widely investigated, and researchers proposed different numerical methods and experimental measurements to predict the cavitating and non-cavitating propeller noise [76]. Kowalczyk and Felicjancik et al. [77] investigated a model scale propeller in a medium-size cavitation tunnel at different propeller loading and used the results to validate the CFD-based numerical model. The measured noise shows excellent compatibility with the calculated noise characteristic. Tani *et al.* [78] conducted round-robin tests of seven propellers in seven different facilities to measure the propeller cavitation noise in an open water set-up. The measured noise deviates 10 dB on average to 20 dB maximum for various facilities due to background noises, tonal disturbances, hydrophone response and boundary conditions.

On the other hand, a non-cavitating propeller generates noise by vibrations due to the fluctuations of hydrodynamic forces acting on the propeller. It can be studied numerically using BEM along with the acoustic analogy approach. Seol *et al*. [79] numerically investigated non-cavitating single propeller noise in various operating conditions using time-domain acoustic analogy and the potential-based panel method. The flow solver was efficient since the numerical values were comparable to the experiments. Kim et al. [80] proposed an appropriate analytical source model to estimate non-cavitating propeller noise. Bagheri et al. [81] studied the hydrodynamic and acoustic behavior of marine propellers using the finite volume method (FVM) and FWH. They validated the model for both cavitating and non-cavitating conditions. Belibassakis [82] proposed a numerical model to predict non-cavitating and blade sheet cavitation noise generated from marine propellers in unsteady inflow conditions using the velocity-based panel method. Ozden *et al*. [83] applied Reynolds Averaged Navier–

Stokes (RANS) and Ffowcs-Williams and Hawkings (FWH) model to predict radiated noise from the submarine propeller at different flow conditions, and the methods showed good agreement with experimental results. However, the implementation of numerical noise modelling strategies is restricted by the reliability, precisions, computational expense, and the inability to model background noise and other experimental factors.

Propeller-induced noise is reliably measured using model-scale tests in a towing tank since full-scale URN measurement in sea trails is highly challenging [84]. However, model-scale tests suffer from several uncertain factors, which may significantly compromise their reliability, such as propeller loading, water quality, model dynamics, etc. [85]. In addition, propeller-induced noise measurement is highly influenced by the acoustic response and reverberation characteristics of the test facility [40], [86]. The model scale experimental setup, testing procedure and instrumentation also affect the precise and reliable noise measurements. Challenges are also associated with the scaling of measured noise spectra to full scale [87].

Li et al. [88] measured the low-frequency propeller noise under different rotational speeds in a towing tank. They used time-frequency theory to measure radiation noise and analyzed the stability of line-spectra at a specific frequency. Brooker and Humphrey [89] measured the underwater noise from a research vessel in shallow water using three hydrophone arrays. They followed ANSI standards for experimental set-up, operating conditions and post-processing of the results. The radiated noise was measured by varying the water depth, engine speed and ship speed. Haimov et al. [29] reported detailed experimental guidelines and procedures for propeller acoustic measurement in an atmospheric tank at different conditions. They thoroughly analyzed the background

noise and uncertainty for each condition. The reflection of sound from the wall and free surface influences the measured noise and requires additional correction factors. However, no such adjustment is developed and adopted by the researchers to account for these effects.

Developing a realistic noise mitigation policy framework for shipping vessels needs extensive research and stakeholder awareness [90]. Vakili *et al.* [91] suggested that multi-interdisciplinary command and control approach should be considered before taking any future policy and decision on URN from commercial vessels. The several recent large collaborative projects by the EU, such as SILENV [92], AQUO [93] and SONIC [94] projects, also recommend further research to enable mitigation strategies for reducing propeller-induced shipping noise. A proper and universally adopted standard to measure the ship radiated noise and understand the radiation characteristics is essential to control and alleviate the ship noise. Unfortunately, there is no widely adopted procedure for URN measurements at model scale despite similar installation methods, test conditions, data acquisition/analysis and scaling techniques to full scale [78]. In contrast, the research communities adopted noise measurement procedures based on the type, size and available range of operating conditions of the facility. In this scenario, the accuracy and reliability of URN measurement is a crucial challenge that necessities the development and validation of reliable noise assessment and prediction tools.

This study focuses on developing appropriate techniques to measure non-cavitating propeller noise at a model scale in an atmospheric towing tank. The study also identifies the background noise sources and estimates their corresponding noise level to distinguish propeller-induced noise. The modal propagation theory of sound is applied

to position the hydrophones properly to avoid any influence of wall reflected noise. Additionally, a correction factor is developed based on Lloyd mirror effect to account for a free surface effect on measured noise. The experimental results will be helpful to validate the CFD model and provide indications to properly conduct underwater radiated noise measurements from non-cavitating propellers in atmospheric tow tanks.

### 3.3 Description of Model Hull and Propeller

This study measured noise from a 4-bladed (NACA 66 modified with 0.8 meanline) fixed-pitch propeller as shown in **Figure 3.1**. The geometrical profile of the propeller is listed in **Table 3.1**. 4-bladed fixed blade propellers are robust and fuel-efficient.

**Table 3.1**: Geometrical profile of the propeller

| **Parameters** | **Description** |
|---|---|
| Diameter (m) | 0.235 |
| Number of blades | 4 |
| Pitch-diameter (P/D) distribution | Constant $\frac{P}{D} = 1.0$ |
| Expanded area ratio (EAR) | 0.65 |
| Section profile | NACA 66 modified with 0.8 meanline |
| Materials | Copper |

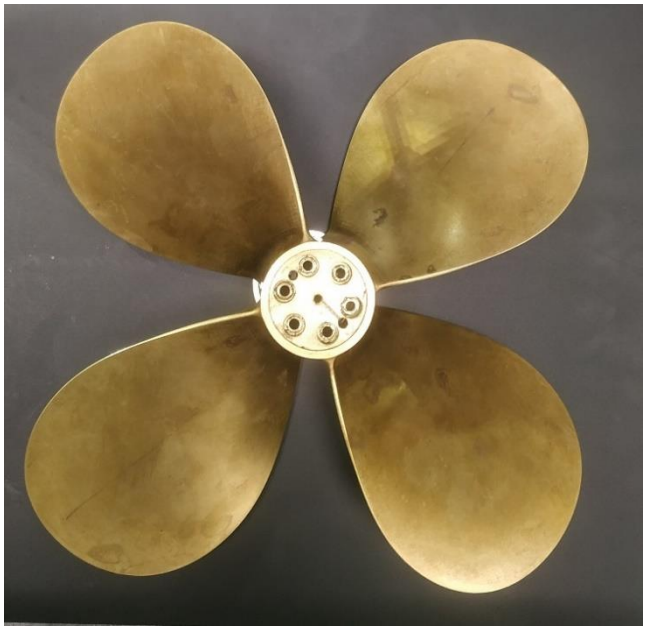

**Fig 3.1**: Photograph of the constant P/D propeller used in the PINOV project

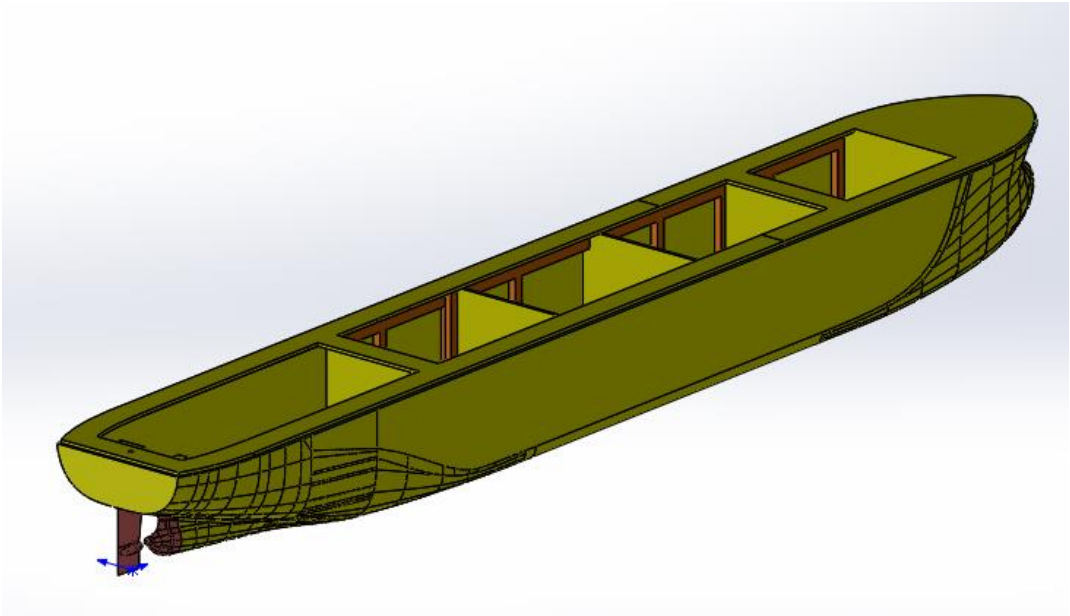

**Fig. 3.2**: CAD design of the model

A scale model of a tanker was used in this study. The model was constructed mainly of wood. A scale of 1:31.7 was used as a compromise between the towing tank size and speed. Additionally, the model has sufficient volume and weight margin to

accommodate the necessary instrumentation. The dimension of the model is presented in **Table 3.2**. Additional weights were used in the model structure to compensate for the lightweight of the materials and get sufficient hydrostatic equilibrium.

**Table 3.2**: Dimension of the model

| **Parameters** | **Description** |
|---|---|
| Model No | OCRE 916 |
| Length Overall (mm) | 7,142 |
| Depth (mm) | 623 |
| Breadth (mm) | 1,024 |
| Draft (mm) | 462 |
| Materials | FRP (3 Layers, 6 Oz WR)<br>SPF Plywood (Spruce, Pine, Fir)<br>Brass<br>RenShape 440<br>Hi-60 Foam |
| Total ballast (kg) | 2260 |
| Model weight (kg) | 425 |
| Total displacement (kg) | 2685 |

### 3.4 Physical Description of the Tank

Propeller-induced non-cavitating noise measurements were performed in the NRC, OCRE towing tank in St. John's, NL, Canada. The detailed layout of the facility is shown in **Figure 3.3**. The tank is 200 m long, 12 m wide, and 7 m in depth. The sidewalls of the tank are made of concrete and painted with 6mm thickness. The sidewalls and the bottom of the tank are flat while the water surface is open to the atmosphere.

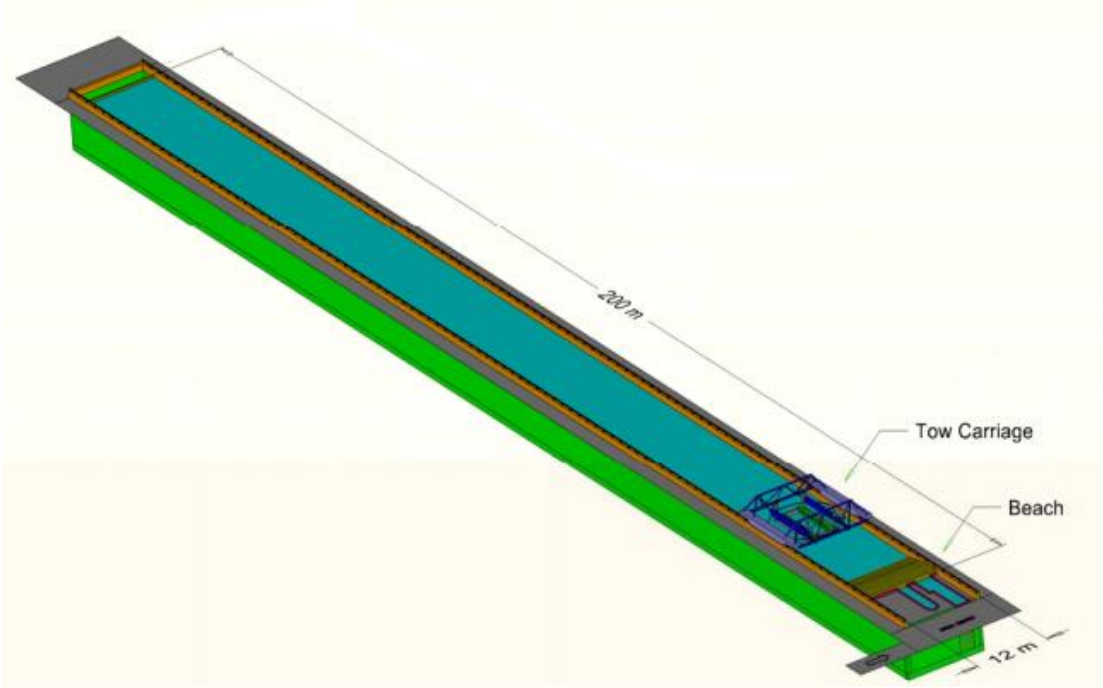


**Fig. 3.3:** Complete layout of the test facility

A carriage that supports the model and measurement system can slide over the railways. The carriage is powered by eight wheels 746 kW synchronous motor drive. The weight of the carriage is 85,000 kg and can achieve a speed range between 0.001 m/s to 10 m/s. The facility can accommodate a maximum model size of 12 m in length, and the test frame could be adjusted for model size. Regular tap water was used in the tank, and the water temperature was 16 to $18^0$C during the experiment.

### 3.5 Methodology

The following section discusses the model testing procedure, experimental set-up, instrumentation and data acquisition systems, and a complete process of pressure signal analysis.

### 3.5.1 Instrumentation and Hydrophones

A set of six(6) hydrophones was used for recording or listening to underwater sounds generated by the ship propeller. They are made of piezoelectric materials that create an electric potential when subjected to a pressure change due to propeller noise. The underwater noise measurements were made using six Bruel & Kjaer hydrophones (Model 8103) because of their high sensitivity relative and good all-round characteristics. They are very compact and have a flat frequency response, especially at low frequency. Additionally, the 8103 is omnidirectional and can measure wide noise ranges from 0.1 Hz to 180 kHz. All the hydrophones were calibrated, and necessary information about the charge sensitivity is given in **Table 3.3**. A charge amplifier (type 2634) was used to condition the output signal from the hydrophone before transmission to the DAQ. The charge amplifier had the sensitivity settings at $\frac{1mV}{pC} \pm 1\%$ (factory pre-set). The sound pressure in (Pa) is given by the following Eq. (3.1)

$$L_p = \frac{e_{ca}}{M_q S_{ca}} \tag{3.1}$$

Where $L$ is the sound pressure (Pa), $e_{ca}$ is the measured voltage (mV), $M_q$ is the charge sensitivity of the hydrophone (pC/Pa), and $S_{ca}$ represents the sensitivity of the pre-amplifier (mV/pC)

**Table 3.3:** Sensitivity Properties of the hydrophones (Factory calibrated)

| Hydrophone | Serial No | Charge sensitivity (pC/Pa) | Sensitivity (kPa/V) |
|---|---|---|---|
| 1 | 2693232 | 0.0930 | 10.753 |
| 2 | 2739227 | 0.0910 | 10.989 |
| 3 | 2739228 | 0.0950 | 10.526 |
| 4 | 2739229 | 0.0930 | 10.752 |
| 5 | 2739231 | 0.0930 | 10.752 |
| 6 | 2739233 | 0.0890 | 11.235 |

The hydrophone signal is then passed through the pre-amplifier and a filter set at 5000 Hz. The sampling frequency of the measurement system is 25 kHz.

### 3.5.2 Acoustic Behaviour of the Towing Tank

The propeller-induced noise measurements need a semi-infinite space under the water surface to freely propagate the radiated noise without disturbing reflections from sidewalls and the bottom [95]. However, the towing tank is a confined space enclosed by five solid walls and a free water surface open to the atmosphere. The tank allows free field conditions only in the longitudinal direction. Acoustically the tank behaviour lies between a room and a tunnel [31]. Due to the high impedance between air and water, the free surface acts as a mirror and reflects almost all the incident sound waves. Therefore, the tank becomes highly reverberated due to the generation of axial, tangential, and obliques modes inside the tank. The facility size and characteristics affect noise propagation and the noise power emitted by the propeller. Tani et al. [86] proposed an acoustic transfer function correction to address the effect of wall reflections for a specific towing tank. However, if the transfer function for the tank is not available, ITTC suggested a distance normalization based on spherical spreading loss theory in a free-field condition. In this study, a distance normalization correction $CF_D$ is used to account for confined environment effects.

$$CF_D = 20log_{10}\left(\frac{r}{r_{ref}}\right) \tag{3.2}$$

Since the hydrophones were used to measure both the near and far-field noise for propeller-induced noise, the reverberation radius of the tank was studied before the experiments. The critical radius for the towing tank is calculated using the following Eq. (3.3) [45].

$$r_c = \sqrt{\frac{55.26 \times V}{c \times 16\pi \times T_{60}}} \quad (3.3)$$

Where $T_{60}$ is the reverberation time, $V$ is the tank's volume, and $c$ is the speed of sound in water. The behaviour of sound waves inside the tank depends on the critical frequency below which separate modes rather than statistical properties influence the noise field. The transition between the normal mode and the statistical model is marked by the Schroeder frequency [32] and easily derived from modal theory using Eq. (3.4).

$$f_c = \sqrt{\frac{C^3}{4\ln(10)} \times \frac{T_{60}}{V}} \quad (3.4)$$

From the ray-tracing model, the average sound absorption coefficient $\alpha$ is 0.065 for reverberation time $T_{60}$ of 1.25s. Using the reverberation time $T_{60} = 1.25\ s$, the average reverberation radius of the towing tank is 3.13 m, and the critical frequency of the tank is $f_c = 162\ Hz$. On the other hand, the free surface effect on the measured noise level is addressed using Lloyd mirror effect as described in **Section 3.4**.

### 3.5.3 Experimental Set-up and Acoustic Frame

Experimental investigations were carried out in a towing tank located in the NRC-OCRE research centre at St. John's, NL, Canada. It is a long narrow channel of enclosed water and is employed for model testing experiments. The model needs to run for some distance in the longitudinal direction of the tank at specific testing conditions. During the experiments, the ship model is towed from a carriage. The carriage is a platform that supports all the machinery, equipment, control room, etc. and can move over rails installed in the lateral walls of the tank. Apart from supporting the model, the carriage also serves various other purposes, such as housing recording instruments, computers, and other data collection systems. Additionally, in noise measurement experiments, the

carriage needs to support an acoustic frame to hold the hydrophones properly against the propeller. The complete experimental set-up with acoustic frame and carriage arrangement is shown in **Figure 3.4**.

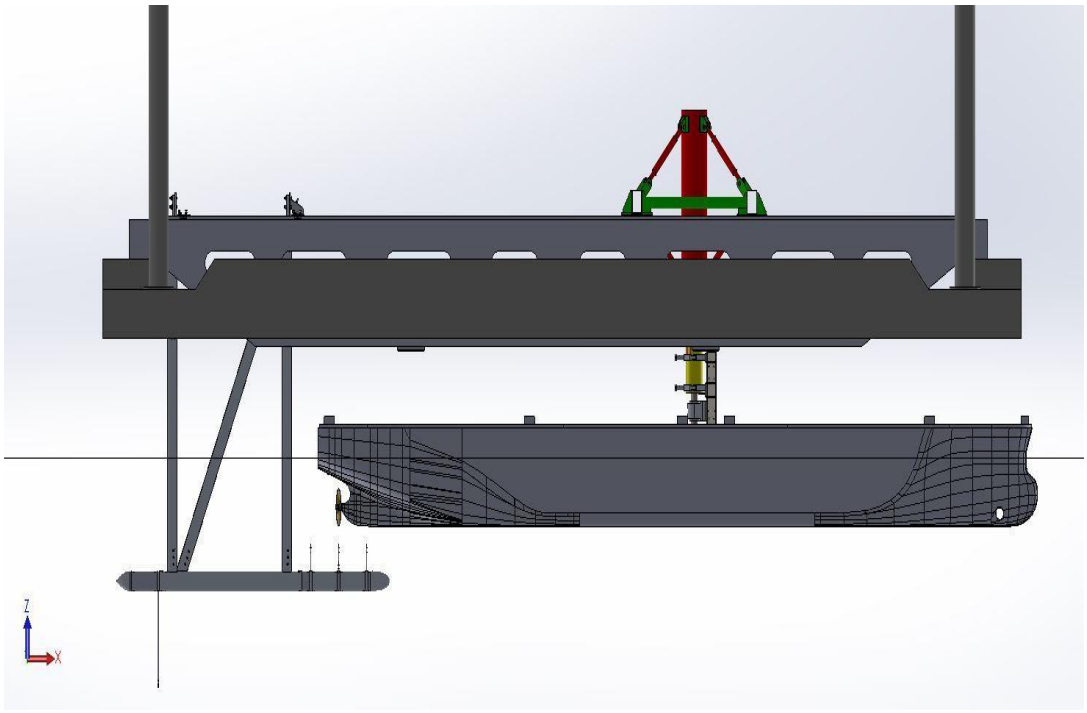

**Fig. 3.4:** Complete test set-up of the model with acoustic frame and carriage

The team at the NRC-OCRE designed and constructed the acoustic frame using steel. The support structure had provisions to facilitate variation of dimensions to adjust hydrophone position with respect to the propeller through movable joints. The main structure was bolted to the carriage and moved with the carriage during experiments.

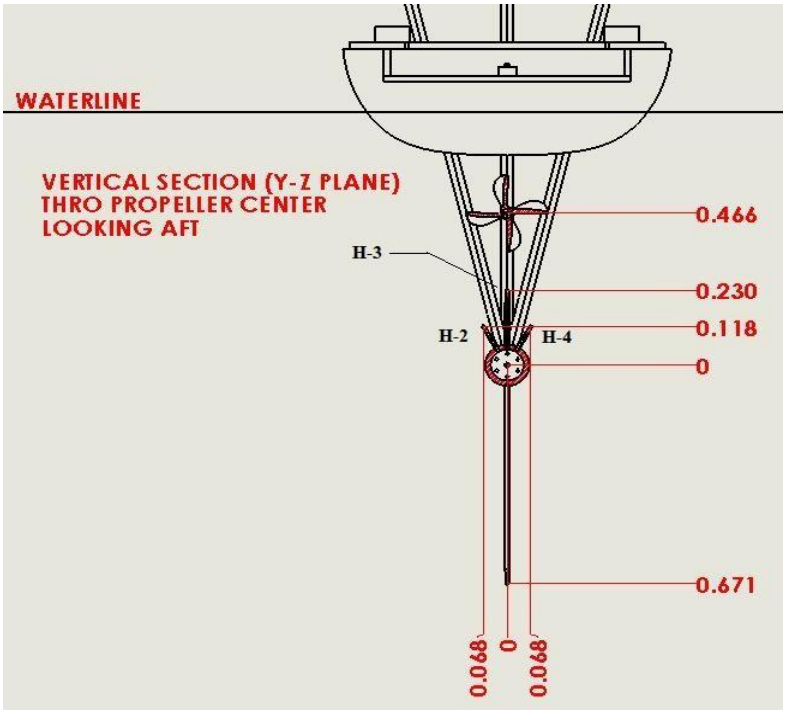


**Fig. 3.5:** Location of hydrophone from the stern end

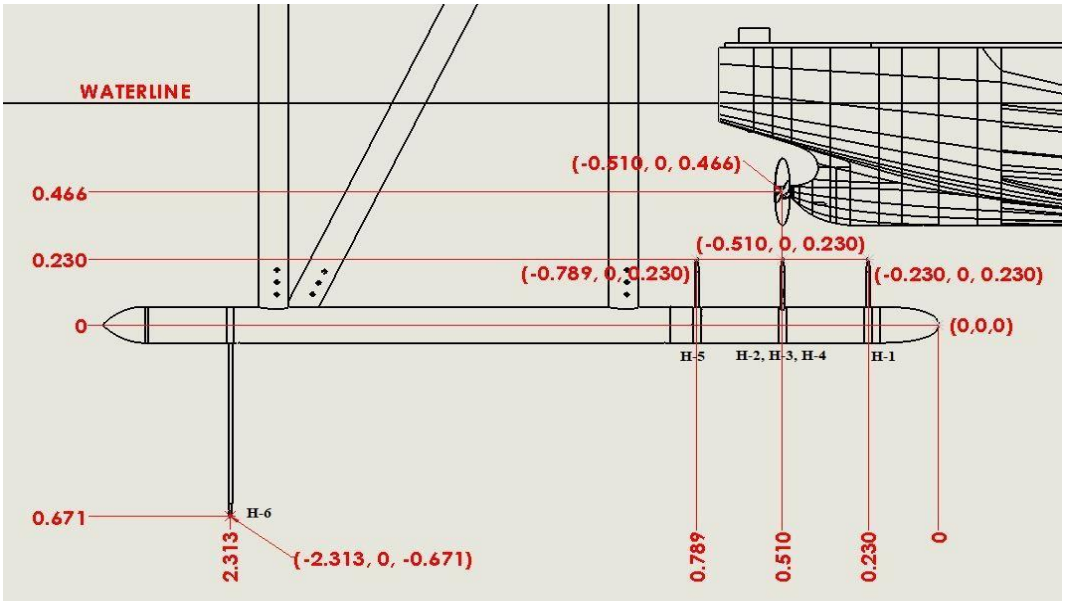


**Fig. 3.6:** Location of hydrophone from starboard end

Figures **Figure 3.5** and **Figure 3.6** show the position of the hydrophone relative to the propeller. Hydrophone **H-2, H-3, H-4** were located in the same propeller plane and exactly located below the propeller. The primary purpose of these hydrophones is to

measure the direct field noise generated by the propeller. Hydrophone **H-1** was positioned 0.23 m ahead of the propeller (upstream), and hydrophone **H-5** was at 0.279 m (downstream) to measure noise generated due to propeller current. Both the hydrophones were within a 1D diameter radial distance from the propeller. The hydrophone **H-6** was located far from the propeller to measure the far-field underwater noise. An additional steel frame supported the hydrophone **H-6** (1.80 m far horizontally from the propeller plane) mounted from the main supporting structure, which was located 1.13 m below from the center of the propeller. The distances from each hydrophone with respect to the center of the propeller are shown in **Table 3.4.**

**Table 3.4:** Position of the hydrophones

| Hydrophone no | Origin (0,0) at propeller center | | |
|---|---|---|---|
| | X-coordinate | Y-coordinate | Radial distance from the origin |
| H-1 | 0.230 | -0.236 | 0.366 m |
| H-2 | 0 | -0.348 | 0.348 m |
| H-3 | 0 | -0.236 | 0.236 m |
| H-4 | 0 | -0.348 | 0.348 m |
| H-5 | -0.279 | -0.236 | 0.365 m |
| H-6 | -2.083 | -1.137 | 2.136 m |

### 3.5.4 Llyod's Correction for Free surface

A reliable procedure to accurately measure the ship radiated noise is essential for assessing and mitigating shipping-related noise. Model testing is conducted in an atmospheric tank. Therefore, the free surface of water affects the overall noise measurements due to the interference between the direct sound from the source and reflected sound from the free surface, widely known as Lloyd mirror effect. The free surface is assumed to be perfectly flat, reflecting all the incident waves with a reflection coefficient of amplitude of one ($R = -1$) and a 180° phase shift. The free surface

reduces the measured noise levels at low frequencies; however, the influences are significantly strong and increase with decreasing frequency. ITTC suggested assessing the impact of the Lloyd mirror effect and correcting them with an acoustic calibration test [96].

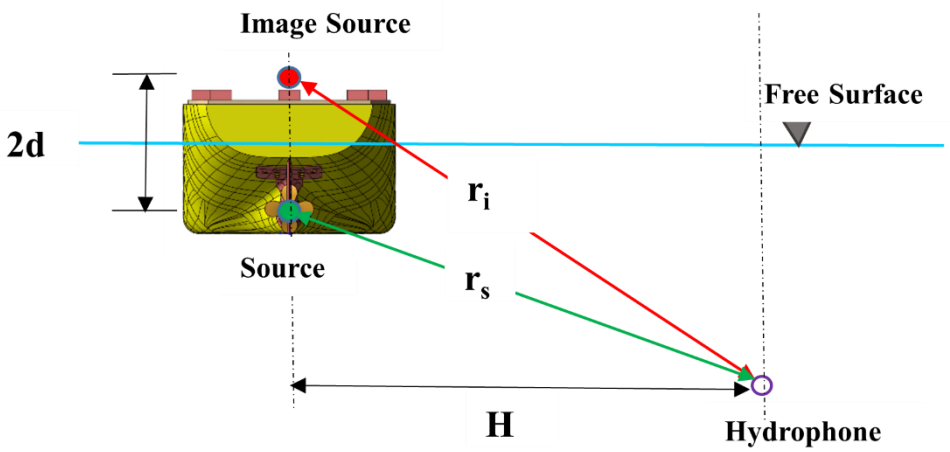


**Fig. 3.7:** The Lloyd mirror effect in relation with ship radiated noise

Audoly and Meyer [97] numerically investigated the influences of sea surface reflection properties on the Llyod mirror effects. They suggested a 3dB correction for ship radiated noise measurements, particularly at low frequency. Lafeber *et al.* [40] described an analytical procedure to calculate the correction for the Lloyd mirror effect in URN measurements for the various position of the source. The free-field pressure produced by a monopole point source is given by Eq. (3.5).

$$P_F = \frac{A}{r} exp[i(\omega t - kr)] \tag{3.5}$$

Where $A$ is the source factor in $[\mu Pa.m]$, $r$ is the distance between source and hydrophone in $[m]$, $\omega$ is the angular frequency $[rad/s]$, and $k$ is the wavenumber $[rad/m]$.

Considering the free surface reflection coefficient $R$, the ratio between the amplitude of total pressure from source and image and pressure from source only in a free field is given by Eq. (3.6)

$$CF_{LM} = 10log_{10}\left|\frac{P^2}{P_F^2}\right| = 10log_{10}\left\{1 + \left(R\frac{r_s}{r_i}\right)^2 + 2R\frac{r_s}{r_i}cos[k(r_i - r_s)]\right\} \qquad (3.6)$$

Where, $r_s$ is the distance of the source from hydrophone in $[m]$, $r_i$ is the distance of the image source from the hydrophone in $[m]$, reflection coefficient $R = -1$. As the propeller was set at a distance of 0.538 m under the water surface, the estimated corrections due to the Lloyd mirror effect for all the hydrophone positions presented in **Table 3.4** are shown in **Figure 3.8.**

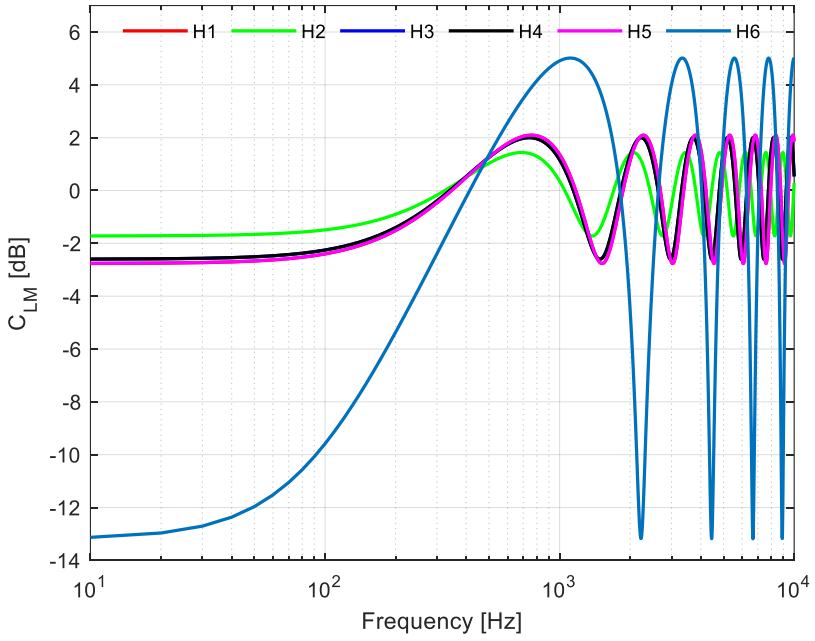


**Fig. 3.8:** Estimated corrections due to Lloyd mirror effects for six hydrophones

It shows the variation of the correction factor as a function of frequency. The Llyod effect is small and almost linear (2 dB) up to 1 kHz for hydrophones H-1 to H-5. However, the effect is significant for hydrophone H6, which is located in the far-field.

Any ship radiated noise measured by H-6 should be corrected by 13 dB, especially at a lower frequency. **Figure 3.8** also indicates that the hydrophones are correctly positioned to measure the propeller-induced noise with a minimum Lloyd mirror effect.

### 3.6 PINOV Test Programme

The team at the NRC-OCRE carried out a model test program for the Propeller Induced Noise and Vibration (PINOV) project to estimate the noise by the rotating propeller under non-cavitating atmospheric conditions between February 14, 2020 to March 11, 2020. The test program includes:

a. Background noise test
b. Resistance test
c. Self-propulsion test
d. Bollard test

The details about the model testing procedure is discussed in the **Appendix A**. The objective of these tests is to evaluate the contribution of background noise, hydrodynamic noise, propeller noise in the overall ship radiated underwater noise. The background noise tests were conducted without the hull model to identify the sources of background noises (carriage, electrical appliances, etc.) and their corresponding noise levels. The flow similarities between the model and full scale were maintained during the tests using equal non-dimensional Froude number (Fr).

Resistance tests are conducted to measure the ship hydrodynamics and acoustics without the propeller. In these tests, the propeller was replaced with a bare hub of the same weight. Acoustically, there is no noise contribution from the rotating propeller and machinery noise (propulsion noise). The resistance tests are helpful to estimate the

hydrodynamic noise produced by the hull with water interaction. Additionally, since the carriage is also moving during the resistance test, the background and carriage noise contributes to the measured noise.

The self-propulsion tests are essential for propeller-induced noise measurements since they provide information about the actual operating conditions. The noise measured from self-propulsion tests includes noise contribution from all the possible sources like background noise, carriage noise, hydrodynamic hull noise, and noise contribution machinery noise and propeller noise. Furthermore, since the resistance and self-propulsion are conducted at the same Froude similarities, the propeller noise could be distinguished from other noises by its tonal frequency (BPF) and its multiple.

Since the model is at rest during the bollard pull test, there are no other noise sources except the propeller-induced noise. The noise generated during the resistance and self-propulsion tests includes the carriage noise, background noise, machinery noise (electric motor, shafting arrangement) and hydrodynamic noise of the hull. As a result, identifying the propeller noise from the noise spectrum becomes very complicated. However, the noise measured in the bollard pull condition is free from other complex noise signatures. The only available noise is the background noise (electric hum) which is distinguished from propeller-induced noise (tonal and multiples). The bollard tests are conducted precisely at self-propulsion RPS. **Table 3.5** shows the test speeds and rotational velocity speeds tested in PINOV model tests.

**Table 3.5:** Test configuration of PINOV model testing

| Test Configuration | | | |
|---|---|---|---|
| **Frame Only** (Advanced Speed [m/s]) | **Resistance** (Advanced Speed [m/s]) | **Self-Propulsion** (Advanced Speed [m/s]) | **Bollard (RPS)** (Advanced Speed [m/s]) |
| 0.50 | 0.728 | 0.917 | 4.45 |
| 0.75 | 0.826 | 1.101 | 5.41 |
| 1.101 | 0.917 | 1.284 | 6.26 |
| 1.192 | 1.101 | 1.376 | 6.80 |
| 1.284 | 1.192 | | |
| 1.376 | 1.284 | | |
| 1.50 | 1.376 | | |
| 1.75 | 1.468 | | |

### 3.7 Signal Analysis Procedure

Acoustic data was acquired with a sampling frequency of 25 kHz. The measured acoustic pressure signals have two parts in the time domain signal: the transient and steady parts. The recorded signal was indexed to remove the transient (tare) part of the signal. However, the time length should not be less than 20sec, as recommended by ITTC [96]. Since the endpoints are discontinuous after indexing, these discontinuities showed up as high-frequency components in Fast Fourier Transform (FFT) analysis even if they are not present in the original signal. In this condition, the energy of one frequency leaks into other frequencies, known as spectral leakage.

A Hamming window function was selected to side lobes of the frames and avoid leakage error. The Hamming window forces the end of time signals to zero regardless of the input signal, which distorted the waveform by varying the signal amplitude over time and needed additional amplitude correction. Moreover, 50% overlap of the frames was used to reduce the error caused by the end shaping effect of the time window [98].

The Power Spectral Density (PSD) was calculated to understand the frequency content of the acquired time data. The PSD was estimated using Welch's method [99], [100] from the FFT signal, as per Eq. (3.7), where $w$ is for Hanning window function.

$$\varphi_{pp}(m) = \frac{1}{W}|A_k(m)|^2 \tag{3.7}$$

$$W = \sum_{m=0}^{M} w^2(m)$$

The noise spectrum obtained from the analysis is represented and reported in several ways. Anthropogenic underwater radiated noise is usually expressed either in radiated noise level (RNL) or monopole source level (MSL). RNL indicates exposures in shallow and deep waters, while MSL refers to the sound power, and therefore independent of the field propagation. These two quantities in full-scale measurements can be obtained according to ISO and ITTC procedures [101], [102]. However, in the case of model-scale measurement, ITTC guidelines are usually followed [96].

The Sound Pressure Level (SPL) is the fundamental quantity for assessing noise, and it is defined in terms of a pressure ratio as Eq. (3.8).

$$SPL = 10log_{10}\left(\frac{\bar{P}_{rms}^2}{P_{ref}^2}\right) \tag{3.8}$$

Where $P_{ref}$ is the reference pressure, normally $1\mu Pa$ for water.

In the present analysis, the spectral representation of a sound pressure signal $P(t)$ was calculated through an FFT, resulting in a PSD function $\varphi_{pp}(f, \Delta f)$. The PSD is most frequently used for spectral representation with the unit $dB\ re\ 1\mu Pa^2/Hz$.

$$SPL(f, \Delta f) = 10log_{10}\left(\frac{\varphi_{pp}(f,\Delta f)}{P_{ref}^2}\right) \tag{3.9}$$

The relationship between power spectrum and power spectral density is given by

$$SPL(f,\Delta f) = 10log_{10}\left(\frac{\varphi_{pp}(f,\Delta f)}{P_{ref}^2}\right) + 10log_{10}(\Delta f) \quad (3.10)$$

A distance normalization was applied as the measured noise levels are heavily influenced by the distance between the noise source and the hydrophones. The SPL was corrected according to spherical spreading loss defines the radiated noise level (RNL).

$$RNL = SPL + CF_D \quad (3.11)$$

$$CF_D = 20log_{10}\left(\frac{r}{r_{ref}}\right) \quad (3.12)$$

Where $r$ is the distance between the propeller and hydrophone position in meter, $r_{ref}$ is reference distance of 1m, and $CF_D$ is the correction for distance normalization.

The RNL was further corrected to account for Lloyd mirror due to the sound interference at the free surface of the tank. The final radiated noise quantity is represented as sound power level (SPL) as follow-

$$SPL = RNL - CF_{LM} \quad (3.13)$$

The conversion from narrowband (SPL) to 1/3 octave is performed using the Matlab function 'poctave' [103]. The poctave spectrum is the average power over octave bands and refers to the ANSI S1.11 standard.

In addition, another frequently used descriptor is the dimensionless pressure as described in [104], [105], obtained from the hydrophone signal using the following expression.

$$K_p = \frac{P(t)}{\rho D^2 n^2} \quad (3.14)$$

Where $P(t)$ is the time domain signal from the hydrophone, $\rho$ is the density of the medium, $D$ is the diameter of the emitter (propeller), and $n$ is the rotation of the propeller (rps). $P(t)$ is the pressure signal measured in Pa and reduced to 1m (reference)

with respect to the propeller center. The decibel level is estimated from the following relationship.

$$\mathrm{L}K_p = 20log_{10}\left(\frac{K_p}{K_{ref}}\right) \tag{3.15}$$

Where, $K_{ref}$ is the reference pressure level, and the corresponding value is $1\mu Pa$. When acoustic descriptor $K_p$ is used to present the noise level, sound pressure level (SPL), and PSD transform, respectively in:

$SPL_{Kp}$ in dB re $K_{Pref}$

$PSD_{Kp}$ in dB re $K^2_{Pref}$

### 3.8 Correction for Background Noise

The propeller-induced noise measurements in a facility are affected by the background noise that is always present in the environment. A correction to the measured model noise can be made using the difference $\Delta SPL$ between the pressure levels, which is defined as Eq. (3.16):

$$\Delta SPL = SPL_{s+n} - SPL_n = 10log_{10}\left(\frac{\bar{p}^2_{rms_{S+n}}}{\bar{p}^2_{rms_n}}\right) \tag{3.16}$$

Where $SPL_{s+n}$ is the sound pressure level of the model noise measurements, and $SPL_n$ is the sound pressure level of the corresponding background noise. If the difference $\Delta SPL$ is greater than 10 dB, the measurements are reliable, and no additional corrections are necessary.

$$SPL_s = 10log_{10}\left(10^{\left(\frac{SPL_{S+n}}{10}\right)} - 10^{\left(\frac{SPL_n}{10}\right)}\right) \tag{3.17}$$

In contrast, $\Delta SPL$ less than 3 dB indicates that measurements are dominated by background noise, and the results are useless. However, if $\Delta SPL$ falls between $3\ dB \leq \Delta SPL < 10\ dB$, adjusting the measurements is required using the following Eq. (3.17).

## 3.9 Results and Discussions

In this section, all the experimental data of the PINOV programme has been analyzed and presented using the signal analysis procedure discussed in **Section 4.5**. Both the narrowband PSD and 1/3 octave band were used to show the experimental results. The narrowband analysis at least distinguishes the contribution of the propeller noise from the whole spectrum. There might be some variation while comparing the results due to the measurement uncertainties. However, the uncertainties of the measurements were studied, and the experiments were replicated at least twice to get the same results within 1% variations. The analysis identifies background noise sources and their corresponding level, followed by the resistance and self-propulsion tests. The results of noise measurements are analyzed in detail in the following section.

### 3.9.1 Background Noise Characterization

The influence of background noise is the major difficulty for propeller-induced noise measurements in the atmospheric tank. The background noise can cover the frequency range from 10 Hz to 10 kHz. At low frequencies below 100 Hz, the noise sources are generally the electrical appliances, surrounding noise, etc. In contrast, high-frequency noises could be generated from a measurement system, battery-operated DAS, electromagnetic interference, etc. In the NRC towing tank, disturbing noises in all frequencies may be propagated from nearby machine shops, compressors, heating

systems, transformers, vehicles, etc. The most dominant background noise source is the towing carriage that generates noise from the low to medium (100 Hz to 1 kHz) frequency region due to the rolling noise of the wheels in the railways. The wheels also create vibrations that transfer through the carriage structure and the hydrophone frame. The flow around the hydrophones and their supporting frame also contribute to the background noise.

The background noise levels were measured from the **'Free Test.'** Only the acoustic frame without the model was tested to characterize the background noise. The tests were performed at eight different advanced speeds of the carriage, starting from 0.5 m/s to 1.75 m/s. To verify the quality of the measured data and reduce the contribution of the background noise, the background noise was estimated according to the following conditions:

a) Carriage at rest, before starting the tests at each test speed presented in **Table 3.5**;
b) Carriage moving at the advanced speed reported in **Table 3.5**, without ship model installed on the carriage.

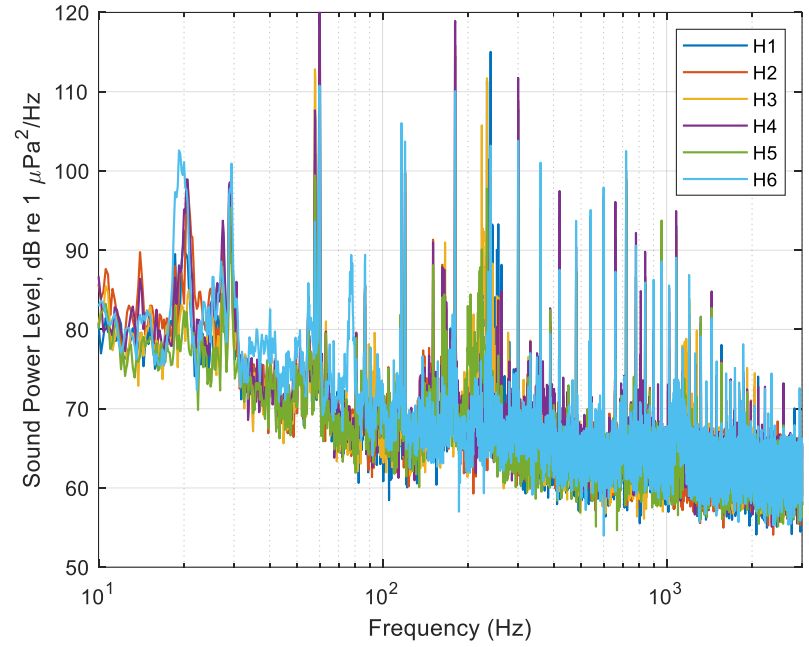


**Fig. 3.9**: Background Noise when the carriage at rest (not normalized)

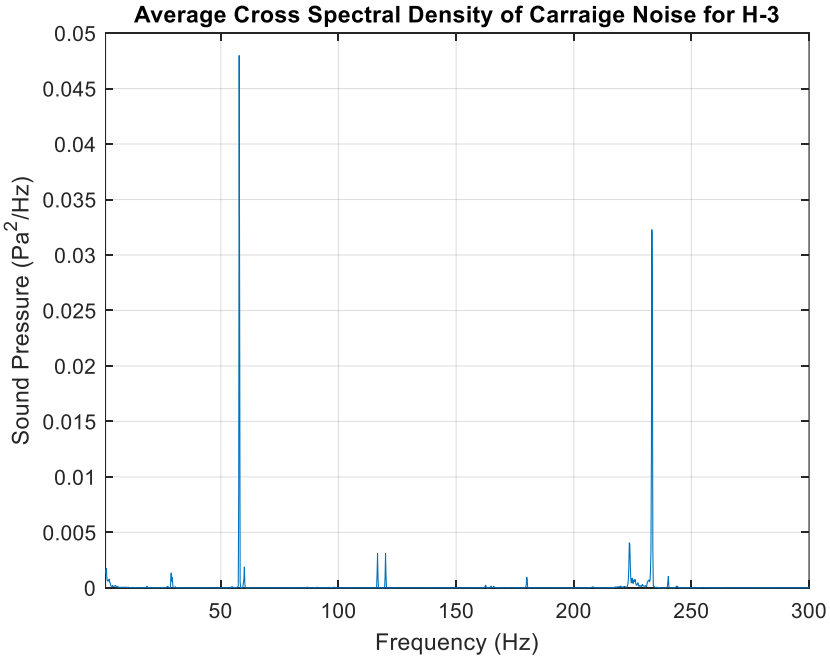


**Fig. 3.10**: Average cross-spectrum density (CSD) for H-3 (Carriage at rest)

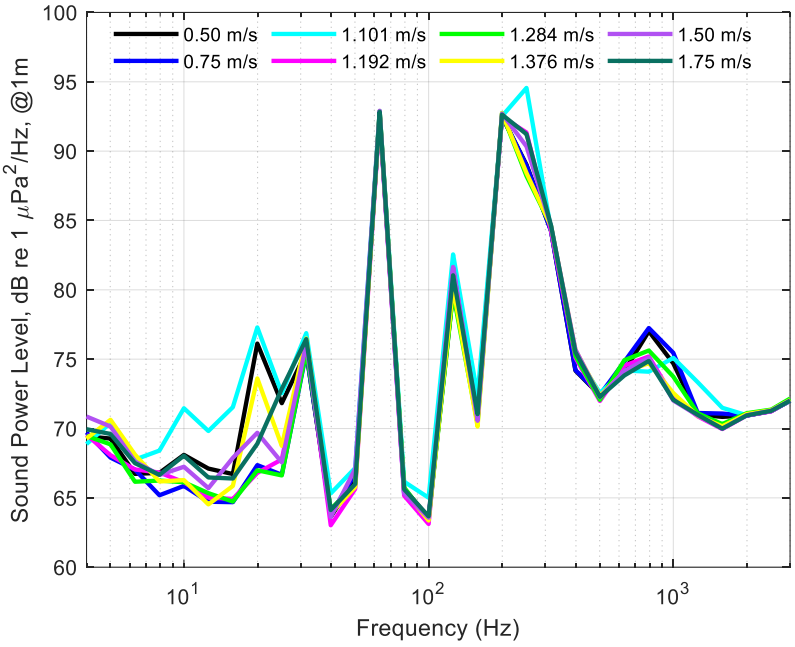


**Fig. 3.11**: Normalized average background noise (SPL) when the carriage is at rest before each test

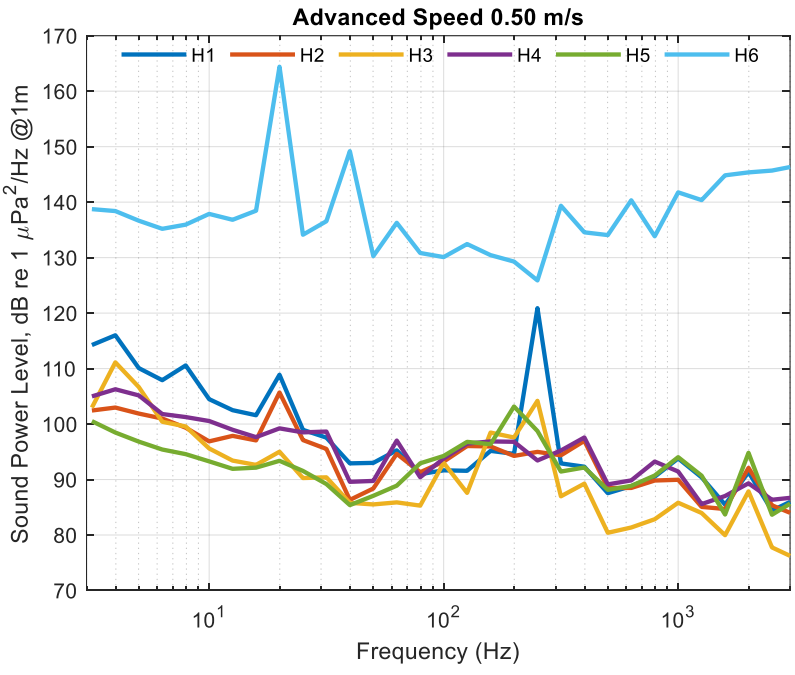


**Fig. 3.12:** Normalized background noise (SPL) at 0.50 m/s

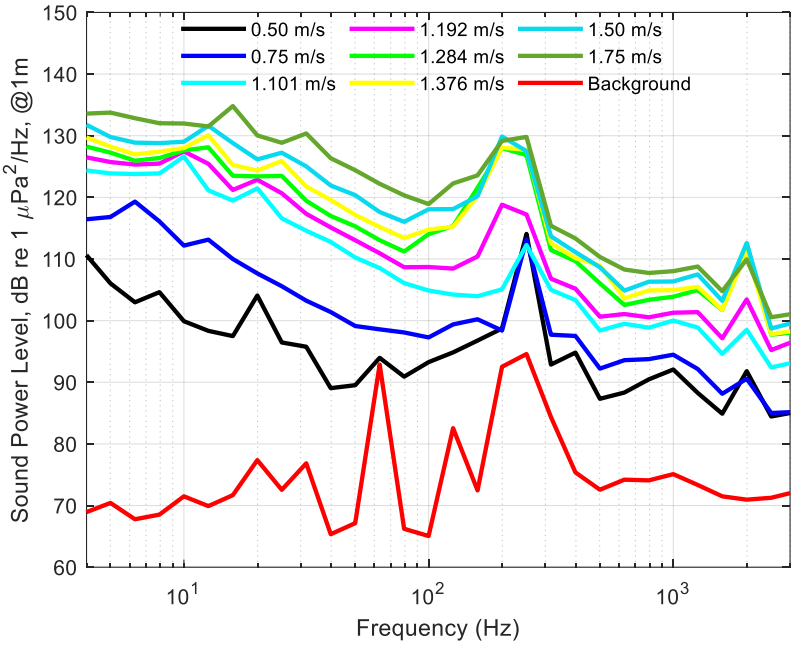


**Fig. 3.13**: Comparison of average background noise measured at test speeds and noise when carriage at rest (H-6 was neglected)

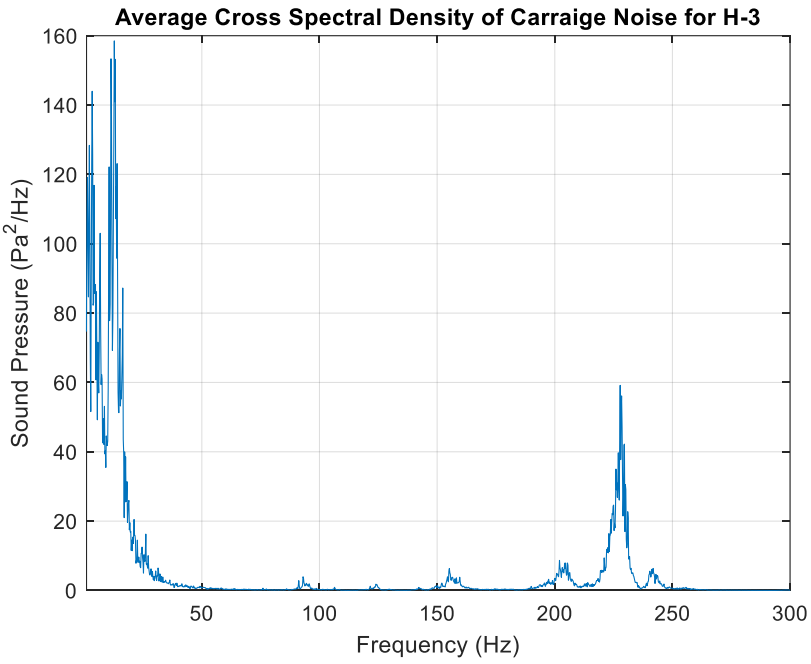


**Fig. 3.14:** Average cross-spectrum density (CSD) of background noise at different speeds for H-3

For accurate propeller noise measurement, a very low background noise level is required. Following the procedure mentioned in **Section 3.6**, the background noise levels are presented in the figures **Figures 3.9** to **3.14** for different advanced speeds. The hydrophone H-6 was very noisy compared to the other five hydrophones, and it increased with the advanced speed. The average of the noises recorded by five hydrophones (H-1 to H-5) was used to compare the carriage noise at different advanced speeds. **Figure 3.9** shows the background noise measured before each test when the carriage was at rest. It shows a steady-state background noise with tonal components as high as 115 dB at the fundamental frequency 60 Hz (electric hum noise) and its harmonics (120 Hz and 180 Hz). In other frequency bands, the background noise ranges between 85 dB and 95 dB. Cross-correlation (CSD) was used to check the similarities of the background tonal components for all possible combinations of eight towing speeds. **Figure 3.10** shows the average CSD spectrum for H-3. However, all the hydrophones show almost similar behaviour with more or fewer tonal lines. **Figure 3.12** represents the background noise generated by the carriage without the ship model at 0.50 m/s.

The results on the measurement of background noise analysis show that:

a) The far-field hydrophone (H6) data show tonal components at approximately 20 Hz and 40 Hz, which change in intensity and frequency as a function of the carriage speed. This suggests the presence of vortex-induced vibration that alter the data from this sensor;
b) The normalization of the background noise SPL indicates that the background noise level is homogenous in the neighbourhood of the frame structure supporting the hydrophones.

c) Background noise increases significantly when the carriage speed increases, and then the carriage motion is responsible for most of the background noise levels. **Figure 3.13** compares the background noise SPL (calculated by averaging the SPL measured by hydrophones H1 to H5) at different advanced speeds. H6 was not considered in the analysis because of the considerations at point 2. It proves the contribution of the carriage to the overall background noise.

d) **Figure 3.13** also compares the average background noise measured with the carriage at test advance speeds and average background noise with the carriage at rest. It is found that the carriage is the main contributor to the background noise and that the 120 Hz tonal component is predominant in all the measurements.

e) The CSD spectrum in **Figure 3.14** shows the correlation between tonal structures at eight different carriage advanced speeds. The discrete line obtained at 240 Hz was the noticeable frequency due to carriage, although the environment was noisy. In addition, 60 Hz electric hum noise and its multiples were present in the water. Therefore, a narrowband analysis is helpful to get essential characteristics of the propeller noise. The detailed analysis of background noise is presented in **Appendix B (B-1 to B-5).**

### 3.9.2 Resistance Tests

The resistances were conducted with the model, maintaining Froude's similarity. However, the propeller was replaced by a bare hub of the same weight during the resistance tests. The addition of the model in the experiments added hydrodynamic noise to the noise spectrum and dampened some vibration of the carriage at high advanced speeds.

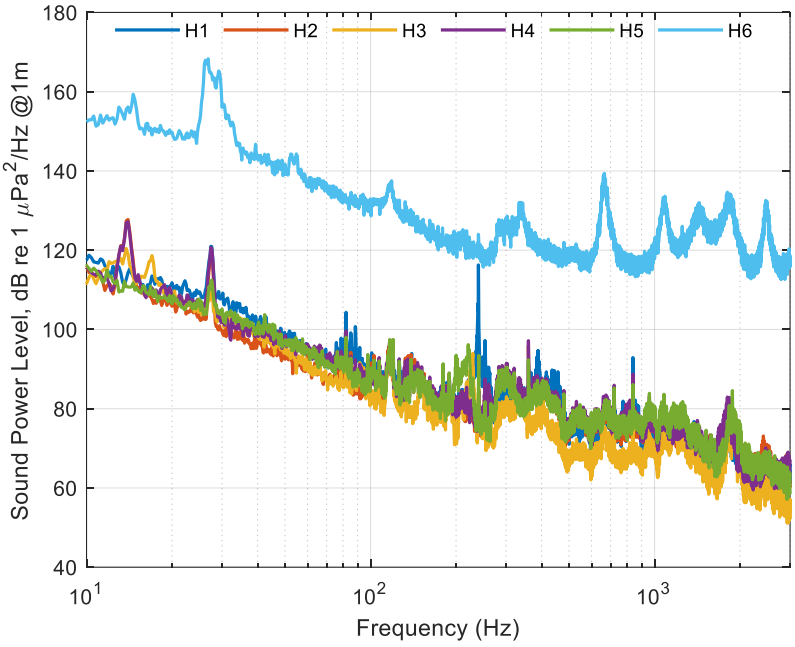


**Fig. 3.15:** Normalized narrowband (0.2 Hz) SPL during resistance test at 1.101 m/s

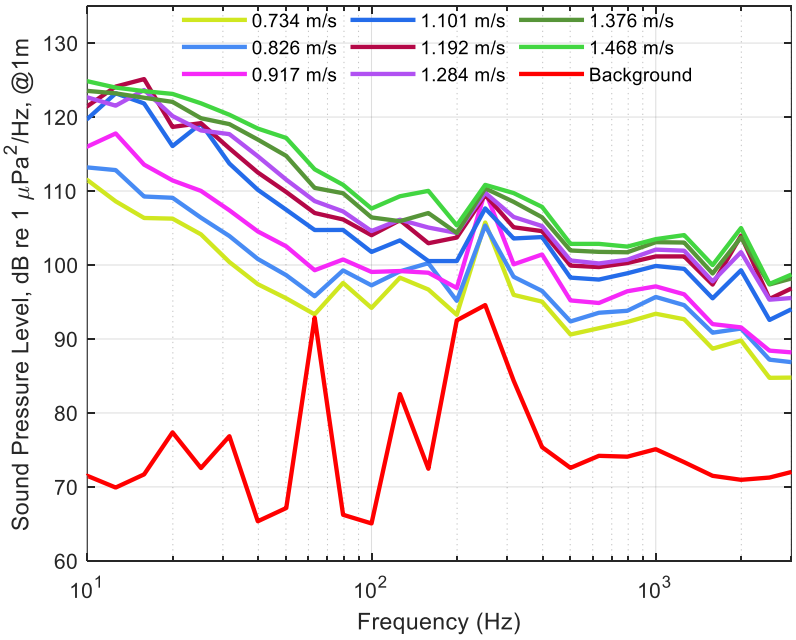


**Fig. 3.16**: Comparison of averaged SPL measured for different speeds during resistance tests and average background noise with the carriage at rest.

**Figures 3.15 to 3.16** show the SPL measured from these tests. The results from the resistant tests show that:

a. The resistance noise consists of broadband noise spectra all over the frequency domain without noticeable tonal components as expected. However, few pure tones exist in the spectrum, as shown in **Figure 3.15**, which is consistent with the carriage and background noise.
b. The far-field hydrophone (H6) records high noise levels due to the potential presence of vortex-induced vibrations, as in **Figure 3.15**. Therefore, it is neglected to calculate the average SPL from the test, as shown in Figure 51, to compare the results at different speeds.
c. **Figure 3.16** shows the results from the resistance test at different speeds. We notice that the noise level increases with the carriage's advanced speeds. Given the high background noise measured during the tests without model, we assume that the noise level from the carriage is dominant.
d. The tonal component at ~120Hz, which is present in all the recorded data, is unrelated to the test itself but a tonal component of the background noise.
**e.** **Figure 3.16** also compares the averaged SPL measured for different speeds during resistance tests and the average background noise with the carriage at rest. Besides a tonal component at 250 Hz, the sound power level is entirely due to the carriage, confirming the conclusions above. The results from all the resistance tests are included in the **Appendix-B (B-6).**

### 3.9.3 Self-Propulsion Tests

It is clear from the background and resistance tests that sound power level is greatly influenced by carriage, and it increases if the carriage speed increases. However, it is

necessary to analyze the contribution of propeller noise on the overall noise level. Therefore, the model is tested at self-propulsion rps regarding the advanced speeds and noise levels were measured. In the self-propulsion tests, the model was tested at speeds maintaining Froude similarity as for the full-scale ship and exactly the same as the resistance test. The effect of propeller speeds on the noise level is analyzed and compared with the background noise level. Noticeable changes in sound power level with varying speeds of the propeller were not found as expected. **Figures 3.17** to **3.18** present the SPL measured in the self-propulsion tests at different advanced speeds. **Figure 3.19** shows the averaged SPL (calculated as the average of the SPL from each hydrophone but H6) at different advance speeds, compared to the tow tank background noise.

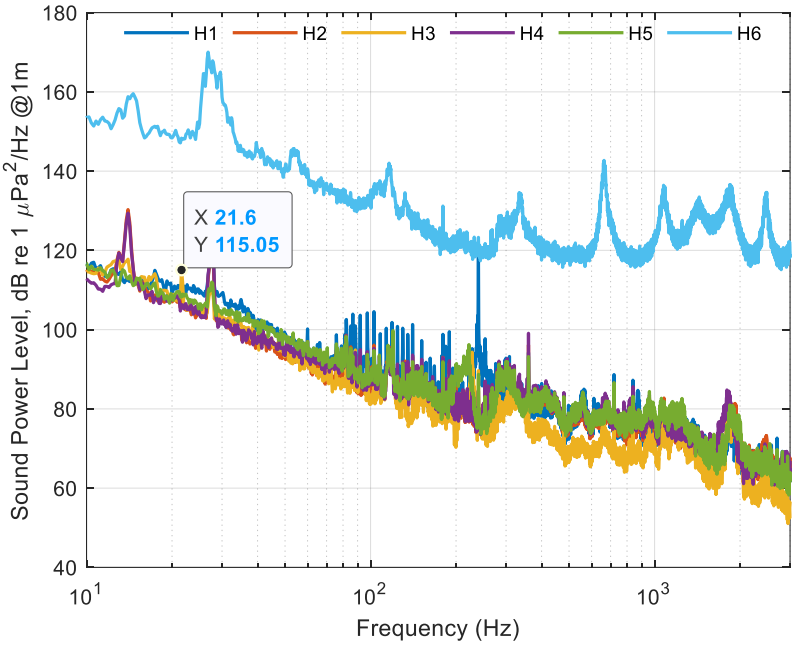


**Fig. 3.17:** SPL from self-propulsion test at 1.101 m/s with propeller speed 5.41 rps

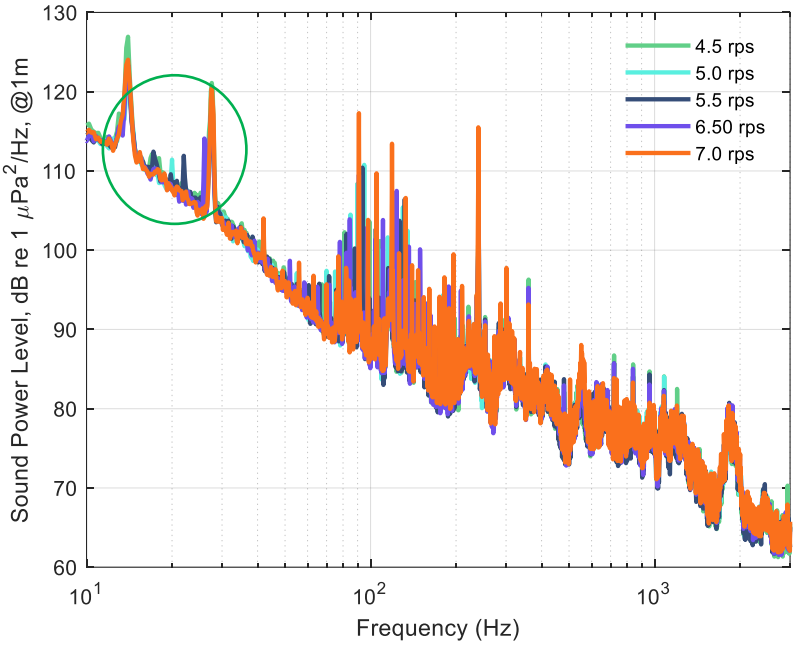


**Fig. 3.18:** Average SPL from self-propulsion test at 1.101 m/s with different propeller speed

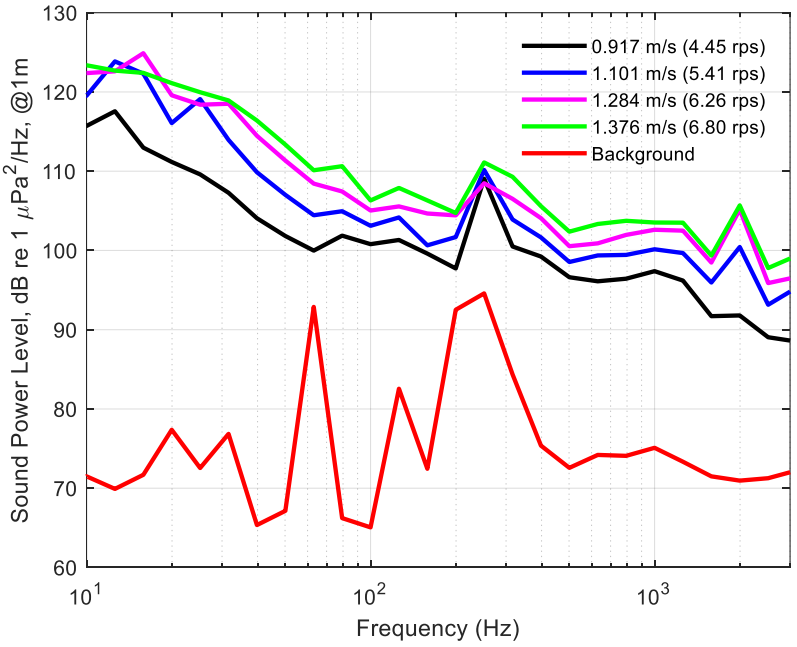


**Fig. 3.19:** Comparison of averaged SPL from Self-propulsion test at different advanced speeds with background noise (H-6 ignored)

a) As expected, the noise measured during the self-propulsion shows similarity to the resistance test for the same advanced speed except for the propeller BPF (21.6 Hz), as shown in **Figure 3.17**. The background tonal 13 Hz, 29 Hz, 240 Hz still existed in the self-propulsion tests.

b) The carriage noise highly influences the overall noise measurements and almost masks the propeller tonal BPF, as shown in **Figure 3.18**. Except for these low-frequency tonals between 10 to 100 Hz, the entire spectrum was dominated by broadband noise. This broadband noise could be generated due to the hydrodynamic or machinery noise along with carriage noise.

c) The narrowband analysis at least shows the propeller signature noise between the background tonals in the circle in **Figure 3.18**. However, the sound power level was much lower compared to background noise/carriage noise.

d) **Figure 3.19** shows the comparison between self-propulsion noises at different advanced speeds and background noise. The overall noise was 40 dB higher than the background noise at the low-frequency region (10 to 100 Hz) and no additional corrections were needed. The additional results from the self-propulsion tests are attached in the **Appendix B** (**B-7 to B-9**)

### 3.9.4 Bollard Pull Tests

Finally, bollard tests were performed to measure the propeller noise only at zero advance speed. The ship model, propeller and measuring equipment are usually the same as the self-propulsion test. Bollard test allows measuring propeller-induced noise only without the influence of the carriage noise. The bollard tests were performed at self-propulsion speeds, for example, 4.45 rps, 5.41 rps, 6.26 rps, and 6.80 rps. It allows observing the precise tonal frequencies corresponding to the blade passing frequencies

(BPF), at least until several BPFs. The results were again averaged for five hydrophones (H-1 to H-5) and compared with the background noise level. In addition, the noise level at a particular hydrophone (H-3) is also presented since it is close to the propeller and responds well at BPF. **Figures 3.20 to 3.22** show the URN (SPL) results measured from the bollard Pull tests at the propeller shaft speeds reported in **Table 3.5**. From the analysis of the Bollard Pull tests, the following conclusions can be made:

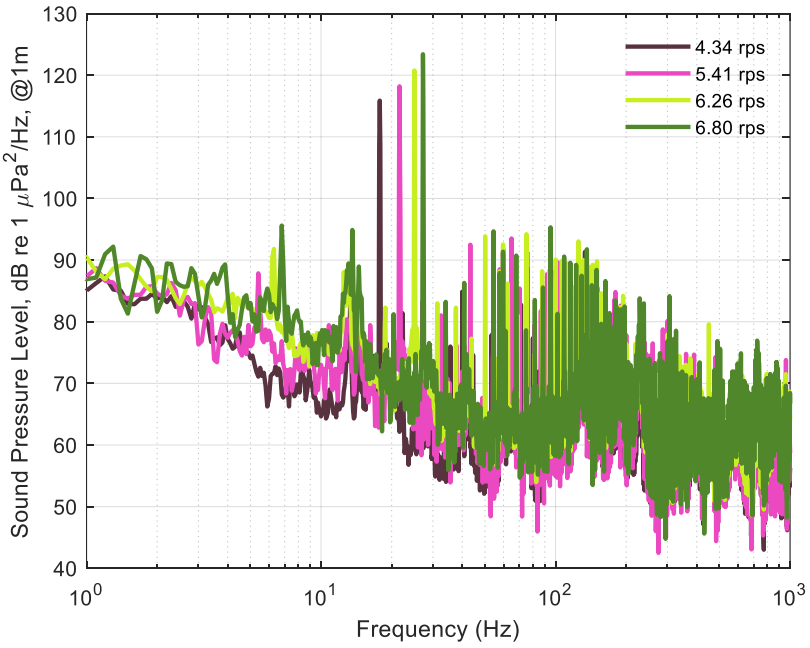


**Fig. 3.20:** SPL measured at H-3 from the bollard Pull test at tested rotational speeds (rps)

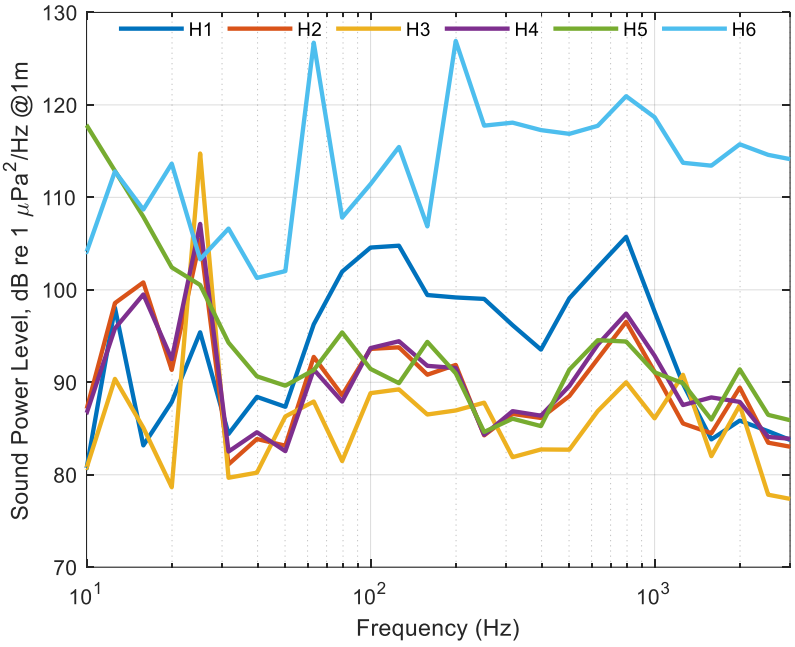


**Fig. 3.21:** 1/3 octave SPL from the bollard Pull test at 6.80 rps

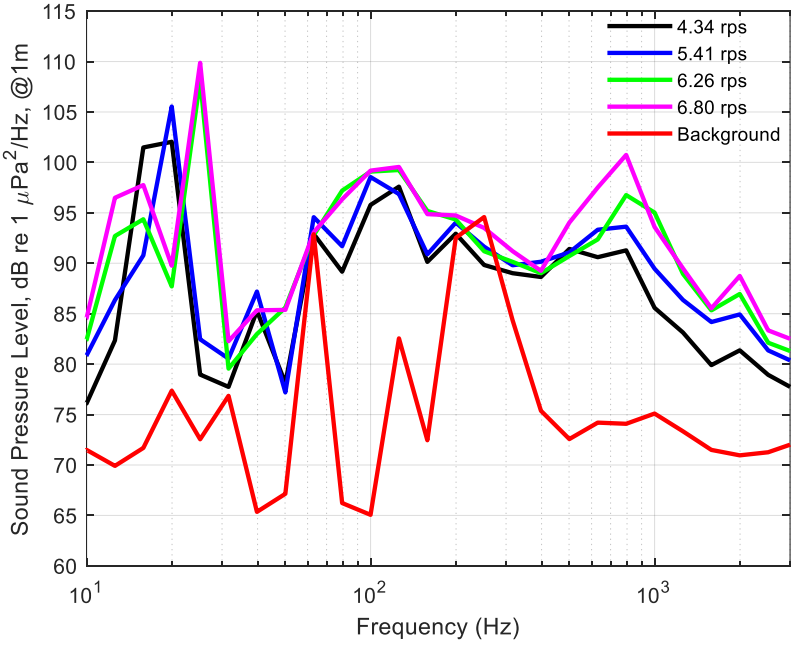


**Fig. 3.22:** Comparison of SPL from Bollard Pull test at different propeller-shaft speeds with Background noise

a) The equipment used to measure underwater radiated noise from a non-cavitating propeller can capture the noise from the propeller, as well as their fundamental excitation frequencies and harmonics, as shown in **Figure 3.20**.

b) As expected, the hydrophone measured the sound levels and fundamental excitation frequency from the propeller at low frequencies (BPF), where a non-cavitating propeller exactly generates the highest sound power.

c) **Figure 3.21** shows that the far-field hydrophone (**H-6**) cannot capture the sound generated from the propeller at high frequencies (i.e. harmonics above ~40Hz). The normalization clearly shows that the hydrophone captures background noise, while the closer hydrophones measure the noise radiated from the propeller.

**d)** **Figure 3.22** confirms the results from **Figure 3.20** as the background noise is about 20 dB lower between 10 Hz and 50 Hz. At higher frequencies, corrections should be used to evaluate the noise from the propeller, considering coherent sources contributing to the noise. Additional analysis of the bollard tests are presented in **Appendix B (B-10).**

### 3.9.5 Comparison of Noise Levels

All the experiments were performed to understand the contribution of the sources to the overall underwater noise measured during the tests. **Figures 3.23 to 3.25** show the SPL measured at tests done at the same advanced speed and propeller-shaft speed (bollard condition) in a 1/3 octave band. Hydrophone 6 (H-6) is neglected for the reasons presented above. The noise generated in the self-propulsion and resistance test was well above the background and propeller-only noise for the same model speeds. By these plots, it can be concluded that the measured noise is mostly coming from the carriage,

as the contribution from the propeller is narrowed to its fundamental frequency and its first harmonics.

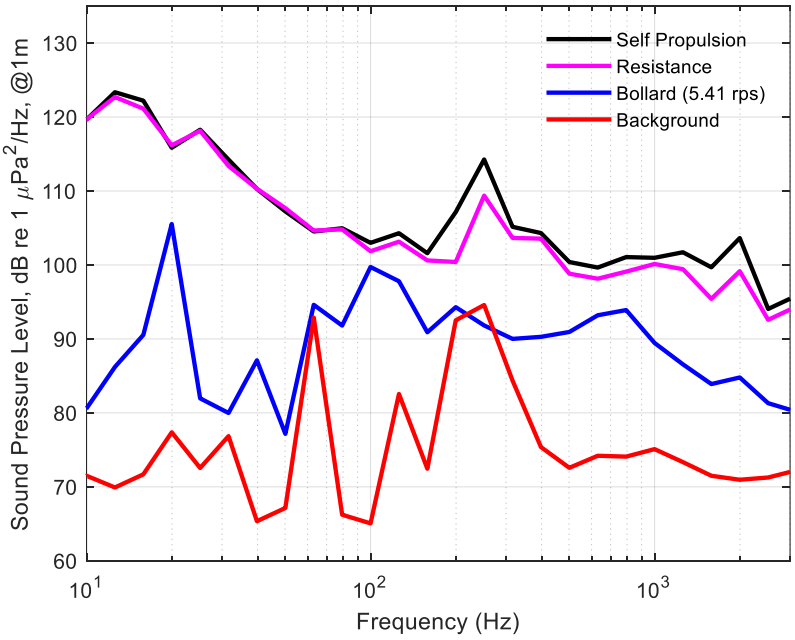


**Fig. 3.23:** Comparison of noise levels from different sources at 1.101 m/s

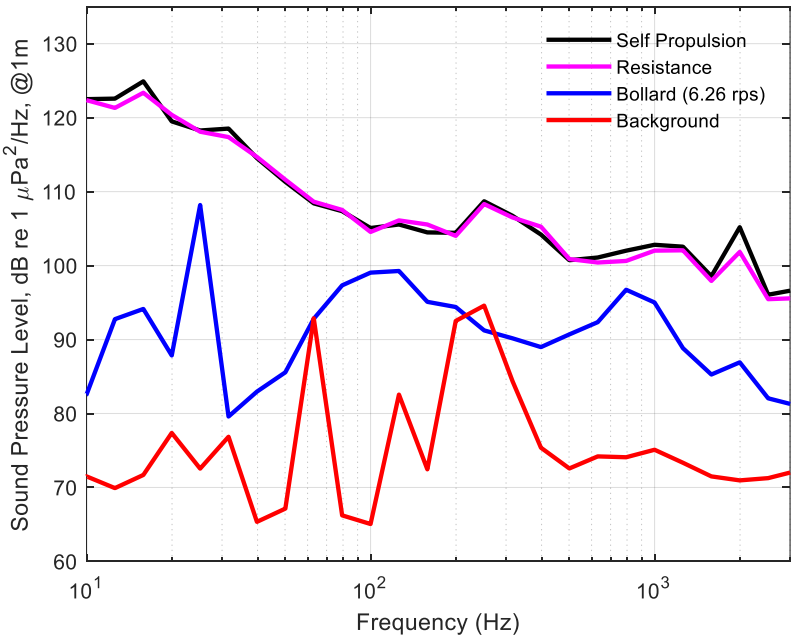


**Fig. 3.24:** Comparison of noise levels from different sources at 1.284 m/s

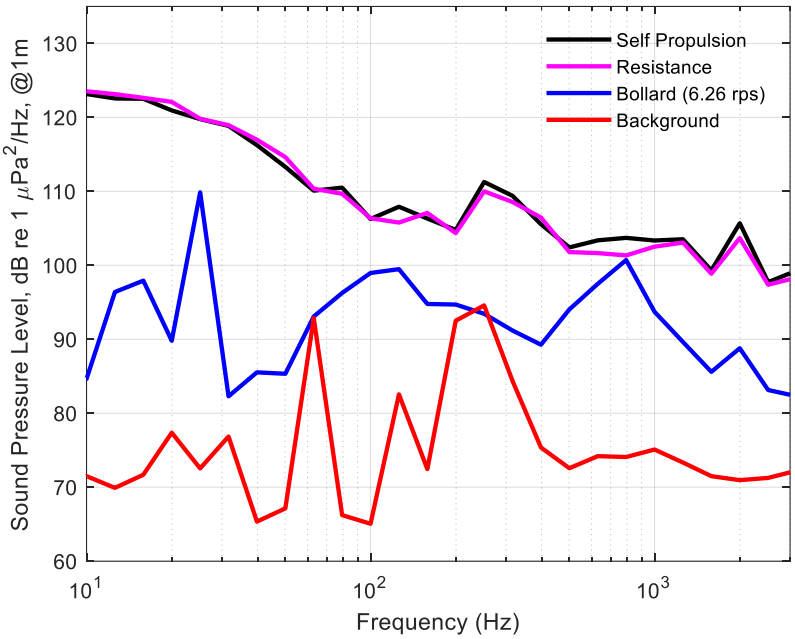


**Fig. 3.25**: Comparison of noise levels from different sources at 1.384 m/s

### 3.9.6 Narrowband Analysis

It is challenging to distinguish between propeller and hull noise from the background noise in a 1/3 octave band. However, narrow-band analysis allows observing the tonal components that separate propeller noise from the background noise.

**Figures 3.26 to 3.28** show some selected narrowband spectra of SPL calculated from the tests reported in **Table 3.5**. The narrowband spectra allow us to verify the effectiveness of the analysis procedure to provide information on the narrowband SPL generated by the propeller and verify the frequency components of background noise and other unwanted input sources. The results are normalized at 1m.

**Figure 3.26** shows the peaks related to the propeller fundamental frequency and its harmonics for the shaft speed at 6.80 rps and 5.41 rps in the bollard condition. These peaks are clearly not affected by the background noise, which is more than 30 dB lower

overall. The background noise (red curve) presents peaks at 60 Hz, 120 Hz, and 180 Hz. This confirms the broadband data presented in **Section 3.9.1**, and they are the frequencies that affect the quality of the measurements of SPL in most of the tests.

**Figure 3.27** shows the averaged SPL from the self-propulsion test (advanced speed 1.376 m/s with 6.80 rps), bollard pull test at 6.80 rps, and background noise. In this case, the peaks of the background noise were not affecting the averaged SPL from the self-propulsion test. The propeller peaks were clearly identifiable in the SPL spectra of the self-propulsion test, and they correspond to the frequencies identified in the correspondent bollard test. Some of the peaks, especially those corresponding to the first harmonics, were not visible, as they are likely covered by the broadband noise generated by the carriage.

**Figure 3.28** shows the narrowband SPL spectra from the self-propulsion test (advanced speed 1.101 m/s with 5.41 rps), resistance test (advanced speed 1.101 m/s), and background noise with a carriage at rest. The results show the fundamental frequency of the propeller, but it also presents some peaks at frequencies different than the fundamental frequency or its harmonics.

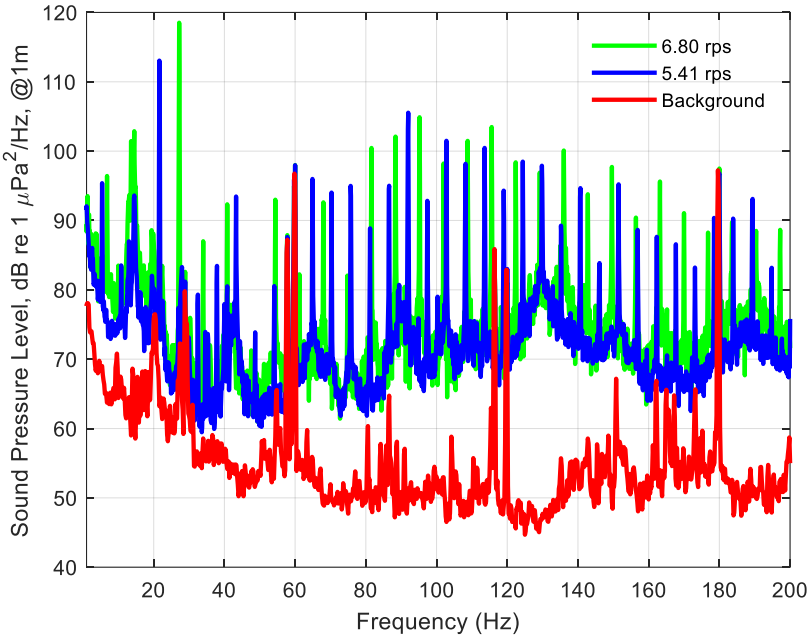


**Fig. 3.26:** Averaged SPL from Bollard pull test at 6.80 rps, 5.41 rps, and background noise.

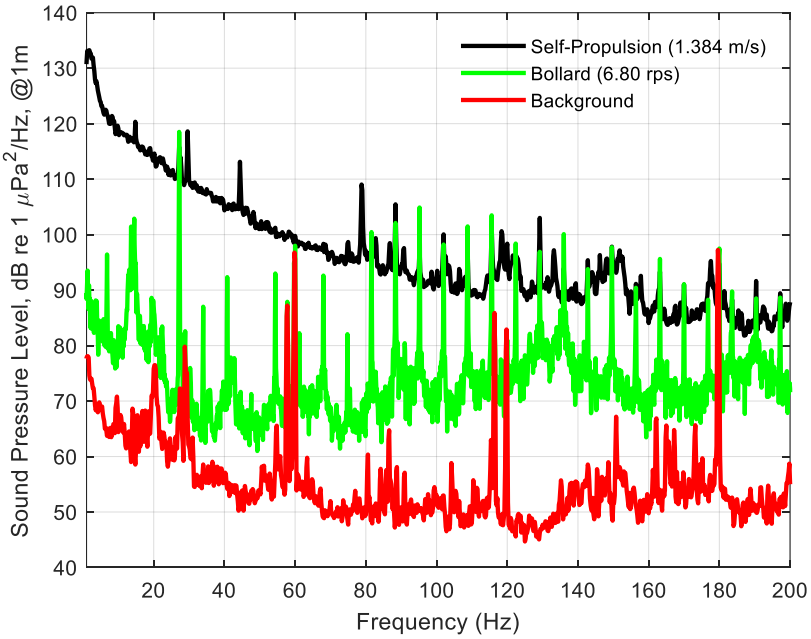


**Fig. 3.27**: Averaged SPL from self-propulsion test, bollard pull test at, and background noise.

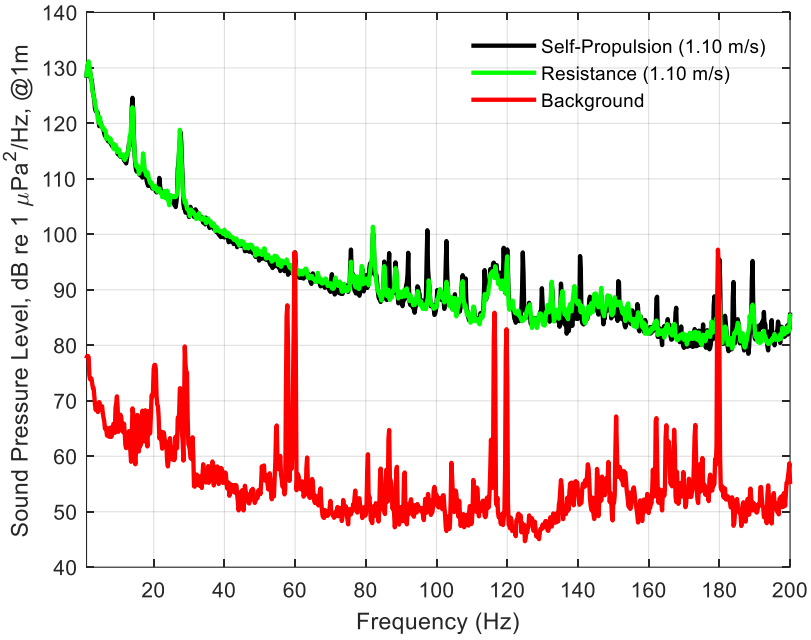


**Fig. 3.28:** Comparison of self-propulsion, resistance, and background noise at 1.10 m/s

### 3.9.7 Effect of Llyod's Mirror on Overall Noise

As discussed in **Section 3.4**, the free surface of the tank affects the accurate propeller-induced noise measurement. As shown in Fig. 7, Llyod's mirror effects depend on the distance between the source and the hydrophone. The effect of free surface on overall noise is significant at the low-frequency range below 1000 Hz. In this analysis, H-6 is neglected, and the noise level was averaged for five hydrophones. The Llyod's mirror effects for 5 hydrophones were calculated in 1/3 octave band. **Figure 3.29** shows the effect of Lloyd mirror correction on SPL measurement for self-propulsion at 1.101 m/s. The correction increases the noise level by 2 dB for frequency below 300 Hz. However, the effect can be neglected at a higher frequency. Similarly, **Figure 3.30** shows the SPL before and after applying the correction for the bollard test at 6.80 rps. The changes in noise level were not significant with the Llyod's mirror correction.

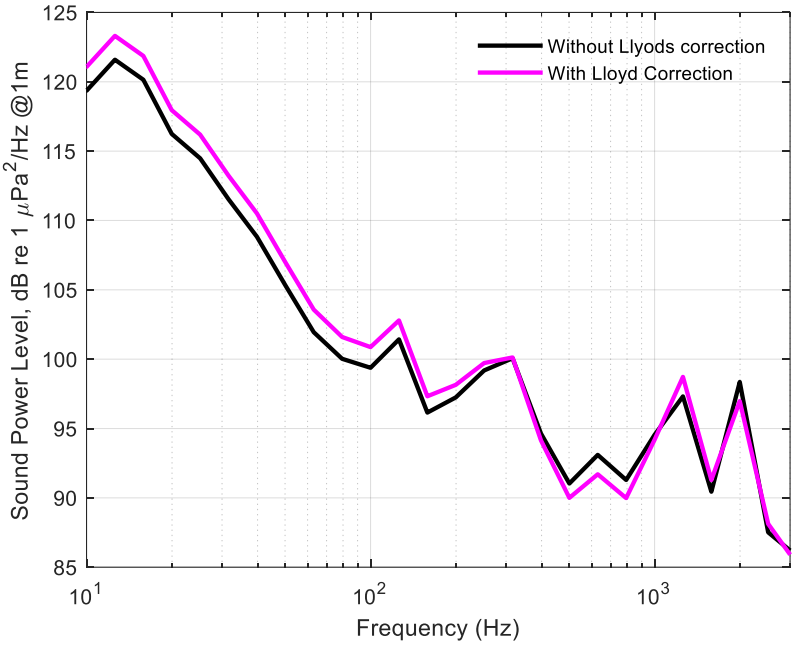


**Fig. 3.29:** Effect of Lloyd mirror correction on SPL measurement for self-propulsion at 1.101 m/s

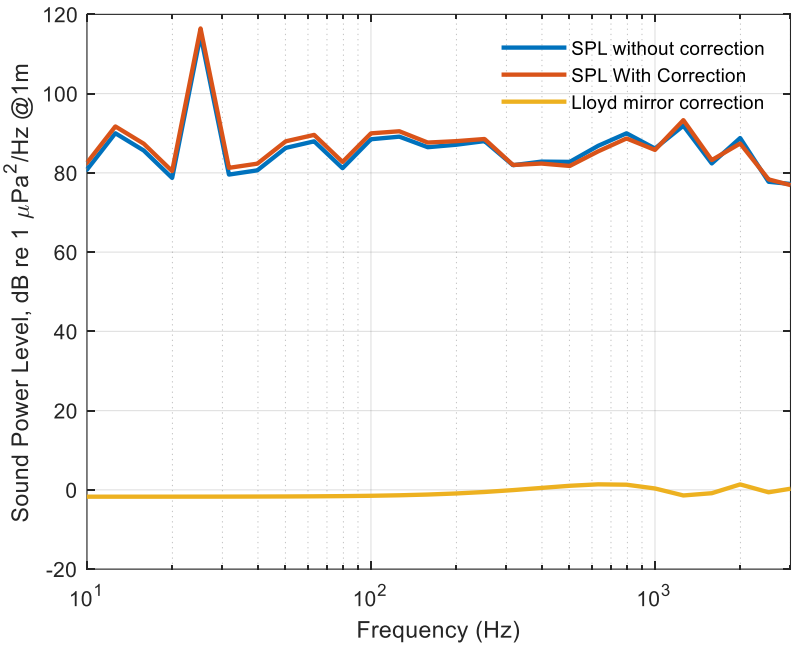


**Fig. 3.30:** Effect of Lloyd mirror correction on SPL measurement for bollard test at 6.80 rps

### 3.9.8 Dimensionless Pressure Descriptor

The measurements for the power spectral density at the conditions widely expressed in dimensionless pressure descriptor $\boldsymbol{LK_p}$ by using Eq. (4.16) for model scale noise analysis. **Figure 3.31** shows the comparison of $LK_p$ level for different tests at advanced speed 1.101 m/s. The peak noise level was 50 dB for bollard condition at 5.41 rps while 65 dB for resistance and self-propulsion tests. **Figure 3.32** compares the narrowband $LK_p$ level for different bollard rps.

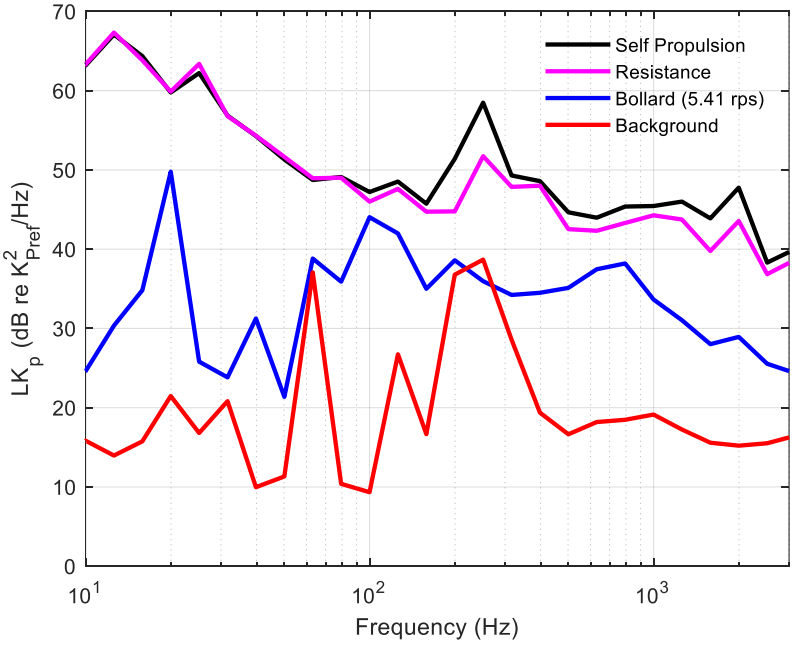


**Fig. 3.31**: Comparison of 1/3 octave $LK_p$ SPL level for advanced speed 1.101 m/s.

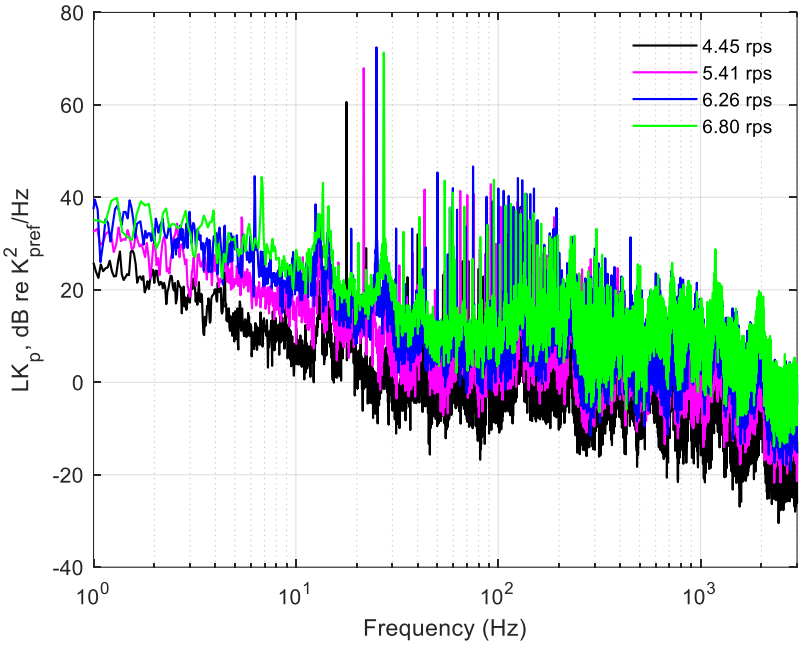


**Fig. 3.32**: Comparison of narrowband $LK_p$ SPL level for different bollard rps

## 3.10 Conclusions

From the analysis of the URN from these tests, the following conclusions could be made:

a) The background noise of the tow tank is generally low, except for three frequencies at 60 Hz, 120 Hz, and 180 Hz, which affect the underwater radiated noise measurements in narrowband and in broadband.

b) The bollard pull test provides good results. The URN from the propeller is above the background noise, and the propeller frequencies are clearly identifiable (except for high-frequency harmonics that correspond to the background noise frequencies of point 1).

c) The noise generated by the carriage is affecting the SPL measurements in the resistance test and in the self-propulsion test. The narrowband analysis of the

latter shows that the first harmonics of the propeller are present and above the background noise levels. Non-cavitating propellers are generally quieter than cavitating propellers, and their noise is narrowband. Consequently, the measurements of their URN require remarkably silent configurations. By comparing the background noise of the carriage with those presented in another study on this topic [29], we can notice that the noise of the carriage is comparable to the noise of the carriage used by the authors of that study. Consequently, it is suggested that the noise levels will be analyzed in narrowband rather than in broadband to capture the nature of the URN from the non-cavitating propeller.

d) Hydrophone 6 provides reliable results when measuring the background noise of the tow tank. In all the other tests, it has demonstrated that it does not measure the URN from the propeller for the following reasons: i) In the bollard test, the normalization of the SPL showed that the hydrophone is not providing reliable results, as it is outside the critical radius of the tank, ii) in the self-propulsion test and in the resistance test, the measurements from this hydrophone show low-frequency components that are likely to be related to vortex-induced vibrations.

Further tests are needed to understand: i) the influence of the motor on the measured SPL, in bollard tests and in self-propulsion tests; ii) the influence of rps on the overall URN; even though the propeller is non-cavitating, tests at high rps will allow us to understand if the formation of cavitation will increase the URN from this source when compared to the background noise, and identify the boundaries of the tests of URN at NRC-OCRE.

# Chapter 4

# Conclusions and Future Recommendations

## 4.1 Conclusions

Aquatic noise pollution and related research work get much attention nowadays to save ocean life and marine biodiversity. Ship radiated underwater noise is the dominant noise source. Therefore, proper assessment and measurement of the propeller-induced noise are necessary to develop any regulations to protect the marine environment.

The propeller-induced non-cavitating noise is generally measured in a towing tank. Acoustic measurements made in such tanks suffer from the effects of reverberation. The research assessed the reverberation characteristics of a tank to analyze the impact of wall reflections and free surface influence on noise measurement. The study considered both the experimental and numerical techniques to determine the reverberation time. The experiments were conducted in a small deep tank (48 $m^3$) with an impulse of white noise driven by a projector at a frequency range of 500 Hz to 16000 Hz. The acoustic response of the tank was recorded for five different hydrophone configurations. The reverberation time is then measured at 1/3 octave frequencies for each hydrophone configuration. The fundamental acoustic characteristics like sound absorption coefficient, critical frequency, and reverberation radius are calculated using modal acoustic theories.

A numerical ray-tracing model is also developed in the COMSOL software to predict the reverberation time of the same deep tank. The numerical results showed excellent

agreement with the experimental results. The validated ray-tracing model is then used to characterize the large NRC tank.

The analysis showed that the noise measurement is free from the wall reflection near the source, i.e., inside the reverberation radius. However, the effect of free surface reflections is found in the impulse response, and the influence of the free surface is needed to be corrected during acoustic measurements. However, if the receiver is just below the source, the free surface effect is negligible. A procedure to correct the free surface effect is also developed based on Llyod's mirror theory. The correction removes the interference pattern of any point source under a free surface from the measured sound level. The proper knowledge of acoustic properties and correction for the free surface could give an equivalent free field condition for any underwater acoustic experiment in the towing tank facility.

Once the reverberation characteristics of the NRC tank were determined, an experimental procedure was developed to measure underwater radiated noise from a non-cavitating propeller in an atmospheric tank. Model testing was performed with a 7m long model to estimate the propeller-induced noise in non-cavitating conditions. The propeller noise was measured at different operating conditions with six hydrophones. H-1 to H-5 was placed inside the direct field while the H-6 was in the reverberate field. A MatLab program is also developed to analyze the results both in narrow and 1/3 octave bands. The sound power level of the noise is estimated to assess propeller-generated noise. The results are also analyzed with a dimensionless acoustic descriptor. The overall noise measurement is heavily affected by the carriage and background noise. However, bollard tests give reliable results for propeller-induced noise. It is found that the background noise of the tow tank is generally low, except for

three frequencies at 60 Hz, 120 Hz, and 180 Hz, which affect the underwater radiated noise measurements in narrowband and in broadband. In bollard conditions, the URN from the propeller is above the background noise, and the propeller frequencies are identifiable. For both resistance and self-propulsion tests, carriage noise directly affects the SPL measurements. The narrowband analysis shows that the first harmonics of the propeller are present and above the background noise levels in self-propulsion tests. The reverberant field hydrophone (H-6) provides reliable results when measuring the background noise of the tow tank. However, for other tests, it does not measure the URN from the propeller since it is outside the reverberation radius and low-frequency vortex-induced vibrations at advanced high speed.

## 4.2 Limitations

a. In this study, acoustic reverberation characteristics of a towing tank have been investigated for the high-frequency range 630 Hz to 12500 Hz. A low-frequency (<200 Hz) characterization is necessary for propeller-induced noise (<100 Hz) measurements in a facility.

b. Non-cavitating propellers are generally quieter than cavitating propellers, and the measurements of their URN require remarkably silent configurations. The background and carriage noises are too loud at high advancing speeds. Therefore, it is difficult to get reliable results.

## 4.3 Recommendations for Future Works

a. It is necessary to extend the experimental study further to characterize the low-frequency (< 200 Hz) response of the towing tank. A good sound projector with a linear response at low frequency will be helpful to perform the analysis. A finite element model can be developed for a low-frequency acoustic response.

b. The carriage induces a high noise level in the measurements. The model testing for noise measurement should be conducted with a silent carriage. A detailed design of quiet carriage design should be performed. However, as general guidelines provided by our results, the carriage needs a coupling system from the tank to minimize structure-borne noise transmitted to water. It can be achieved either by using rubber wheels or rubber mounts that couple the carriage structure from the hydrophone supporting frame. In addition, the background noise sources should be kept as low as possible during the experiments.

c. Further tests are needed to understand: i) the influence of the motor on the measured SPL, in bollard tests and self-propulsion tests; ii) the influence of propeller speed on the overall URN; even though the propeller is non-cavitating, tests at high rps will provide information regarding the cavitation formation and increase in the URN from this source when compared to the background noise, and identify the maximum propeller speeds in the tests of URN at NRC-OCRE.

**Works Cited**


[1] E. Di Franco *et al.*, "Effects of marine noise pollution on Mediterranean fishes and invertebrates: A review," *Marine Pollution Bulletin*, vol. 159, p. 111450, Oct. 2020, doi: 10.1016/j.marpolbul.2020.111450.

[2] C. Erbe, R. Dunlop, and S. Dolman, "Effects of Noise on Marine Mammals," in *Effects of Anthropogenic Noise on Animals*, H. Slabbekoorn, R. J. Dooling, A. N. Popper, and R. R. Fay, Eds. New York, NY: Springer, 2018, pp. 277–309. doi: 10.1007/978-1-4939-8574-6_10.

[3] G. Nabi *et al.*, "The possible effects of anthropogenic acoustic pollution on marine mammals' reproduction: an emerging threat to animal extinction," *Environ Sci Pollut Res*, vol. 25, no. 20, pp. 19338–19345, Jul. 2018, doi: 10.1007/s11356-018-2208-7.

[4] S. B. Blackwell and A. M. Thode, "Chapter 35 - Effects of noise," in *The Bowhead Whale*, J. C. George and J. G. M. Thewissen, Eds. Academic Press, 2021, pp. 565–576. doi: 10.1016/B978-0-12-818969-6.00035-2.

[5] C. Peng, X. Zhao, and G. Liu, "Noise in the Sea and Its Impacts on Marine Organisms," *Int J Environ Res Public Health*, vol. 12, no. 10, pp. 12304–12323, Oct. 2015, doi: 10.3390/ijerph121012304.

[6] W. D. Halliday, S. J. Insley, R. C. Hilliard, T. de Jong, and M. K. Pine, "Potential impacts of shipping noise on marine mammals in the western Canadian Arctic," *Marine Pollution Bulletin*, vol. 123, no. 1, pp. 73–82, Oct. 2017, doi: 10.1016/j.marpolbul.2017.09.027.

[7] E. Chou, B. L. Southall, M. Robards, and H. C. Rosenbaum, "International policy, recommendations, actions and mitigation efforts of anthropogenic underwater noise," *Ocean & Coastal Management*, vol. 202, p. 105427, Mar. 2021, doi: 10.1016/j.ocecoaman.2020.105427.

[8] G. V. Frisk, "Noiseonomics: The relationship between ambient noise levels in the sea and global economic trends," *Sci Rep*, vol. 2, no. 1, p. 437, Jun. 2012, doi: 10.1038/srep00437.

[9] National Research Council, *Ocean Noise and Marine Mammals*. Washington, DC: The National Academies Press, 2003. doi: 10.17226/10564.

[10] M. André *et al.*, “Best practices in management, assessment and control of underwater noise pollution,” Jun. 2009, Accessed: Aug. 29, 2021. [Online]. Available: https://recercat.cat//handle/2072/227591

[11] J. A. Hildebrand, “Anthropogenic and natural sources of ambient noise in the ocean,” *Marine Ecology Progress Series*, vol. 395, pp. 5–20, Dec. 2009, doi: 10.3354/meps08353.

[12] L. Bittencourt, M. Barbosa, T. L. Bisi, J. Lailson-Brito, and A. F. Azevedo, “Anthropogenic noise influences on marine soundscape variability across coastal areas,” *Marine Pollution Bulletin*, vol. 160, p. 111648, Nov. 2020, doi: 10.1016/j.marpolbul.2020.111648.

[13] R. L. Putland, N. D. Merchant, A. Farcas, and C. A. Radford, “Vessel noise cuts down communication space for vocalizing fish and marine mammals,” *Global Change Biology*, vol. 24, no. 4, pp. 1708–1721, 2018, doi: 10.1111/gcb.13996.

[14] M. L. Lancaster, P. Winsor, and A. Dumbrille, “Underwater Noise from Shipping: A Special Case for the Arctic,” in *Sustainability in the Maritime Domain: Towards Ocean Governance and Beyond*, A. Carpenter, T. M. Johansson, and J. A. Skinner, Eds. Cham: Springer International Publishing, 2021, pp. 271–289. doi: 10.1007/978-3-030-69325-1_14.

[15] B. Aktas *et al.*, “Propeller cavitation noise investigations of a research vessel using medium size cavitation tunnel tests and full-scale trials,” *Ocean Engineering*, vol. 120, pp. 122–135, Jul. 2016, doi: 10.1016/j.oceaneng.2015.12.040.

[16] “Review of the Maritime Transport_ Structure, Ownership and Registration of the World Fleet (2017).” Accessed: Aug. 25, 2021. [Online]. Available: https://unctad.org/system/files/official-document/rmt2017ch2_en.pdf

[17] M. A. McDonald, J. A. Hildebrand, and S. M. Wiggins, “Increases in deep ocean ambient noise in the Northeast Pacific west of San Nicolas Island, California,” *The Journal of the Acoustical Society of America*, vol. 120, no. 2, pp. 711–718, Aug. 2006, doi: 10.1121/1.2216565.

[18] D. Wittekind and M. Schuster, “Propeller cavitation noise and background noise in the sea,” *Ocean Engineering*, vol. 120, pp. 116–121, Jul. 2016, doi: 10.1016/j.oceaneng.2015.12.060.

[19] R. J. Urick, “Principles of underwater sound - 2. ed.,” New York, N.Y. (USA) McGraw-Hill Book, 1975.

[20] T. Yang, L. Wu, X. Li, M. Zhu, M. J. Brennan, and Z. Liu, “Active Vibration Isolation of a Diesel Generator in a Small Marine Vessel: An Experimental Study,” *Applied Sciences*, vol. 10, no. 9, Art. no. 9, Jan. 2020, doi: 10.3390/app10093025.

[21] P. Kellett, O. Turan, and A. Incecik, “A study of numerical ship underwater noise prediction,” *Ocean Engineering*, vol. 66, pp. 113–120, Jul. 2013, doi: 10.1016/j.oceaneng.2013.04.006.

[22] C. Park, G. D. Kim, G.-T. Yim, Y. Park, and I. Moon, “A validation study of the model test method for propeller cavitation noise prediction,” *Ocean Engineering*, vol. 213, p. 107655, Oct. 2020, doi: 10.1016/j.oceaneng.2020.107655.

[23] “Final Report and Recommendations to the 28th ITTC.” Accessed: Jan. 22, 2022. [Online]. Available: https://www.ittc.info/media/7837/17-sc-hydrodynamic-noise-compressed.pdf

[24] Bosschers, J., Lafeber, F.H., de Boer, J., Bosman, R., and Bouvy, A, “Underwater radiated noise measurements with a silent towing carriage in the depressurized wave basin,” presented at the 3rd International Conference on Advanced Model Measurement Technology for the EU Maritime Industry, Gdansk, Poland, Aug. 2013.

[25] R. Rosli, W. Shi, B. Aktas, R. Norman, and M. Atlar, “Cavitation observations, underwater radiated noise measurements and full-scale predictions of the Hydro-Spinna turbine,” *Ocean Engineering*, vol. 210, p. 107536, Aug. 2020, doi: 10.1016/j.oceaneng.2020.107536.

[26] C. Audoly *et al.*, “Mitigation of Underwater Radiated Noise Related to Shipping and Its Impact on Marine Life: A Practical Approach Developed in the Scope of AQUO Project,” *IEEE Journal of Oceanic Engineering*, vol. 42, no. 2, pp. 373–387, Apr. 2017, doi: 10.1109/JOE.2017.2673938.

[27] H. Bailey, B. Senior, D. Simmons, J. Rusin, G. Picken, and P. M. Thompson, “Assessing underwater noise levels during pile-driving at an offshore windfarm and its potential effects on marine mammals,” *Marine Pollution Bulletin*, vol. 60, no. 6, pp. 888–897, Jun. 2010, doi: 10.1016/j.marpolbul.2010.01.003.

[28] N. Rako-Gospić and M. Picciulin, “Chapter 20 - Underwater Noise: Sources and Effects on Marine Life,” in *World Seas: an Environmental Evaluation (Second Edition)*, C. Sheppard, Ed. Academic Press, 2019, pp. 367–389. doi: 10.1016/B978-0-12-805052-1.00023-1.

[29] H. Haimov, V. Gallego, E. Molinelli, and B. Trujillo, “Propeller acoustic measurements in atmospheric towing tank,” *Ocean Engineering*, vol. 120, pp. 190–201, Jul. 2016, doi: 10.1016/j.oceaneng.2015.06.047.

[30] P. H. Rogers, A. D. Hawkins, A. N. Popper, R. R. Fay, and M. D. Gray, “Parvulescu Revisited: Small Tank Acoustics for Bioacousticians,” *Adv Exp Med Biol*, vol. 875, pp. 933–941, 2016, doi: 10.1007/978-1-4939-2981-8_115.

[31] H. Way, P. Joseph, S. Turnock, R. Leung, and V. Humphrey, “Acoustic characterisation of towing tanks,” *Ocean Engineering*, vol. 220, p. 108338, Jan. 2021, doi: 10.1016/j.oceaneng.2020.108338.

[32] R. Boucheron, “About acoustic field characteristics in the test section of a cavitation tunnel,” *Ocean Engineering*, vol. 211, p. 107616, Sep. 2020, doi: 10.1016/j.oceaneng.2020.107616.

[33] S.-K. Lau and E. A. Powell, “Effects of absorption placement on sound field of a rectangular room: A statistical approach,” *Journal of Low Frequency Noise, Vibration and Active Control*, vol. 37, no. 2, pp. 394–406, Jun. 2018, doi: 10.1177/1461348418780027.

[34] H. Nélisse and J. Nicolas, “Characterization of a diffuse field in a reverberant room,” *The Journal of the Acoustical Society of America*, vol. 101, no. 6, pp. 3517–3524, Jun. 1997, doi: 10.1121/1.418313.

[35] E. Accolti and F. di Sciascio, “Room acoustics: Idealized field and real field considerations,” *Proc. Mtgs. Acoust.*, vol. 31, no. 1, p. 015003, Dec. 2017, doi: 10.1121/2.0000795.

[36] J. van der Kooij and A. Bruijn, “Acoustic measurements in the NSMB depressurized towing tank,” *International Shipbuilding Progress*, vol. 31, no. 353, pp. 13–23, Jan. 1984, doi: 10.3233/ISP-1984-3135302.

[37] L. L. Beranek and T. J. Mellow, “Chapter 10 - Sound in enclosures,” in *Acoustics: Sound Fields and Transducers*, L. L. Beranek and T. J. Mellow, Eds. Academic Press, 2012, pp. 449–479. doi: 10.1016/B978-0-12-391421-7.00010-5.

[38] N. Cochard, J. L. Lacoume, P. Arzelies, and Y. Gabillet, “Underwater acoustic noise measurement in test tanks,” *IEEE Journal of Oceanic Engineering*, vol. 25, no. 4, pp. 516–522, Oct. 2000, doi: 10.1109/48.895359.

[39] V. Trinh, L. Chen, and J. Forrest, “Free-Field Acoustic Source Levels from Measurements conducted in a Water Tank,” *Australian Acoustical Society*, vol. 1, 2018, [Online]. Available: https://acoustics.asn.au/conference_proceedings/AAS2018/

[40] F. H. Lafeber, J. Bosschers, F. Graafland, and C. Jong, “Acoustic Reverberation Measurements in the Depressurized Wave Basin,” presented at the Advanced Model Measurement Technology for the Maritime Industry (AMT’15), Istanbul, Turkey, Sep. 2015.

[41] G. C. Eastland and W. C. Buck, “Reverberation characterization inside an anechoic test chamber at the Weapon Sonar Test Facility at NUWC Division Keyport,” *Proc. Mtgs. Acoust.*, vol. 26, no. 1, p. 030003, May 2016, doi: 10.1121/2.0000508.

[42] G. Tani, M. Viviani, M. Ferrando, and E. Armelloni, “Aspects of the measurement of the acoustic transfer function in a cavitation tunnel,” *Applied Ocean Research*, vol. 87, pp. 264–278, Jun. 2019, doi: 10.1016/j.apor.2019.02.017.

[43] A. J. Duncan, K. Lucke, C. Erbe, and R. D. McCauley, “Issues associated with sound exposure experiments in tanks,” *Proc. Mtgs. Acoust.*, vol. 27, no. 1, p. 070008, Jul. 2016, doi: 10.1121/2.0000280.

[44] V. Meyer and C. Audoly, “Influence of the measurement configuration for the assessment of underwater noise radiated from ships in shallow water,” in *OCEANS 2019 - Marseille*, Jun. 2019, pp. 1–4. doi: 10.1109/OCEANSE.2019.8867091.

[45] H. Kuttruff, *Room acoustics*, 4th ed. London, [England] ; New York, NY: Spon Press, 2000.

[46] A. Novak, M. Bruneau, and P. Lotton, “Small-Sized Rectangular Liquid-Filled Acoustical Tank Excitation: A Modal Approach Including Leakage Through the Walls,” *Acta Acustica united with Acustica*, vol. 104, no. 4, pp. 586–596, Jul. 2018, doi: 10.3813/AAA.919199.

[47] M. Harrison, “4 - Interior noise: assessment and control,” in *Vehicle Refinement*, M. Harrison, Ed. Oxford: Butterworth-Heinemann, 2004, pp. 145–233. doi: 10.1016/B978-075066129-4/50006-7.

[48] R. D. Blevins, “Modal density of rectangular volumes, areas, and lines,” *The Journal of the Acoustical Society of America*, vol. 119, no. 2, pp. 788–791, Jan. 2006, doi: 10.1121/1.2159293.

[49] Y.-M. Zhang, R. Tang, Q. Li, and D.-J. Shang, “The low-frequency sound power measuring technique for an underwater source in a non-anechoic tank,” *Meas. Sci. Technol.*, vol. 29, no. 3, p. 035101, Feb. 2018, doi: 10.1088/1361-6501/aa9f6e.

[50] A. Prato, F. Casassa, and A. Schiavi, “Reverberation time measurements in non-diffuse acoustic field by the modal reverberation time,” *Applied Acoustics*, vol. 110, pp. 160–169, Sep. 2016, doi: 10.1016/j.apacoust.2016.03.041.

[51] W. C. Sabine and M. D. Egan, “Collected Papers on Acoustics,” *The Journal of the Acoustical Society of America*, vol. 95, no. 6, pp. 3679–3680, Jun. 1994, doi: 10.1121/1.409944.

[52] M. Skålevik, “Schroeder Frequency revisited,” in *Forum Acusticum 2011*, Aalborg, Denmark, 2011, p. 6.

[53] M. Long, *Architectural Acoustics*. Elsevier, 2005.

[54] G. Müller and M. Möser, *Handbook of Engineering Acoustics*. Springer Science & Business Media, 2012.

[55] B. Dushaw and J. Colosi, “Ray Tracing for Ocean Acoustic Tomography,” *undefined*, 1998, Accessed: Jan. 19, 2022. [Online]. Available: https://www.semanticscholar.org/paper/Ray-Tracing-for-Ocean-Acoustic-Tomography-Dushaw-Colosi/a5ac8e329883027fef44e2641f4ee5a8d22c81e3

[56] L. Savioja and U. P. Svensson, “Overview of geometrical room acoustic modeling techniques,” *The Journal of the Acoustical Society of America*, vol. 138, no. 2, pp. 708–730, Aug. 2015, doi: 10.1121/1.4926438.

[57] J. M. Hovem, *Ray trace modeling of underwater sound propagation. Documentation and use of the PlaneRay model*. 2011. Accessed: Aug. 28, 2021. [Online]. Available: https://sintef.brage.unit.no/sintef-xmlui/handle/11250/2380647

[58] A. M. Ondet and J. L. Barbry, “Modeling of sound propagation in fitted workshops using ray tracing,” *The Journal of the Acoustical Society of America*, vol. 85, no. 2, pp. 787–796, Feb. 1989, doi: 10.1121/1.397551.

[59] T. K. Kim, “T test as a parametric statistic,” *Korean J Anesthesiol*, vol. 68, no. 6, pp. 540–546, Dec. 2015, doi: 10.4097/kjae.2015.68.6.540.

[60] C. Peng, X. Zhao, and G. Liu, “Noise in the Sea and Its Impacts on Marine Organisms,” *Int J Environ Res Public Health*, vol. 12, no. 10, pp. 12304–12323, Oct. 2015, doi: 10.3390/ijerph121012304.

[61] T. Markus and P. P. S. Sánchez, “Managing and Regulating Underwater Noise Pollution,” in *Handbook on Marine Environment Protection : Science, Impacts and Sustainable Management*, M. Salomon and T. Markus, Eds. Cham: Springer International Publishing, 2018, pp. 971–995. doi: 10.1007/978-3-319-60156-4_52.

[62] S. Vakili, A. I. Ölçer, and F. Ballini, “The development of a transdisciplinary policy framework for shipping companies to mitigate underwater noise pollution from commercial vessels,” *Marine Pollution Bulletin*, vol. 171, p. 112687, Oct. 2021, doi: 10.1016/j.marpolbul.2021.112687.

[63] B. Aktas, M. Atlar, P. Fitzsimmons, and W. Shi, “An advanced joint time-frequency analysis procedure to study cavitation-induced noise by using standard series propeller data,” *Ocean Engineering*, vol. 170, pp. 329–350, Dec. 2018, doi: 10.1016/j.oceaneng.2018.10.026.

[64] M. K. Pine, D. E. Hannay, S. J. Insley, W. D. Halliday, and F. Juanes, “Assessing vessel slowdown for reducing auditory masking for marine mammals and fish of the western Canadian Arctic,” *Marine Pollution Bulletin*, vol. 135, pp. 290–302, Oct. 2018, doi: 10.1016/j.marpolbul.2018.07.031.

[65] C. Erbe, R. Dunlop, and S. Dolman, “Effects of Noise on Marine Mammals,” in *Effects of Anthropogenic Noise on Animals*, H. Slabbekoorn, R. J. Dooling, A. N. Popper, and R. R. Fay, Eds. New York, NY: Springer, 2018, pp. 277–309. doi: 10.1007/978-1-4939-8574-6_10.

[66] N. Rako-Gospić and M. Picciulin, “Chapter 20 - Underwater Noise: Sources and Effects on Marine Life,” in *World Seas: an Environmental Evaluation (Second*

*Edition)*, C. Sheppard, Ed. Academic Press, 2019, pp. 367–389. doi: 10.1016/B978-0-12-805052-1.00023-1.

[67] B. L. Southall *et al.*, "Underwater Noise from Large Commercial Ships—International Collaboration for Noise Reduction," in *Encyclopedia of Maritime and Offshore Engineering*, American Cancer Society, 2017, pp. 1–9. doi: 10.1002/9781118476406.emoe056.

[68] M. A. McDonald, J. A. Hildebrand, and S. M. Wiggins, "Increases in deep ocean ambient noise in the Northeast Pacific west of San Nicolas Island, California," *The Journal of the Acoustical Society of America*, vol. 120, no. 2, pp. 711–718, Aug. 2006, doi: 10.1121/1.2216565.

[69] J. Fragasso and L. Moro, "Design Procedure to Estimate the Mechanical Behaviour of Resilient Mounting Elements for Marine Applications," in *Practical Design of Ships and Other Floating Structures*, Singapore, 2021, pp. 408–423. doi: 10.1007/978-981-15-4672-3_26.

[70] J. Fragasso and L. Moro, "Dynamic analysis of the stationary behavior of resilient mounting elements for marine applications," in *Sustainable Development and Innovations in Marine Technologies*, CRC Press, 2019.

[71] G. Burella, L. Moro, and B. Colbourne, "Noise sources and hazardous noise levels on fishing vessels: The case of Newfoundland and Labrador's fleet," *Ocean Engineering*, vol. 173, pp. 116–130, Feb. 2019, doi: 10.1016/j.oceaneng.2018.12.062.

[72] C. Audoly *et al.*, "Mitigation of Underwater Radiated Noise Related to Shipping and Its Impact on Marine Life: A Practical Approach Developed in the Scope of AQUO Project," *IEEE Journal of Oceanic Engineering*, vol. 42, no. 2, pp. 373–387, Apr. 2017, doi: 10.1109/JOE.2017.2673938.

[73] D. Wittekind and M. Schuster, "Propeller cavitation noise and background noise in the sea," *Ocean Engineering*, vol. 120, pp. 116–121, Jul. 2016, doi: 10.1016/j.oceaneng.2015.12.060.

[74] M. Yusvika, A. R. Prabowo, D. D. D. P. Tjahjana, and J. M. Sohn, "Cavitation Prediction of Ship Propeller Based on Temperature and Fluid Properties of Water," *Journal of Marine Science and Engineering*, vol. 8, no. 6, Art. no. 6, Jun. 2020, doi: 10.3390/jmse8060465.

[75] J. Hildebrand, “Sources of Anthropogenic Sound in the Marine Environment,” p. 16.

[76] S. Sezen, M. Atlar, and P. Fitzsimmons, “Prediction of cavitating propeller underwater radiated noise using RANS & DES-based hybrid method,” *Ships and Offshore Structures*, vol. 0, no. 0, pp. 1–13, Apr. 2021, doi: 10.1080/17445302.2021.1907071.

[77] S. Kowalczyk and J. Felicjancik, “Numerical and experimental propeller noise investigations,” *Ocean Engineering*, vol. 120, pp. 108–115, Jul. 2016, doi: 10.1016/j.oceaneng.2016.01.032.

[78] G. Tani *et al.*, “Noise measurements of a cavitating propeller in different facilities: Results of the round robin test programme,” *Ocean Engineering*, vol. 213, p. 107599, Oct. 2020, doi: 10.1016/j.oceaneng.2020.107599.

[79] H. Seol, B. Jung, J.-C. Suh, and S. Lee, “Prediction of non-cavitating underwater propeller noise,” *Journal of Sound and Vibration*, vol. 257, no. 1, pp. 131–156, Oct. 2002, doi: 10.1006/jsvi.2002.5035.

[80] D. Kim, K. Lee, and W. Seong, “Non-cavitating propeller noise modeling and inversion,” *Journal of Sound and Vibration*, vol. 333, no. 24, pp. 6424–6437, Dec. 2014, doi: 10.1016/j.jsv.2014.07.025.

[81] M. R. Bagheri, M. S. Seif, H. Mehdigholi, and O. Yaakob, “Analysis of noise behaviour for marine propellers under cavitating and non-cavitating conditions,” *Ships and Offshore Structures*, vol. 12, no. 1, pp. 1–8, Jan. 2017, doi: 10.1080/17445302.2015.1099224.

[82] K. Belibassakis, “Generation and propagation of underwater noise from marine propellers,” in *Conference Proceedings*, Crete, Greece, 2018, p. 10.

[83] M. C. Özden, A. Y. Gürkan, Y. A. Özden, T. G. Canyurt, and E. Korkut, “Underwater radiated noise prediction for a submarine propeller in different flow conditions,” *Ocean Engineering*, vol. 126, pp. 488–500, Nov. 2016, doi: 10.1016/j.oceaneng.2016.06.012.

[84] J. Jiao, H. Ren, S. Sun, N. Liu, H. Li, and C. A. Adenya, “A state-of-the-art large scale model testing technique for ship hydrodynamics at sea,” *Ocean Engineering*, vol. 123, pp. 174–190, Sep. 2016, doi: 10.1016/j.oceaneng.2016.06.028.

[85] H. C. Raven, “Shallow-water effects in ship model testing and at full scale,” *Ocean Engineering*, vol. 189, p. 106343, Oct. 2019, doi: 10.1016/j.oceaneng.2019.106343.

[86] G. Tani, M. Viviani, M. Ferrando, and E. Armelloni, “Aspects of the measurement of the acoustic transfer function in a cavitation tunnel,” *Applied Ocean Research*, vol. 87, pp. 264–278, Jun. 2019, doi: 10.1016/j.apor.2019.02.017.

[87] D.-Q. Li, J. Hallander, and T. Johansson, “Predicting underwater radiated noise of a full scale ship with model testing and numerical methods,” *Ocean Engineering*, vol. 161, pp. 121–135, Aug. 2018, doi: 10.1016/j.oceaneng.2018.03.027.

[88] S. Li, D. Yang, and H. Zhang, “Experimental study of underwater propeller low-frequency noise flied,” in *2016 IEEE/OES China Ocean Acoustics (COA)*, Jan. 2016, pp. 1–4. doi: 10.1109/COA.2016.7535778.

[89] A. Brooker and V. Humphrey, “Measurement of radiated underwater noise from a small research vessel in shallow water,” *Ocean Engineering*, vol. 120, pp. 182–189, Jul. 2016, doi: 10.1016/j.oceaneng.2015.09.048.

[90] D. McIntyre, W. Lee, H. Frouin-Mouy, D. Hannay, and P. Oshkai, “Influence of propellers and operating conditions on underwater radiated noise from coastal ferry vessels,” *Ocean Engineering*, vol. 232, p. 109075, Jul. 2021, doi: 10.1016/j.oceaneng.2021.109075.

[91] S. V. Vakili, A. I. Ölcer, and F. Ballini, “The development of a policy framework to mitigate underwater noise pollution from commercial vessels,” *Marine Policy*, vol. 118, p. 104004, Aug. 2020, doi: 10.1016/j.marpol.2020.104004.

[92] R. E. Kurt, H. Khalid, O. Turan, M. Houben, J. Bos, and I. H. Helvacioglu, “Towards human-oriented norms: Considering the effects of noise exposure on board ships,” *Ocean Engineering*, vol. 120, pp. 101–107, Jul. 2016, doi: 10.1016/j.oceaneng.2016.03.049.

[93] C. Audoly, C. Rousset, E. Rizzuto, R. S. Mullor, J. Hallander, and E. Baudin, “Mitigation measures for controlling the ship underwater radiated noise, in the scope of AQUO project,” in *OCEANS 2015 - Genova*, May 2015, pp. 1–6. doi: 10.1109/OCEANS-Genova.2015.7271381.

[94] H. J. Prins *et al.*, “Suppression of Underwater Noise Induced by Cavitation: SONIC,” *Transportation Research Procedia*, vol. 14, pp. 2668–2677, Jan. 2016, doi: 10.1016/j.trpro.2016.05.439.

[95] Bosschers, J., Lafeber, F.H., de Boer, J., Bosman, R., and Bouvy, A., “Underwater radiated noise measurements with a silent towing carriage in the Depressurized Wave Basin,” presented at the 3rd International Conference on Advanced Model Measurement Technology for the EU Maritime Industry, Gdansk, Poland, Aug. 2013.

[96] “Model-Scale Propeller Cavitation Noise Measurements, ITTC-Recommended Procedures and Guidelines. Revision 01, Effective 2017.” Accessed: Aug. 04, 2021. [Online]. Available: https://www.ittc.info/media/7993/75-02-01-05.pdf

[97] C. Audoly and V. Meyer, “Measurement of radiated noise from surface ships - influence of the sea surface reflection coefficient on the Lloyd’s mirror effect,” presented at the Acoustics 2017, Perth, Australia, 2017.

[98] C. W. de Silva, *Vibration: Fundamentals and Practice, Second Edition*. CRC Press, 2006.

[99] M. H. J. Gruber, “Statistical Digital Signal Processing and Modeling,” *Technometrics*, vol. 39, no. 3, pp. 335–336, Aug. 1997, doi: 10.1080/00401706.1997.10485128.

[100] P. Stoica and R. L. Moses, *Spectral analysis of signals*. Upper Saddle River, N.J: Pearson/Prentice Hall, 2005.

[101] “ISO 17208-1:2016. Underwater acoustics — Quantities and procedures for description and measurement of underwater sound from ships — Part 1: Requirements for precision measurements in deep water used for comparison purposes,” *ISO*.

[102] “Underwater Noise from Ships, Full Scale Measurements, ITTC-Recommended Procedures and Guidelines. Revision 01, Effective 2017.” Accessed: Aug. 09, 2021. [Online]. Available: https://www.ittc.info/media/8183/75-04-04-01.pdf

[103] “Generate octave spectrum - MATLAB poctave - MathWorks.” https://in.mathworks.com/help/signal/ref/poctave.html (accessed Sep. 09, 2021).

[104] G. Bark, “Prediction of Propeller Cavitation Noise From Model Tests and Its Comparison With Full Scale Data,” *Journal of Fluids Engineering*, vol. 107, no. 1, pp. 112–119, Mar. 1985, doi: 10.1115/1.3242424.

[105] D. Bertetta, S. Brizzolara, S. Gaggero, M. Viviani, and L. Savio, “CPP propeller cavitation and noise optimization at different pitches with panel code and validation by cavitation tunnel measurements,” *Ocean Engineering*, vol. 53, pp. 177–195, Oct. 2012, doi: 10.1016/j.oceaneng.2012.06.026.

[106] “Resistance Test, ITTC recommended procedures and guidelines.” Accessed: Aug. 02, 2021. [Online]. Available: https://ittc.info/media/1217/75-02-02-01.pdf

[107] “Propulsion/Bollard Pull Test, ITTC recommended procedures and guidelines.” Accessed: Aug. 02, 2021. [Online]. Available: https://www.ittc.info/media/8011/75-02-03-011.pdf

# Appendix A

## Model Testing

Model testing in a towing tank is the most effective way to assess the power requirements, hydrodynamic responses, maneuvering, stability, etc. Model testing information is further used to correlate full-scale measurements and validate CFD simulations. Various model tests like resistance, self-propulsions, bollard pull, open water tests, etc., are performed to support ship design and detect any design issue.. ITTC recommended procedure guidelines for test methodology, post-processing, and extrapolation to full-scale [106], [107].

Model tests need a physical ship model to be towed. Physical models are intended to represent the full-scale system but at a smaller scale. Proper properties and dimensions of the model are determined by using scaling law that ensures similar characteristics in the model and full scale. Geometric, kinematic, and dynamic similarities are used to achieve the similarity between model and full scale. Dimensionally the model should be sufficiently large to minimize viscosity scale effects. However, it should not be too large to avoid the restricted size of the towing tank. Propeller size is designed according to the scaling of the actual ship. The model is rigid and made from primarily wood, wax, fibre-reinforced plastic, cast lead, and special papers. They commonly performed model tests to predict the full-scale performance of the resistance test, self-propulsion test and bollard pull test.

**A-1. Resistance Test**

The force experienced by a ship opposite to its motion direction while the ship moves through calm water is known as total hull resistance. The hull resistance increases with the ship speed and largely depends on ship length, density and viscosity of the fluid, and acceleration due to gravity. Model scale resistance tests are conducted to determine the model resistance at any desired speed. The total resistance coefficient of the model is calculated from the following equation

$$C_T = \frac{R_T}{\frac{1}{2}\rho S V^2} \quad (3.1)$$

Residual resistance coefficient, $C_R = C_{TM} - C_{FM}(1 + k)$

ITTC 57 model-ship correlation line for form friction, $C_F = \frac{0.075}{(log_{10}Re-2)^2} = (1 + 0.1194)\frac{0.067}{(log_{10}Re-2)^2}$ (3.2)

The flow similarities are maintained between the model and full scale using equal non-dimensional numbers like Reynold's number or Froude number.

Mathematically Reynold's number similarity:

$$Re_M = Re_S$$

$$V_M = \frac{L_S}{L_M} V_S$$

Froude number similarity:

$$Fr_M = Fr_S$$

$$V_M = \sqrt{\frac{L_M}{L_S}} V_S$$

However, it is difficult to simultaneously satisfy the flow similarities of Reynold's and Froude's numbers. On the other hand, model dimensions from Reynold's number do not allow model testing equality. Therefore, the model is towed at speeds giving the same Froude number as for the full-scale ship.

Resistance force is measured at model scale and extrapolated to full scale. Resistance tests are performed in one or both of the following conditions-

a. Resistance test of the model to determine the resistance coefficients of the basic hull without any appendages
b. Resistance test of the model with appendages to determine the increase in resistance coefficients due to appendages

During the tests, model resistance and advanced speed are simultaneously measured. The sinkage fore and aft or the running trim and sinkage are also measured. The test procedure includes the following steps

a. The model is accelerated to the estimated model speed.
b. The average speed is kept constant for 10 secs (or at least ten load cycles).
c. Average values of measurement for the period of constant speed are calculated.
d. The model is towed at a constant speed, and it is generally free to heave, surge, pitch and roll.
e. The test is repeated at different speeds.

The fundamental steps are followed for scaling total resistance from model to ship-

a. Measure the resistance force of the geometrically similar model at corresponding model speed derived from Froude similarity
b. Estimate the form friction from the experiments
c. Calculate the residuary resistance by subtracting form friction from the total resistance
d. Estimate ship residuary resistance by multiplying model residuary resistance with the ship to model displacements ratio
e. Estimate total ship resistance by adding skin friction resistance

Resistance tests are conducted to measure the nominal wake, i.e., the wake of the ship without the propeller. However, the propeller is replaced with a bare hub of the same weight. Acoustically, there is no noise contribution from the rotating propeller and machinery noise (propulsion noise). The resistance test is very useful to estimate the hydrodynamic noise produced by the hull with water interaction. Additionally, since the carriage is also moving during the resistance test, the background and carriage noise contributes to the measured noise. However, the hydrodynamic noise could be recognized due to its broadband characteristics. Further details on these tests are presented in [106].

**A-2. Self-propulsion tests**

Self-propulsion tests on the model scale are conducted to estimate ship power requirements at various speeds. The model is prepared in the same way for the resistance with turbulence stimulation and appendages. However, a propeller used in the open

water test is fitted to the model. The size of the model propeller for propulsion tests is determined based on the size of the ship model and its scale ratio. The stock propeller has the similarity in diameter, pitch and blade area to the full-scale propeller. In addition, the hull model is equipped with a propulsive drive, typically a small electro-motor and propeller shafting system. The other measuring (dynamometer) and acquisition instruments are fitted inboard.

In the self-propulsion test, the model is tested at speeds maintaining Froude similarity as for the full-scale ship and exactly the same as the resistance test. In propulsion experiments, an external tow force is applied along the same line of action as the tow force in the resistance experiment during a self-propulsion test. During the test, propeller thrust, torque and propeller rotation are measured. Propulsion tests are performed to determine the power requirements, supply wake and thrust deduction, and other input data for the propeller design. The model can heave and pitch the same as the resistance test.

Propulsion tests are performed in two parts. The test begins with a load variation test at one or more advanced speeds to find a self-propulsion point, while the second part consists of a test at the self-propulsion point of the ship. The ship's self-propulsion point is achieved if the towing force on the carriage is equal to the scale effect correction on viscous resistance. For self-propulsion, the propeller just need to produce a thrust to overcome the total resistance, $R_T$ minus the correction force, $F_D$. Since the model moves at a constant speed, the rpm of the propeller is varied until a self-propelled equilibrium is reached. The required thrust and self-propulsion point can be transformed from model to full scale using similarity laws.

$$T_S = \left[T_M + (F_D - F)\frac{\delta T_M}{\delta F}\right]\frac{\rho_S}{\rho_M}\lambda^3$$

The skin-friction correction force, $F_D = \frac{1}{2}\rho_M V_M^2 S_M\left(C_{FM} - (C_{FS} + \Delta C_F + C_A)\right)$(3.3)

ITTC 57 model-ship correlation line for form friction, $C_F = \frac{0.075}{(log_{10}Re-2)^2}$ (3.4)

The first part of the self-propulsion test determines the derivative $\frac{\delta T_M}{\delta F}$ from the load variation tests. The load test of the propeller can be conducted either by varying load, constant load, or mixed loading. However, varying load method is widely used by the researchers.

The model advanced speed and desired propeller loading are estimated before each run in the load varying method. The corresponding propeller thrust force is also calculated. Both the towing carriage and propeller accelerate from the rest to reach the estimated thrust as soon as the carriage attained its steady speed. The model is released to tow it by the resistance dynamometer and running condition allowed to settle. The measurements should be recorded after a short pause. The tests are repeated for several propeller loading but at the same advanced speed, and the whole series of runs is then repeated at each of the speeds within the test range.

The loading range should extend from the lowest to the highest load factors at which ship performance estimates are required, always providing that this range includes a load factor of unity (external force $F_D = F$). The loading should cover the condition of model-self-propulsion (zero tow force) in all cases. Experiments should be done at no less than four different overload levels, such as -10%, 0%, 10%, and 20%. Further details on these tests are presented in [107]**.**

The self-propulsion tests are essential for propeller-induced noise measurements since they provide information about the actual operating conditions. The noise measured from self-propulsion tests includes noise contribution from all the possible sources like background noise, carriage noise, hydrodynamic hull noise, and noise contribution machinery noise and propeller noise. Since the resistance and self-propulsion are conducted at the same Froude similarities, the propeller noise could be distinguished from other noises by its tonal frequency (BPF) and its multiple.

**A-3. Bollard Pull Test**

Bollard pull is the static tractive force produced by the propulsion systems of a ship on a fixed towline when it has a zero advanced speed. The mathematical model does not accurately determine bollard pull; therefore, it is calculated by model testing. Bollard test is a part of self-propulsion. Thus, the model, propeller, measuring equipment, and instrumentation is the same as self-propulsion tests. Although self-propulsion results can not be extrapolated to full scale, bollard pull can be directly correlated to full scale. The bollard pull of a ship depends on propeller type, shape and size of the submerged hull, draught, and trim.

For a scale factor $\lambda$, the full-scale bollard pull, propeller speed and power can be calculated using the following equations

$$F_{PS} = F_{PM} \frac{\rho_S}{\rho_M} \lambda^3$$

$$n_s = \frac{n_M}{\sqrt{\lambda}}$$

$$P_S = 2\pi n_M Q_M \frac{\rho_S}{\rho_M} \lambda^{3.5} \qquad (3.5)$$

The thrust deduction factor for the bollard pull test can be estimated from the following equation

$$t = 1 - \frac{F_{PM}}{\sum T_M} \quad (3.6)$$

The bollard pull tests should be conducted in some ideal conditions:

4 No current and disturbances in the water

5 Free propeller wake and stream

6 Sufficient and even draft of the vessel along the length

7 Clearance on the direction of motion

The bollard pull test is different from self-propulsion tests due to some specific reasons-

a. The test is conducted at zero advanced speed
b. The wake and relative rotative efficiency is not considered in the bollard pull test. However, the hull interaction is accounted for by the thrust deduction coefficient.
c. The propeller acts as an axial pump due to the high axial and tangential velocities generated during bollard pull. The strong current produced by the propeller in the tank depends on propeller type, tank size and longitudinal position of the model regarding the tank length.
d. The interaction between the rudder and propeller due to heavy propeller loading exhibits an internal force that further added to the total bollard pull.
e. The propeller blades can start ventilating due to air suction from the free surface at high loading
f. The effect of cavitating propellers on the bollard force can not be modelled in an atmospheric tank.

Since the model is at rest during the bollard pull test, there are no other noise sources except the propeller-induced noise. The noise generated during the resistance and self-propulsion tests includes the carriage noise, background noise, machinery noise (electric motor, shafting arrangement) and hydrodynamic noise of the hull. As a result, identifying the propeller noise from the noise spectrum becomes very complicated. However, the noise measured in the bollard pull condition is free from other complex noise signatures. The only available noise is the background noise (electric hum), which is identifiable from propeller-induced noise (tonal and multiples). The bollard tests are conducted precisely at self-propulsion RPS.

# Appendix B

## Analysis of Experimental Results

### B-1.Background Noise in Different Advanced Speeds

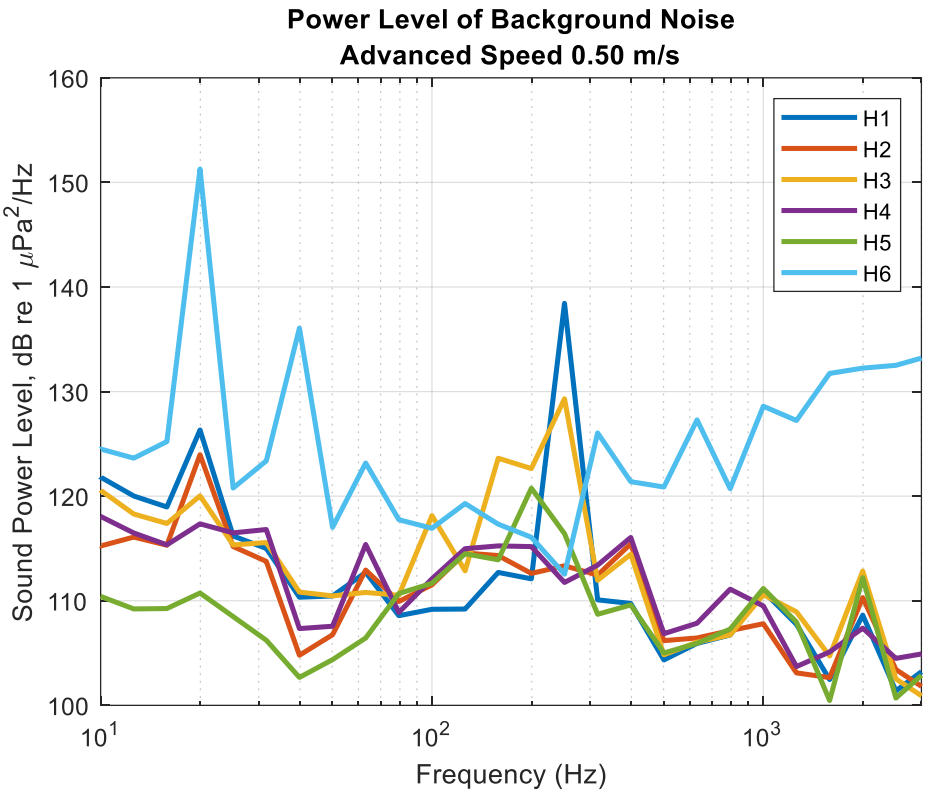

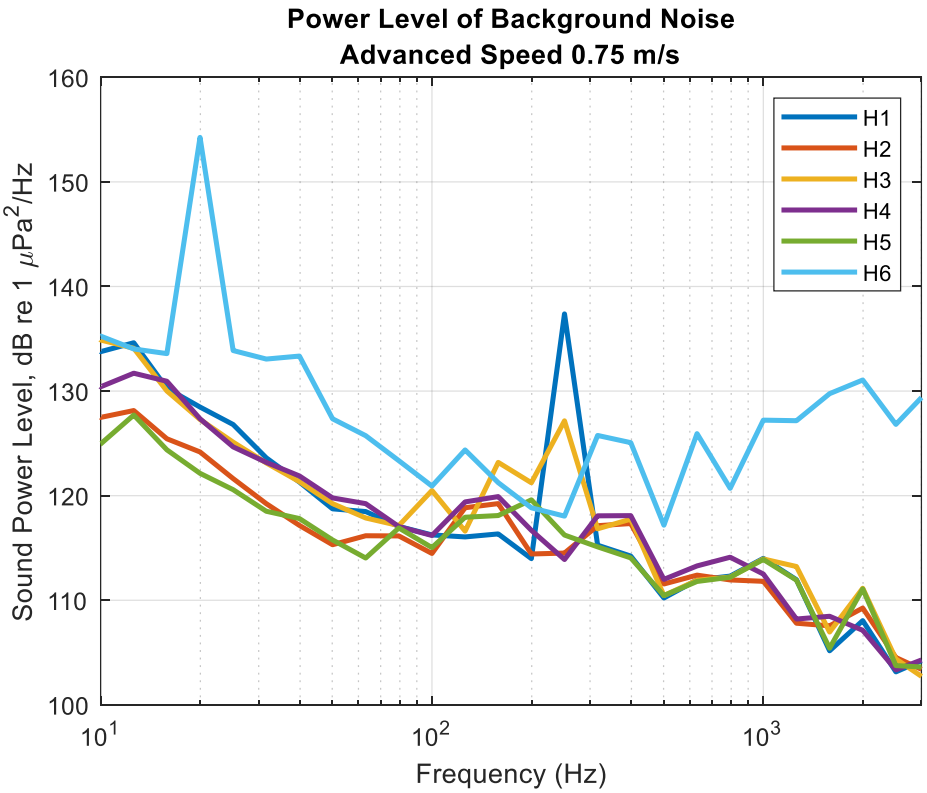
Power Level of Background Noise
Advanced Speed 0.75 m/s
Sound Power Level, dB re 1 μPa²/Hz
Frequency (Hz)
H1
H2
H3
H4
H5
H6
160
150
140
130
120
110
100
10¹
10²
10³

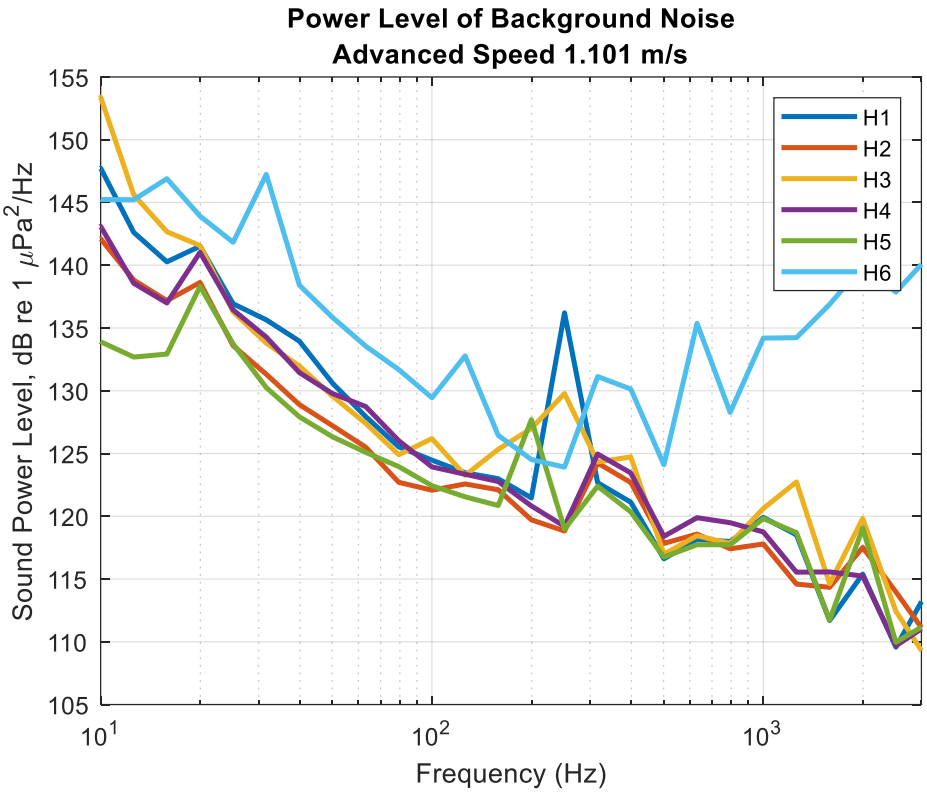
Power Level of Background Noise
Advanced Speed 1.101 m/s
Sound Power Level, dB re 1 μPa²/Hz
Frequency (Hz)
H1
H2
H3
H4
H5
H6
155
150
145
140
135
130
125
120
115
110
105
10¹
10²
10³

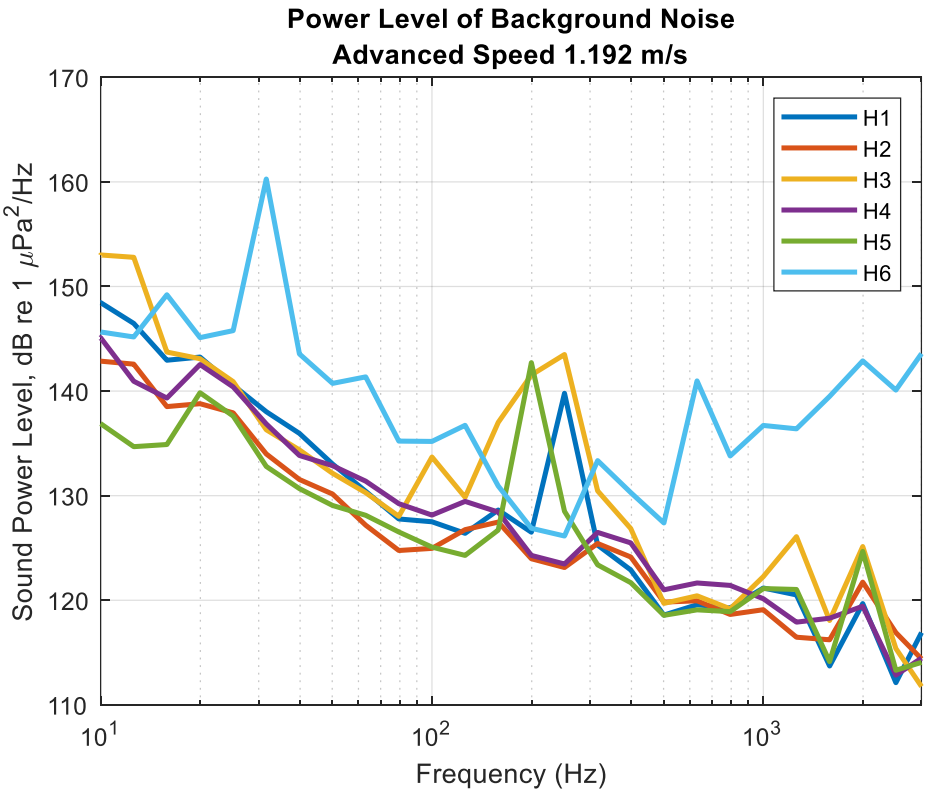
Power Level of Background Noise
Advanced Speed 1.192 m/s
Sound Power Level, dB re 1 μPa²/Hz
Frequency (Hz)
H1
H2
H3
H4
H5
H6

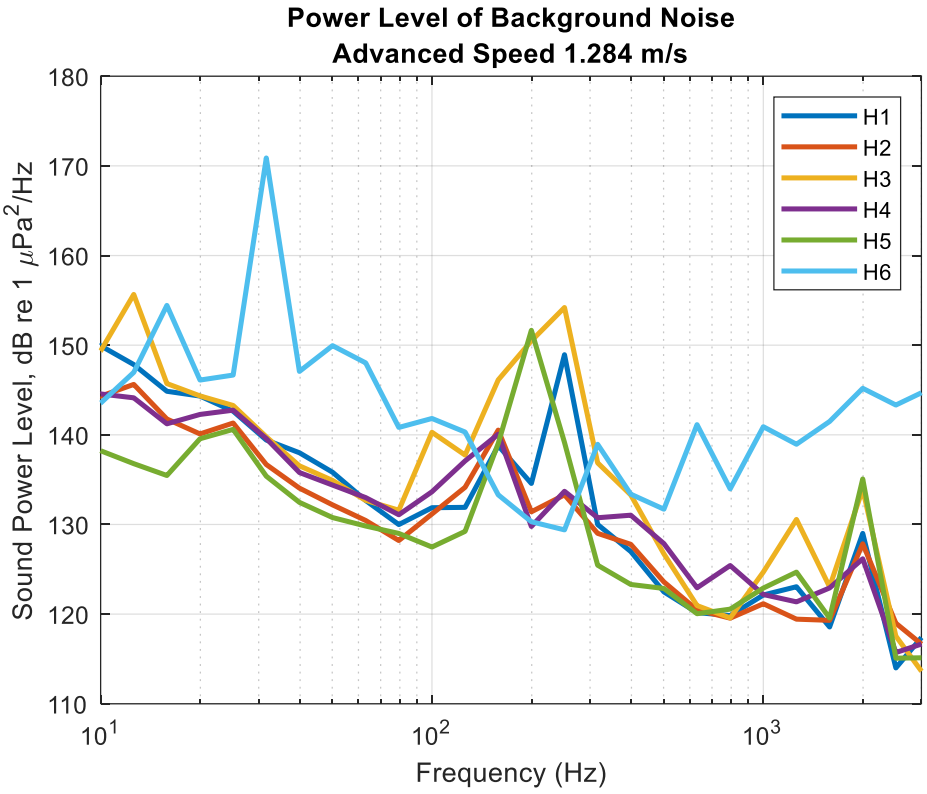
Power Level of Background Noise
Advanced Speed 1.284 m/s
Sound Power Level, dB re 1 μPa²/Hz
Frequency (Hz)
H1
H2
H3
H4
H5
H6

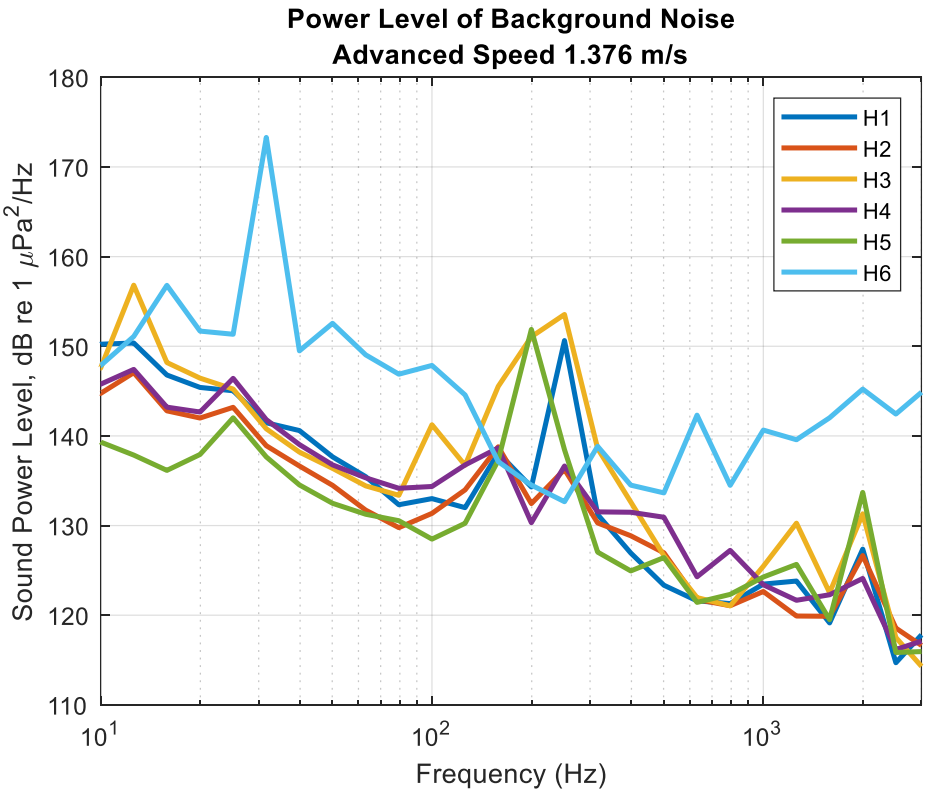
Power Level of Background Noise
Advanced Speed 1.376 m/s
Sound Power Level, dB re 1 μPa²/Hz
Frequency (Hz)
H1
H2
H3
H4
H5
H6
180
170
160
150
140
130
120
110
10¹
10²
10³

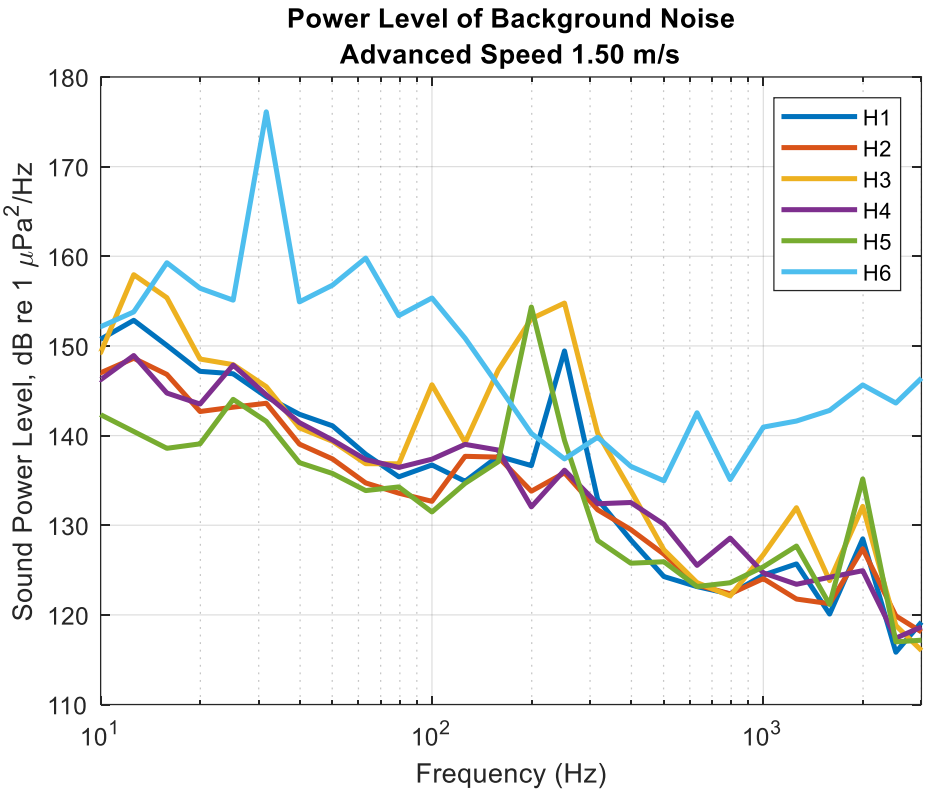
Power Level of Background Noise
Advanced Speed 1.50 m/s
Sound Power Level, dB re 1 μPa²/Hz
Frequency (Hz)
H1
H2
H3
H4
H5
H6
180
170
160
150
140
130
120
110
10¹
10²
10³

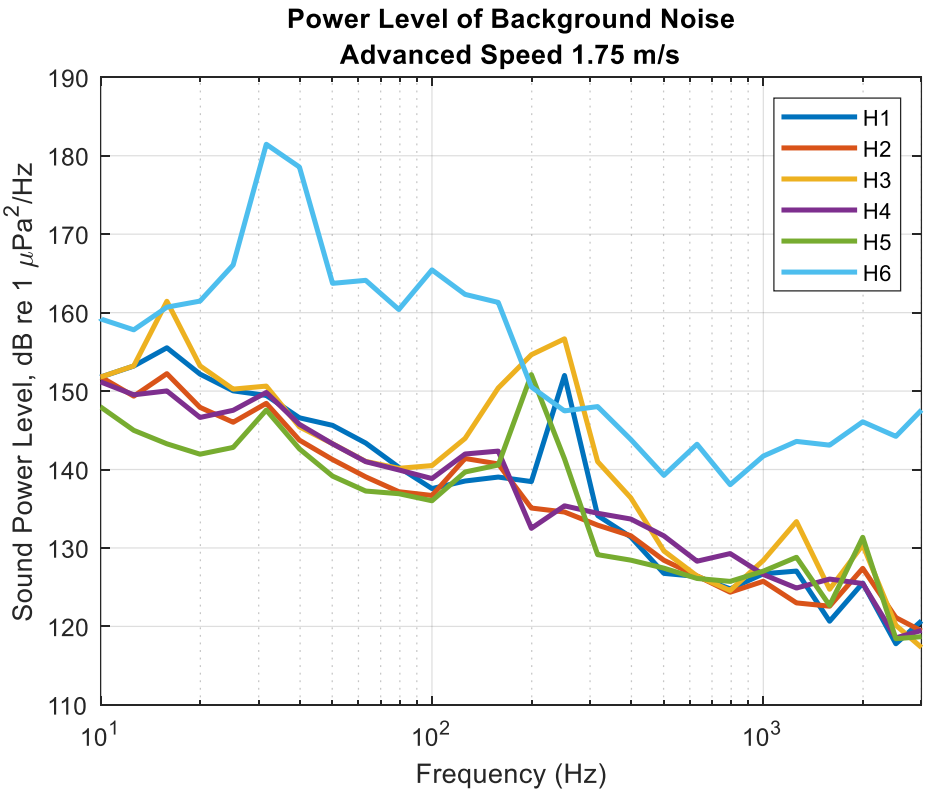


## B-2. Background Noise When Carriage at Rest

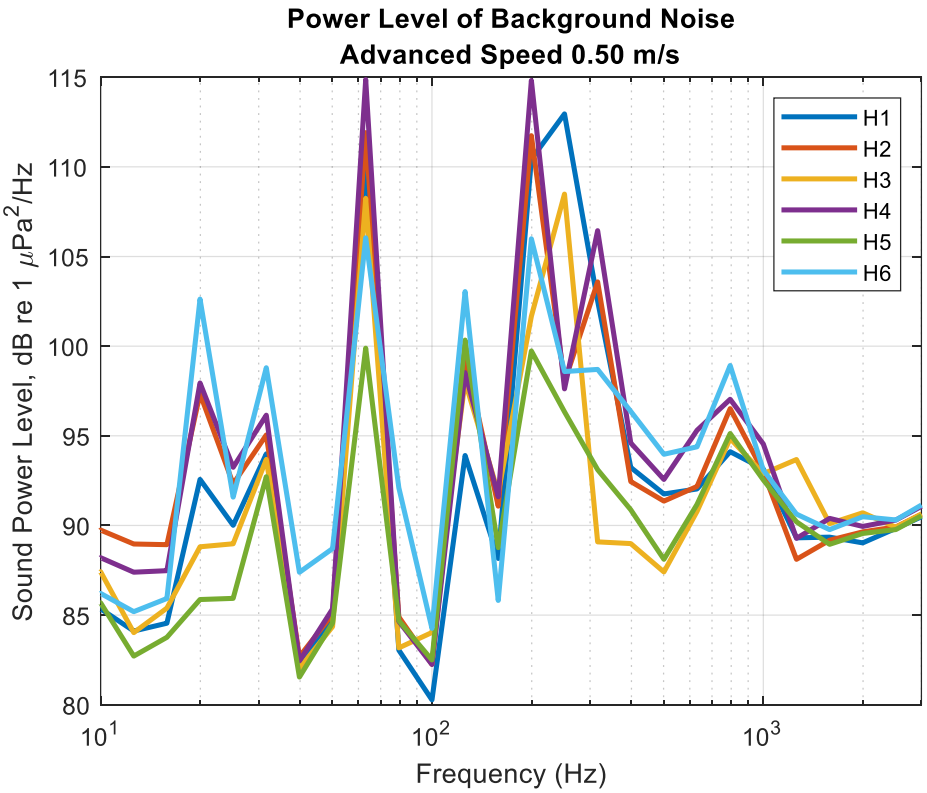

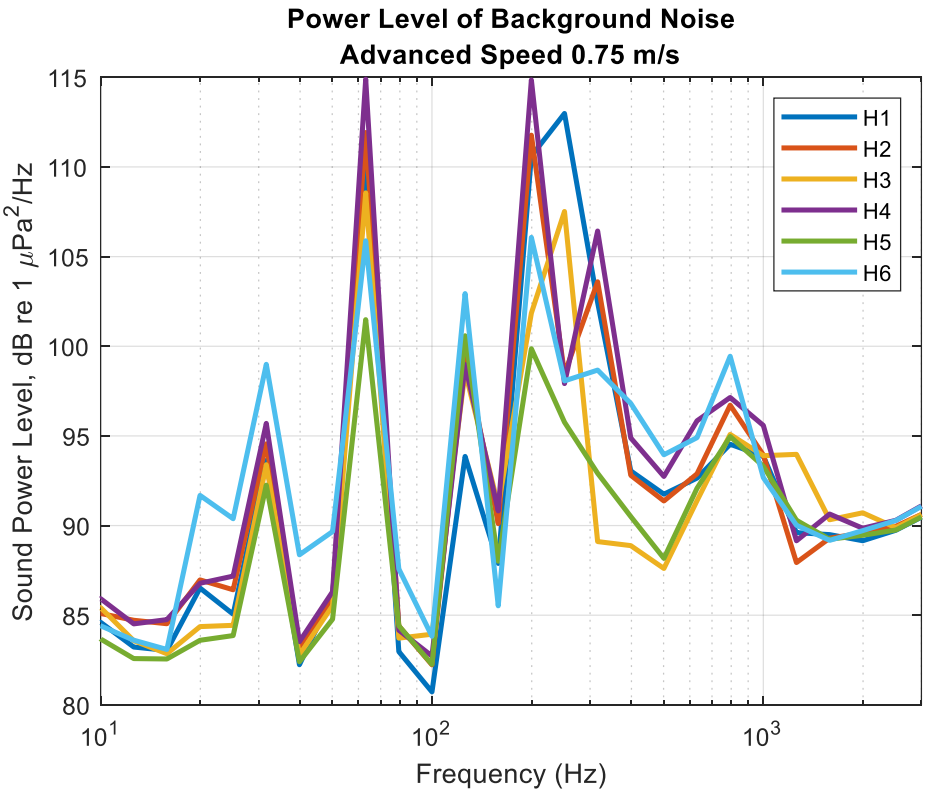
Power Level of Background Noise
Advanced Speed 0.75 m/s
Sound Power Level, dB re 1 μPa²/Hz
Frequency (Hz)
H1
H2
H3
H4
H5
H6

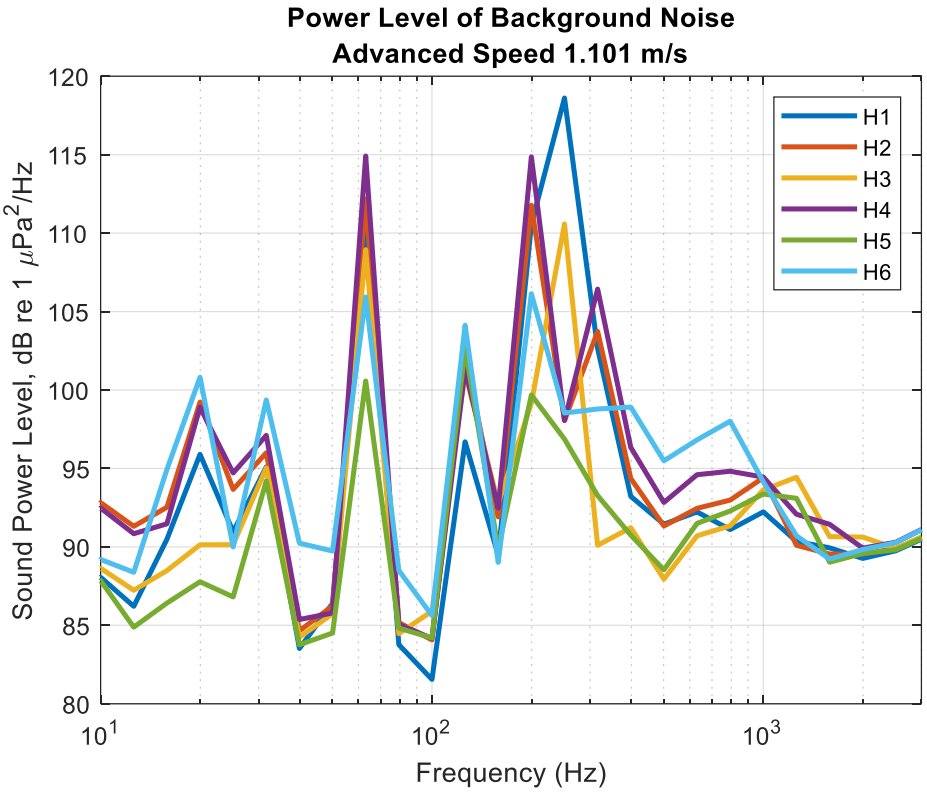
Power Level of Background Noise
Advanced Speed 1.101 m/s
Sound Power Level, dB re 1 μPa²/Hz
Frequency (Hz)
H1
H2
H3
H4
H5
H6

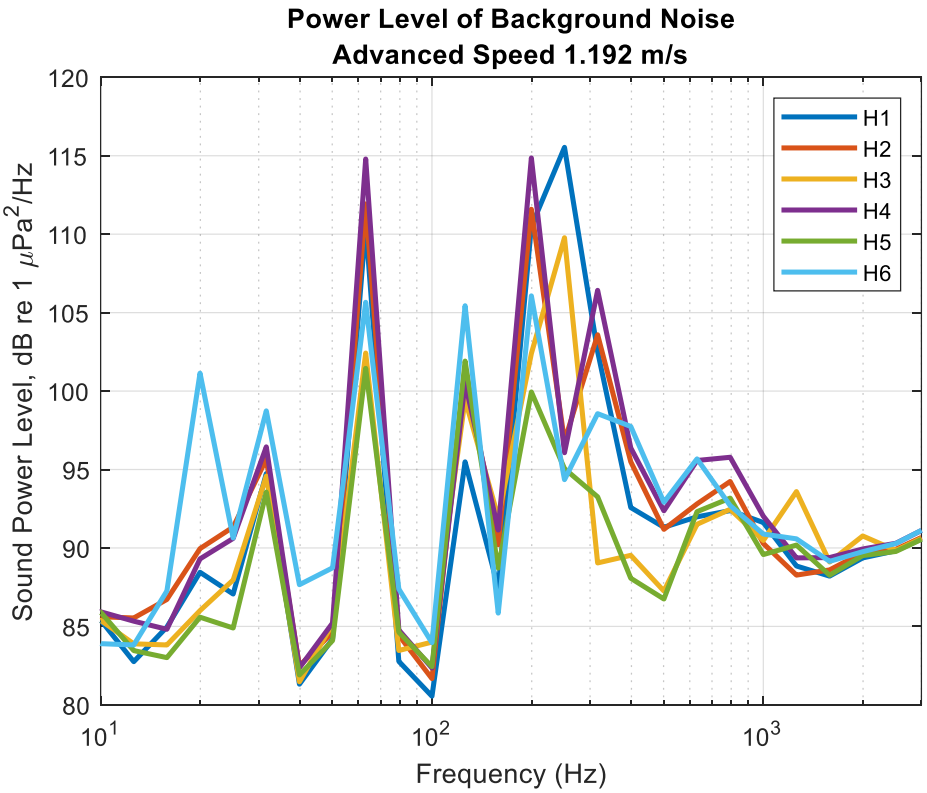
Power Level of Background Noise
Advanced Speed 1.192 m/s
Sound Power Level, dB re 1 μPa²/Hz
Frequency (Hz)
H1
H2
H3
H4
H5
H6
120
115
110
105
100
95
90
85
80
10¹
10²
10³

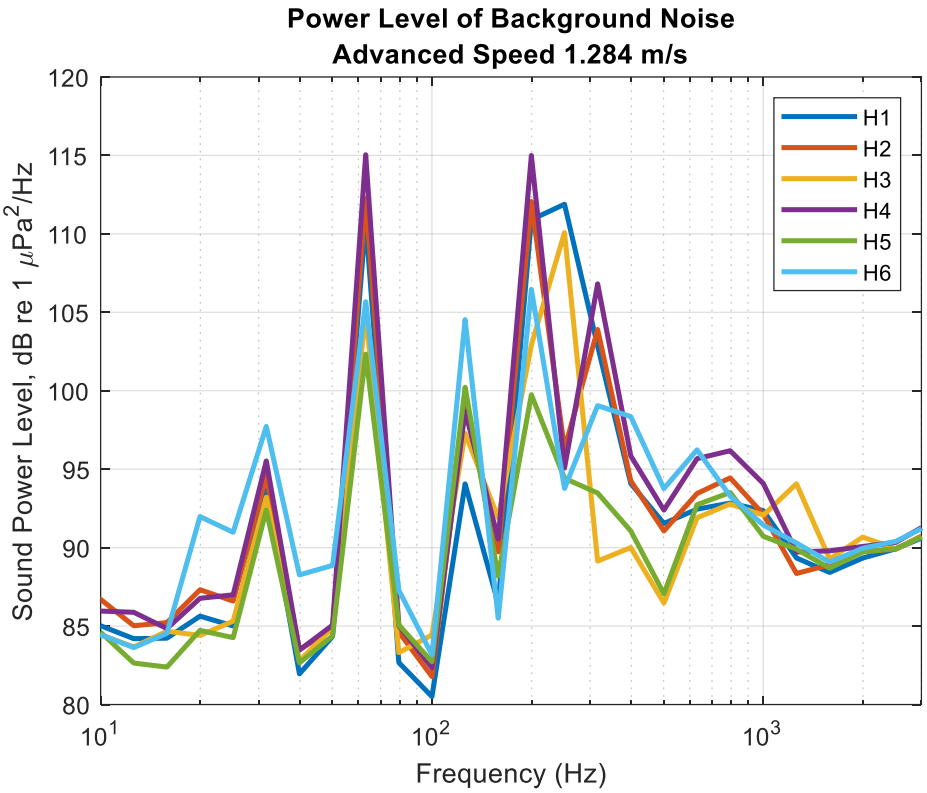
Power Level of Background Noise
Advanced Speed 1.284 m/s
Sound Power Level, dB re 1 μPa²/Hz
Frequency (Hz)
H1
H2
H3
H4
H5
H6
120
115
110
105
100
95
90
85
80
10¹
10²
10³

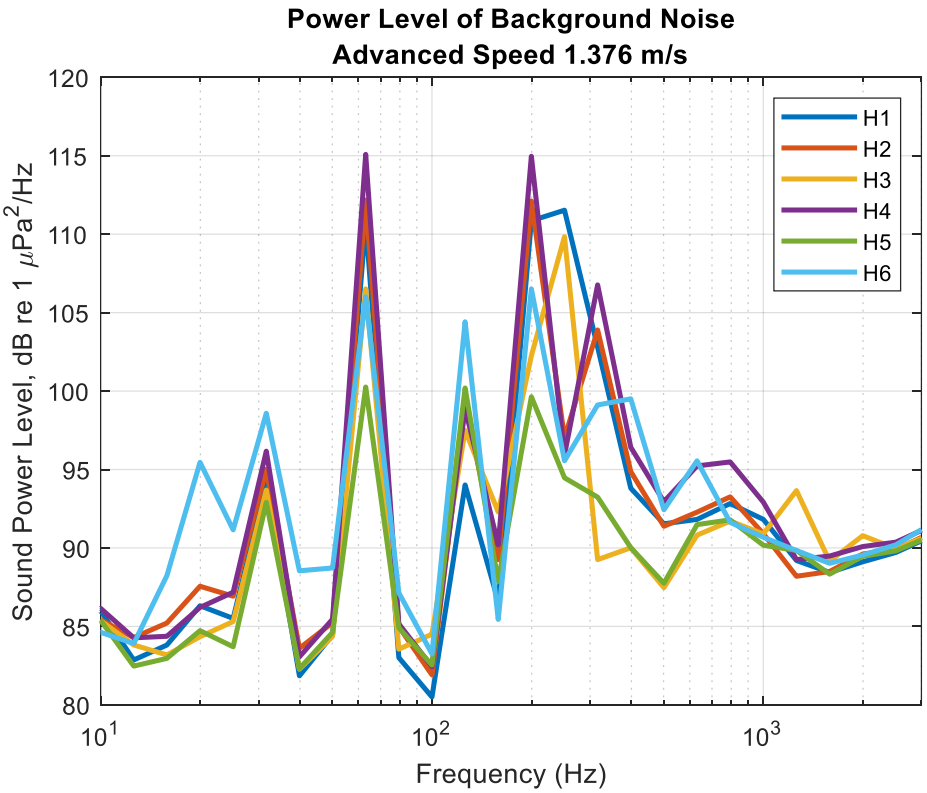
Power Level of Background Noise
Advanced Speed 1.376 m/s
Sound Power Level, dB re 1 μPa2/Hz
Frequency (Hz)
H1
H2
H3
H4
H5
H6

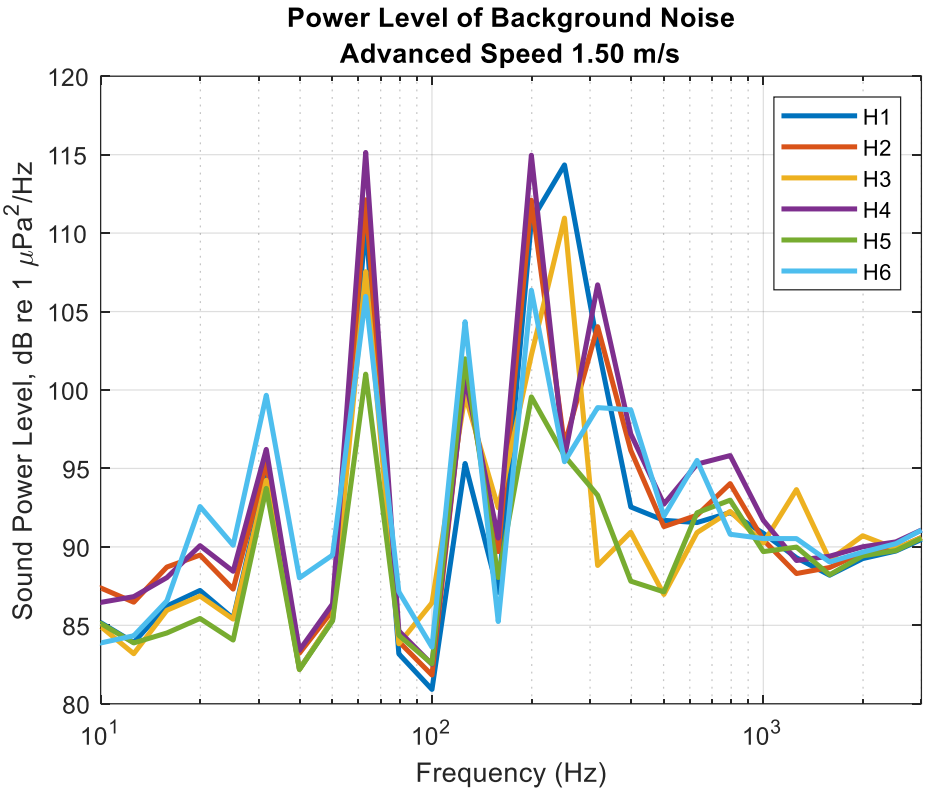
Power Level of Background Noise
Advanced Speed 1.50 m/s
Sound Power Level, dB re 1 μPa2/Hz
Frequency (Hz)
H1
H2
H3
H4
H5
H6

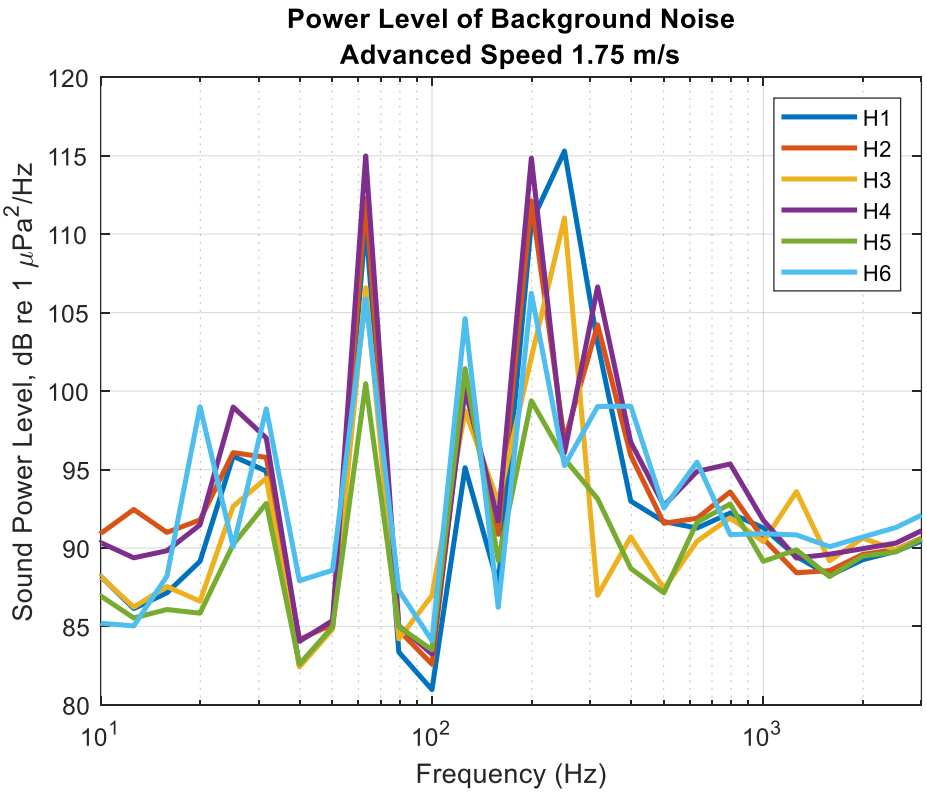


## B-3. Effect of Normalization on Background Noise (Reduced to 1 m)

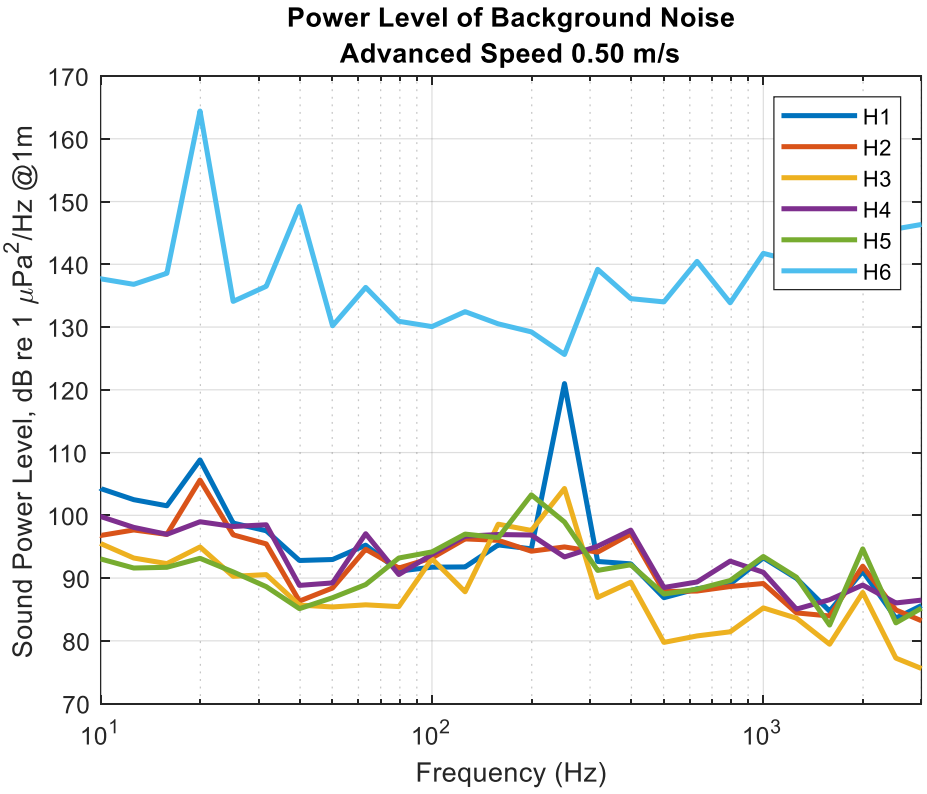

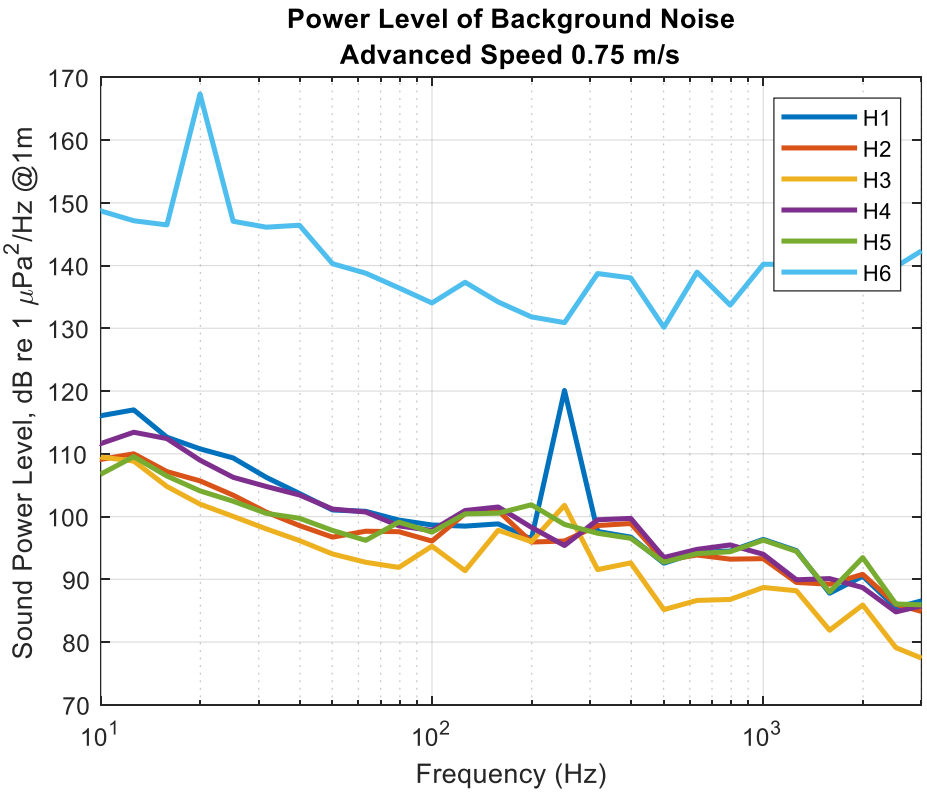
Power Level of Background Noise
Advanced Speed 0.75 m/s
Sound Power Level, dB re 1 μPa²/Hz @1m
Frequency (Hz)
H1
H2
H3
H4
H5
H6

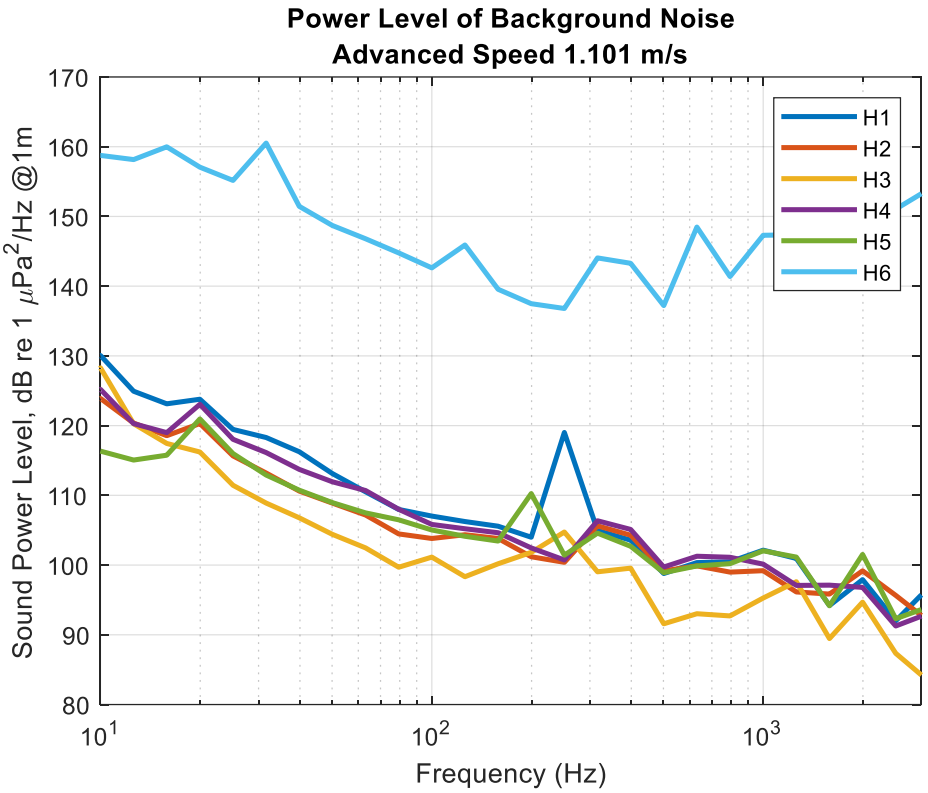
Power Level of Background Noise
Advanced Speed 1.101 m/s
Sound Power Level, dB re 1 μPa²/Hz @1m
Frequency (Hz)
H1
H2
H3
H4
H5
H6

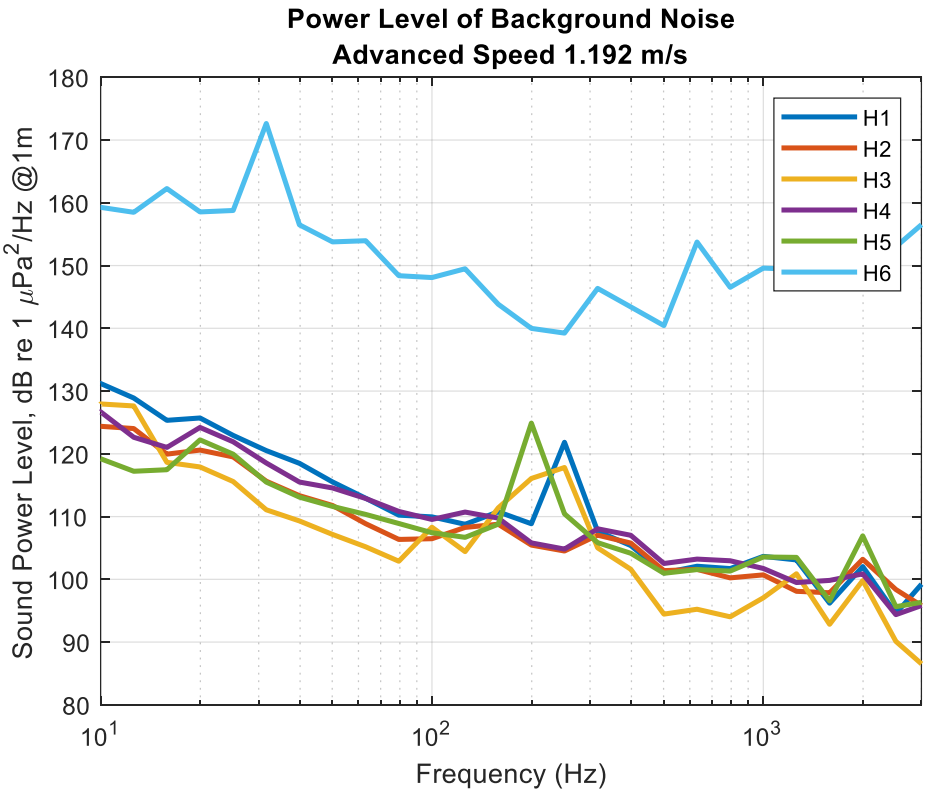
Power Level of Background Noise
Advanced Speed 1.192 m/s
Sound Power Level, dB re 1 μPa²/Hz @1m
Frequency (Hz)
H1
H2
H3
H4
H5
H6

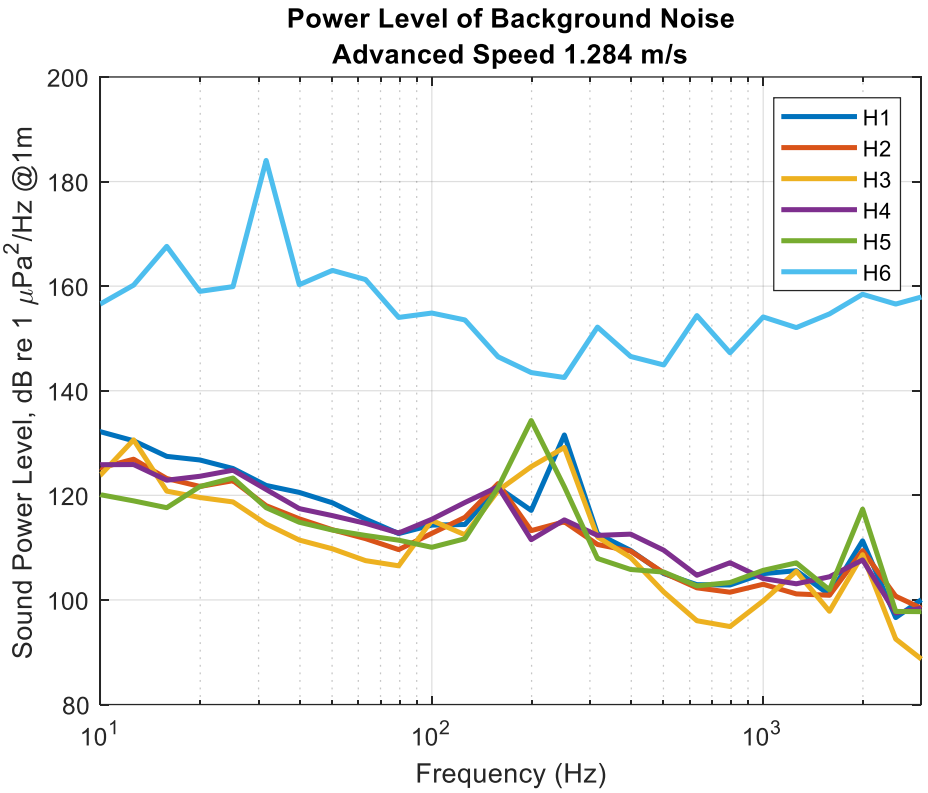
Power Level of Background Noise
Advanced Speed 1.284 m/s
Sound Power Level, dB re 1 μPa²/Hz @1m
Frequency (Hz)
H1
H2
H3
H4
H5
H6

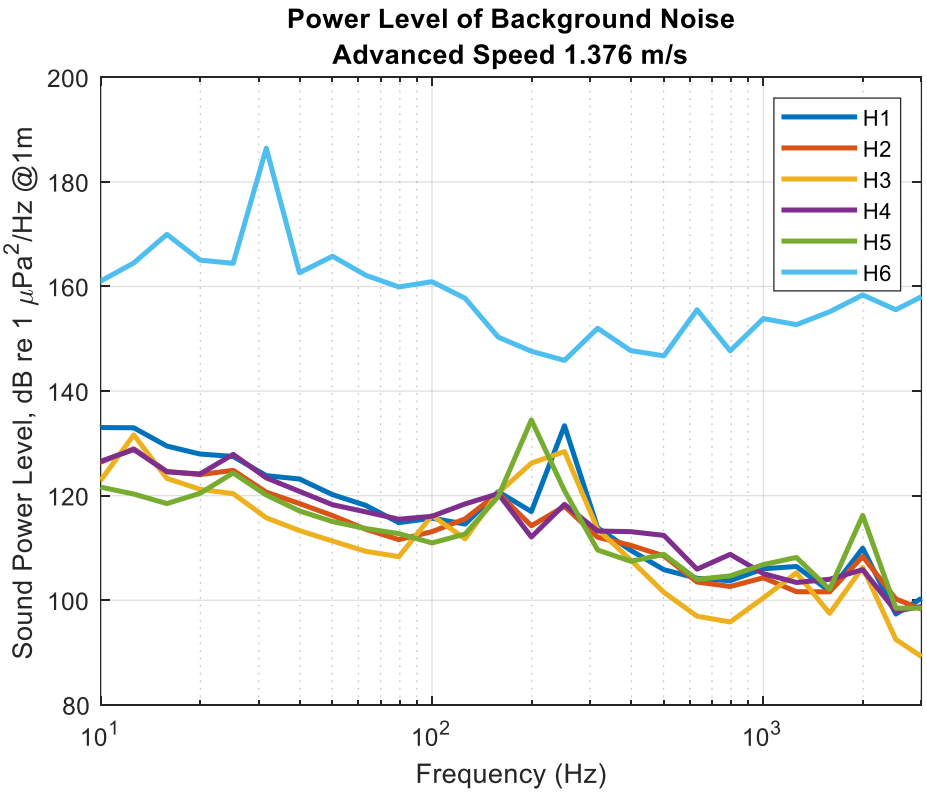
Power Level of Background Noise
Advanced Speed 1.376 m/s
Sound Power Level, dB re 1 μPa²/Hz @1m
Frequency (Hz)
H1
H2
H3
H4
H5
H6
200
180
160
140
120
100
80
10¹
10²
10³

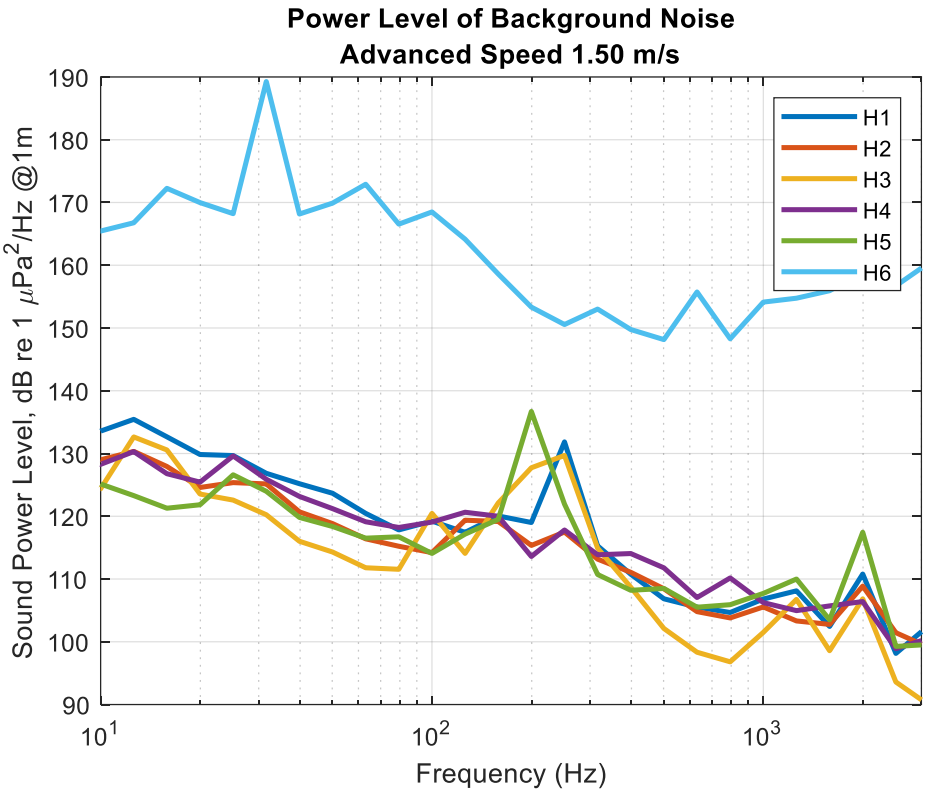
Power Level of Background Noise
Advanced Speed 1.50 m/s
Sound Power Level, dB re 1 μPa²/Hz @1m
Frequency (Hz)
H1
H2
H3
H4
H5
H6
190
180
170
160
150
140
130
120
110
100
90
10¹
10²
10³

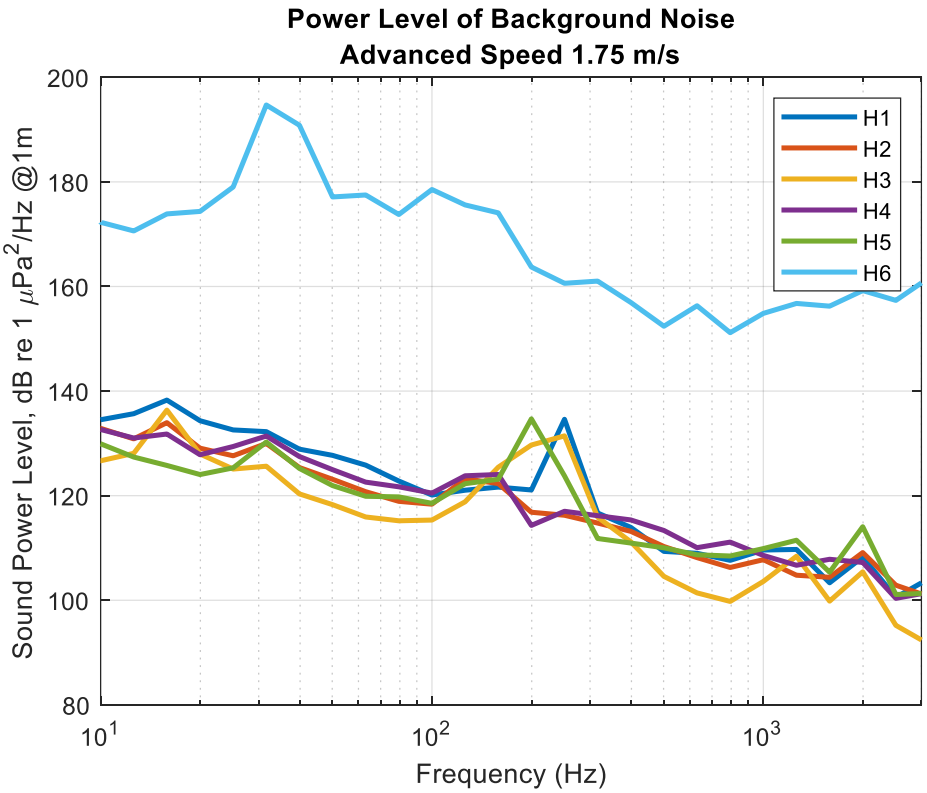


**B-4. Effect of Normalization When the Carriage at Rest (Reduced to 1 m)**

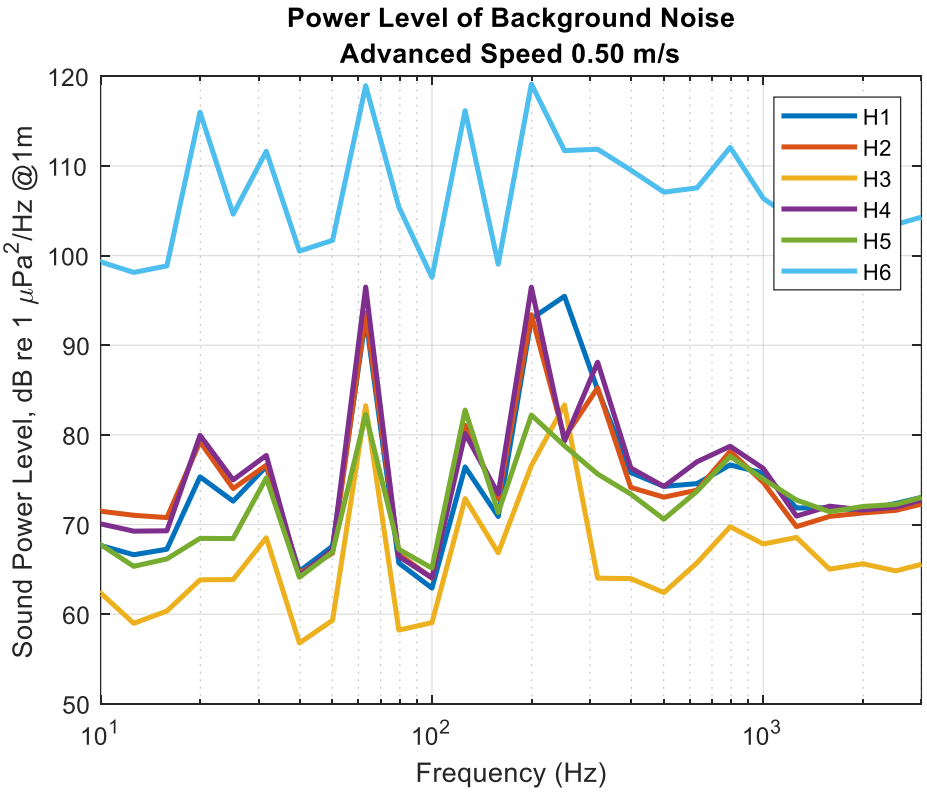

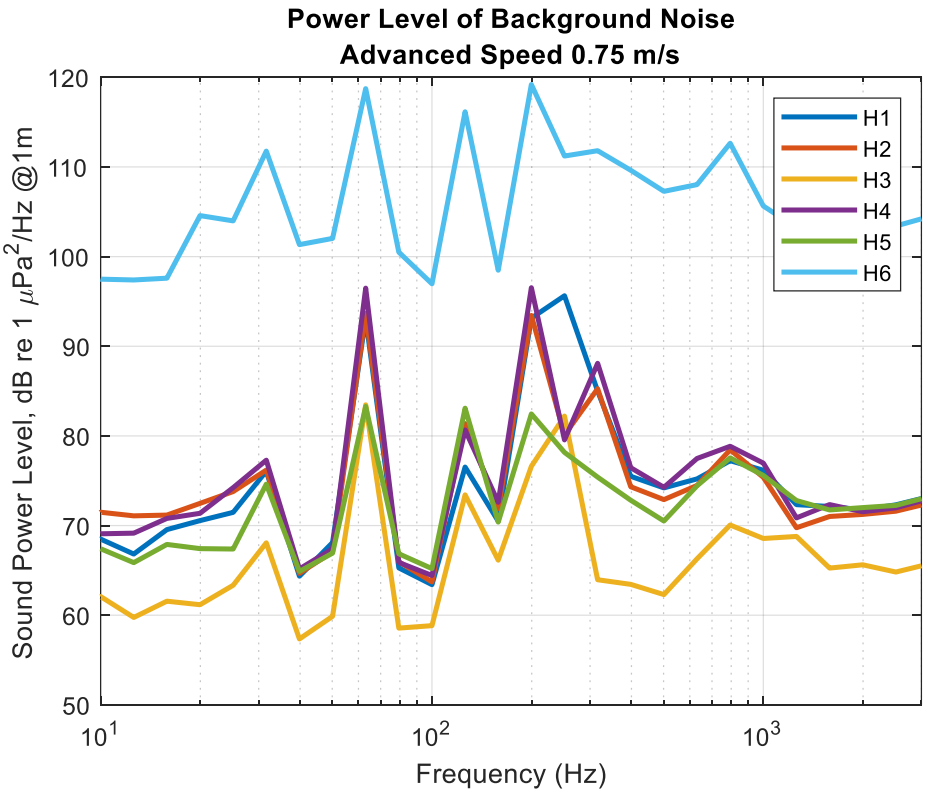
Power Level of Background Noise
Advanced Speed 0.75 m/s
Sound Power Level, dB re 1 μPa²/Hz @1m
Frequency (Hz)
H1
H2
H3
H4
H5
H6
120
110
100
90
80
70
60
50
10¹
10²
10³

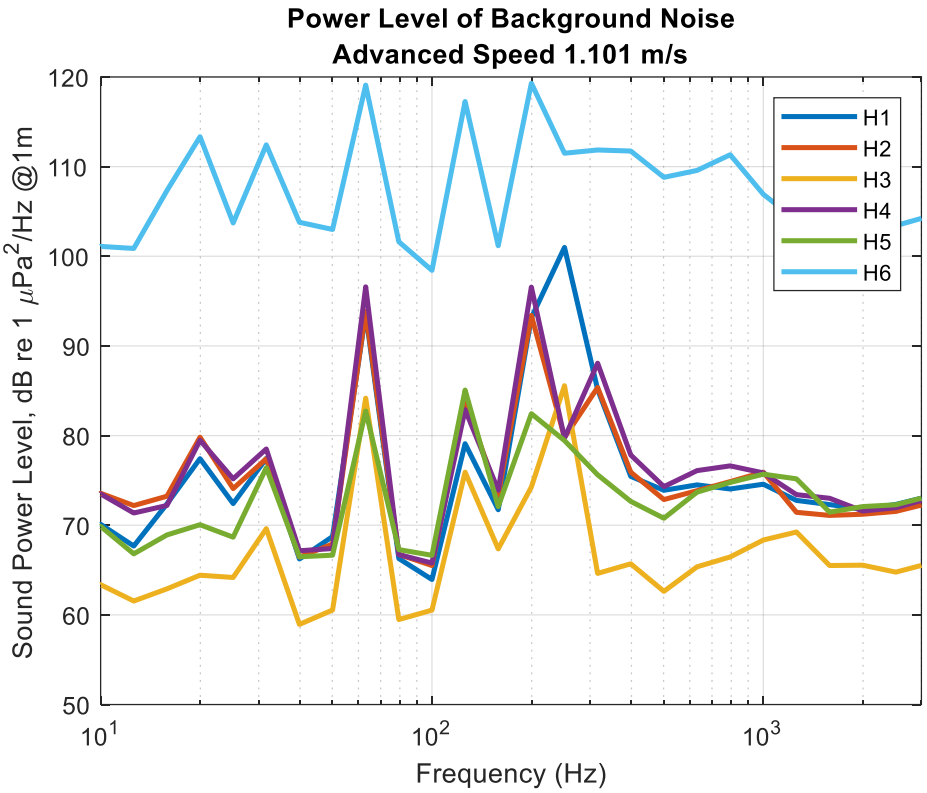
Power Level of Background Noise
Advanced Speed 1.101 m/s
Sound Power Level, dB re 1 μPa²/Hz @1m
Frequency (Hz)
H1
H2
H3
H4
H5
H6
120
110
100
90
80
70
60
50
10¹
10²
10³

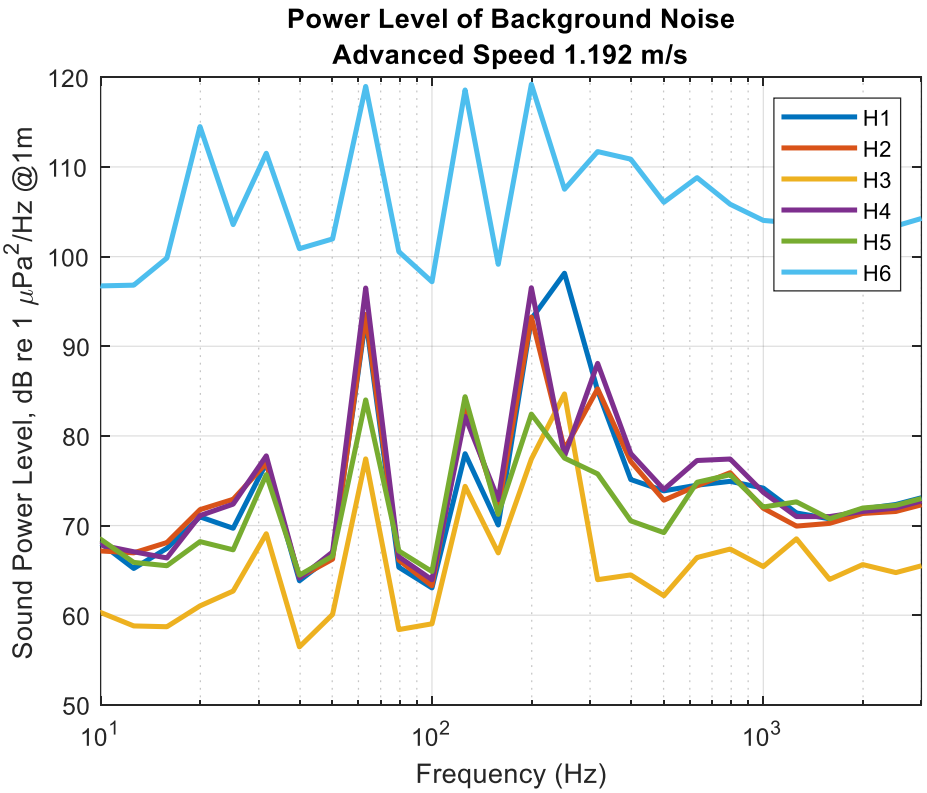
Power Level of Background Noise
Advanced Speed 1.192 m/s
Sound Power Level, dB re 1 μPa²/Hz @1m
Frequency (Hz)
H1
H2
H3
H4
H5
H6

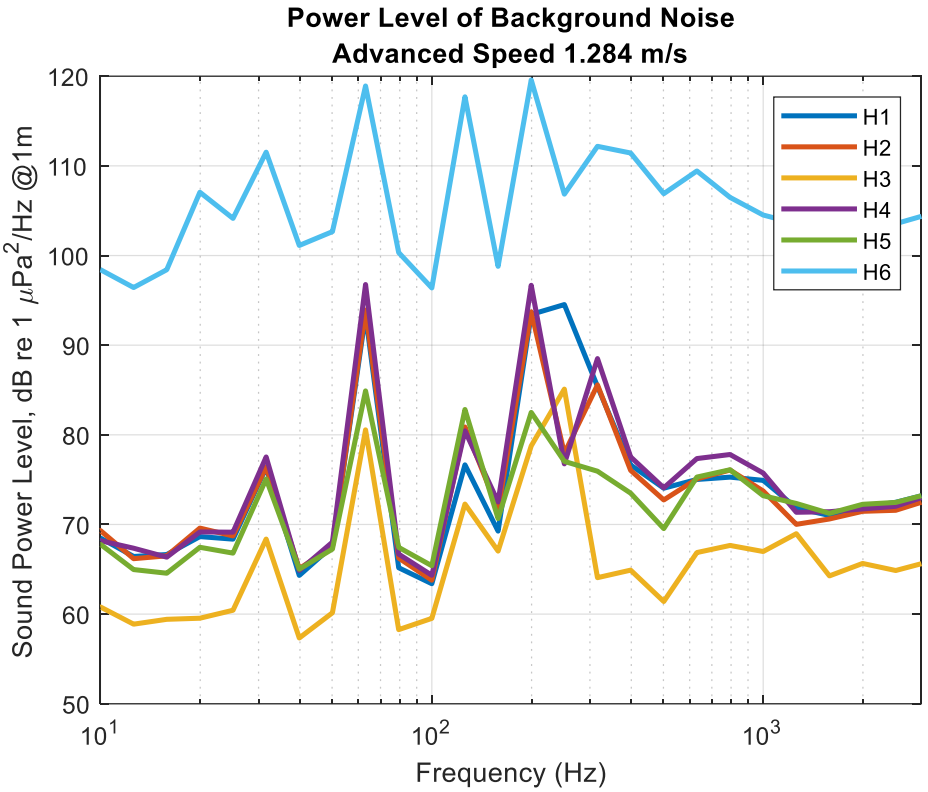
Power Level of Background Noise
Advanced Speed 1.284 m/s
Sound Power Level, dB re 1 μPa²/Hz @1m
Frequency (Hz)
H1
H2
H3
H4
H5
H6

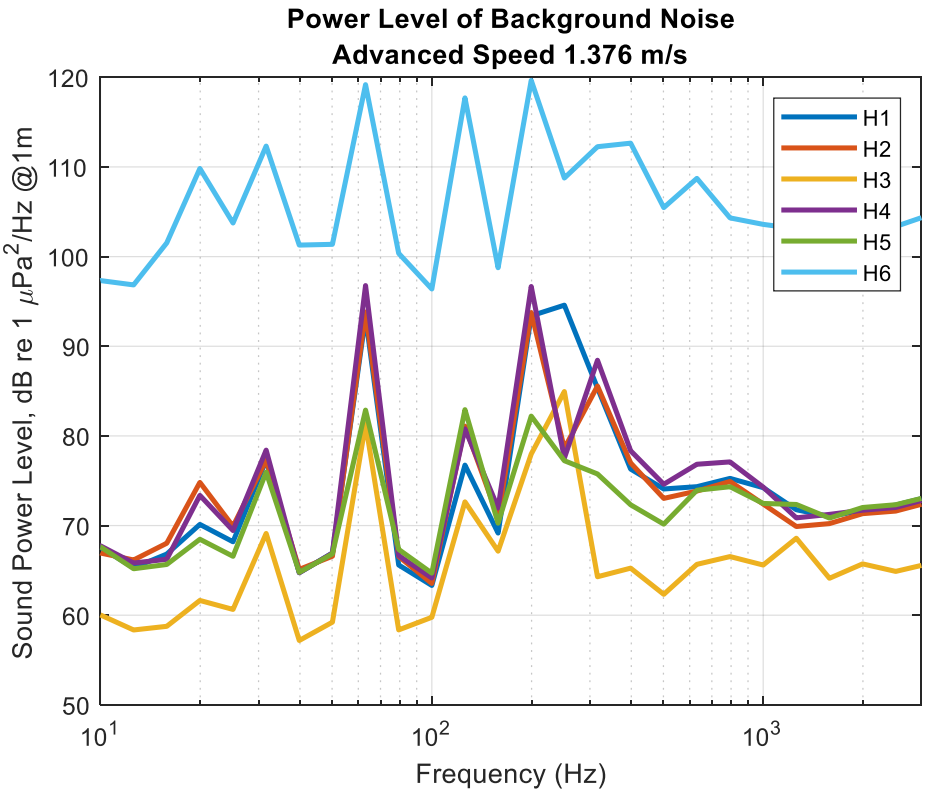
Power Level of Background Noise
Advanced Speed 1.376 m/s
Sound Power Level, dB re 1 μPa²/Hz @1m
Frequency (Hz)
H1
H2
H3
H4
H5
H6
120
110
100
90
80
70
60
50
10¹
10²
10³

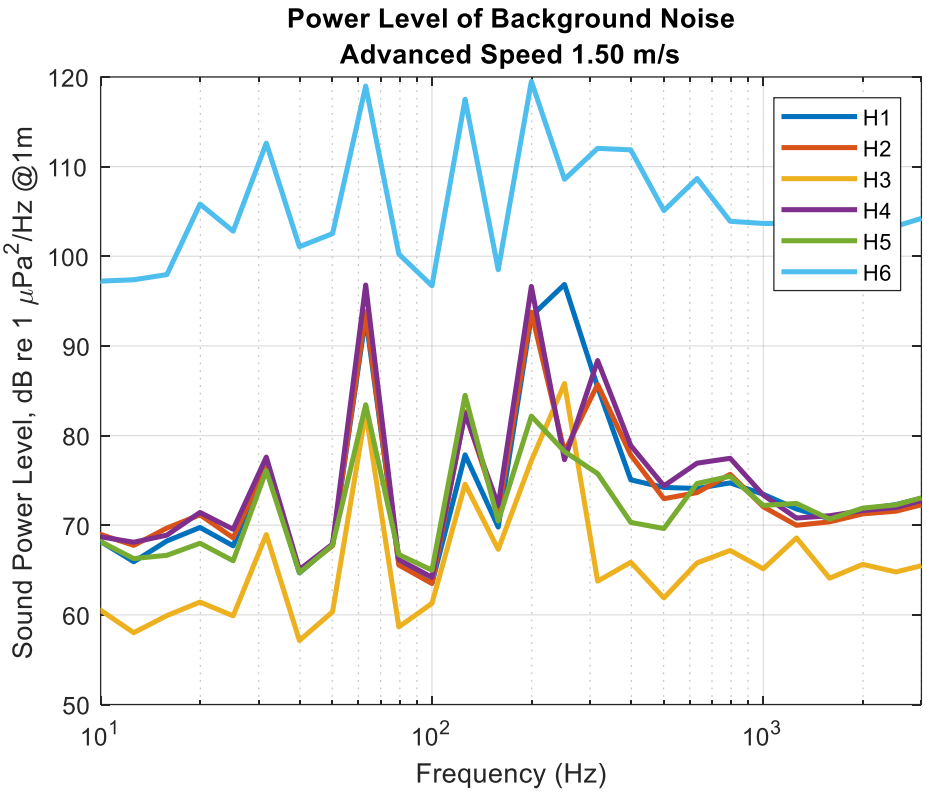
Power Level of Background Noise
Advanced Speed 1.50 m/s
Sound Power Level, dB re 1 μPa²/Hz @1m
Frequency (Hz)
H1
H2
H3
H4
H5
H6
120
110
100
90
80
70
60
50
10¹
10²
10³

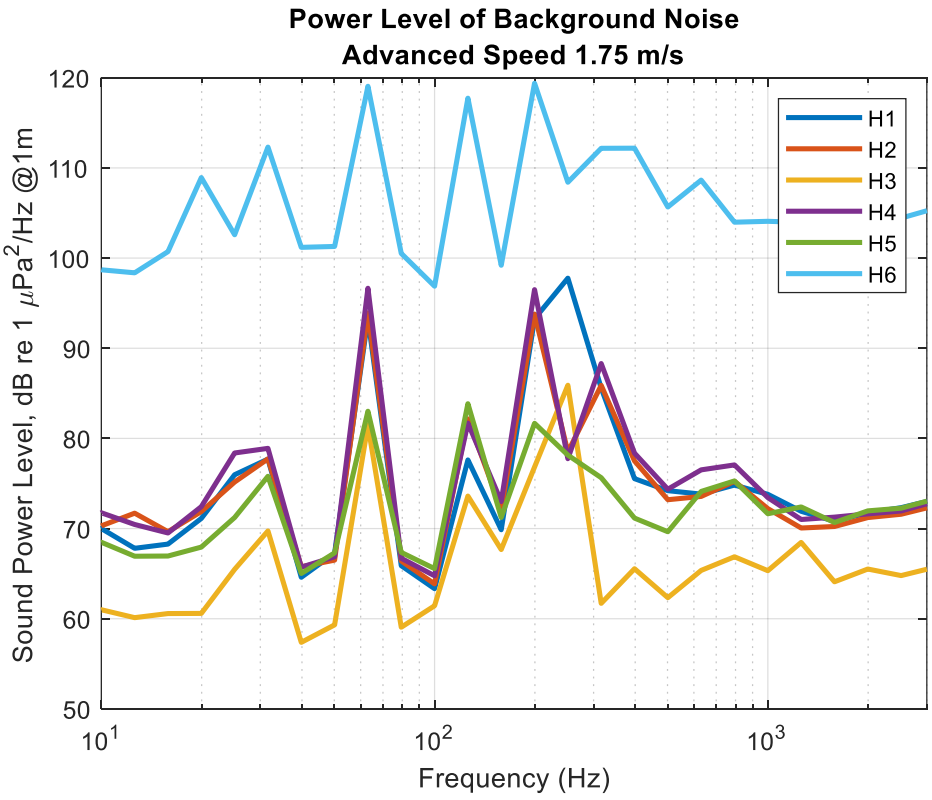


## B-5. Comparison of Background Noises at Different Advanced Speeds

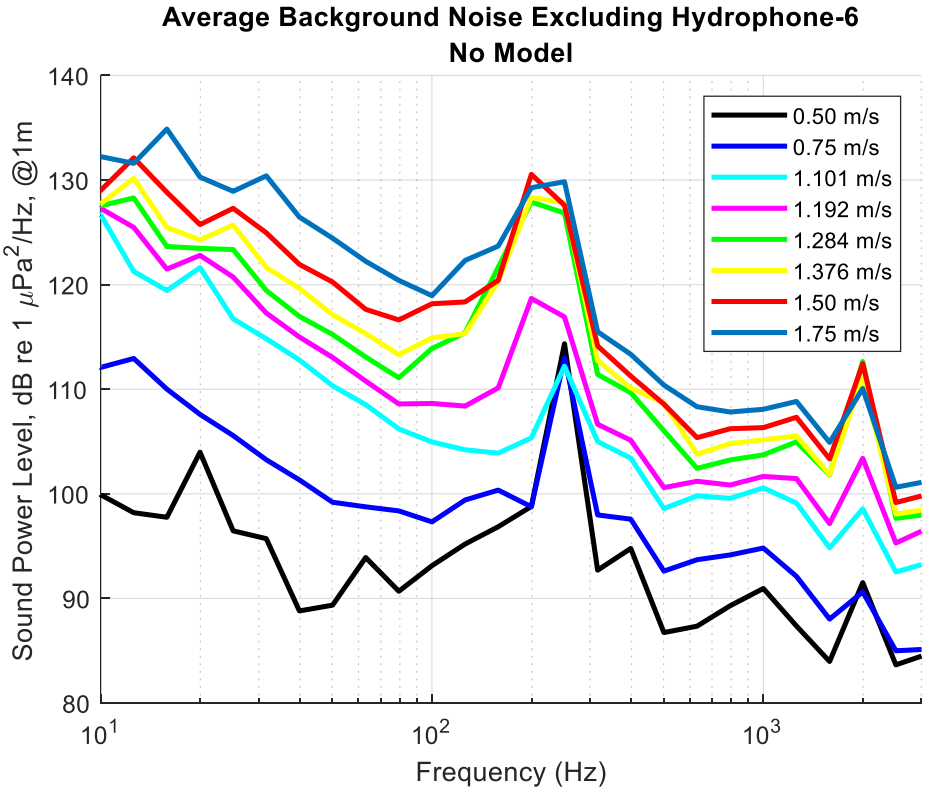

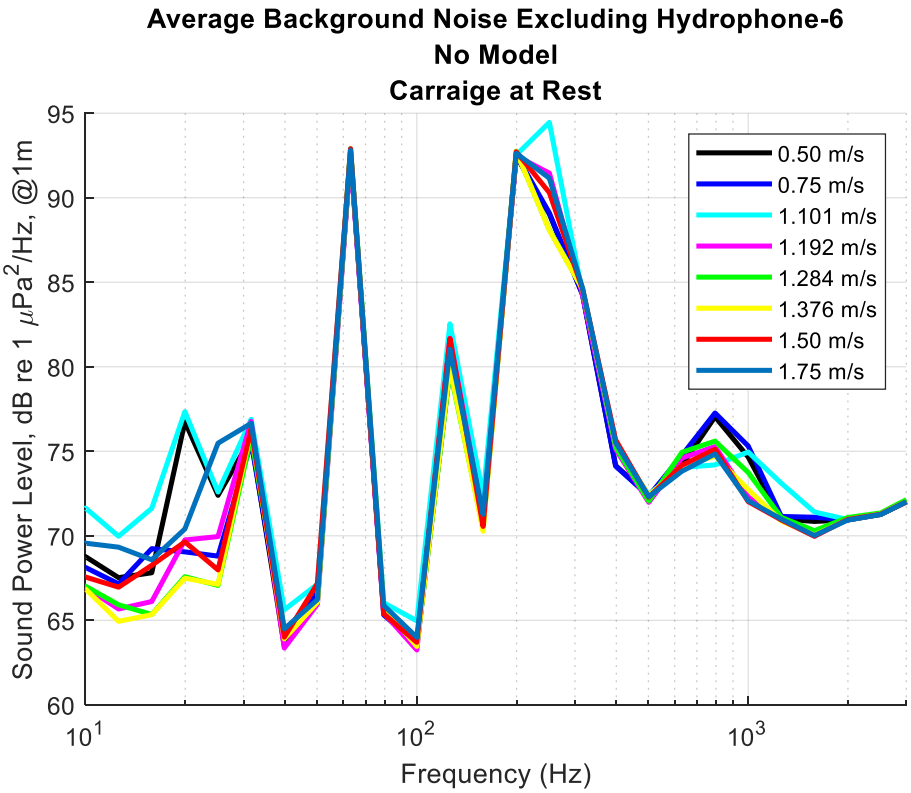


## B-6. Resistance Test (Model without Propeller)

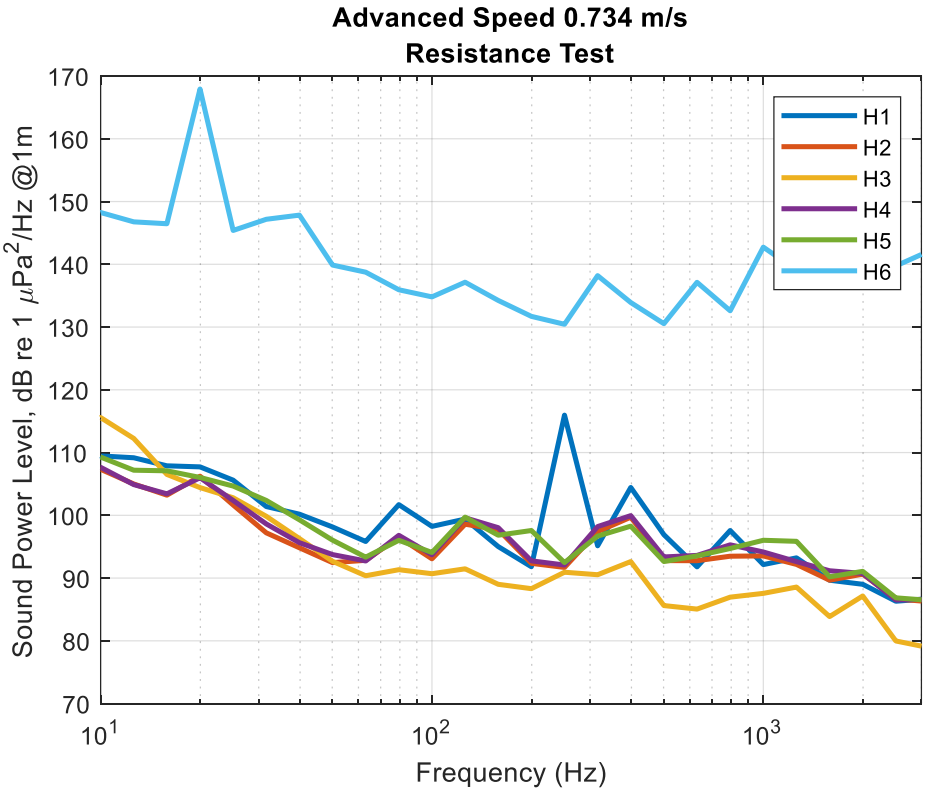

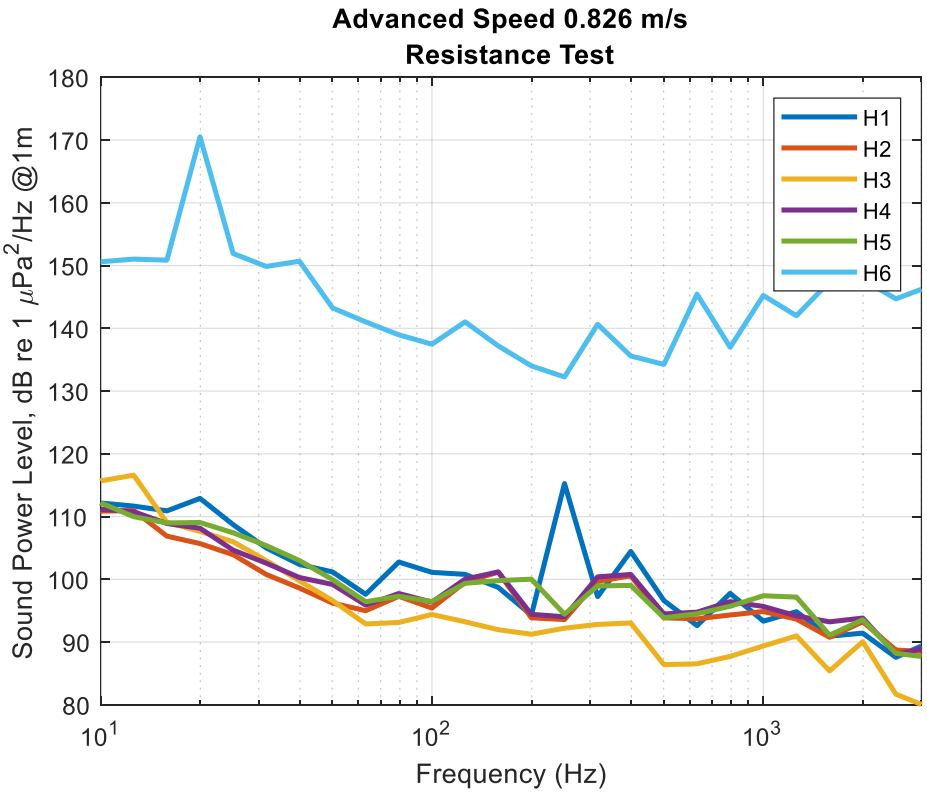
Advanced Speed 0.826 m/s
Resistance Test
Sound Power Level, dB re 1 μPa²/Hz @1m
Frequency (Hz)
H1
H2
H3
H4
H5
H6

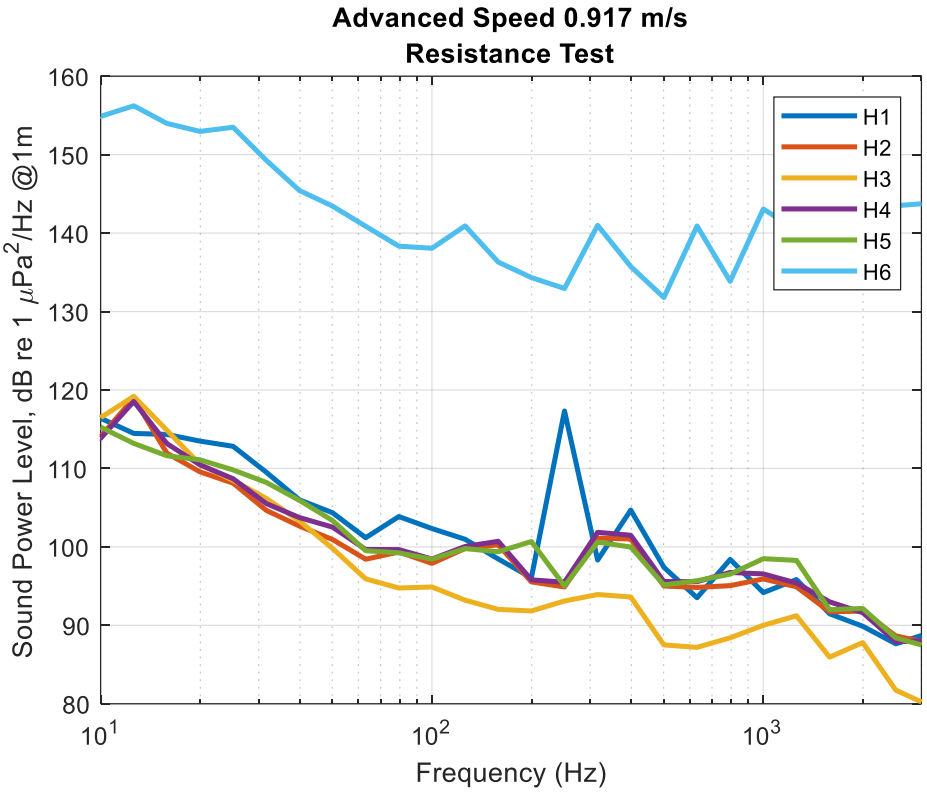
Advanced Speed 0.917 m/s
Resistance Test
Sound Power Level, dB re 1 μPa²/Hz @1m
Frequency (Hz)
H1
H2
H3
H4
H5
H6

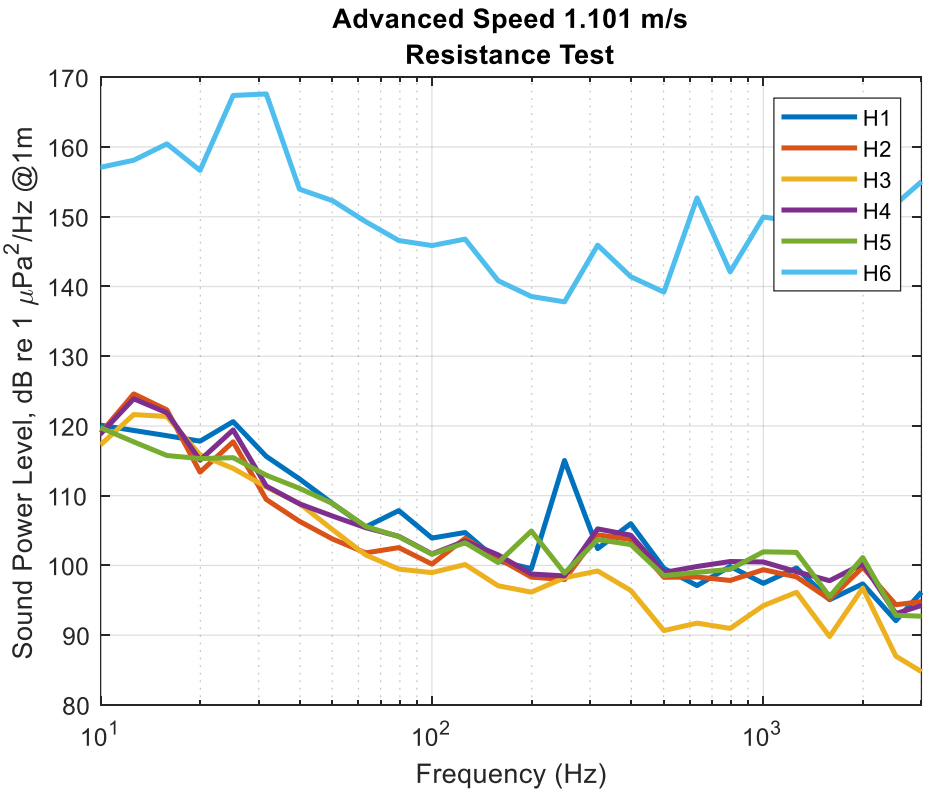
Advanced Speed 1.101 m/s
Resistance Test
Sound Power Level, dB re 1 μPa²/Hz @1m
Frequency (Hz)
H1
H2
H3
H4
H5
H6

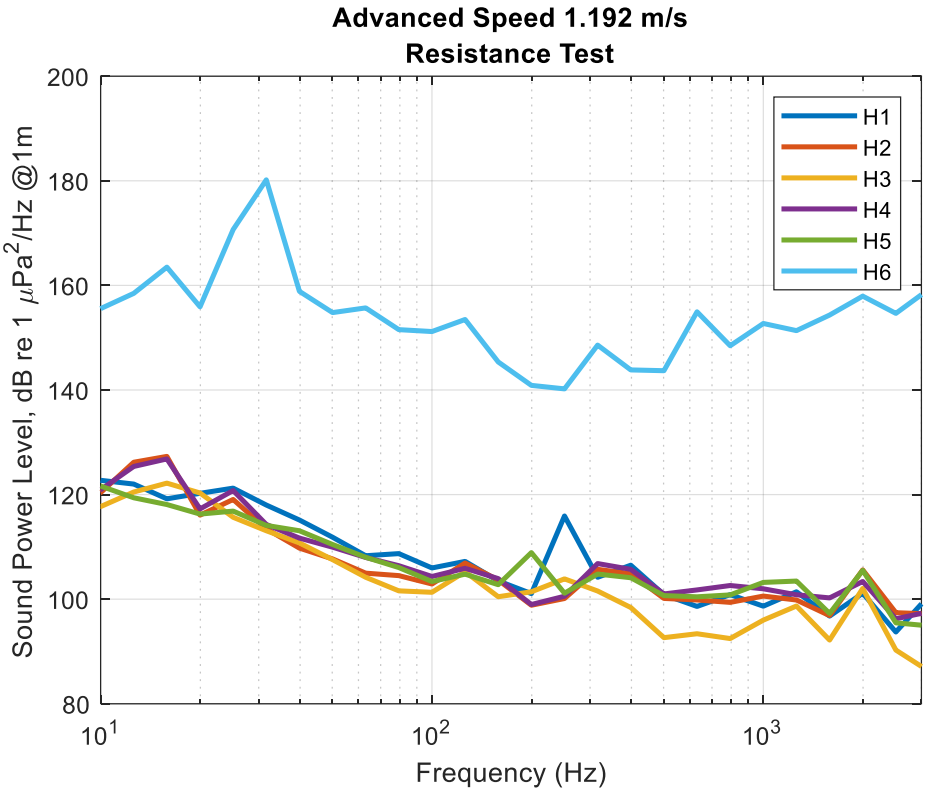
Advanced Speed 1.192 m/s
Resistance Test
Sound Power Level, dB re 1 μPa²/Hz @1m
Frequency (Hz)
H1
H2
H3
H4
H5
H6

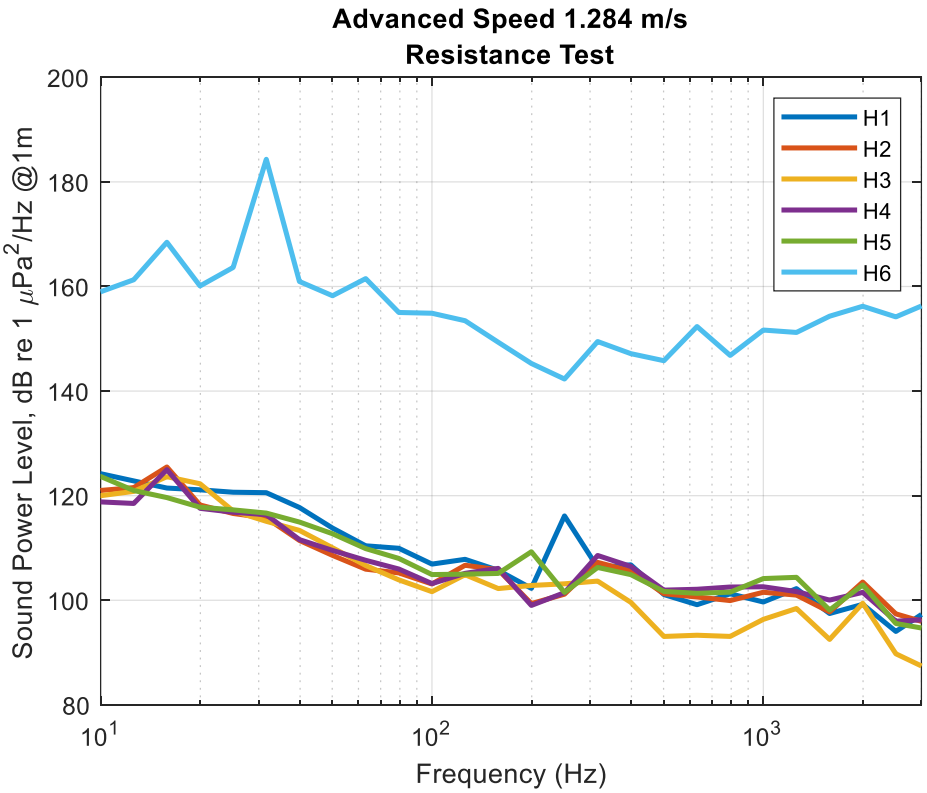
Advanced Speed 1.284 m/s
Resistance Test
Sound Power Level, dB re 1 μPa²/Hz @1m
Frequency (Hz)
H1
H2
H3
H4
H5
H6

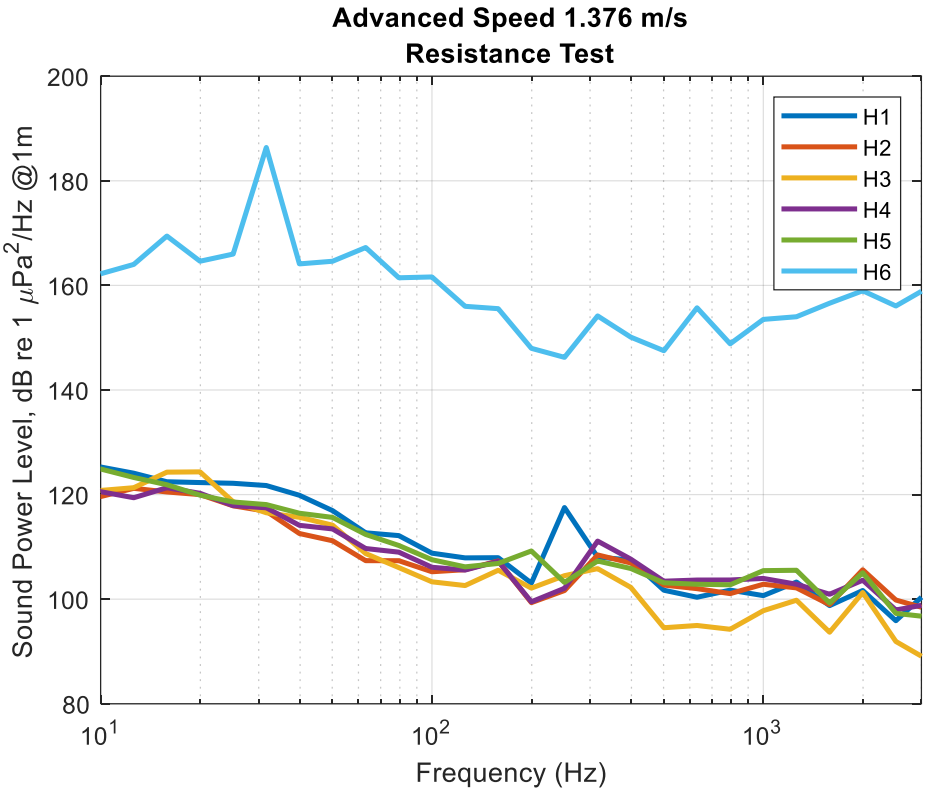
Advanced Speed 1.376 m/s
Resistance Test
Sound Power Level, dB re 1 μPa²/Hz @1m
Frequency (Hz)
H1
H2
H3
H4
H5
H6

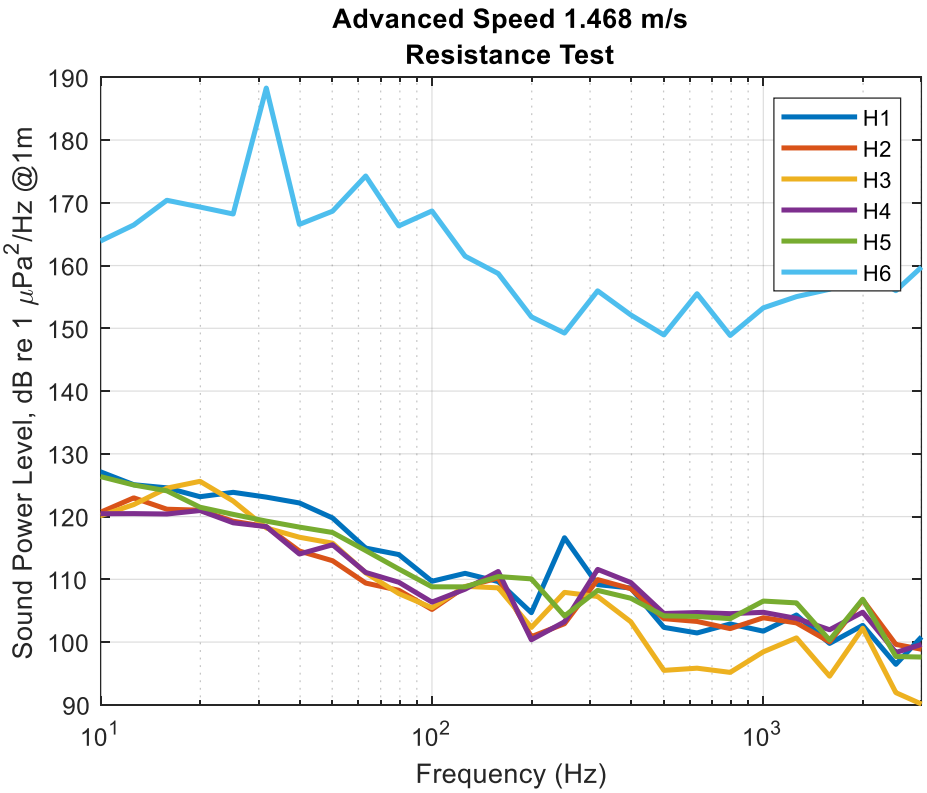
Advanced Speed 1.468 m/s
Resistance Test
Sound Power Level, dB re 1 μPa²/Hz @1m
Frequency (Hz)
H1
H2
H3
H4
H5
H6

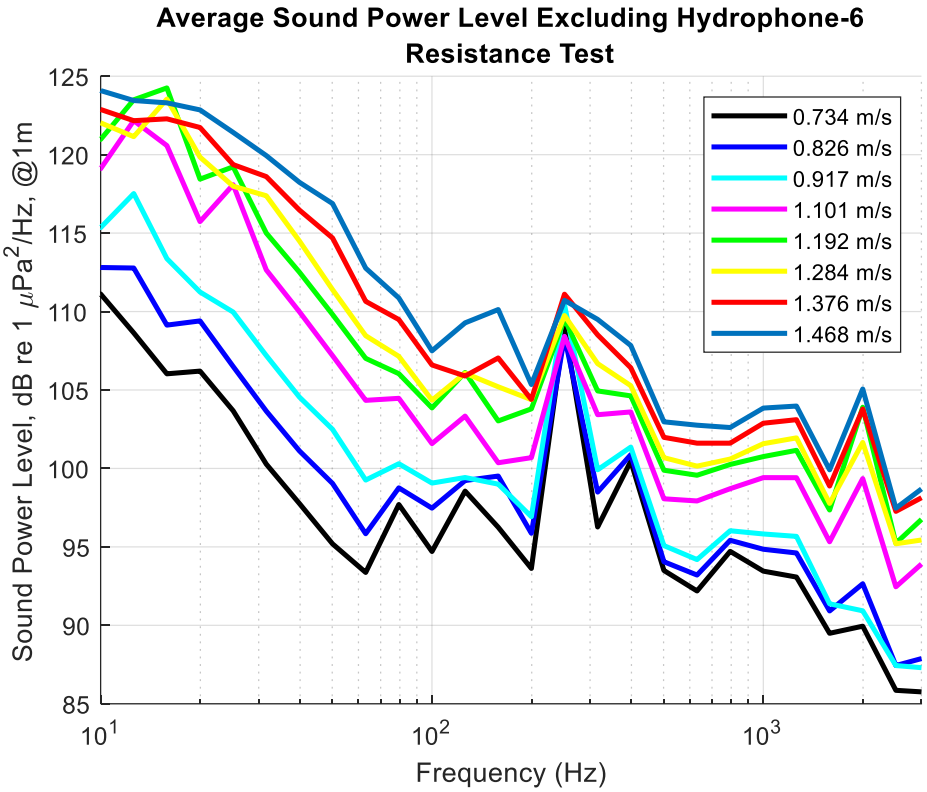
Average Sound Power Level Excluding Hydrophone-6
Resistance Test
Sound Power Level, dB re 1 μPa²/Hz, @1m
Frequency (Hz)
0.734 m/s
0.826 m/s
0.917 m/s
1.101 m/s
1.192 m/s
1.284 m/s
1.376 m/s
1.468 m/s

## B-7. Effect of RPS on Sound Power Level during Self-Propulsion

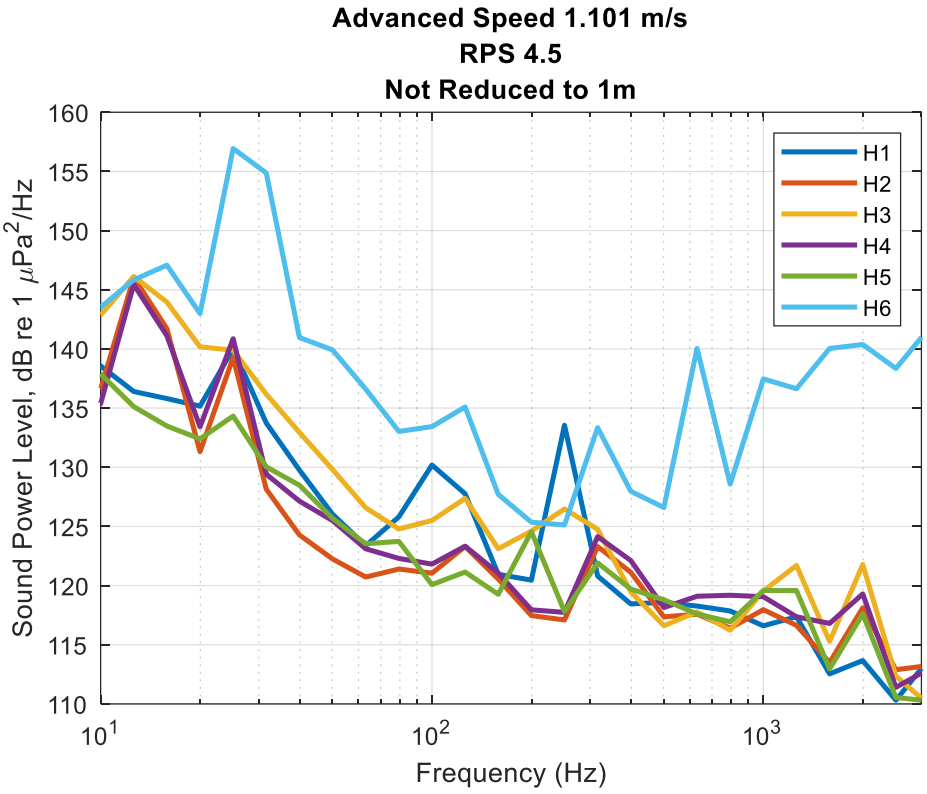


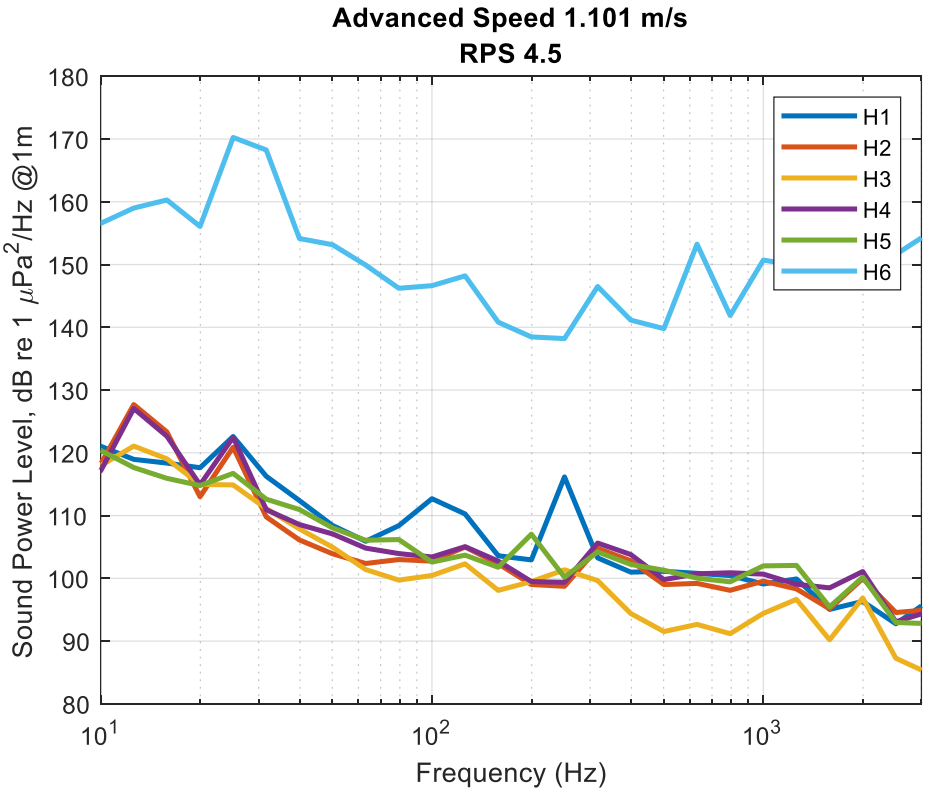

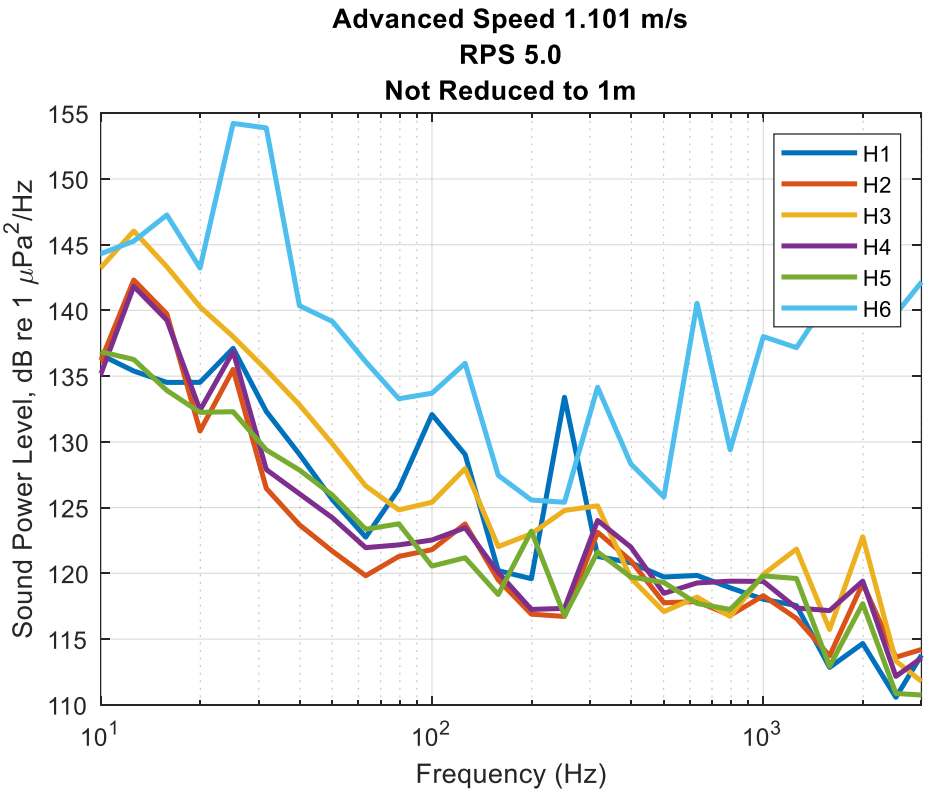
Advanced Speed 1.101 m/s
RPS 5.0
Not Reduced to 1m
Sound Power Level, dB re 1 μPa²/Hz
Frequency (Hz)
H1
H2
H3
H4
H5
H6

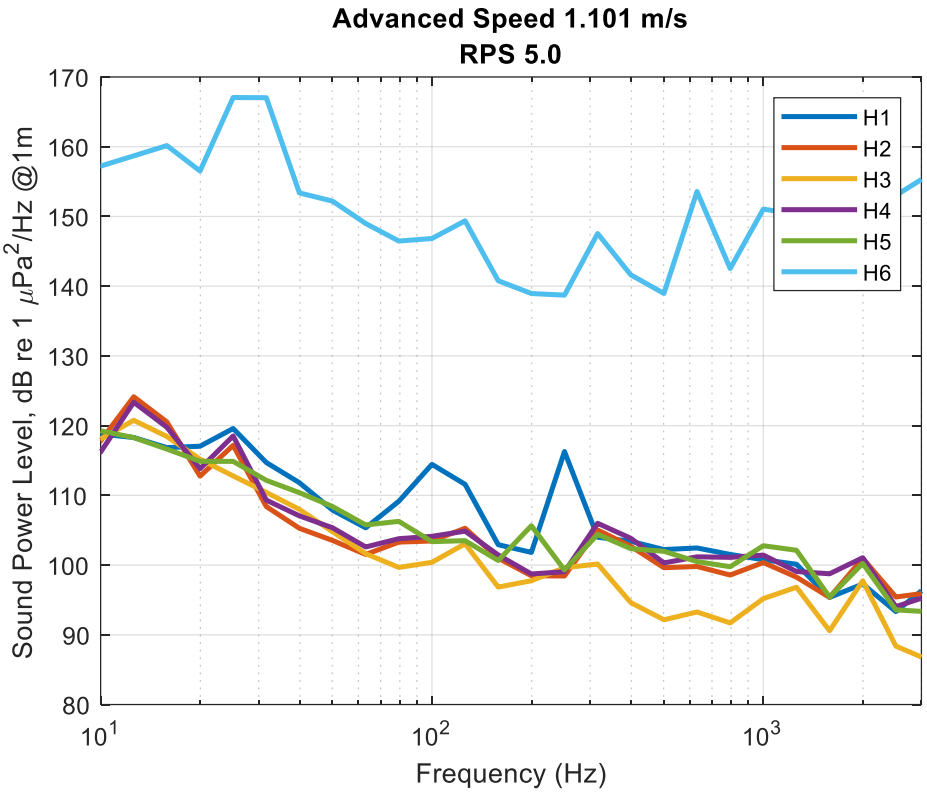
Advanced Speed 1.101 m/s
RPS 5.0
Sound Power Level, dB re 1 μPa²/Hz @1m
Frequency (Hz)
H1
H2
H3
H4
H5
H6

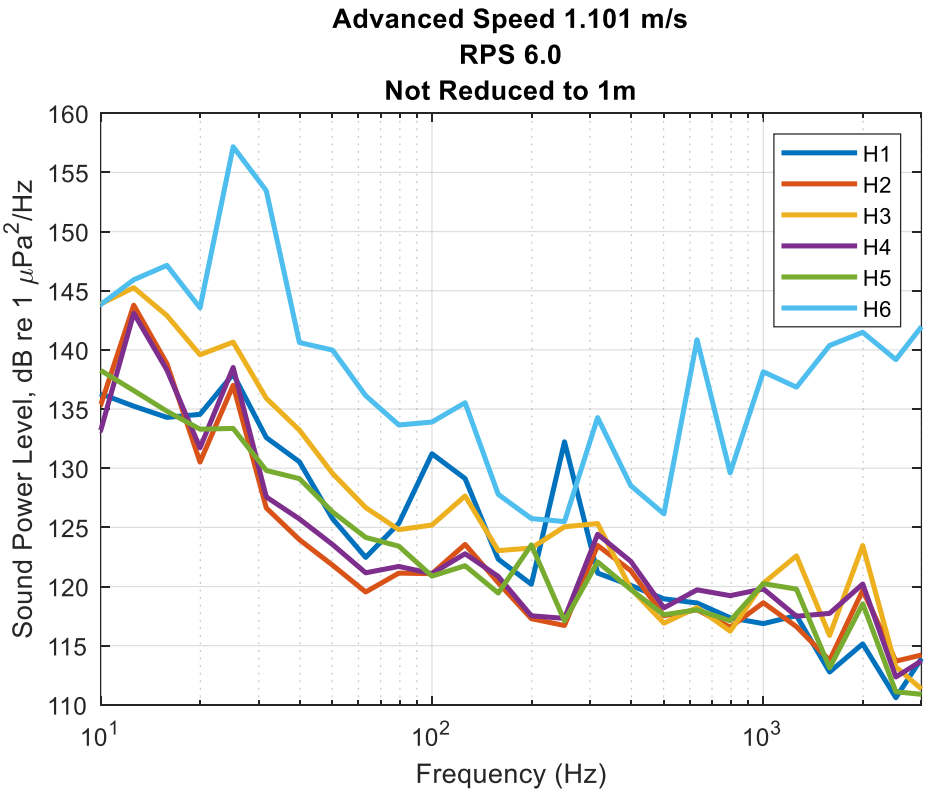
Advanced Speed 1.101 m/s
RPS 6.0
Not Reduced to 1m
Sound Power Level, dB re 1 μPa²/Hz
Frequency (Hz)
H1
H2
H3
H4
H5
H6

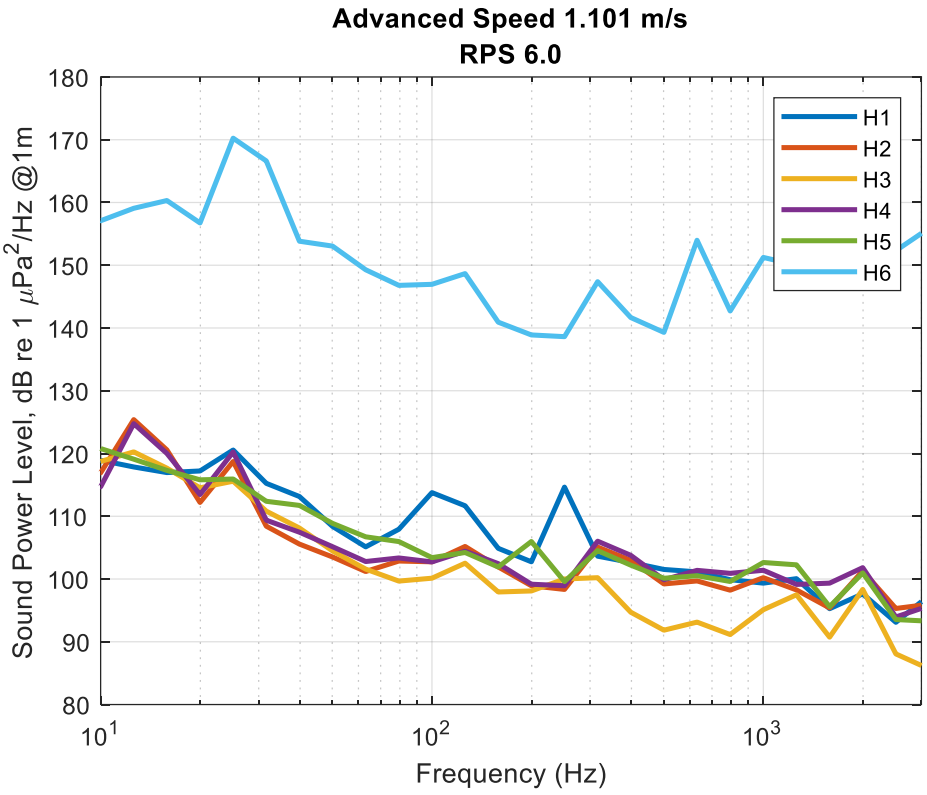
Advanced Speed 1.101 m/s
RPS 6.0
Sound Power Level, dB re 1 μPa²/Hz @1m
Frequency (Hz)
H1
H2
H3
H4
H5
H6

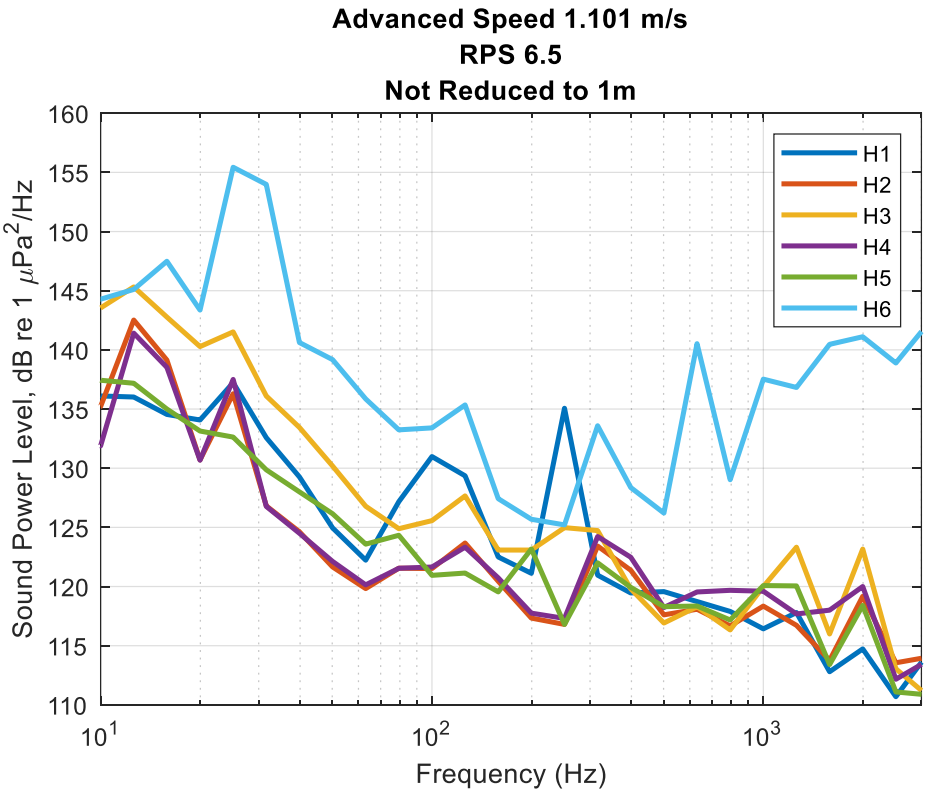
Advanced Speed 1.101 m/s
RPS 6.5
Not Reduced to 1m
Sound Power Level, dB re 1 μPa²/Hz
Frequency (Hz)
H1
H2
H3
H4
H5
H6

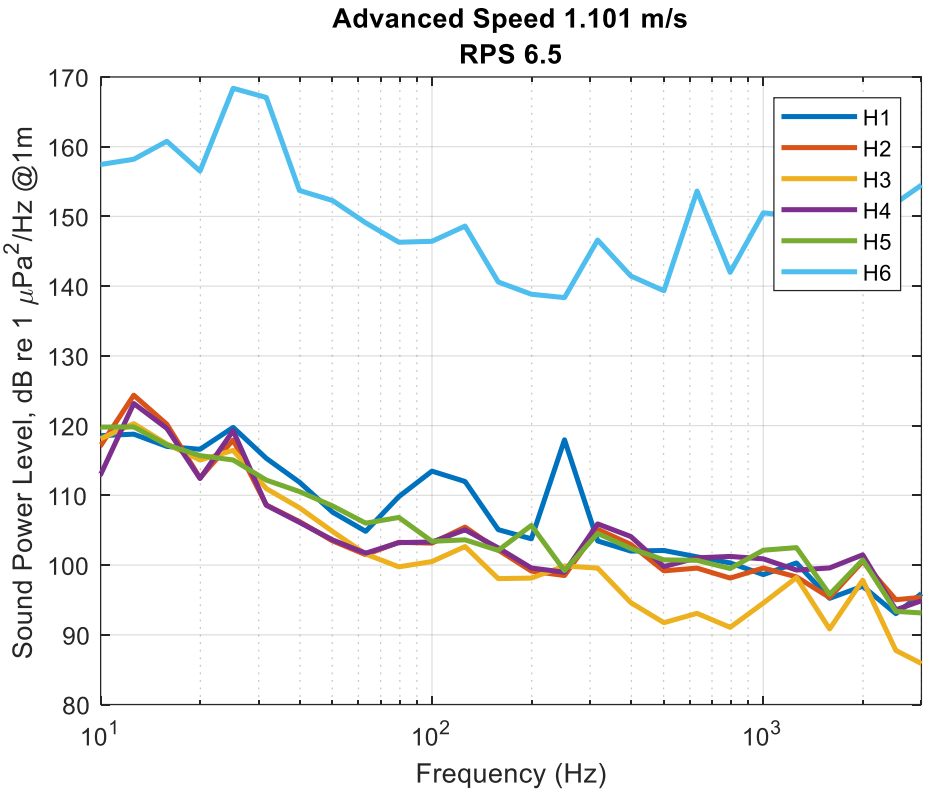
Advanced Speed 1.101 m/s
RPS 6.5
Sound Power Level, dB re 1 μPa²/Hz @1m
Frequency (Hz)
H1
H2
H3
H4
H5
H6

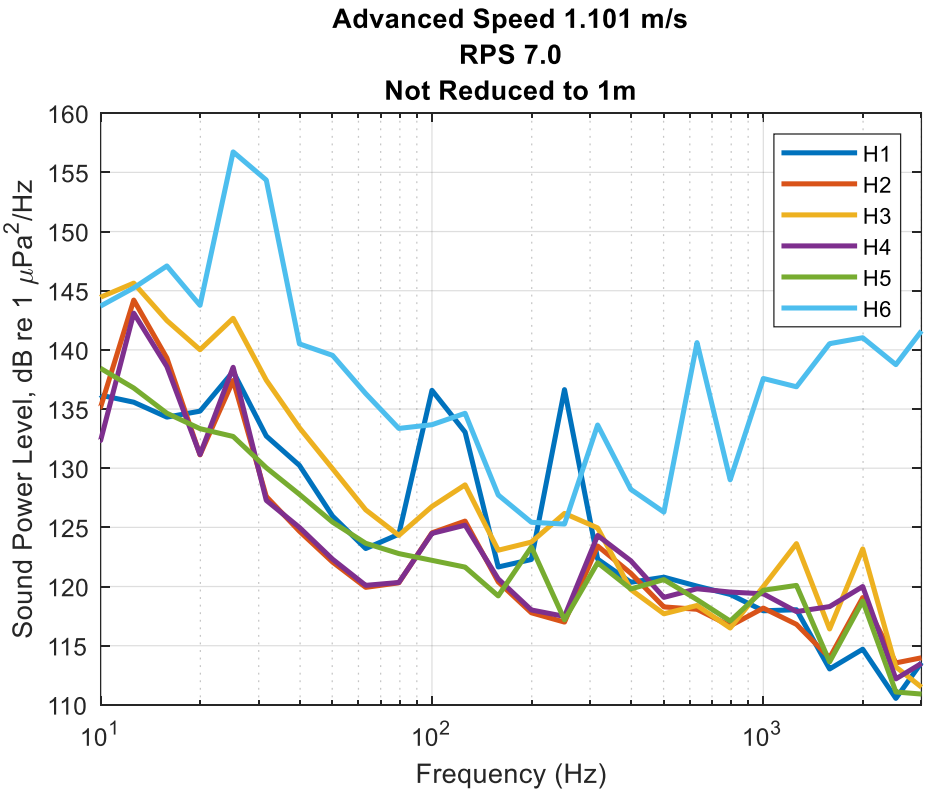
Advanced Speed 1.101 m/s
RPS 7.0
Not Reduced to 1m
Sound Power Level, dB re 1 μPa²/Hz
Frequency (Hz)
H1
H2
H3
H4
H5
H6

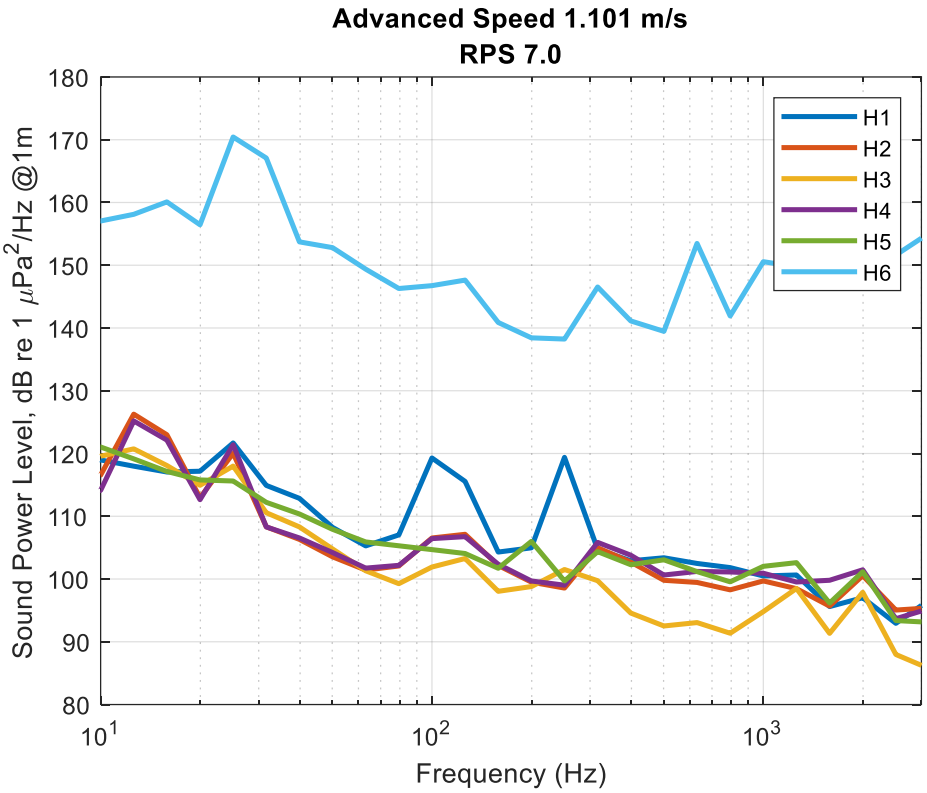
Advanced Speed 1.101 m/s
RPS 7.0
Sound Power Level, dB re 1 μPa²/Hz @1m
Frequency (Hz)
H1
H2
H3
H4
H5
H6

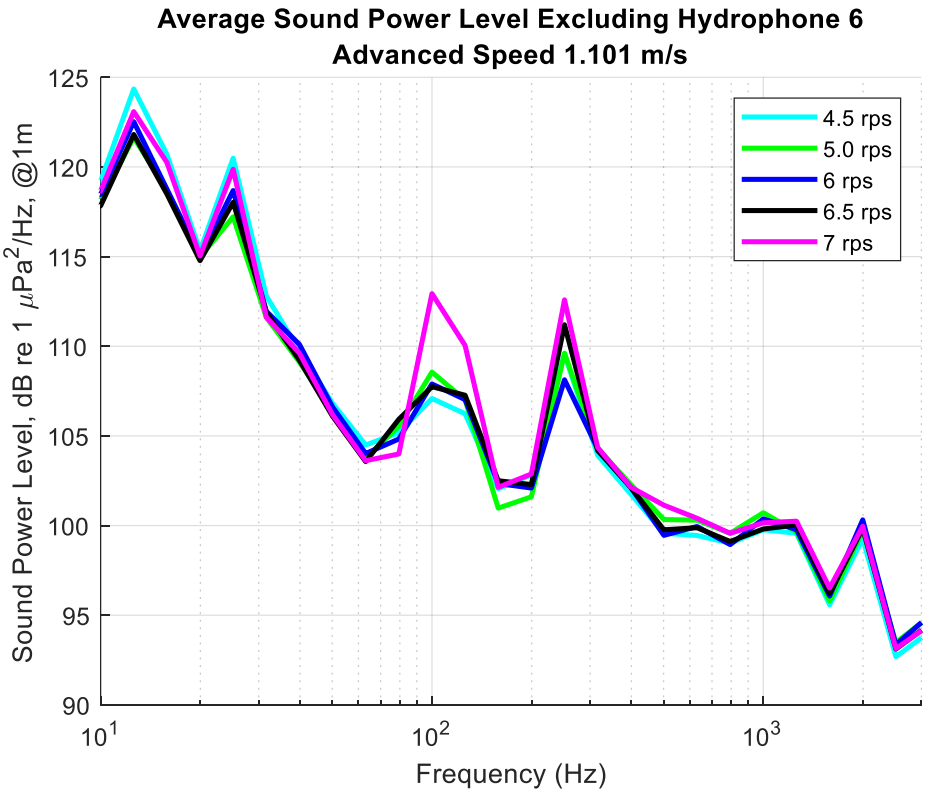
Average Sound Power Level Excluding Hydrophone 6
Advanced Speed 1.101 m/s
Sound Power Level, dB re 1 μPa²/Hz, @1m
Frequency (Hz)
4.5 rps
5.0 rps
6 rps
6.5 rps
7 rps

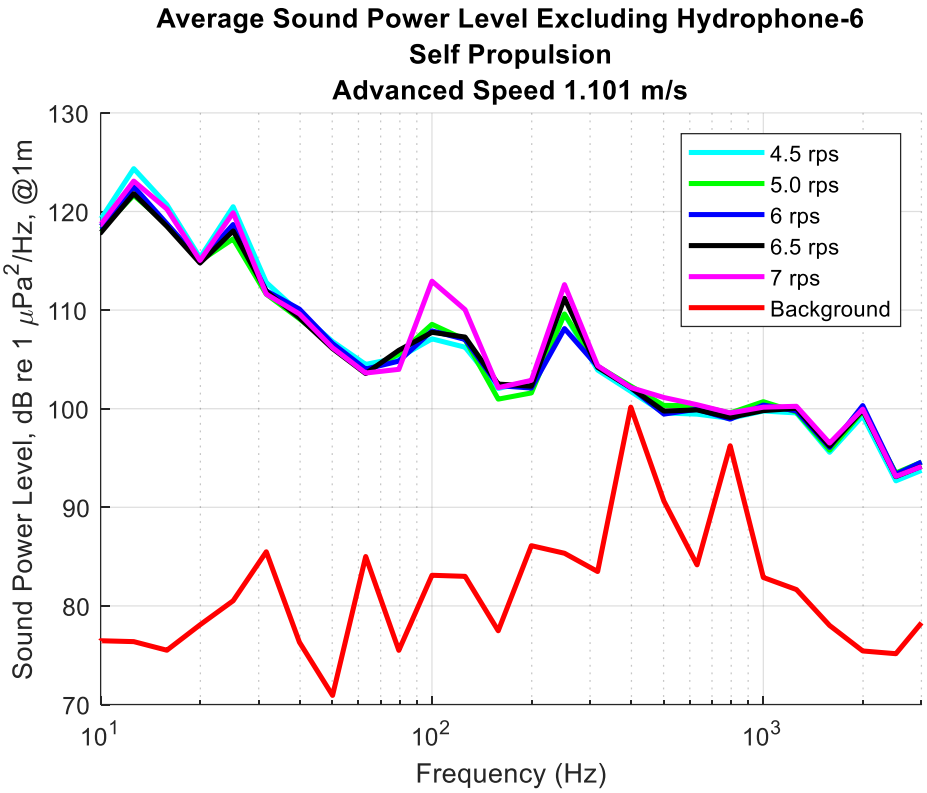
Average Sound Power Level Excluding Hydrophone-6
Self Propulsion
Advanced Speed 1.101 m/s
Sound Power Level, dB re 1 μPa²/Hz, @1m
Frequency (Hz)
4.5 rps
5.0 rps
6 rps
6.5 rps
7 rps
Background

## B-8. Effect of RPS on Different Hydrophones

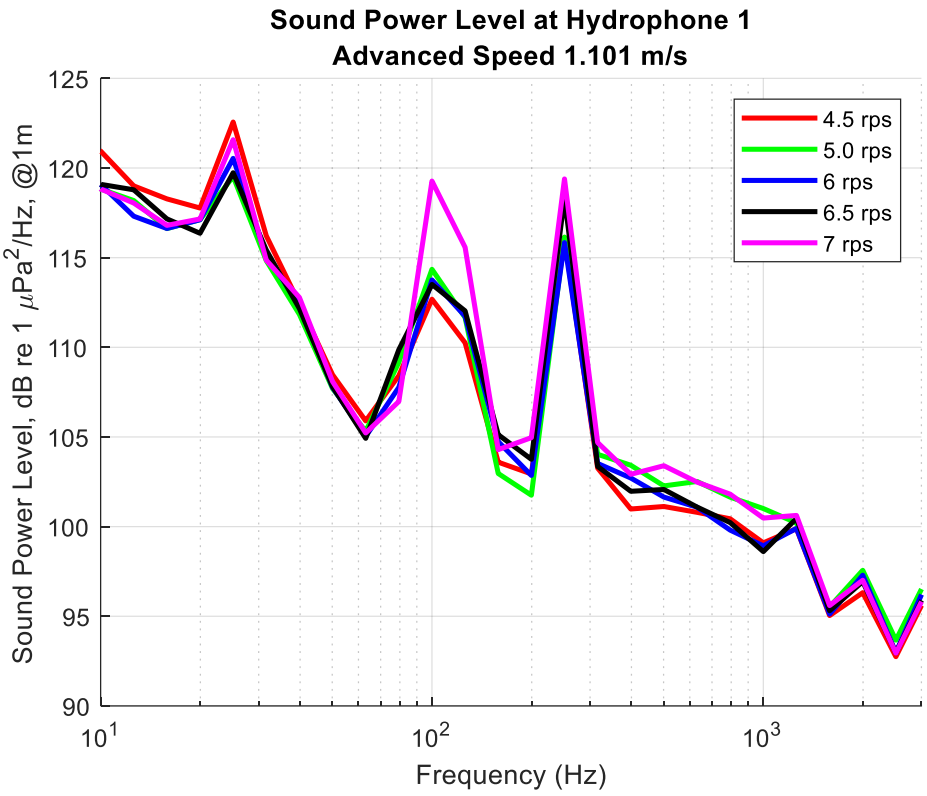


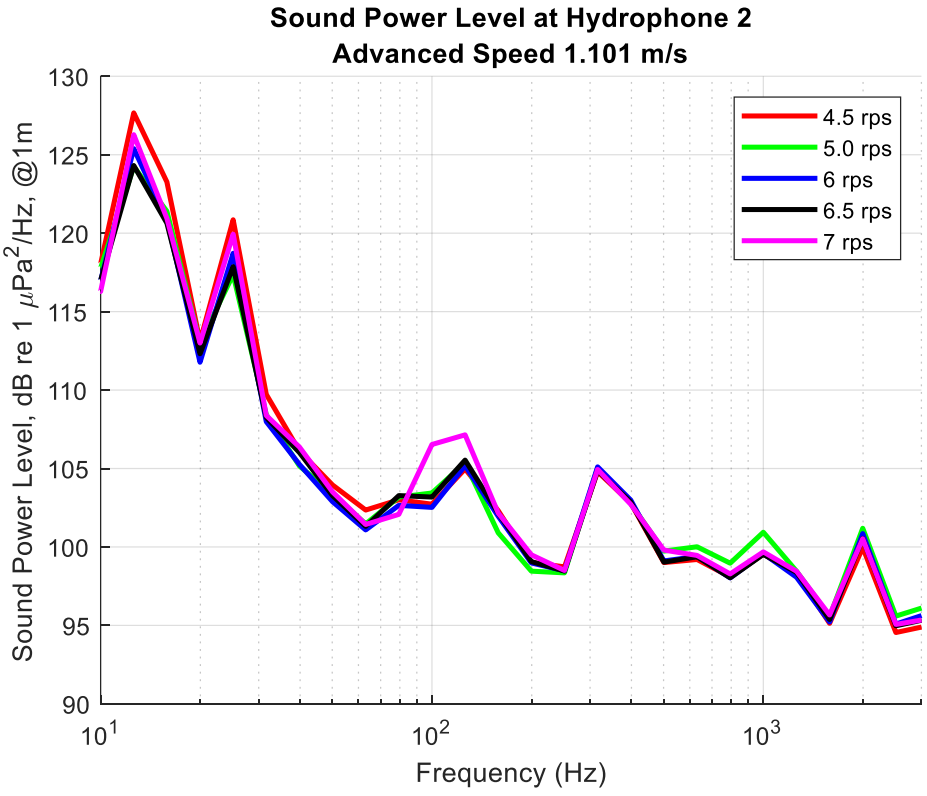

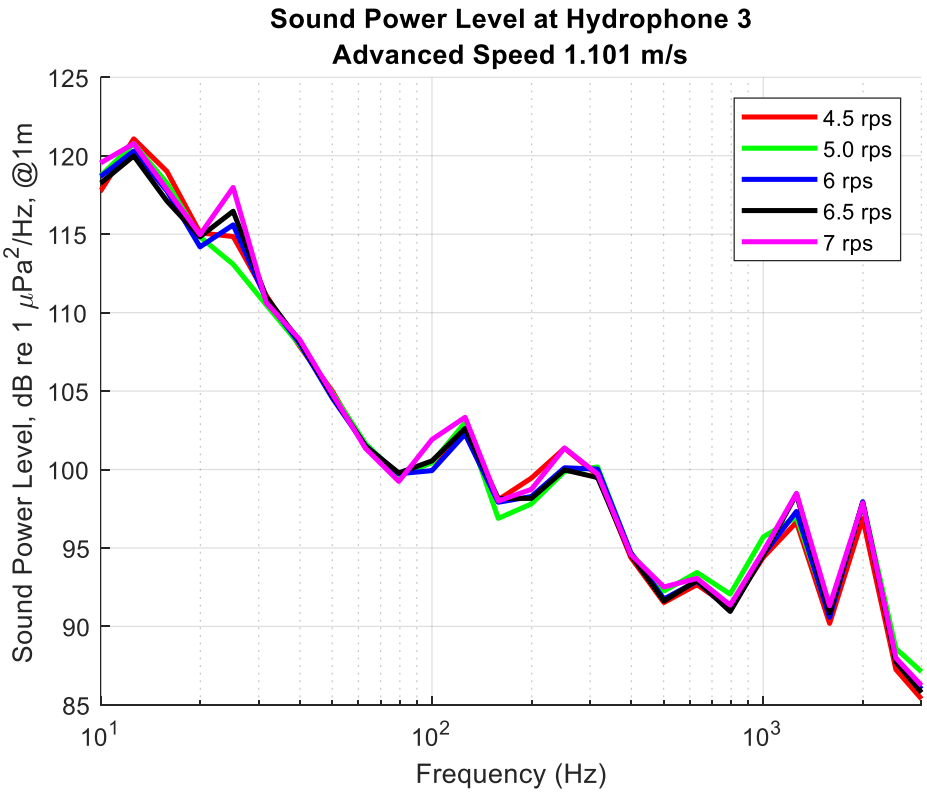
Sound Power Level at Hydrophone 3
Advanced Speed 1.101 m/s
Sound Power Level, dB re 1 μPa²/Hz, @1m
Frequency (Hz)
4.5 rps
5.0 rps
6 rps
6.5 rps
7 rps
125
120
115
110
105
100
95
90
85
10¹
10²
10³

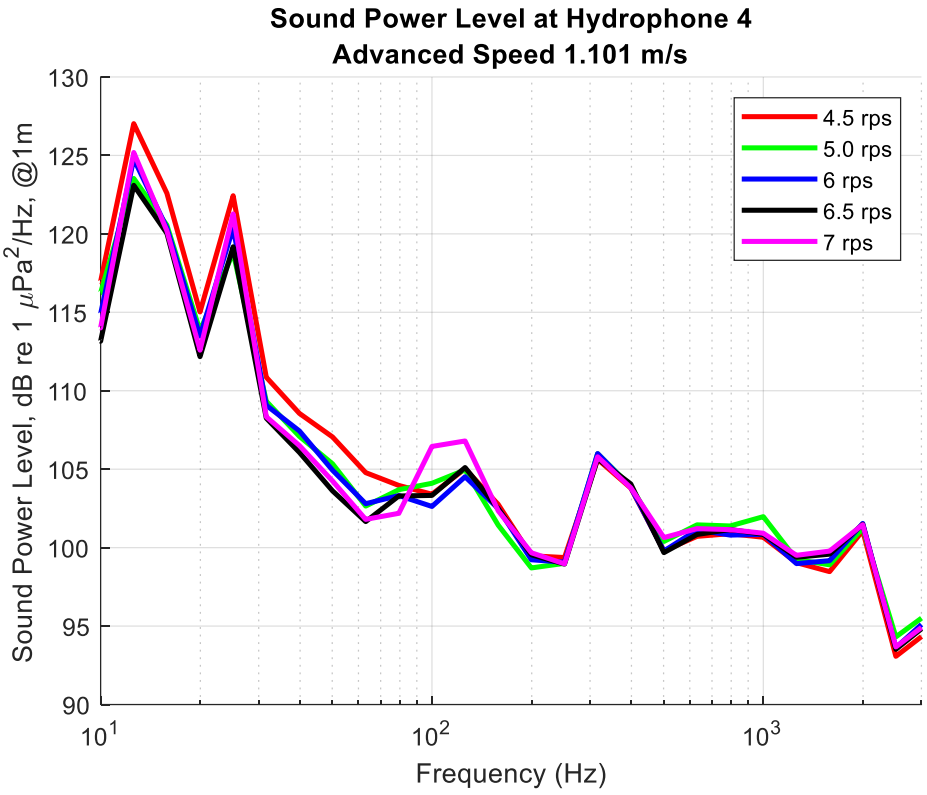
Sound Power Level at Hydrophone 4
Advanced Speed 1.101 m/s
Sound Power Level, dB re 1 μPa²/Hz, @1m
Frequency (Hz)
4.5 rps
5.0 rps
6 rps
6.5 rps
7 rps
130
125
120
115
110
105
100
95
90
10¹
10²
10³

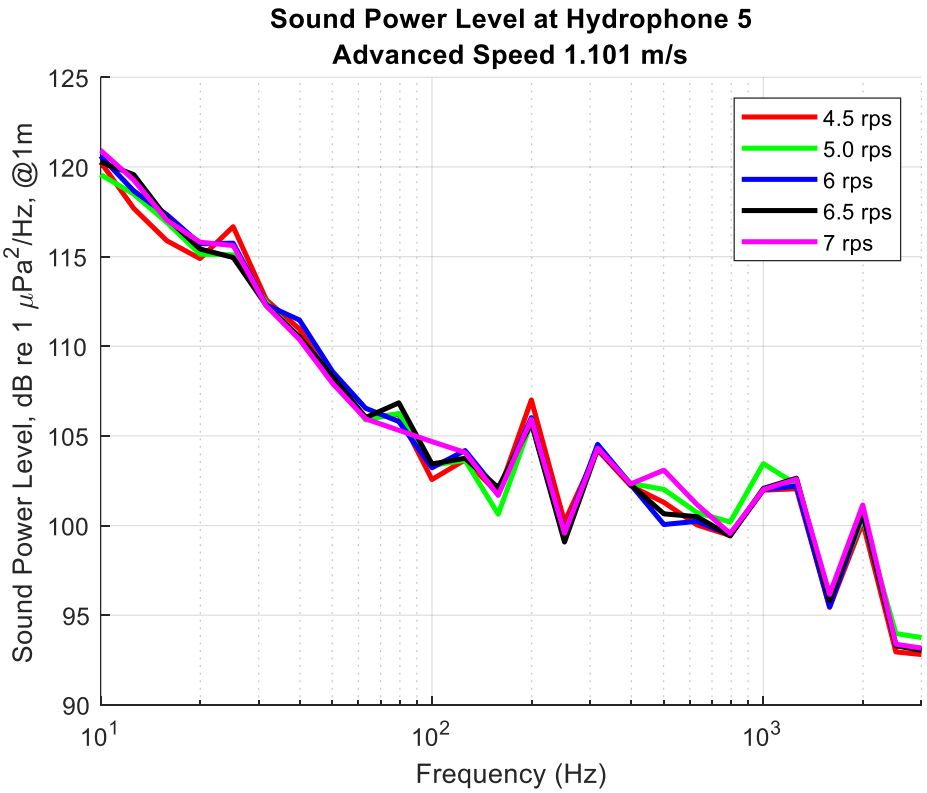
Sound Power Level at Hydrophone 5
Advanced Speed 1.101 m/s
Sound Power Level, dB re 1 μPa²/Hz, @1m
Frequency (Hz)
4.5 rps
5.0 rps
6 rps
6.5 rps
7 rps
125
120
115
110
105
100
95
90
10¹
10²
10³

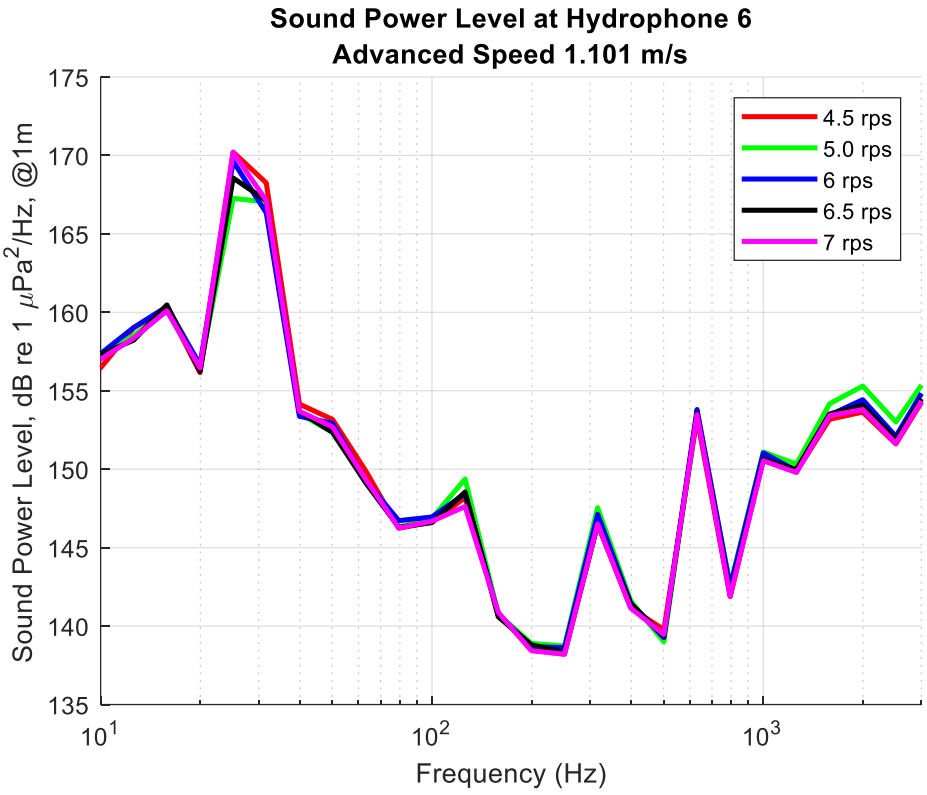
Sound Power Level at Hydrophone 6
Advanced Speed 1.101 m/s
Sound Power Level, dB re 1 μPa²/Hz, @1m
Frequency (Hz)
4.5 rps
5.0 rps
6 rps
6.5 rps
7 rps
175
170
165
160
155
150
145
140
135
10¹
10²
10³

## B-9. Effect of Advanced Speeds on Sound Power level (Constant RPS)

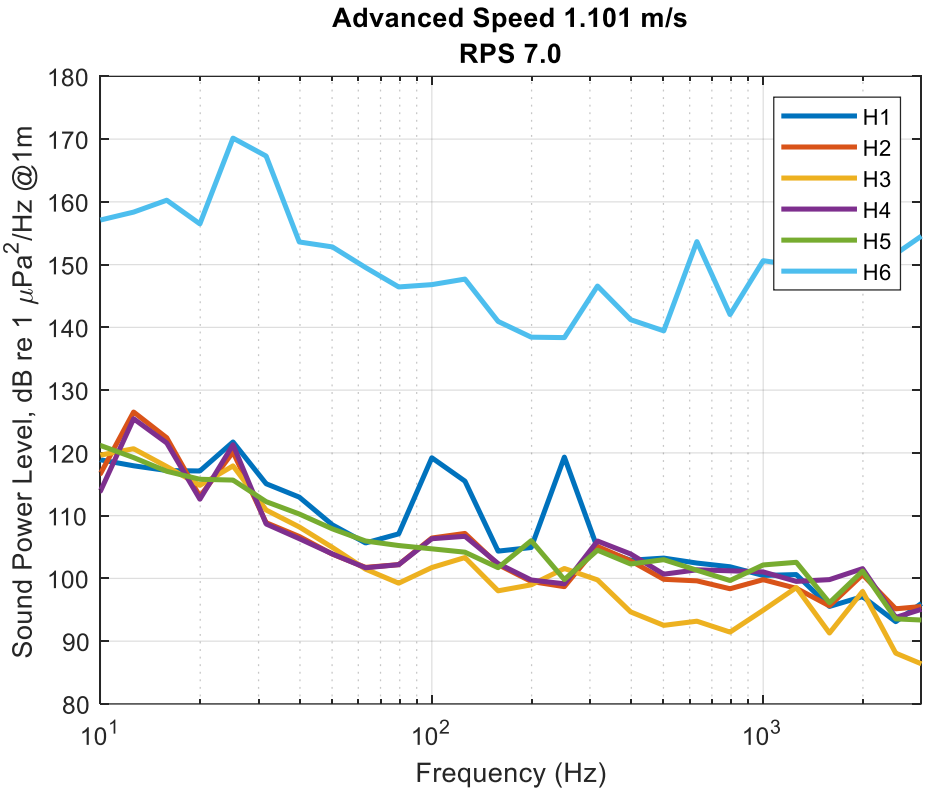


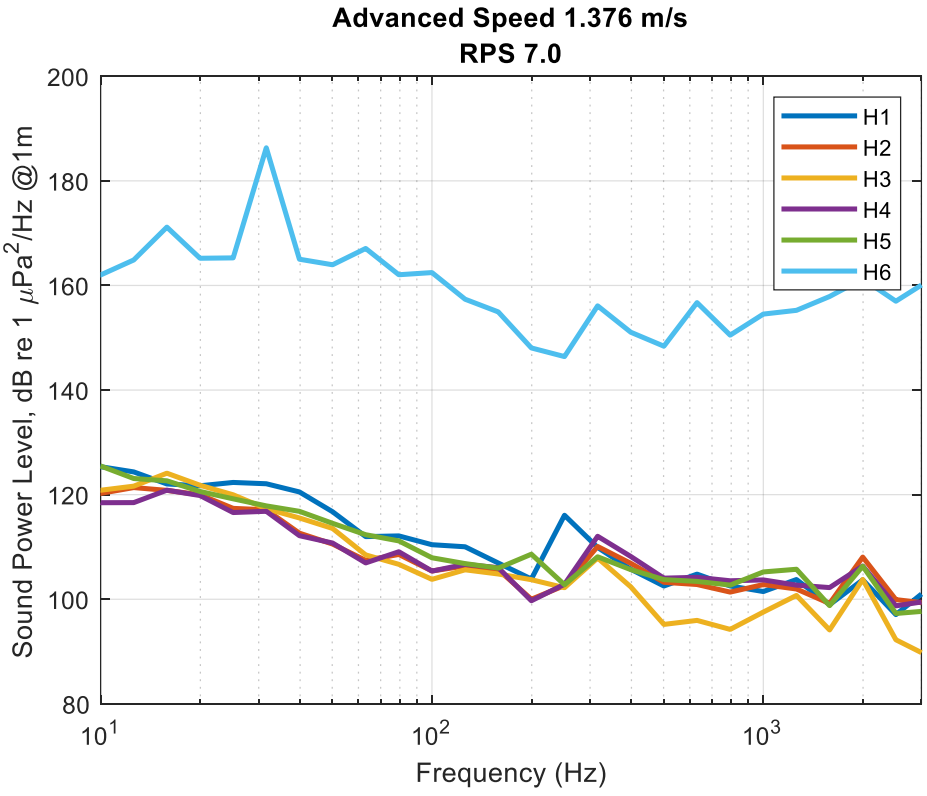

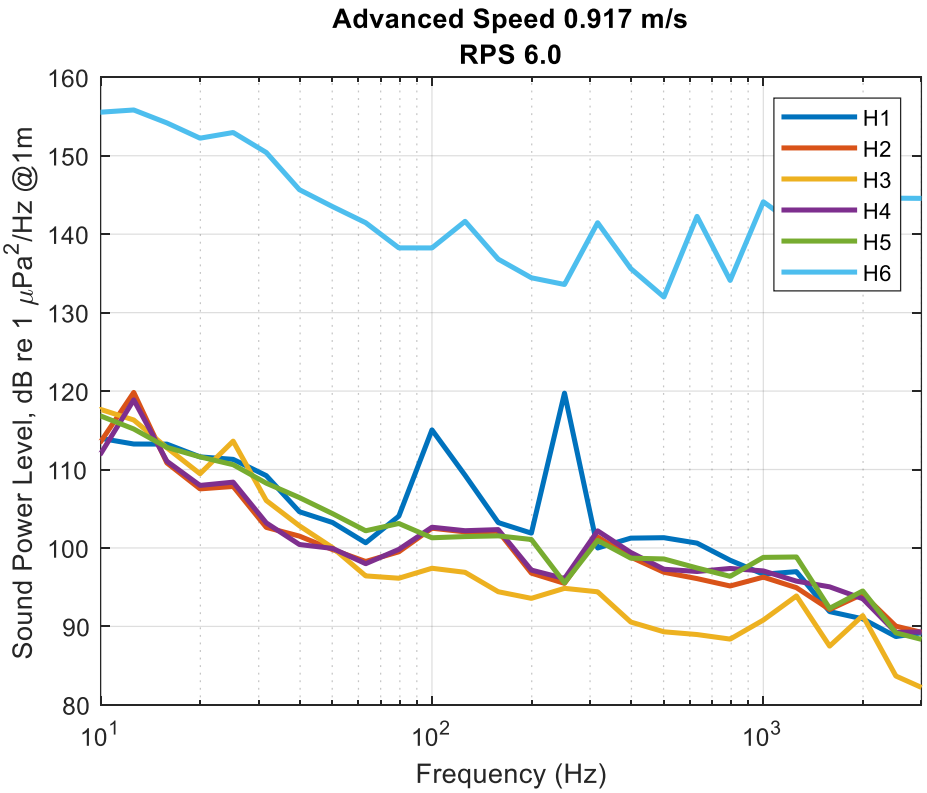
Advanced Speed 0.917 m/s
RPS 6.0
Sound Power Level, dB re 1 μPa²/Hz @1m
Frequency (Hz)
H1
H2
H3
H4
H5
H6

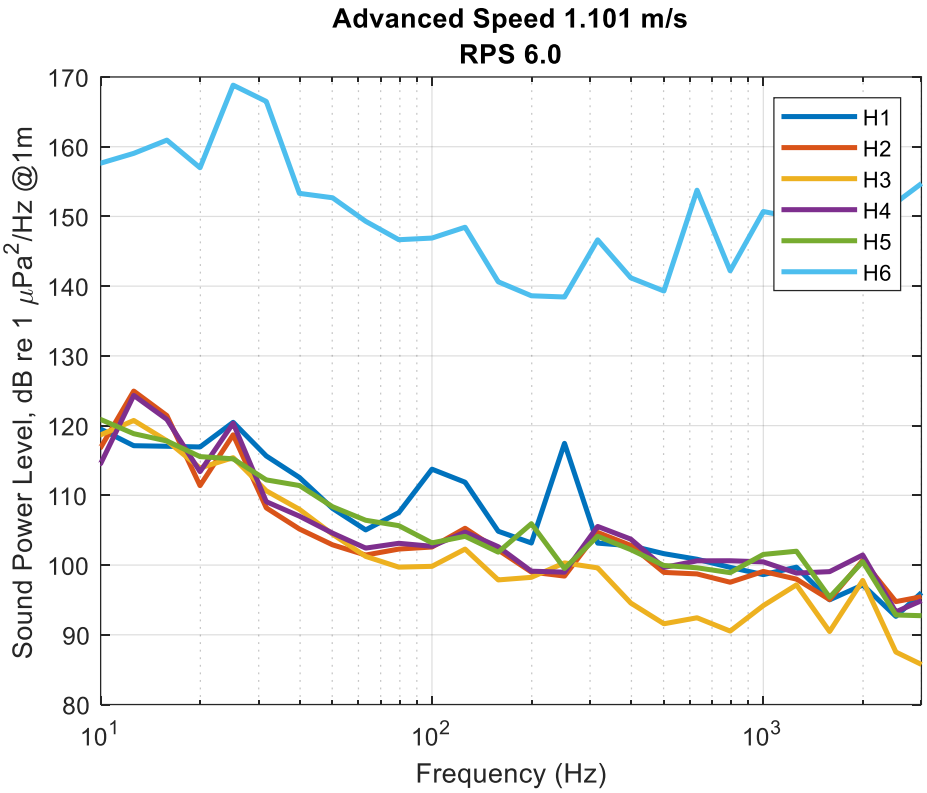
Advanced Speed 1.101 m/s
RPS 6.0
Sound Power Level, dB re 1 μPa²/Hz @1m
Frequency (Hz)
H1
H2
H3
H4
H5
H6

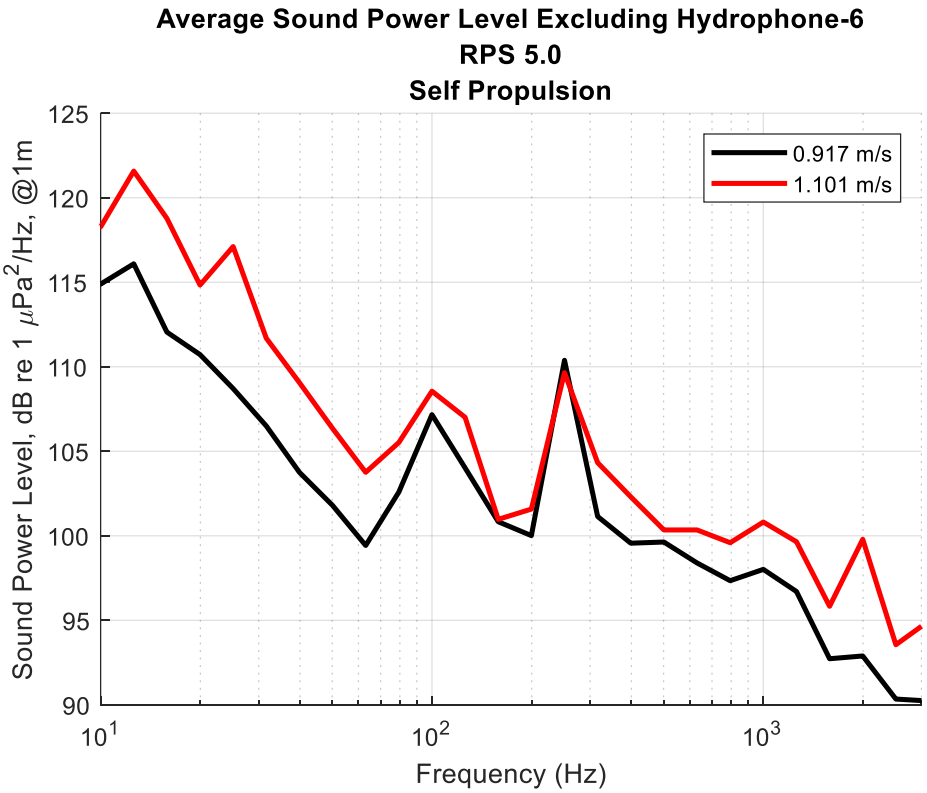
Average Sound Power Level Excluding Hydrophone-6
RPS 5.0
Self Propulsion
0.917 m/s
1.101 m/s
Sound Power Level, dB re 1 μPa²/Hz, @1m
Frequency (Hz)
125
120
115
110
105
100
95
90
10¹
10²
10³

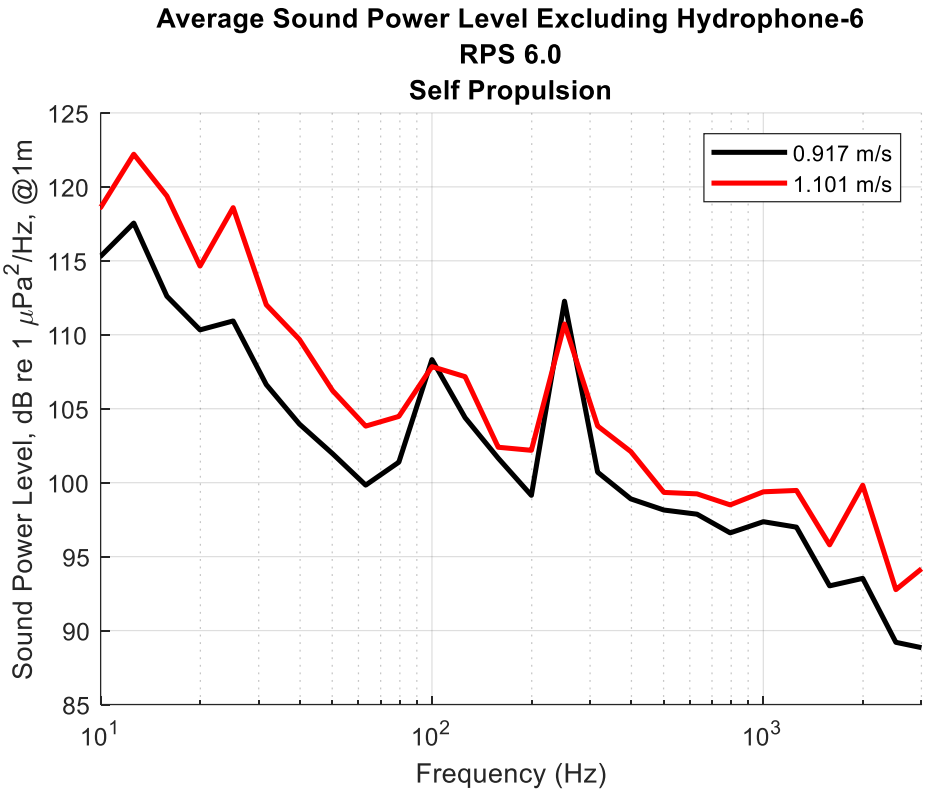
Average Sound Power Level Excluding Hydrophone-6
RPS 6.0
Self Propulsion
0.917 m/s
1.101 m/s
Sound Power Level, dB re 1 μPa²/Hz, @1m
Frequency (Hz)
125
120
115
110
105
100
95
90
85
10¹
10²
10³

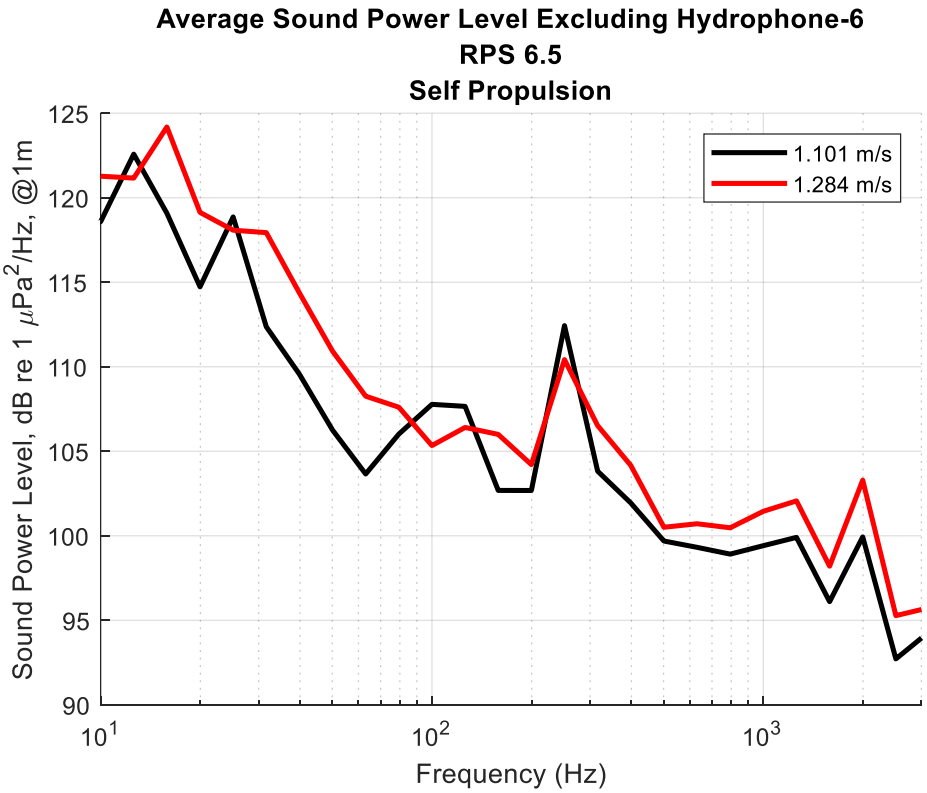
Average Sound Power Level Excluding Hydrophone-6
RPS 6.5
Self Propulsion
1.101 m/s
1.284 m/s
Sound Power Level, dB re 1 μPa²/Hz, @1m
Frequency (Hz)
125
120
115
110
105
100
95
90
10¹
10²
10³

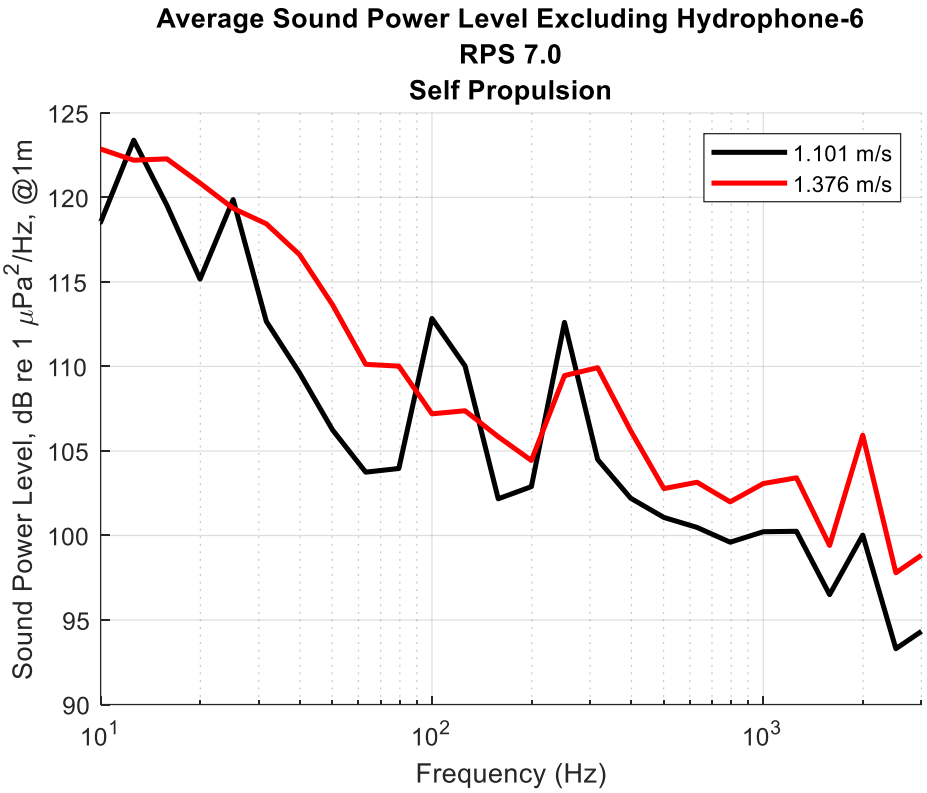
Average Sound Power Level Excluding Hydrophone-6
RPS 7.0
Self Propulsion
1.101 m/s
1.376 m/s
Sound Power Level, dB re 1 μPa²/Hz, @1m
Frequency (Hz)
125
120
115
110
105
100
95
90
10¹
10²
10³

## B-10. Bollard Test (Carriage at Rest, Propeller rotating)

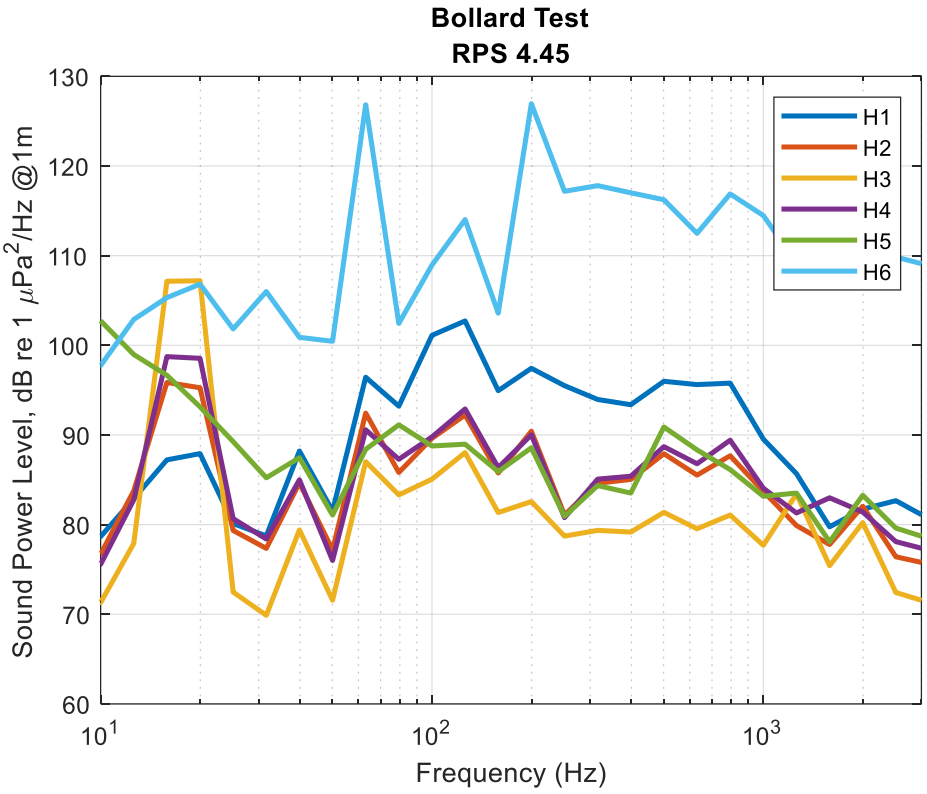


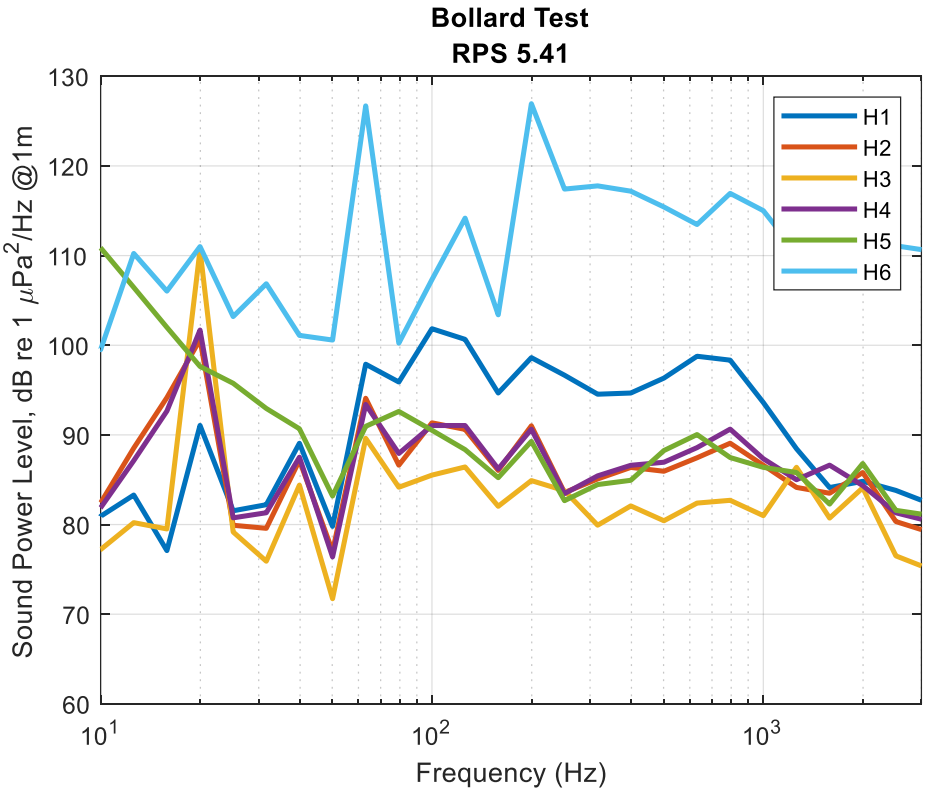

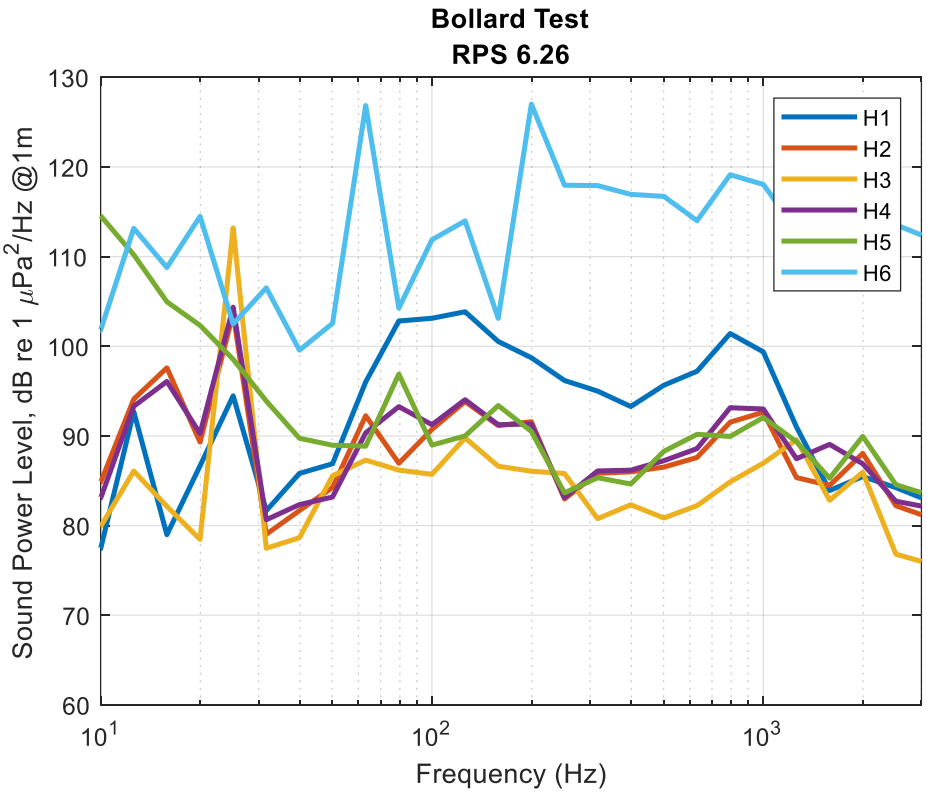
Bollard Test
RPS 6.26
Sound Power Level, dB re 1 μPa²/Hz @1m
Frequency (Hz)
H1
H2
H3
H4
H5
H6

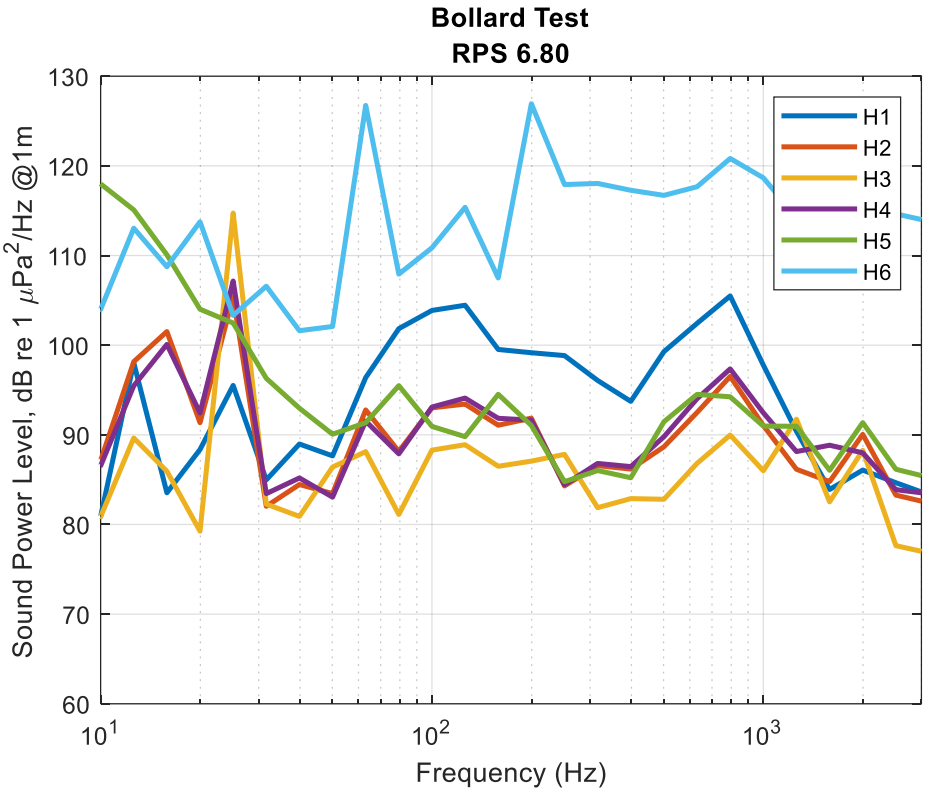
Bollard Test
RPS 6.80
Sound Power Level, dB re 1 μPa²/Hz @1m
Frequency (Hz)
H1
H2
H3
H4
H5
H6

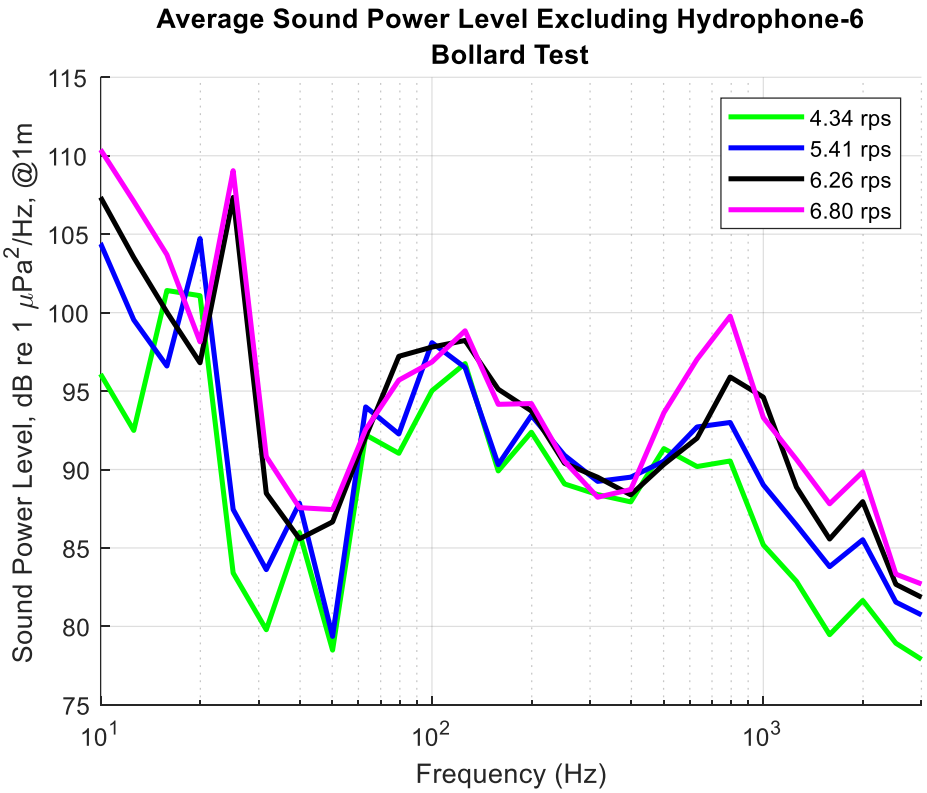


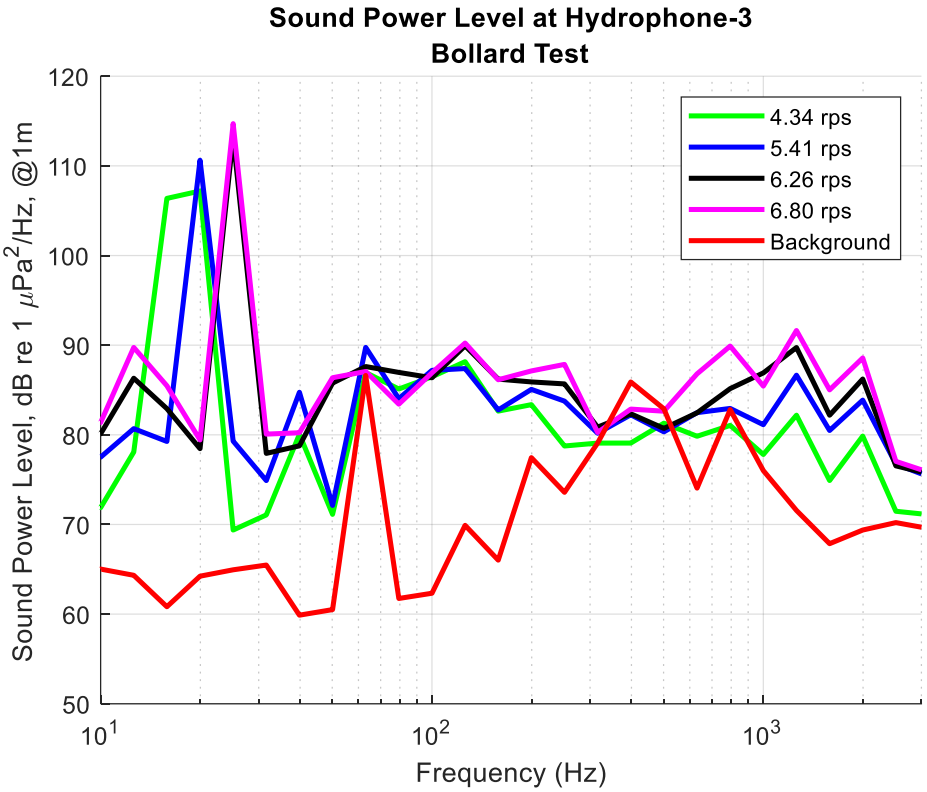


## B-11. Narrow Band Analysis

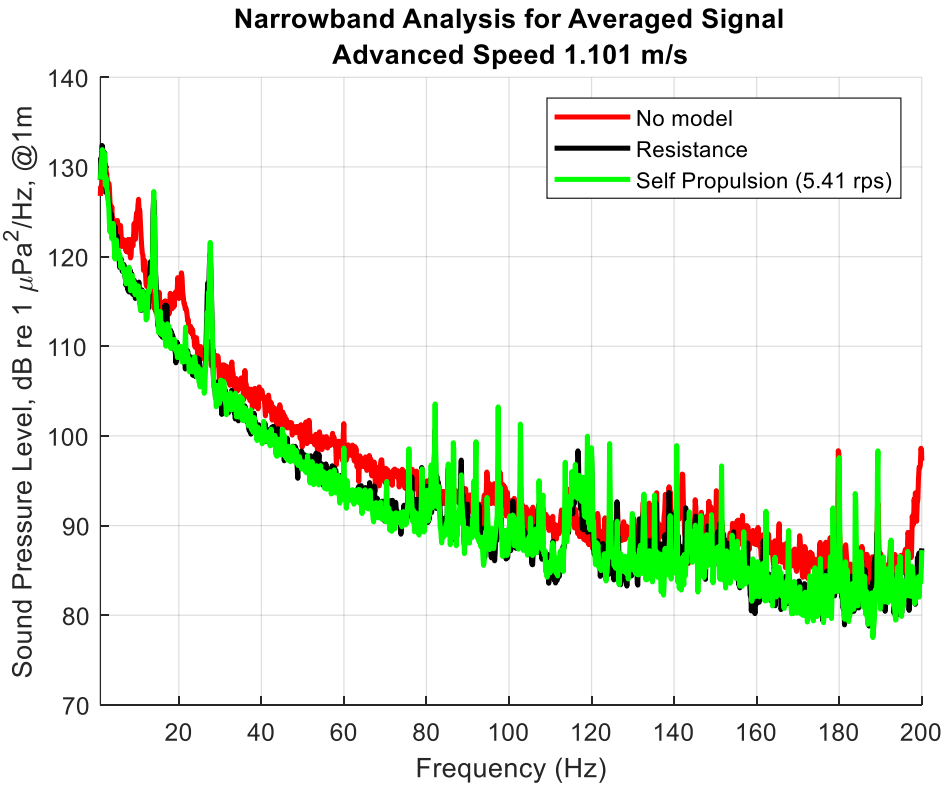
Narrowband Analysis for Averaged Signal
Advanced Speed 1.101 m/s
No model
Resistance
Self Propulsion (5.41 rps)
Sound Pressure Level, dB re 1 μPa²/Hz, @1m
Frequency (Hz)
140
130
120
110
100
90
80
70
20
40
60
80
100
120
140
160
180
200

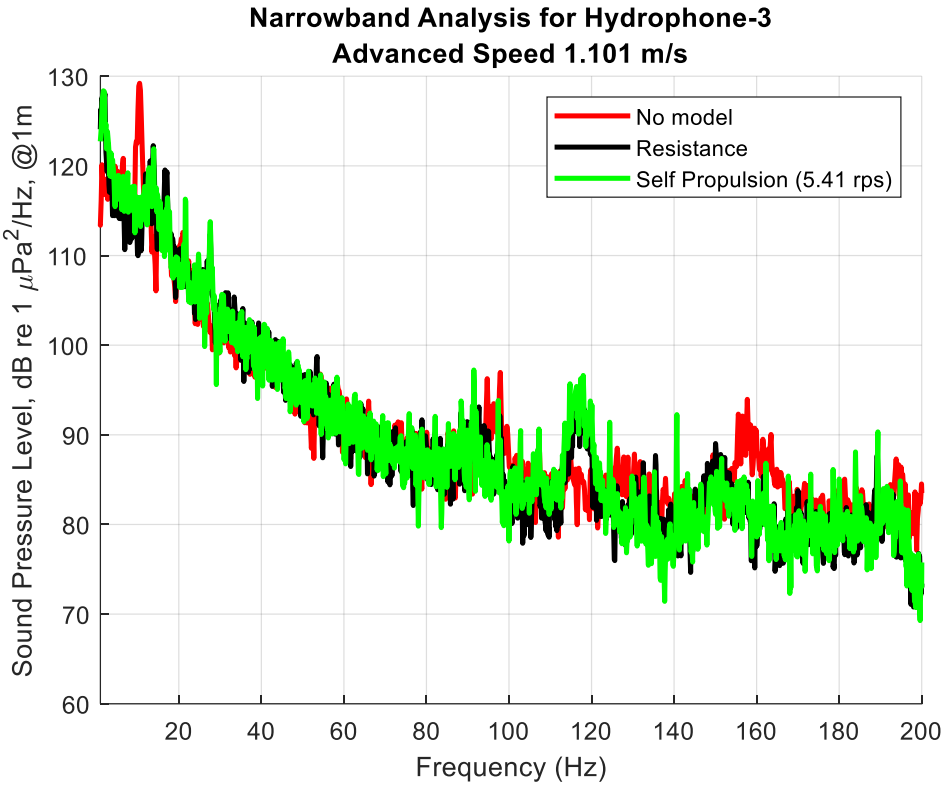
Narrowband Analysis for Hydrophone-3
Advanced Speed 1.101 m/s
No model
Resistance
Self Propulsion (5.41 rps)
Sound Pressure Level, dB re 1 μPa²/Hz, @1m
Frequency (Hz)
130
120
110
100
90
80
70
60
20
40
60
80
100
120
140
160
180
200

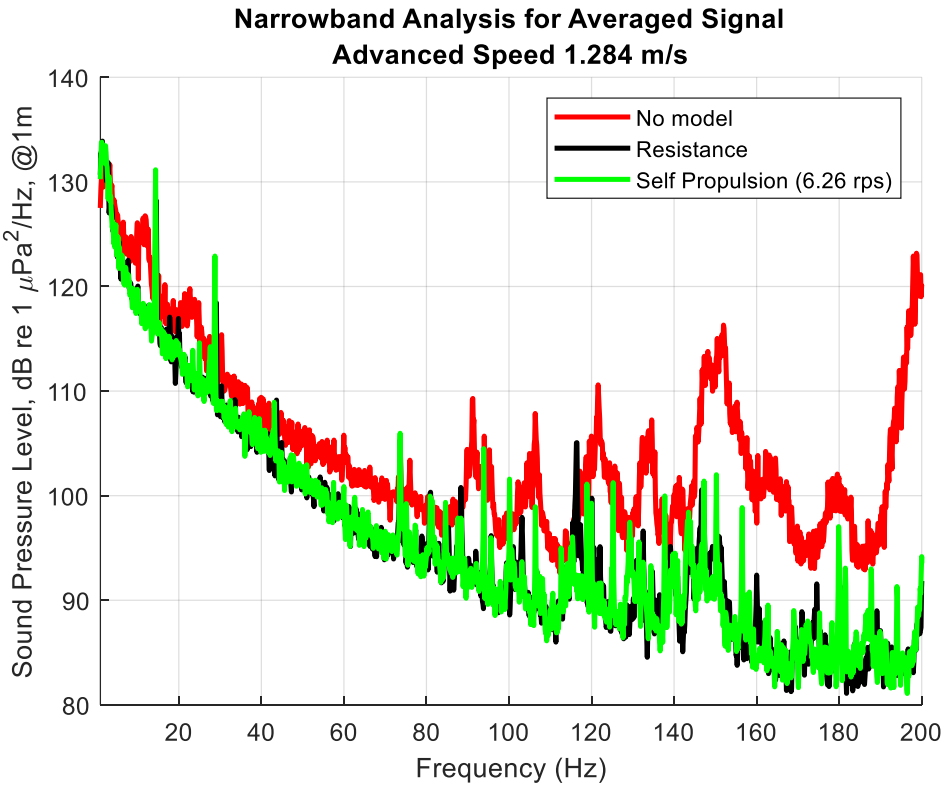
Narrowband Analysis for Averaged Signal
Advanced Speed 1.284 m/s
No model
Resistance
Self Propulsion (6.26 rps)
Sound Pressure Level, dB re 1 μPa²/Hz, @1m
Frequency (Hz)
140
130
120
110
100
90
80
20
40
60
80
100
120
140
160
180
200

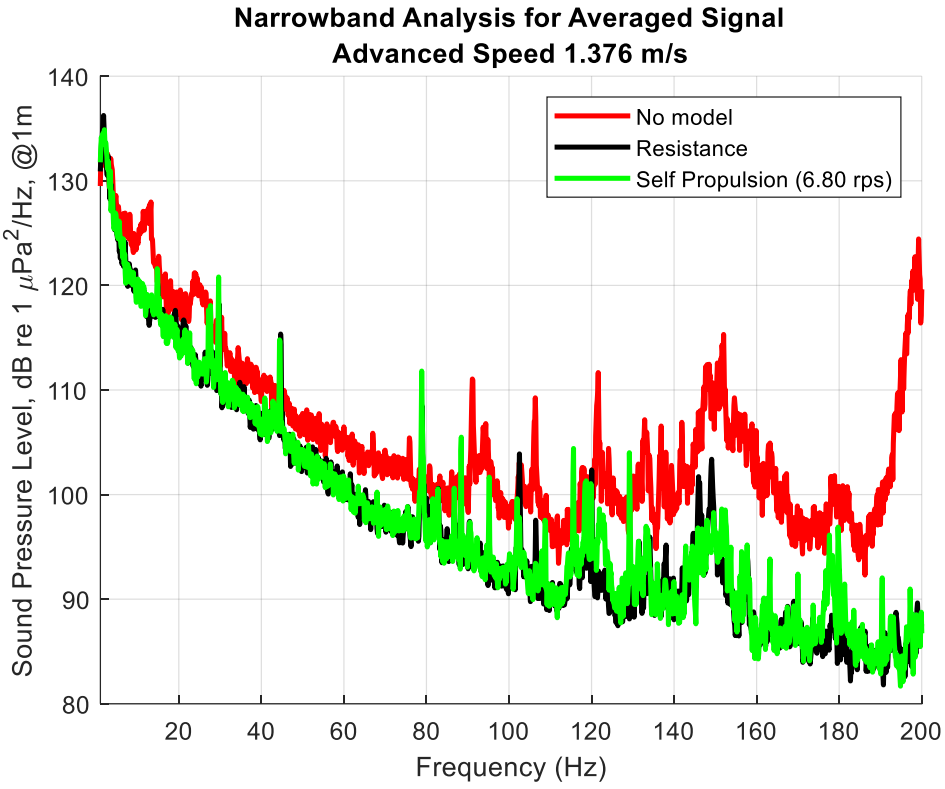
Narrowband Analysis for Averaged Signal
Advanced Speed 1.376 m/s
No model
Resistance
Self Propulsion (6.80 rps)
Sound Pressure Level, dB re 1 μPa²/Hz, @1m
Frequency (Hz)
140
130
120
110
100
90
80
20
40
60
80
100
120
140
160
180
200

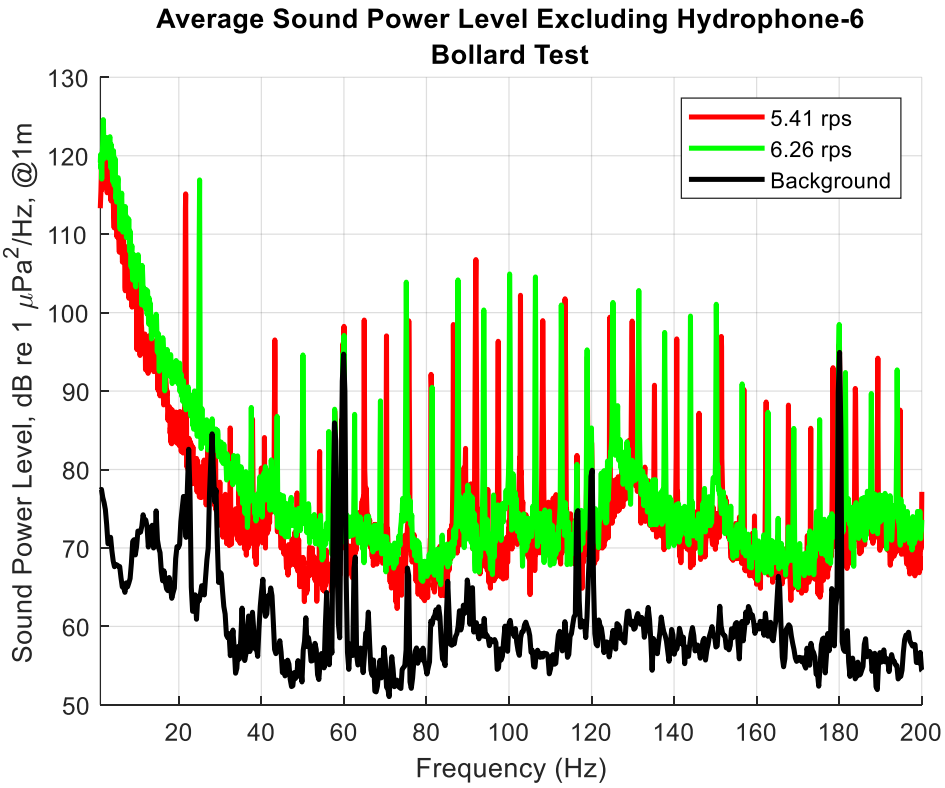
Average Sound Power Level Excluding Hydrophone-6
Bollard Test
5.41 rps
6.26 rps
Background
Sound Power Level, dB re 1 μPa²/Hz, @1m
Frequency (Hz)
130
120
110
100
90
80
70
60
50
20
40
60
80
100
120
140
160
180
200